Mechanistic Physiologically Based Pharmacokinetic (PBPK) Modeling of Renal and Systemic Disposition of Drugs and Metabolites

Weize Huang

A dissertation submitted in partial fulfillment of the requirements for the degree of

Doctor of Philosophy

University of Washington

2020

Reading Committee:

Nina Isoherranen, Chair

Kenneth Thummel

Catherine Yeung

Program Authorized to Offer Degree:

Pharmaceutics

University of Washington

Abstract

Mechanistic Physiologically Based Pharmacokinetic (PBPK) Modeling of Renal and Systemic Disposition of Drugs and Metabolites

Weize Huang

Chair of the Supervisory Committee:

Nina Isoherranen

Department of Pharmaceutics

Physiologically-based pharmacokinetic (PBPK) models integrate system specific anatomy and physiology information with drug specific physicochemical and pharmacokinetic properties to predict drug disposition. Such integration permits items, events, processes, and pathways to communicate and influence each other interactively. By taking advantage of such mechanistic nature of PBPK modeling, drug dispositions under untested scenarios could be predicted by extrapolation from observed data in known conditions. Renal clearance is one of the major pathways governing drug dispositions, which has three main mechanisms: unbound filtration, passive reabsorption, and active secretion. In comparison to intestinal absorption and hepatic metabolism, renal clearance has been relatively underappreciated. Controlled clinical

experiments that test renal clearance changes under altered conditions and mechanisms have been primarily focusing on drug-drug interaction on active secretion. However, huge gaps in understanding renal clearance still exist in other areas such as altered urine pH and impaired renal function. Further, passive reabsorption has not been paid significant attention by the pharmaceutical field. Therefore, the overarching goal of this thesis is to leverage mechanistic PBPK modeling technique to understand and predict renal clearance of drugs and metabolites under altered urine pH and impaired renal function, with a special focus on compounds undergoing significant renal passive reabsorption.

In Chapter 2, to predict the spatiodynamic process of renal passive reabsorption in human, we developed a dynamic physiologically-based mechanistic kidney model based on human data that can integrate drug permeability, tubular surface area, ionization status, and drug concentration gradient between lumen and system to estimate renal passive reabsorption and predict renal clearance of drugs. Using 46 test compounds with a variety of physicochemical properties, the model successfully predicted the renal clearances of 87% compounds within 2-fold and 98% compounds within 3-fold. Further, by incorporating active secretion, the model also successfully predicted the renal clearances of para-aminohippuric acid (PAH), cimetidine, salicylic acid, and memantine.

In Chapter 3, to ensure the simulation output from PBPK models can be meaningfully compared to the arm vein plasma drug concentrations collected in clinical studies, we developed a forearm model that captures the tissue distribution at the peripheral sampling site using human arm physiology data, allowing for a better prediction of plasma drug concentrations that are comparable to observed data. The model was successfully verified using arterial and venous concentrations of nicotine, ketamine, lidocaine, and fentanyl simultaneously. Further, I

demonstrated that use of a discrepant sampling site in PBPK modeling than observed clinical studies may lead to biased model evaluation, erroneous model parameterization, and misleading prediction in unstudied clinical scenarios.

In Chapter 4, to predict the altered renal excretion and systemic AUC of drug and metabolite when urine pH is changed, the mechanistic kidney model developed and verified from Chapter 2 was integrated with the peripheral arm sampling and full body PBPK model developed from Chapter 3. The model was successfully verified with methamphetamine and amphetamine under varying urine pH statuses, and showed feasibility to predict quantitatively and clinically significant changes in drug and metabolite disposition under comedications and diseases that can alter urine pH.

In Chapter 5, to predict renal clearance in patients with impaired renal function such as chronic kidney diseases, physiological changes in tubular flow and urine flow observed in chronic kidney disease patients were incorporated into the mechanistic kidney model developed and verified from Chapter 2. The model accounts for the adaptive renal tubular filtrate flows that decrease disproportionately with glomerular filtration rate, and was successfully verified using three parent-metabolite pairs, six non-permeable drugs, six permeable drugs, and two secreted drugs.

In conclusion, in this thesis, I developed and verified a physiologically-based mechanistic kidney model to translate drug properties such as plasma protein binding, transcellular permeability, and active transport into renal clearance of drugs and metabolites. This mechanistic kidney model allows prediction of alterations in renal clearance of drugs and metabolites upon changes in urine pH and renal functions, and can be incorporated into a full-body PBPK model to predict alterations in systemic disposition of drugs and metabolites.

TABLE OF CONTENTS

LIST OF FIGURES

LIST OF TABLES

ACKNOWLEDGEMENTS

I would like to express my immense gratitude to my advisor, Professor Nina Isoherranen. I was given a huge amount of trust, freedom, and autonomy during my doctoral training, to create ideas, to design plans, and to execute studies. I had all the treasured opportunities to lead my research projects, to explore my career interest, and to pursue everything that adds value to me. I am forever indebted to her for all the trainings, challenges, support, and advise. In the past 7 years, from my Pharm.D. to my Ph.D., I have grown and learned way more than what I could expect.

I would like to express my sincere appreciation to my committee members, Drs. Kenneth Thummel, Catherine Yeung, Jashvant Unadkat, and Beth Devine for their time, guidance, and contributions to my thesis projects. My appreciation also extends to the faculties in the Department of Biostatistics and the Comparative Health Outcomes, Policy, and Economics (CHOICE) Institute for all the didactic trainings that transformed me into a scientist with multi-perspective thinking.

I would like to thank many members in the Dr. Isoherranen's Lab, past and present, for their high tolerance, supports, encouragement, and friendship. I enjoyed all the lab meetings, happy hours, activities, conferences, and philosophical discussions we had together.

Finally, to my Ph.D. cohort and my Pharm.D. study group, thank you for all your help, kindness, and presence in my life. To my family and friends, near or far, thank you for your love and care. To Melody, thank you for taking this journey with me side by side.

DEDICATION

To all beings who wish the best for me

Chapter 1. INTRODUCTION

1.1 Pharmacokinetic (PK) and physiologically-based pharmacokinetic (PBPK) modeling

Pharmacokinetics (PK) is a discipline that describes the fate of substances mainly as biotransformation and movement in a continuous time course. When substances such as therapeutic molecular entities (drugs) are administered into the human body, their fates are governed by four important pharmacokinetic processes: absorption, distribution, metabolism, and elimination (ADME) (Nelson, 1961). Together, these processes determine at what moments these drug substances will be in specific tissues or compartments within the human body, and how long, on average, the drug substances will be in those tissues/compartments once arrived. Blood or plasma is a very special, and conveniently accessible, component of the human body. Bestowed with unique anatomical and physiological characteristics, blood delivers oxygen and nutrients to different organs and tissues at different rates and returns with carbon dioxide and waste to support life. This central function of circulation that the blood provides as a "common convective conduit" (Rowland *et al.*, 2011) allows drug transfer and subsequent important events to take place. As such, the blood/plasma drug concentration is crucial for drug distribution and other pharmacokinetic and pharmacodynamic processes, and has been deemed the central indicator of drug disposition.

1.1.1 Pharmacokinetic modeling

To study drug pharmacokinetics via blood/plasma drug concentration, mathematical instruments are of tremendous help. The pharmacokinetic parameters such as clearance (Möller *et al.*, 1928), mean residence time (Hamilton *et al.*, 1932), volume of the distribution (Hamilton *et al.*, 1932), and half-life ($t_{1/2}$) (Butler *et al.*, 1954; Butler, 1958) were first mentioned in the context of

pharmacokinetics nearly a century ago, to lay the mathematical foundation for the basis of drug elimination and disposition. Soon after, compartmental modeling was introduced (Solomon, 1949, 1953; Reiner, 1953) to further advance the field of pharmacokinetics and bring special values to clinical therapeutics. Driven and defined by clinical PK data, compartmental models empirically address drug transfer rates entering and exiting different compartments, and presumptively assign drug elimination to either central or peripheral compartments, that can collectively best explain the observed PK data. As pharmacokinetics field matured, statistical population modeling was invented (Boxenbaum *et al.*, 1974; Sheiner *et al.*, 1977) and applied alone or with compartmental modeling to explore and determine the sources of variability, the degrees of uncertainty, and the confidence of model parameter estimates from a population perspective, given the individual experimental data. Despite the fact that mathematical compartmental modeling and statistical population modeling provide adequate description and valuable understanding of pharmacokinetic drug properties, certain questions remain difficult to answer: What is the pharmacokinetic and therapeutic impact if one or several processes governing drug disposition (e.g. organ perfusion rate, effective transcellular permeability, protein binding, transporter-mediated uptake and efflux, enzyme-mediated metabolism) are altered? What is the dynamic (i.e. time dependent) magnitude of PK changes when patients take multiple medications or have multiple diseases? What are the intracellular drug concentrations in a specific organ that is the site of pharmacologic action or toxicologic effect? To address the lack of incorporation of anatomy, physiology, and mechanisms in compartmental and population PK modeling, physiologically-based pharmacokinetic (PBPK) models were developed.

1.1.2 **Physiologically-based pharmacokinetic (PBPK) modeling**

Physiologically-based pharmacokinetic (PBPK) models (Figure 1) integrate population or system specific physiological features with drug specific physicochemical and pharmacokinetic properties to describe and predict drug disposition in the populations/systems of interest (Jones *et al.*, 2009). This integration allows different items (e.g. drug entities, proteins, membranes), events (e.g. drug-protein binding, catalytic reaction), processes (e.g. blood flow, drug movement and permeation), and pathways (e.g. cascade signaling, enzyme-mediated sequential metabolism, transporter-mediated vectorial uptake and efflux) to communicate and influence each other within a single system as drugs and different components of human bodies indeed interact interdependently. By capturing this complicated network weaved by mechanisms, in principle, we may gain a better insight on how exactly the human body handles drugs (i.e. pharmacokinetics), and how drugs in turn affect the human body (i.e. pharmacodynamics). This holistic concept could potentially date back to as early as 1937 where Teorell generated the idea of simulating drug disposition in a multi-compartment environment that represents the actual physiology (Teorell, 1937a; b). To mathematically realize this multi-compartment concept to resemble human physiology and simulate drug disposition, a matrix of at least three sets of differential equations and parameters need to be specified. The first set describes the systemic circulation and the transfer/delivery of drugs to the site of entry of different compartments, the second set describes the drug entry into different compartments (usually either perfusion rate-limited or membrane permeability-limited) governed by passive diffusion or active processes, the third set describes the events and pathways occurring within each compartment including intracellular binding, enzymatic reactions, active efflux, and other biochemical processes. The whole system can be written in ordinary differential equations which assume that all

compartments are homogeneous and drug distribution within an individual compartment is instantaneously complete. Alternatively, partial differential equations can be used to describe both spatial and temporal profile of drugs if necessary. For example, to simulate drug handling within the liver compartment and how intracellular hepatic metabolism affects overall hepatic clearance, two models were created: well-stirred (i.e. venous equilibrium) (Wilkinson and Shand, 1975) and parallel-tube (i.e. undistributed sinusoidal) (Pang and Rowland, 1977) hepatic models. The former model represents a homogeneous liver compartment with drug concentrations from all regions within liver being the same, while the latter model assumes a gradient of drug concentrations established within the liver, decreasing from the locations near the portal vein to the locations near the hepatic vein. More complicated heterogeneous hepatic models such as the distributed model and the dispersion model were also introduced and applied (Roberts and Rowland, 1986). Yet, even today, a consensus on model appropriateness and superiority has not been reached within the pharmacokinetics community (Sodhi *et al.*, 2020). To generalize the lessons learned from hepatic organ modeling to PBPK systemic modeling, when given different perspectives (temporal or spatial), assumptions (homogeneous or heterogeneous), and objectives, different mathematical framework (ordinary or partial differential) can be constructed as the underpinning infrastructure of PBPK models to answer questions of particular interest. One significant technique to capture the heterogeneous nature of the physiological system while remaining computationally inexpensive, is to generate a series of ordinary differential equation-based homogeneous compartments that are connected sequentially to portray the longitudinal characteristics of the system. This transit modeling technique was shown to produce satisfactory mathematical approximation when compared to partial differential equation-based solutions (Bischoff, 1967; Himmelstein and Lutz, 1979), and meanwhile retain the readiness of

computation and allow meaningful physiologically-based interpretation. Further, the transit modeling technique had been successfully applied decades ago to describe drug disposition in segment-based intestinal lumen to accurately predict drug absorption in a longitudinal fashion (Agoram *et al.*, 2001; Jamei *et al.*, 2009). In this thesis, the transit modeling technique was also applied to establishing an *in silico* kidney model (Chapter 2) that resembled the longitudinal nature of renal tubules.

1.1.3 A brief history of PBPK model development and applications

Solving a multi-compartment system (either ordinary or partial differential-based) demands adequate *in silico* power for efficient execution/numerical calculation. As such, PBPK modeling was not carried out until 1960s and 1970s, when PBPK models of thiopental (Bischoff and Dedrick, 1968), methotrexate (Dedrick *et al.*, 1973), lidocaine (Benowitz *et al.*, 1974), and digoxin (Harrison and Gibaldi, 1977) were initially developed and verified in animals such as dog, rat, and monkey, using physiological values, observed plasma and tissue binding, and relevant pharmacokinetic parameters in respective species. Later in the 1980s and 1990s, many PBPK models were developed to estimate environmental toxin exposures within the human body since it is unethical to characterize toxins in humans; *in silico* methods are the most appropriate approaches for risk assessment (Andersen *et al.*, 1987, 1991; Bois *et al.*, 1991). For drug discovery and development, it was gradually realized that unfavorable pharmacokinetic properties observed in humans that were not anticipated before clinical trials were the main reasons for drug candidate failure (Prentis *et al.*, 1988; Kennedy, 1997). As such, after 2000, PBPK modeling started to attract attention from the pharmaceutical industry because of its great promise to *a priori* predict drug pharmacokinetics and disposition parameters in humans, such as

absorption profile and bioavailability (Agoram *et al.*, 2001). Such predictions facilitate decision making and optimizes the development pipeline (Rowland *et al.*, 2011). Over the recent decade, PBPK modeling has been implemented into many commercial and open source platforms such as Simcyp, Gastroplus, and PK-Sim to maximize convenience of user experience. The application of PBPK modeling has grown to more than simulations in animals, simulations of toxin disposition, and estimations of pharmacokinetic properties (e.g. bioavailability) in humans; nowadays, PBPK modeling has a multitude of valuable applications ranging from designing optimal first-in-human (FIH) dose to predicting drug disposition in vulnerable patient populations (Jones *et al.*, 2006a; Rowland *et al.*, 2011; Grillo *et al.*, 2012; Huang and Rowland, 2012; Jones *et al.*, 2013; Wagner *et al.*, 2015a). These modeling applications have also been accepted and endorsed by regulatory agencies. Specifically, the FDA has reported that 61%, 30%, and 9% of PBPK simulations in NDA submissions were used for PK predictions in DDI, specific populations, and different absorption scenarios, respectively (Huang *et al.*, 2013).

1.1.4 **Existing knowledge gaps in PBPK modeling**

Despite the great potential and variety of applications of PBPK modeling, knowledge gaps remain in model development, verification, and application. Specifically, system models that can sufficiently capture physiological characteristics and integrate them with pharmacokinetic processes for unique organs such as kidney, brain, and lung have not been well-developed and extensively verified. Further, model verification of independent mechanisms such as hepatic uptake vs hepatic metabolism, or renal secretion vs renal reabsorption, have not been commonly adopted. Rather, AUC and C_{max} remain as the primary targets used for model verification, and scalars are commonly applied to different individual pathways to recover observed AUC and

C_{max}. When directly comparing simulated to observed plasma drug concentrations, a discrepancy of sampling sites often exists between PBPK models and clinical studies. This could lead to false comparisons between simulation and observation and therefore misleading model evaluation and verification. Finally, model application has not been extended to all clinical scenarios such as altered urine pH. Certain applications, such as predicting drug disposition in patient populations including chronic kidney disease patients, have demonstrated feasibility but are considered to be low-confidence. In this thesis, I address these knowledge gaps in PBPK modeling, with a special focus on the prediction of renal and systemic disposition of drugs and metabolites in multiple settings.

1.2 Development of physiologically-based pharmacokinetic (PBPK) models

The development of PBPK models consists of two independent steps, 1) establishing the drug-specific model that contains the physicochemical (e.g. molecular weight, LogP, pK_a) and pharmacokinetic (e.g. tissue-to-plasma partition coefficient, enzyme-mediated metabolic clearance, transporter-mediated uptake/efflux clearance) properties of the molecules of interest, and 2) establishing the system-specific model that sufficiently describes the anatomical and physiological characteristics of the biological system of interest (e.g. rat, monkey, human) at appropriate level [e.g. cell type level (hepatocyte vs hepatic stellate cells), organ level (different segments of gastrointestinal tract), whole body level] to capture the specific processes (cell type-specific metabolism/uptake, organ-specific elimination).

1.2.1 Development of drug model

For drug model development, there are three mainstays of methodology: the bottom-up, top-down, and middle-out approach. The bottom-up approach uses in vitro experiments and in silico algorithms to estimate key parameters such as permeability, protein/tissue binding, and intrinsic clearance as model inputs. This approach can be helpful and informative during the early drug discovery phase as a part of high-throughput tasks to select the best drug candidates with optimal PK characteristics such as intestinal absorption (Kaur et al., 2018), and can also be used to predict first-in-human (FIH) dose for optimal clinical trial design (Offman and Edginton, 2015; Miller et al., 2019). On the contrary, the top-down approach uses pharmacokinetic data collected in human subjects and pharmacokinetic parameters such as systemic clearance and volume of distribution to back-calculate intrinsic and mechanistic parameter values as model inputs using retrograde calculation or empirical optimization. This approach can be used to identify the need

to conduct certain clinical studies such as drug-drug interaction studies (Zhao et al., 2011) to facilitate internal decision making and regulatory submissions for new drug entities (Huang and Rowland, 2012). Lastly, the middle-out approach combines the strength of both bottom-up approach (e.g. deeper mechanistic insight) and top-down approach (e.g. better accuracy). It has recently gained increasing popularity in the field (Tsamandouras et al., 2015; Rostami-Hodjegan, 2018) and showed successful applications to predict drug disposition in varying populations (Rowland Yeo et al., 2011; Zhang and Unadkat, 2017) and may be extended to untested clinical scenarios.

1.2.2 Development of system model

For system model development, the anatomical and physiological characteristics of the biological system at appropriate level need to be captured and incorporated into the model for specific purposes. For example, when drug absorption and bioavailability after oral dosing are of interest, the advanced compartmental absorption and transit (ACAT) model (Agoram *et al.*, 2001) and advanced dissolution, absorption and metabolism (ADAM) model (Jamei *et al.*, 2009) that capture gastrointestinal physiology can be useful. In short, the ACAT and ADAM models integrate physiological processes and parameters such as gastric emptying, intestinal transit, luminal surface area, volume, and pH of all relevant intestinal segments with pharmacokinetic drug properties such as dissolution rate, solubility, permeability, and intestinal uptake, efflux, and metabolism to simulate the drug absorption profile after oral administration. This allows translation from *in vitro* data to pharmacokinetic parameters in humans (e.g. oral absorption rate constant (k_a) and oral absorption extent/fraction absorbed (F_a)), that may drive drug discovery and development decisions. In addition, complicated physiologically-based liver models such as the hepatic zonal model that incorporates the differential expression of enzyme at different

locations within the liver has also been developed (Liu and Pang, 2006) to allow a potentially more accurate prediction of hepatic clearance from *in vitro* data.

1.2.3 Knowledge gaps in system model of kidney and predicting renal clearance

Kidney is an extremely important organ from both a vitality perspective and a drug disposition perspective, in addition to intestine and liver. Surprisingly, physiologically-based kidney models have received little attention and renal clearance has been overall underappreciated in comparison to hepatic drug clearance and intestinal drug absorption. Renal clearance has been estimated as the major clearance pathway for 25-31% of medications (Williams *et al.*, 2004; Varma *et al.*, 2009), and contributes as a minor elimination pathway to the clearance of majority of drugs. Renal clearance has three main mechanisms: unbound filtration, transporter-mediated secretion, and bidirectional passive diffusion; transporter/receptor-mediated active reabsorption and intracellular and intraluminal renal metabolism may also take place in rare occasions (Knights *et al.*, 2013).

Two kinds of empirical methods have been used to predict renal drug clearance in humans without detailed understanding of individual renal drug handling mechanisms: 1) quantitative structure activity relationship (QSAR) analysis (Manga *et al.*, 2003; Doddareddy *et al.*, 2006; Paine *et al.*, 2010) that is useful in large scale screening and provides a qualitative prediction of high or low renal clearance, and 2) allometric scaling (Huh *et al.*, 2011; Paine *et al.*, 2011) from animal renal clearance to human renal clearance. However, inter-species differences in kidney structure and physiology (e.g. GFR, tubular surface area, urine pH), transporter expression and activity, and plasma protein binding remain as challenges for allometric scaling (Huang and Riviere, 2014). Further, neither empirical method allows differentiation of clearance mechanisms or dynamic simulations of renal handling of drugs.

Because of the convoluted interplay between multiple mechanisms in the renal handling of drugs, detailed understanding of individual mechanisms is critical for successful renal clearance predictions. To predict renal clearance mechanistically, two static renal clearance prediction approaches have been published (Kunze *et al.*, 2014; Scotcher *et al.*, 2016) and a dynamic mechanistic kidney model has been reported and incorporated into Simcyp software (Neuhoff *et al.*, 2013). However, static approaches do not incorporate how water reabsorption and subsequently increasing drug concentrations affect passive diffusion processes as no concentration gradient is established between blood, tubular cells, and tubular lumen. For the reported dynamic kidney model (Neuhoff *et al.*, 2013) comprehensive validation of the model structure, physiological parameters (e.g. tubular pH, flow, and surface area), and performance of predicting passive diffusion with a variety of drugs with known renal clearances and *in vitro* permeability data has not been reported. Still, several studies have used the Simcyp kidney model to simulate drug renal clearances (Posada *et al.*, 2015; Burt *et al.*, 2016; Emami Riedmaier *et al.*, 2016; Mori *et al.*, 2016; Scotcher *et al.*, 2017; Wang *et al.*, 2017) with the application of a variety of scaling factors in order to accurately capture observed data. This suggests a considerable knowledge gap in establishing high-confidence kidney models and producing accurate renal clearance prediction.

In Chapter 2, I created a physiologically-based mechanistic kidney model that captures unbound filtration, passive diffusion, and active secretion, and longitudinally incorporates all the renal segments parameterized with actual surface areas and tubular filtrate flows observed in humans. We further verified the kidney model using 46 test drugs and demonstrated successful prediction of renal drug clearance using plasma unbound fraction, *in vitro* permeability data and proximal cell-based active secretion data.

1.3 Verification of physiologically-based pharmacokinetic (PBPK) models

After the development of PBPK models, it is critical to conduct appropriate and rigorous model evaluation and verification before the ultimate use of the model for interpolation and extrapolation to untested scenarios. Importantly, the mechanistic basis of PBPK model is what enables its tremendous potential. Therefore, the evaluation and verification of individual mechanistic process and pathways is necessary if these mechanisms are pivotally involved at the heart of the ultimate applications. To test if the pertinent mechanisms are incorporated appropriately, simulation exercises and observed data with altered metabolism (e.g. CYP3A4 inhibition) or a gradient of varying parameters (e.g. urine pH varying from 5 to 8) are needed to demonstrate the mechanistic credibility/confidence in PBPK models. This is critically necessary as parameter unidentifiability issues are notorious for causing failure in model extrapolation. For example, hepatic clearance, renal clearance, and volume of distribution can be readily determined as single parameters from *in vivo* studies after intravenous dosing; however, the delineated individual contribution from hepatic uptake, enzyme metabolism, and biliary excretion towards to the hepatic clearance is difficult to determine. Likewise, renal transporter-mediated secretion and passive reabsorption are challenging to differentiate, and individual tissue-to-plasma partition coefficients for the 12 major organs/tissues within a conventional full-body PBPK model are often unknown. This is concerning as unlimited combinations of hepatic pathways, renal pathways, and tissue-to-plasma coefficients can give rise to the exact same observed single value of hepatic clearance, renal clearance, and total body volume of distribution, respectively. Consequently, due to parameter unidentifiability, empirically optimized PBPK models are likely to contain mis-specified mechanistic parameters which may lead to erroneous estimation of plasma drug concentration time profile, systemic AUC, and

tissue accumulation when part of the mechanisms (e.g. enzyme activity, transporter activity) are altered during extrapolation (e.g. coadministration with drugs that inhibit relevant enzymes and transporters). To address this issue, it is essential to verify the individual mechanisms separately in the absence of other processes or keeping all other processes constant.

1.3.1 Verification of renal clearance mechanisms

Renal clearance has three predominant mechanisms: unbound filtration, transporter-mediated secretion, and bidirectional passive diffusion. Unbound filtration can be readily and accurately determined by plasma unbound fraction and glomerular filtration rate. In contrast, transporter-mediated secretion is usually estimated *in vitro* by comparing cellular uptake between transfected cells and mock cells, which currently has low confidence for extrapolation to *in vivo* mainly due to the lack of total quantification of transporter expression at the barrier epithelium in both experimental cell lines and human proximal cells. Further, bidirectional passive diffusion is also challenging to quantify as it depends on not only transcellular permeability of drug, but also the ionization status at different environments/milieu within the body and the available surface area that allows drug molecules to encounter and pass through.

Despite the high uncertainty in understanding and quantifying active secretion and passive diffusion, several studies have recently used the Simcyp kidney model to simulate drug renal clearance (Posada *et al.*, 2015; Burt *et al.*, 2016; Emami Riedmaier *et al.*, 2016; Mori *et al.*, 2016; Scotcher *et al.*, 2017; Wang *et al.*, 2017). Most of these studies used a top-down or middle-out approach and applied a variety of scaling factors to simulate plasma concentrations or renal clearance with either fitted active secretion (Posada *et al.*, 2015; Burt *et al.*, 2016; Emami Riedmaier *et al.*, 2016; Scotcher *et al.*, 2017; Wang *et al.*, 2017) or passive diffusion clearance

(Mori *et al.*, 2016) in order to accurately capture observed data. Although the passive diffusion clearance in these studies was based on permeability values from PAMPA, Caco-2, and HEK cells, these values were further scaled using either sensitivity analyses or presumed total tubular surface area without systematic verification to recapitulate observed data. This introduces potential bias to the modeling approach, as fitting active secretion values requires high confidence in the passive diffusion clearance in the kidney as the observed renal clearance is highly dependent on both parameters. In the absence of validation of the passive diffusion clearance in the kidney, the confidence in scaled secretion clearance is low and interdependent on the error in predicted diffusion clearance. Furthermore, most studies do not consider the different ionization of the test compounds in blood, cells, and tubular fluid, and assume that passive diffusion is equal for apical and basolateral sides and across different tubular segments despite known physiological differences between these sites.

As such, there is a critical need to validate the physiological and permeability components of a mechanistic kidney model using drugs that are not subject to significant active transport, to allow better mechanistic predictions of renal drug clearance, and to estimate the contribution of active transport processes to renal clearance. Therefore, the aim of Chapter 2 of this thesis was to develop and validate a physiologically-based mechanistic kidney model that allows prediction of renal drug reabsorption by considering *in vitro* permeability data from multiple sources, human physiology of renal tubular surface area and filtrate flow of each renal segment, and segment-dependent microvilli and filtrate pH value. This kidney model with extensively verified passive diffusion parameters allows much higher confidence when optimizing active secretion and extrapolating to untested scenarios.

1.3.2 Verification of simulated plasma concentration-time profile

For full body PBPK models where absorption, distribution, metabolism, and elimination are all accounted for simultaneously, metrics such as simulated/observed AUC or C_{max} ratio may not be the most appropriate indicators to assess model verification. Rather, a useful evaluation metric should assess the concordance between simulated and observed plasma drug concentration directly and provide holistic appraisal of the model quality. For example, the absolute average fold error (AAFE) (eq. 1).

$$AAFE = 10^{\frac{1}{n}\Sigma\left|log_{10}\frac{Simulated}{Observed}\right|} \quad (1)$$

In general, the AAFE calculation treats all the time data points equally, in some cases, a pre-specified weighing scheme may be applied to the AAFE calculation if absorption phase or terminal phase are of particular interest. In addition, appropriate statistical criteria are also needed to interpret the calculated metrics that essentially translate into successful or unsuccessful model verification. It could be argued that a 1.25-fold range can be deemed as the most rigorous criteria as FDA uses a 0.8-1.25-fold range for the 90% confidence interval of the ratio of the log-transformed AUC or C_{max} from reference drug and test drug when evaluating generic drug bioequivalence.

With a useful metric (e.g. AAFE) and a stringent criterion (e.g. 1.25-fold), the last component for appropriate PBPK model evaluation and verification is conducting meaningful comparisons. In other words, deciding what is outputted from PBPK model simulation, and whether it matches the pharmacokinetic data collected from clinical study. Can the PBPK model simulation output be meaningfully compared to the observed pharmacokinetic data? Typically, the simulation output of a PBPK model is the drug concentration in the central venous compartment that drains blood from the tissue/organ compartments (Kuepfer *et al.*, 2016). This central compartment is

built into the PBPK models as a mixed compartment that merges all the tissue/organ-specific veins. Physiologically, this central venous compartment resembles the right atrium where the superior and inferior vena cava merge together. However, in clinical practice and in pharmacokinetic studies, plasma samples (i.e. the observed data) are usually taken from a peripheral sampling site such as the median cubital vein (i.e. arm vein). This generates a concerning discrepancy between the modelled and observed data, as measured drug concentrations from arm artery, which are essentially equivalent to the drug concentrations in the right atrium (assuming lung distribution is not significant and distribution equilibrium in the lung is reached instantaneously), have been shown to differ from concentrations in peripheral vein for multiple drugs (Chiou, 1989; Gourlay and Benowitz, 1997; Ericsson *et al.*, 2000; Rentsch *et al.*, 2001; Persson *et al.*, 2002; Darwish, Kirby, *et al.*, 2006; Olofsen *et al.*, 2010). This arteriovenous difference has been shown to affect pharmacokinetic-pharmacodynamic (PK-PD) modeling (Gumbleton *et al.*, 1994; Jacobs and Nath, 1995; Tuk *et al.*, 1997), resulting in mis-specified PK-PD models that fail to predict PD in untested scenarios. Similarly, for PBPK modeling, the simulated concentration profiles, model evaluation, model verification, and model extrapolation can also be impacted by the choice of the model sampling site.

In Chapter 3, to address this concern in model verification and assessment of model performance, a physiologically-based forearm compartment was developed and verified as the peripheral sampling site in the PBPK model using fentanyl, lidocaine, ketamine, and nicotine as model compounds. The verified peripheral sampling site allows collection of simulation results that can be meaningfully compared to observed pharmacokinetic data sampled from arm vein for appropriate model evaluation and verification.

1.4 Application of physiologically-based pharmacokinetic (PBPK) models

Successfully developed and verified PBPK models have a multitude of valuable applications (Jones *et al.*, 2006a; Rowland *et al.*, 2011; Huang and Rowland, 2012; Jones *et al.*, 2013; Wagner *et al.*, 2015a). These applications range from estimating optimal PK characteristics such as intestinal absorption in the drug discovery phase (Agoram *et al.*, 2001; Jamei *et al.*, 2009; Kaur *et al.*, 2018), to optimizing first-in-human (FIH) dose for better clinical trial design in the early development phase (Offman and Edginton, 2015; Miller *et al.*, 2019), to predicting drug disposition in specific patient populations in late development or even post-marketing phases for appropriate drug labeling (Johnson *et al.*, 2010; Zhao *et al.*, 2011; Grillo *et al.*, 2012; Zhang *et al.*, 2017).

Despite the many successful applications shown so far, PBPK modeling has not been extended to all clinical scenarios such as altered urine pH. Certain applications have demonstrated feasibility but are still considered low-confidence, such as predicting drug disposition in chronic kidney disease patients. In Chapters 4 and 5, I will address these knowledge gaps in PBPK modeling of altered renal clearance due to changes in urine pH and the presence of chronic kidney disease.

1.4.1 Predicting altered renal clearance with varying urine pH

To further appreciate renal clearance and the convoluted interplay between different mechanisms, it is instrumental to understand how urine pH affects renal clearance. The effect of urine pH on renal clearance was discovered for weak acids and bases more than half a century ago in studies with salicylic acid (Macpherson *et al.*, 1955) and methamphetamine (Beckett and Rowland, 1965c). The mechanism behind this phenomenon is believed to be the altered

ionization status of weak acids and bases with changes in renal tubular filtrate pH, and the subsequent alterations in renal passive reabsorption of unionized drugs (Milne *et al.*, 1958; Tucker, 1981). Changes in renal passive reabsorption can have a drastic impact on renal clearance. For example, with urine pH decrease from alkaline (pH ≈ 7.5-8.5) to acidic (pH ≈ 4.5-5.5), the amount of drug excreted unchanged in urine for weak bases such as pethidine, methamphetamine, and mexiletine can increase up to 21-fold (Chan, 1979), 48-fold (Beckett and Rowland, 1965c), and 87-fold (Kiddie *et al.*, 1974), respectively, while the renal clearance of weak acids such as chlorpropamide (Neuvonen and Kärkkäinen, 1983) and salicylic acid (Macpherson *et al.*, 1955) can decrease by 99% and 97%, respectively. Also, after dosing of imipramine, methamphetamine, and amitriptyline, the urinary excretion of their respective metabolites desipramine, amphetamine, and nortriptyline has been shown to increase up to 5-fold (Gram *et al.*, 1971), 11-fold (Beckett and Rowland, 1965b), and 93-fold (Kärkkäinen and Neuvonen, 1986) respectively, in acidic urine condition in comparison to alkaline urine condition. These findings demonstrate the pronounced and broad significance of the urine pH effect on both drugs and metabolites.

Overall, approximately 31% of marketed drugs are significantly excreted unchanged via the kidney (Varma *et al.*, 2009), and 70% of marketed drugs are either monoprotic weak acids or monoprotic weak bases (Manallack, 2007) that may have varying ionization statuses in the tubular lumen. In addition, the mean logP of patented compounds across 18 pharmaceutical companies ranged from 3.5 to 4.5 (Leeson and St-Gallay, 2011), suggesting that the majority of drugs have a moderate- to high- intrinsic lipophilicity and therefore transcellular permeability. Together, these data suggest that many drugs are potentially subject to significant renal clearance and effective renal passive reabsorption that can be altered due to urine pH changes. As such, the

variability of renal clearance with urine pH can be surprisingly common. Indeed, more than a dozen drugs have been shown to have urine pH-dependent renal excretion (Macpherson *et al.*, 1955; Beckett and Rowland, 1965a; c; Sharpstone, 1969; Sjöqvist *et al.*, 1969; Gerhardt *et al.*, 1969; Gram *et al.*, 1971; Kiddie *et al.*, 1974; Chan, 1979; Neuvonen and Kärkkäinen, 1983; Muhiddin *et al.*, 1984; Benowitz and Jacob, 1985; Aoki and Sitar, 1988; Freudenthaler *et al.*, 1998).

If renal excretion is an important elimination pathway for the drug of interest, the systemic drug disposition will also be affected by altered urine pH. For example, for weak bases memantine and flecainide, the area under the plasma drug concentration-time curve ($AUC_{0\text{-}inf}$) increased by 5.3-fold (Freudenthaler *et al.*, 1998) and 3.6-fold (Muhiddin *et al.*, 1984), respectively, while for weak acids cinoxacin and chlorpropamide, the plasma $AUC_{0\text{-}inf}$ decreased by 67% (Barbhaiya *et al.*, 1982) and 81% (Neuvonen and Kärkkäinen, 1983), respectively, in alkaline urine condition in comparison to acidic urine condition. This demonstrates that the magnitude of urine pH effect on plasma AUC could be as significant as drug-drug interactions resulting from co-administration with a strong inhibitor or inducer (i.e. AUC increased by 5-fold or decreased by 80%). Given the number of known drugs affected by urine pH and the substantial magnitude of observed urine pH effects on drug and metabolite disposition, it is striking that urine pH effects on drug and metabolite renal and systemic disposition are not routinely examined for weak acids and bases in clinical studies, and regulatory agencies have not developed guidelines to assess drug safety under different urine pHs.

In Chapter 4, I applied PBPK modeling to predict the urine pH effect on parent and metabolite renal and systemic drug disposition. Specifically, I integrated the developed and verified dynamic physiologically-based mechanistic kidney model from Chapter 2 (Huang and

Isoherranen, 2018) with a parent-metabolite full body physiologically based pharmacokinetic (PBPK) model from Chapter 3 (Huang and Isoherranen, 2020) to simulate the effect of altered urine pH on parent-metabolite systemic disposition and urinary excretion using methamphetamine and amphetamine as model compounds.

1.4.2 Predicting altered renal clearance with varying stages of chronic kidney disease

Chronic kidney disease (CKD) is a progressive illness that is pathologically heterogeneous (Levey and Coresh, 2012) and systemic (Zoccali *et al.*, 2017). It is mainly characterized by declining functional nephron mass and glomerular filtration rate (GFR) (Bricker *et al.*, 1960). As such, GFR is a critical index for CKD diagnosis, progression, and classification (KDIGO, 2013). Clinically, patients with severe (stage 4, GFR~15-29 mL/min) and end stage (stage 5, GFR<15 mL/min) CKD are at high risk for comorbidities, polypharmacy, and adverse drug reactions (Thomas *et al.*, 2008; Chapin *et al.*, 2010; Secora *et al.*, 2018; Schmidt *et al.*, 2019), necessitating careful medication management due to dramatically altered pharmacokinetics (PK) associated with CKD. As a result, clinical characterization of drug disposition in CKD patients is critically important. Prior to dedicated renal impairment studies during drug development, predicting the disease effects on drug PK and estimating the optimal dosing regimen is challenging and often unreliable. Empirically, for highly renally eliminated drugs, the optimal regimen can be estimated by reducing the dosage proportionally with the estimated (Cockcroft and Gault, 1976; Levey *et al.*, 2009) GFR lost in target patient population. This assumes all renal drug handling pathways and therefore renal clearance (CL_r) decrease proportionally with filtration. Indeed, this proportional assumption is supported by clinical data for multiple predominantly filtered drugs (Blair *et al.*, 1981; Blum *et al.*, 1994) without significant secretion

or reabsorption. However, for highly renally secreted drugs, CL_r may decrease more than proportionally with GFR in stage 4/5 CKD (Hsueh *et al.*, 2016; Chapron *et al.*, 2017), possibly due to inhibition of renal transporters by accumulated uremic solutes. Further, for highly renally reabsorbed drugs, CL_r can decrease less than proportionally with GFR in stage 4/5 CKD (Welling *et al.*, 1975; Houghton *et al.*, 1985; Montay *et al.*, 1985). Together, observed clinical data consistently show that empirical/proportional GFR scaling approach may not accurately predict CL_r in severe CKD due to the multiplicity and convoluted interaction of disease effects on renal drug handling. To overcome this challenge, physiologically-based pharmacokinetic (PBPK) models that capture the disease-specific characteristics are potentially able to predict CKD effects on drug PK, although such practice is currently considered as a low-confidence application by regulatory agencies (Grimstein *et al.*, 2019). Recently, PBPK modeling has been used to specifically predict the CKD effect on renal active secretion (Hsu *et al.*, 2014; Hsueh *et al.*, 2018; Yee *et al.*, 2018), but the test drugs used for model verification all lack significant permeability and hence passive reabsorption. At present, no PBPK model can quantitatively predict the alterations in renal passive reabsorption or CL_r for highly reabsorbed drugs in CKD, let alone systematically capture the diverse effects of CKD on renal elimination.

Physiologically, CKD patients have demonstrated reduced water reabsorption/increased tubular filtrate flows per remaining functional nephron (Lindberg *et al.*, 1966; Sharpstone, 1969; Welling *et al.*, 1973, 1975; Yeh *et al.*, 1975; Fukuda *et al.*, 2006; Nechita *et al.*, 2015) as an adaptative mechanism. This adjusts for the reduced number of functional nephrons and reduced GFR, to maintain critical homeostasis such as extracellular fluid volume and plasma sodium concentration (Biber *et al.*, 1968; McNay and Miyazaki, 1973; Yeh *et al.*, 1975; Pennell and Bourgoignie, 1981; Fukuda *et al.*, 2006). In Chapter 5, we tested the hypothesis that such

physiological adaptation in renal tubular water reabsorption and tubular filtrate flow will dramatically decrease the drug concentration gradient between intratubular filtrate and peritubular blood, leading to reduced passive reabsorption and higher CL_r than expected from residual GFR alone in CKD. This hypothesis is supported by observed data (Welling *et al.*, 1975; Houghton *et al.*, 1985; Montay *et al.*, 1985) for various permeable drugs such as pefloxacin, metronidazole, and minocycline. For these drugs, the observed CL_r in CKD patients was reduced to 30-37% compared with healthy subjects when residual GFR was only 4-9% compared with healthy subjects (Welling *et al.*, 1975; Houghton *et al.*, 1985; Montay *et al.*, 1985), demonstrating an over 7-fold disproportionality between resulting CL_r and GFR.

In Chapter 5, I developed a disease model to predict the effect of CKD on tubular passive reabsorption and renal clearance for hydrophobic permeable drugs. Specifically, this work expands our previously developed and verified mechanistic kidney model from Chapter 2 (Huang and Isoherranen, 2018) to incorporate the physiologically-based tubular changes of reduced water reabsorption/increased tubular filtrate flow per remaining functional nephron for each renal subsegment across varying CKD stages. The final adaptive kidney model enables the translation from *in vitro* drug permeability into degree of passive reabsorption and renal clearance, and was validated using a set of 20 compounds with differing properties without any optimization or empirical scaling throughout the progression of CKD from healthy to stage 5 kidney disease.

1.5 Hypothesis and aims

The overarching hypothesis of this thesis was that mechanistic physiologically-based kidney modeling can be used to predict renal clearance of drugs and metabolites with a variety of physicochemical properties and under different clinical conditions such as altered urine pH and chronic kidney disease. This mechanistic kidney model can be further integrated into full body PBPK models to simulate both renal and systemic disposition in a multitude of scenarios.

To test this hypothesis, my specific aims were:

Aim 1) To develop a dynamic physiologically-based 35-compartment mechanistic kidney model that addresses the impact of dynamic tubular flow, tubular pH, microvilli, and multi-source permeability on effective passive diffusion and subsequent renal clearance simulation, verify the model with 46 test compounds including neutrals, acids, bases, and zwitterions, and demonstrate the feasibility of incorporating active secretion and pH-dependent bidirectional passive diffusion.

Aim 2) To develop a physiologically-based peripheral forearm sampling site model together with a full body PBPK model that allows the output of simulated peripheral venous concentrations to be meaningfully compared to the observed pharmacokinetic data from arm vein, verify the model with nicotine, ketamine, lidocaine, and fentanyl, and demonstrate the consequentially biased model evaluation, erroneous model parameterization, and misleading prediction in unstudied clinical scenarios when using a discrepant sampling site in PBPK modeling than observed clinical studies.

Aim 3) To integrate the mechanistic kidney model with peripheral arm sampling and full body PBPK model to predict the altered renal excretion and systemic AUC of drugs when urine pH is changed, verify the combined final model with methamphetamine and amphetamine under varying urine pH statuses, and demonstrate the feasibility of predicting quantitatively and

clinically significant changes in drug and metabolite disposition under comedications and diseases that can alter urine pH.

Aim 4) To incorporate relevant physiological changes in chronic kidney disease patients into the mechanistic kidney model including adaptive renal tubular filtrate flows that decrease disproportionately with glomerular filtration rate, verify the model with three parent-metabolite pairs, six non-permeable drugs, six permeable drugs, and two secreted drugs, and demonstrate the impact of physiologically-based adaptive changes in tubular filtrate flow on renal clearance prediction for reabsorbed, non-reabsorbed, secreted, and non-secreted compounds in chronic kidney disease patients.

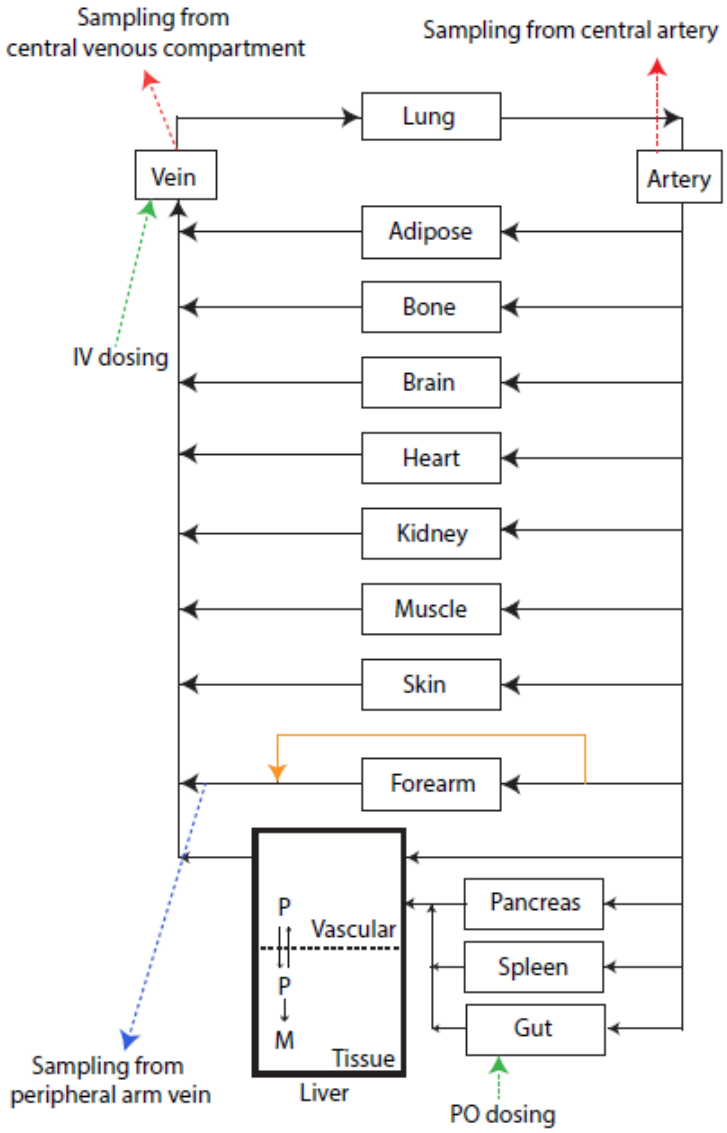

Figure 1.1. The schematic representation of a full body PBPK model structure.

Chapter 2. DEVELOPMENT OF A DYNAMIC PHYSIOLOGICALLY-BASED MECHANISTIC KIDNEY MODEL TO PREDICT RENAL CLEARANCE

This chapter was published in *CPT: Pharmacometrics & Systems Pharmacology (2018) 7, 593-602*

2.1 Abstract

Renal clearance is usually predicted via empirical approaches including QSAR and allometric scaling. Recently, more mechanistic prediction approaches using in silico kidney models have been proposed. However, empirical scaling factors are typically used to adjust for either passive diffusion or active secretion, to acceptably predict renal clearances. The goal of this study was to establish a renal clearance simulation tool that allows prediction of renal clearance (filtration and pH-dependent passive reabsorption) from in vitro permeability data. A 35-compartment physiologically-based mechanistic kidney model was developed based on human physiology. The model was verified using 46 test compounds including neutrals, acids, bases, and zwitterions. The feasibility of incorporating active secretion and pH-dependent bidirectional passive diffusion into the model was demonstrated using cimetidine, memantine, and salicylic acid. The developed model enables simulation of renal clearance from in vitro permeability data, and predicted the renal clearance of 87% of the test drugs within 2-fold.

2.2 Introduction

Renal clearance has been estimated as the major clearance pathway for 25-31% of medications (Williams *et al.*, 2004; Varma *et al.*, 2009) and contributes as a minor elimination pathway to the clearance of majority of drugs. Therefore, prediction of renal clearance during drug development is important. In addition, detailed understanding of renal clearance processes is critical to delineate the quantitative contributions of passive diffusion and active secretion in renal drug elimination. Finally, increased interest in renal toxicity and accumulation of drugs in renal tubular cells necessitates improved physiological and mechanistic modeling of drug distribution and clearance in the kidney.

To predict renal clearance, quantitative structure activity relationship (QSAR) methods have been proposed (Manga *et al.*, 2003; Doddareddy *et al.*, 2006; Paine *et al.*, 2010). While QSAR methods are useful in large scale screening and provide a qualitative prediction of high or low renal clearance, they do not allow mechanistic understanding or dynamic simulations of renal disposition. Allometric scaling from animals has also been used extensively (Huh *et al.*, 2011; Paine *et al.*, 2011) to predict human renal clearance. However, inter-species differences in kidney structure and physiology (e.g. GFR, tubular surface area, urine pH), transporter expression and activity, and plasma protein binding remain as challenges for allometric scaling (Huang and Riviere, 2014). Similarly, allometric scaling does not allow differentiation of clearance mechanisms or dynamic simulations of renal handling of drugs. To address the weaknesses of QSAR and allometric scaling, two static renal clearance prediction approaches have been published (Kunze *et al.*, 2014; Scotcher *et al.*, 2016), and a dynamic mechanistic kidney model has been reported and incorporated into Simcyp software (Neuhoff *et al.*, 2013). However, static approaches do not incorporate how water reabsorption and subsequently increasing drug

concentrations affect passive diffusion processes as no concentration gradient is established between blood, tubular cells, and tubular lumen. For the reported dynamic kidney model (Neuhoff *et al.*, 2013), comprehensive validation of the model structure, physiological parameters (e.g. tubular pH, flow, and surface area), and performance of predicting passive diffusion with a variety of drugs with known renal clearances and in vitro permeability data has not been reported. Still, several studies have used the Simcyp kidney model to simulate drug renal clearances (Posada *et al.*, 2015; Burt *et al.*, 2016; Emami Riedmaier *et al.*, 2016; Mori *et al.*, 2016; Scotcher *et al.*, 2017; Wang *et al.*, 2017). Most of these studies used a top-down or middle-out approach and applied a variety of scaling factors to simulate plasma concentrations or renal clearance with either fitted active secretion (Posada *et al.*, 2015; Burt *et al.*, 2016; Emami Riedmaier *et al.*, 2016; Scotcher *et al.*, 2017; Wang *et al.*, 2017) or passive diffusion clearance (Mori *et al.*, 2016) to accurately capture observed data. Although the passive diffusion clearance in these studies was based on permeability values from PAMPA, Caco-2, and HEK cells, these values were further scaled using presumed total tubular surface area without systematic verification, or using sensitivity analyses to fit observed data. This introduces potential bias to the modeling approach. Most studies did not consider the different ionization of the test compounds in blood, cells, and tubular fluid, and assumed that passive diffusion is equal for apical and basolateral sides and across different tubular segments despite known physiological differences between these sites. It is important to note that fitting active secretion values requires high confidence in the passive diffusion clearance in the kidney as the observed renal clearance is highly dependent on both parameters. In the absence of validation of the passive diffusion clearance in the kidney, the confidence in scaled secretion clearance is low and interdependent on the error in predicted diffusion clearance. As limited in vitro-to-in vivo scaling data exists for renal transport clearances for the specific segments of the

kidney, the uncertainty of active transport predictions is high. As such, there is a critical need to validate the physiological and permeability components of a mechanistic kidney model using drugs that are not subject to significant active transport, to allow better mechanistic predictions of renal clearance of novel compounds, and to estimate the contribution of active transport processes to renal clearance. The aim of this study was to develop and validate a dynamic physiologically-based mechanistic kidney model that allows prediction of drug renal clearance using in vitro permeability data and incorporates unbound filtration, active tubular secretion, and pH dependent bidirectional passive diffusion.

2.3 Methods

2.3.1 Structure of the mechanistic kidney model

The 35 compartment mechanistic kidney model (Figure 2.1) was developed using MATLAB and Simulink platform (MATLAB, 2016). The detailed description of model development and the governing equations are shown below:

The equation describing the change of blood drug concentration in the central compartment (the circulation component) with respect to time is:

$$V_c \frac{d[C_b]}{dt} = Ro\left(1 - e^{-\frac{Q_c}{V_b}.t}\right) + Q_{other}C_b(t) + Q_{kidney}C_{CDB,5}(t) - Q_cC_b(t)$$

$$Q_c = Q_{other} + Q_{kidney}$$

where C_b is blood concentration (mg/L), V_b is central compartment volume (L), R_0 is iv infusion rate (mg/hr), Q_c is cardiac output (330 L/hr), Q_{kidney} is blood flow to kidney (90 L/hr), Q_{other} is blood flow to other organs (L/hr), $C_{CDB,5}$ is blood concentration in the vascular section of the fifth subsegment of collecting duct (L/hr)

After the infusion began, the drug could partition into red blood cells and bind to plasma proteins, but only unbound drug in plasma could be filtered into Bowman's capsule from glomerular blood (renal inflow). The equation describing the change of drug concentration in the Bowman's capsule with respect to time is:

$$C_{bowman}(t) = \frac{f_{u,p}}{BP} C_b(t)$$

where $f_{u,p}$ is plasma unbound fraction, BP is blood to plasma concentration ratio and C_{bowman} is drug concentration in the Bowman's capsule after filtration (mg/L).

After the drug in the blood is filtered into the Bowman's capsule, it enters the mechanistic kidney model divided into the various subsegments and sections as described above. The segments and sections are linked in series as shown in Figure 2.1.

The filtered drug will first enter the tubular lumen of the proximal tubule. Bidirectional passive diffusion across the apical tubular membrane, active secretion from proximal tubule cells, active reabsorption from the tubular lumen, and tubular fluid inflow and outflow occur in the tubular lumen. The equation describing the change of drug concentration in the proximal tubular lumen at each subsegment with respect to time is:

$$V_{PT} \frac{d\left[C_{PT,i}\right]}{dt} = Q_{PT,i} C_{PT,i-1}(t) - Q_{PT,i+1} C_{PT,i}(t)$$
$$+ CL_{Api,scr,i} C_{PC,i}(t) f_{u,cell} - CL_{Api,reabs,i} C_{PT,i}(t)$$
$$+ CL_{PD,PT,api,i} (C_{PC,i}(t) f_{u,cell} \cdot \beta - C_{PT,i}(t) \cdot \alpha_i))$$

where i=1, 2, and 3, represent the three different proximal tubule subsegments, $C_{PT,i}$ is the drug concentration in the tubular lumen of i^{th} subsegment of proximal tubule (mg/L), $C_{PT,0}= C_{bowman}$, V_{PT} is the volume of each subsegment of proximal tubular lumen (L) as listed in Table 2.1, $Q_{PT,i}$ is the tubular flow rate into the tubular lumen of i^{th} subsegment of proximal tubule (L/hr), $Q_{PT,i+1}$ is the tubular flow rate out of tubular lumen of i^{th} subsegment of proximal tubule (L/hr). The flow rates for each subsegment are listed in Table 2.2. Of note, $Q_{PT,1}= Q_{GFR}$ (120mL/min). Subsequently the tubular flowrate out of any subsegment is always equal to the tubular flow rate into the next subsegment. $CL_{Api,scr,i}$ is the active transporter-mediated secretion clearance on the apical side of cell compartment of i^{th} subsegment of proximal tubule (L/hr). $CL_{Api,reabs,i}$ is the active transporter-mediated reabsorption clearance on the apical side of cell compartment of i^{th} subsegment of proximal tubule (L/hr), $f_{u,cell}$ is the intracellular unbound fraction in the renal cell, $CL_{PD,PT,api,i}$ is the intrinsic passive diffusion clearance on the apical side of cell compartment of i^{th} subsegment of proximal tubule (L/hr), α_i is the uncharged fraction inside the tubular lumen of i^{th} subsegment of proximal tubule, and β is the uncharged fraction inside cell. As the pH inside tubular cells is 7.2 through the kidney, β is a constant value for a specific drug defined by the pKa of the drug. The α and β are calculated from the known pKa and acid/base characteristics of the drug.

Once the drug flows out of the proximal tubule, it flows into the loop of Henle (descending and ascending), distal tubule, and collecting duct (connecting tubule, initial collecting duct, cortical collecting duct, medullary collecting duct, and papillary duct). No active secretion or active reabsorption was assumed to occur in the loop of Henle, in the distal tubule or in the collecting duct. Only bidirectional passive diffusion and tubular inflow and outflow were incorporated. The equation describing the change of tubular drug concentration in the loop of Henle, distal tubule, and collecting duct with respect to time is:

$$V_{Tj,i}\frac{d[C_{Tj,i}]}{dt} = Q_{Tj,i}C_{Tj,i-1}(t) - Q_{Tj,i+1}C_{Tj,i}(t)$$
$$+ CL_{PD,j,i}(C_{Cj,i}(t)\,f_{u,cell}\cdot\beta - C_{Tj,i}(t)\cdot\alpha_{j,i}))$$

where i=1,2 for loop of Henle, i=1 for distal tubule, i=1,2,3,4,5 for collecting duct, j=loop of Henle, distal tubule, or collecting duct. $C_{Tj,i}$ is the drug concentration of the tubular lumen of i^{th} subsegment of j segment (mg/L), $V_{Tj,i}$ is the volume of the tubular lumen of i^{th} subsegment of j segment (L), $Q_{Tj,i}$ is the renal tubule inflow of the tubular lumen of i^{th} subsegment of proximal tubule of j segment (L/hr), $Q_{PT,i+1}$ is the renal tubule outflow of the tubular lumen of i^{th} subsegment of proximal tubule of j segment (L/hr), $CL_{PD,j,i}$ is the intrinsic passive diffusion clearance of both apical and basolateral sides of cell compartment of i^{th} subsegment of j segment (L/hr), $\alpha_{j,i}$ is the uncharged fraction inside the tubular lumen of i^{th} subsegment of segment j.

In terms of the renal cellular compartment, at the proximal region, the drug enters and leaves the renal cell compartment by bidirectional passive diffusion, active secretion, and active reabsorption. Inside the renal cell, the drug can also be metabolized. The equation describing the change of drug concentration in the proximal renal cell with respect to time is:

$$V_{PC}\frac{d[C_{PC,i}]}{dt} = CL_{bsl,scr,i}C_{PB,i}(t)\frac{f_{u,p}}{BP} - CL_{Api,scr,i}C_{PC,i}(t)\,f_{u,cell}$$
$$+ CL_{Api,reabs,i}C_{PT,i}(t) - CL_{bsl,reabs,i}C_{PC,i}(t)\,f_{u,cell}$$
$$+ CL_{PD,PT,bsl,i}(C_{PB,i}(t)\cdot\frac{f_{u,p}}{BP}\cdot\gamma - C_{PC,i}(t)\,f_{u,cell}\cdot\beta)$$
$$+ CL_{PD,PT,api,i}(C_{PT,i}(t)\cdot\alpha_i - C_{PC,i}(t)\,f_{u,cell}\cdot\beta)$$
$$- CL_{\text{int},i}(C_{PC,i}(t)\,f_{u,cell})$$

where i=1, 2, and 3, are the three different proximal tubule subsegments, $C_{PC,i}$ is the drug concentration of the cell compartment of i^{th} subsegment of proximal tubule (mg/L), V_{PC} is the volume of kidney proximal cell compartment of each subsegment (L), $CL_{PD,PT,bsl,i}$ is the intrinsic

passive diffusion clearance on the basolateral side of the cell compartment of i^{th} subsegment of proximal tubule (L/hr), $CL_{int,i}$ is the intrinsic metabolic clearance due to enzymes residing in the cell compartment of i^{th} subsegment of proximal tubule (L/hr), γ is uncharged fraction in the plasma (plasma pH is always 7.4, hence γ is a constant value for a specific drug).

At the other regions (except proximal region), the drug enters and leaves the renal cell compartment by bidirectional passive diffusion or metabolic clearance, without active secretion and active reabsorption. The equation describing the change of drug concentration in the proximal renal cell with respect to time is:

$$V_{Cj,i}\frac{d\left[C_{Cj,i}\right]}{dt} = CL_{PD,j,i}(C_{Bj,i}(t)\cdot\frac{f_{u,p}}{BP}\cdot\gamma + C_{Tj,i}(t)\cdot\alpha_{j,i} - 2\times C_{Cj,i}(t)\,f_{u,cell}\cdot\beta)$$

where i=1,2 for loop of Henle, i=1 for distal tubule, i=1,2,3,4,5 for collecting duct, j=loop of Henle, distal tubule, or collecting duct, $C_{Cj,i}$ is the drug concentration of the cell compartment of i^{th} subsegment of j segment (mg/L), $V_{Cj,i}$ is the volume of the cell compartment of i^{th} subsegment of j segment (L)

In terms of the vascular section, right after glomerular filtration, the equation describing the change of drug concentration in the blood with respect to time is:

$$C_{PB,0}(t) = (1-\frac{\frac{f_{u,p}}{BP}Q_{GFR}}{Q_{kidney}})C_b(t)$$

where $C_{PB,0}$ is the drug concentration in the blood right after glomerular filtration.

At the proximal region, the drug enters and leaves the vascular section by bidirectional passive diffusion, active secretion, active reabsorption, and inflow and outflow processes. The equation describing the change of drug concentration in the blood with respect to time is:

$$V_{PB}\frac{d[C_{PB,i}]}{dt} = Q_{Kidney}(C_{PB,i-1}(t) - C_{PB,i}(t))$$
$$- CL_{bsl,scr,i}C_{PB,i}(t)\frac{f_{u,p}}{BP} + CL_{bsl,reabs,i}C_{PC,i}(t)f_{u,cell}$$
$$+ CL_{PD,PX,bsl,i}(C_{PC,i}(t)f_{u,cell}\cdot\beta - C_{PB}(t)\cdot\frac{f_{u,p}}{BP}\cdot\gamma)$$

where i=1, 2, or 3, stand for three different proximal subsegments, $C_{PB,i}$ is the drug concentration of the vascular section of i^{th} proximal tubule subsegment (mg/L), V_{PB} is the volume of vascular section of each proximal tubule subsegment (L), $CL_{PD,PX,bsl,i}$ is the intrinsic passive diffusion clearance on the basolateral side of the renal cell of the i^{th} proximal tubule subsegment (L/hr)

At the other regions (except proximal region), the drug enters and leaves the vascular section by bidirectional passive diffusion, inflow, and outflow processes. The equation describing the change of drug concentration in the blood with respect to time is:

$$V_{Bj,i}\frac{d[C_{Bj,i}]}{dt} = Q_{Kidney}(C_{Bj,i-1}(t) - C_{Bj,i}(t))$$
$$+ CL_{PD,j,i}(C_{Cj,i}(t)f_{u,cell}\cdot\beta - C_{Bj,i}(t)\cdot\frac{f_{u,p}}{BP}\cdot\gamma)$$

where i=1,2 for loop of Henle, i=1 for distal tubule, i=1,2,3,4,5 for collecting duct, j=loop of Henle, distal tubule, or collecting duct, $C_{Bj,i}$ is the drug concentration of the vascular section of i^{th} subsegment of j segment (mg/L), $V_{Bj,i}$ is the volume of vascular section of i^{th} subsegment of j segment (L), $CL_{PD,j,i}$ is the intrinsic passive diffusion clearance of both apical and basolaterial sides of i^{th} subsegment of j segment (L/hr)

The diameters, lengths, and tubular flow rates of different segments of the kidney were collected from literature (Scotcher *et al.*, 2016) and are listed in Table 2.2. The physiological volume of each tubular segment was calculated as a cylinder and the physiological volume of the cellular compartment of each segment was assumed to be the same as the tubular volume. The

physiological surface area of each tubular segment was calculated as a cylinder except for the collecting duct which was calculated using a previously published exponential method (Scotcher *et al.*, 2016) due to the merging of the tubules. The surface area of apical side of proximal tubule was set 30-fold higher than basolateral side (Brown and McKnight, 2010) to account for the effect of brush border on increasing the apical side surface area. No other scaling factors or adjustments were made for surface area at other segments due to the sparsity of microvilli (Welling and Welling, 1988). The final volumes, surface areas and flow rates of each subsegment of the kidney model are listed in Table 2.2. The physiological fluid flow in the renal tubule was adapted from previous publication (Scotcher *et al.*, 2016) with further expansion (Table 2.2). The pH at each tubule decreased from 7.2 in the proximal segment to 6.5 in the bladder in a stepwise manner across the length of the tubule as detailed in Table 2.2. Glomerular filtration rate (Q_{GFR}), kidney blood flow (Q_{kidney}), and cardiac output (Q_c) were set as 7.2L/hr, 60L/hr, and 330 L/hr, respectively. Blood volume (V_b) in the simple circulation model was set to 42 L to mimic total body water. Blood to plasma ratio (*B/P*) was 1 and unbound fraction in the renal epithelial cells ($f_{u,cell}$) was the same as plasma unbound fraction ($f_{u,p}$) for all simulations. Renal intracellular pH and blood pH were set as 7.2 and 7.4, respectively.

2.3.2 Sensitivity analysis of renal clearance

To examine the impact of general structural and physiological assumptions on model performance, a sensitivity analysis of the renal clearance of a hypothetical neutral drug with permeability of 10 (10^{-6}cm/s) and plasma unbound fraction of 0.1 was done. The sensitivity analysis was conducted according to the general guidance of PBPK model development. The covariates tested and expected not to impact renal clearance based on pharmacokinetic principles included blood-to-plasma ratio (0.5-5), intracellular unbound fraction (0.1-1), volume of renal tubule (0.1-10 fold),

and volume of renal cell (0.1-10 fold). The covariates tested and expected to impact renal clearance included permeability (0.01-200×10^{-6}cm/s), plasma unbound fraction (0.1-1), tubular surface area (0.1-10 fold), and glomerular filtration rate (15 to 120mL/min).

2.3.3 Model verification and prediction of renal clearance for a set of test compounds

To validate the model, 46 drugs (Table 2.3) that had a renal clearance (CL_r) < 2×$f_{u,p}$×GFR and for which adequate data of in vitro permeability, plasma unbound fraction, and in vivo renal clearance from healthy adult subjects or patients with normal creatinine renal clearance was available, were selected to test whether the developed model could accurately predict renal clearance, and to validate the passive diffusion component of the model. Of the selected drugs 6 had an $f_{u,p}$×GFR value >1.5 (Table 2.3), and therefore they would be considered to be subject to active renal secretion based on the International Transporter Consortium recommendation (Huang *et al.*, 2010). However, as the criterion for model acceptance was set as 2-fold, these compounds were included in the analysis and analyzed also as net secreted compounds for the prediction accuracy. While this inclusion likely decreases the overall model performance presented, this approach was adopted to allow sufficient numbers of ionized compounds to be included in the analysis. For each drug, the observed renal clearance and plasma unbound fraction values were collected from literature (Table 2.3) (Varma *et al.*, 2009; Zhang *et al.*, 2012; Bjelland *et al.*, 2013; Ito *et al.*, 2013; Scotcher *et al.*, 2016). Predicted pK_a values for the test drugs were collected from https://www.drugbank.ca. Caco-2 and MDCK permeability values for the drugs of interest were collected from literature (Table 2.3) (Artursson and Karlsson, 1991; Hovgaard *et al.*, 1995; Yee, 1997; Grès *et al.*, 1998; Yazdanian *et al.*, 1998; Irvine *et al.*, 1999; Yamashita *et al.*, 2000; Alsenz and Haenel, 2003; Di *et al.*, 2011; Scotcher *et al.*, 2016). Drugs were categorized into 4 groups based on ionization at pH 7: drugs with >1% ionized as negatively charged at pH 7 were classified as acids, drugs with >1%

ionized as positively charged at pH 7 as bases, drugs with <1% ionization at pH 7 as neutrals and drugs with >1% ionized at pH 7 with both positively and negatively charged groups were classified as zwitterions. The drugs were also categorized to net secreted and net reabsorbed based on comparison of observed renal clearance with $f_{u,p}$×GFR (Table 2.3). Overall, the test compound dataset included 11 neutrals, 12 weak bases, 9 weak acids, and 14 zwitterions. The compounds had a wide range of pKa's (-2.2 – 11.62), in vitro permeabilities (0.01–160×10^{-6}cm/s), $f_{u,p}$'s (0.01-0.99), and observed renal clearances (0.5-145mL/min) providing a robust dataset for model validation.

The methods to account for the effect of pH-dependent drug ionization and microvilli expression in in vitro and in vivo systems are described in Supplementary Materials. Renal clearances were simulated at distribution equilibrium. For test compounds with more than one published in vitro permeability value, the renal clearance was predicted separately using each of the reported values and the mean predicted renal clearance was calculated from individual predictions.

To evaluate the quality and accuracy of the renal clearance predictions, average fold error (AFE), also called geometric mean fold error (equation 1) was used to measure the extent of underprediction and overprediction. Absolute average fold error (AAFE) and root mean square error (RMSE) were also calculated according to equations 2 and 3 for all compound categories. In addition, a 2-fold acceptance criterion was applied to determine whether renal clearances were successfully simulated. A 3-fold criterion was reported to allow comparison to previous publications predicting renal clearance.

$$AFE = 10^{\frac{1}{n}\sum log_{10}\frac{Predicted}{Observed}} \quad (1)$$

$$AAFE = 10^{\frac{1}{n}\sum\left|log_{10}\frac{Predicted}{Observed}\right|} \quad (2)$$

$$RMSE = \sqrt{\frac{1}{n}\sum(Observed - Predicted)^2} \quad (3)$$

2.3.4 Incorporation of active secretion to simulate renal clearance

The mechanistic kidney model also allows incorporation of active secretion and active reabsorption in the relevant subsegments of the kidney. To test the feasibility of incorporating in vitro transporter data along with in vitro permeability data to simulate renal clearance, the renal clearances of para-aminohippuric acid (PAH) and cimetidine were simulated. PAH ($f_{u,p}$ of 1, pKa of 2.7 and 4.24 (drugbank.ca,), in vitro permeability of 0.72 (10^{-6}cm/s) (Naruhashi *et al.*, 2001)) and cimetidine ($f_{u,p}$ of 0.8 (Burt *et al.*, 2016), pKa of 6.91 (drugbank.ca,), in vitro permeability of 1.37 (10^{-6}cm/s) (Yazdanian *et al.*, 1998)) are well-known renal secretion substrates. Literature in vitro experimental data of OAT1 mediated basolateral secretion (Hotchkiss *et al.*, 2015), and NPT1, MRP2, and MRP4 mediated apical secretion (Uchino *et al.*, 2000; Smeets *et al.*, 2004) of PAH were used (Table 2.4) and scaled to in vivo assuming the transporter expression level per mg of in vitro system is equal to the transporter expression level per mg of human kidney and 300 grams of kidney per person. Total in vivo secretion clearances of 884 and 22.3 L/hr were calculated for basolateral and apical side respectively (Table 2.4). Literature in vitro experimental data of OAT3 and OCT2 mediated basolateral secretion and MATE1/2-K mediated apical secretion of cimetidine (Burt *et al.*, 2016) were used with scaling to 60 million proximal tubule cells per gram of kidney (Neuhoff *et al.*, 2013) and 300 grams of kidney per person. Total in vivo secretion clearances of 31.8 and 40.5L/hr were calculated for basolateral and apical side respectively (Table 2.5).

To explore the possibility and effect of distribution of transporter expression along the proximal tubule, the overall secretion clearance was incorporated differently as follows: either uniform

distribution across all three proximal tubule subsegments or all the secretion clearance occurring only at a single tubular subsegment (1^{st}, 2^{nd} or 3^{rd}).

2.3.5 Simulation of urine pH-dependent renal clearance

Urine pH-dependent renal clearance has been observed for many drugs due to different ionization and subsequently different effective permeabilities at different urine pHs (Rowland and Tozer, 2012). The pH-dependent effective passive diffusion was incorporated into the model by calculating the ionization status of test drugs in the specific tubule subsegment based on the predicted pH gradient across the tubule from the glomerulus to the bladder (Tables 2.1, 2.6, and 2.7). To simulate changes in renal clearance upon altered urine pH, the renal clearances of memantine (a weak base) and salicylic acid (a weak acid) were predicted at different urine pHs.

The intrinsic permeability of memantine ($f_{u,p}$ 0.55,(FDA, 2010) pKa of 10.7 (drugbank.ca,), in vitro permeability of 25-43.4 (10^{-6}cm/s) (Beconi *et al.*, 2012; Müller *et al.*, 2017)) was calculated as 0.087-0.06 (average 0.073) cm/s. At acidic urine, when >99.99% of memantine is charged, the observed renal clearance of memantine considerably exceeds the unbound filtration clearance suggesting that memantine is a substrate for active tubular secretion. This secretion clearance was estimated via parameter optimization based on the observed renal clearance at urine pH 5 (>99.99% ionized) and the average intrinsic permeability. The secretion clearance value ($CL_{api,scr}$ and $CL_{bsl,scr}$) was set as 10L/hr in the apical and basolateral side of each subsegment of proximal tubule. The renal clearance was then predicted for urine pH of 5.0, 7.9, and 8.1 as described (Freudenthaler *et al.*, 1998), using a predicted pH gradient in the kidney segments (Table 2.6). In addition, the effect of the described changes of urine flow (Freudenthaler *et al.*, 1998) on renal clearance were simulated by changing the tubular flow (rate exiting the last subsegment of collecting duct) from 1 mL/min to 0.99, 1.15, 2.6, and 2.73mL/min. A 99% confidence interval of

observed renal clearances was calculated from reported median and 25% and 75% quantiles of renal clearance, and predictions within the 99% confidence interval were considered successful.

The intrinsic permeabilities of salicylic acid (pKa 2.98 (drugbank.ca)) were calculated as 0.088, 0.26, 0.32, 0.34, and 0.58 (average 0.32) cm/s based on in vitro permeabilities of 3.35, 10, 12, 13, and 22 (10^{-6}cm/s) (Artursson and Karlsson, 1991; Yazdanian *et al.*, 1998; Irvine *et al.*, 1999; Yamashita *et al.*, 2000). The salicylic acid $f_{u,p}$ used was 0.1 based on the reported relationship of salicylic acid $f_{u,p}$ and plasma concentration (Furst *et al.*, 1979), and salicylic acid plasma concentration of 150-180mg/L in the study reporting pH-dependent renal clearance (Macpherson *et al.*, 1955). The observed renal clearance of salicylic acid under basic urine exceeded the unbound glomerular filtration rate, suggesting active secretion of salicylic acid. The secretion clearance was calculated via parameter optimization based on the observed renal clearance under urine pH of 8 (>99.99% ionized) and the average intrinsic permeability value. An apical and basolateral secretion clearance value ($CL_{api,scr}$ and $CL_{bsl,scr}$) of 36L/hr was incorporated in each proximal tubule subsegment. The renal clearance was then simulated at urine pH values 5.0, 6.0, 7.0, and 8.0 to mimic the published range of urine pH(Macpherson *et al.*, 1955) using pH gradient in the kidney (Table 2.7).

2.4 Results

2.4.1 Model construction and sensitivity analysis

A 35-compartment model consisting of a simple circulation component and a mechanistic kidney model was developed based on the physiological segmentation of the human kidney (Figure 2.1). The simple circulation model was used to connect the renal blood flow out of the kidney with the blood flow into the kidney. The Bowman's capsule was the entrance site of the flow into the mechanistic kidney model which only allowed unbound drugs to be filtered into proximal tubule. Longitudinally, the kidney was divided into 4 major segments: proximal tubule, loop of Henle, distal tubule, and collecting duct (Figure 2.1). The proximal tubule was further divided into 3 subsegments (S1, S2, and S3), the loop of Henle into 2 subsegments (descending and ascending), and collecting duct into 5 subsegments (connecting tubule, initial collecting duct, cortical collecting duct, medullary collecting duct, and papillary duct) based on kidney physiology. Each subsegment was divided into 3 sections: tubular lumen, cellular compartment, and vascular section. A compartment for the bladder was created to serve as a compartment collecting eliminated drug. The surface areas, volumes and flow rates in the various model compartments were assigned based on known physiology (Tables 2.1 and 2.2). Glomerular filtration was incorporated into the Bowman's capsule, bidirectional passive diffusion was incorporated throughout the entire nephron, and renal metabolism and active transporter-mediated secretion and reabsorption were included only at proximal tubule.

To confirm the structural integrity of the model, sensitivity analysis was conducted. As expected from pharmacokinetic principles, blood-to-plasma ratio, intracellular unbound fraction, volume of tubular lumen and volume of cell compartment did not affect simulated renal clearance (Figure 2.2). Similarly, as expected, the plasma unbound fraction and glomerular plasma flow positively

and linearly correlated with simulated renal clearance, while the permeability and surface area negatively and nonlinearly correlated with simulated renal clearance (Figure 2.2). Notably, the sensitivity analysis shows that with different tubular dimensions (length and radius) tubular surface area but not volume impacts renal clearance.

2.4.2 Prediction of renal clearance of test drugs and model verification

The predictive performance of the model was evaluated using 46 test drugs (Table 2.3). First, the validity of the surface area scaling from in vitro experimental systems was tested using neutral compounds (Figure 2.3). Calculation of permeability values assuming no microvilli expression in in vitro cell systems resulted in a systematic over-prediction of renal clearances (Figure 2.3a), likely due to an underestimation of in vitro surface area and consequently under-prediction of passive reabsorption. To account for the expression of microvilli in vitro, a surface area scaling factor was optimized using neutral compounds. Scaling factors of 1.25, 1.5, and 2 resulted in AFE's of 0.77, 0.93, and 1.25, respectively, and therefore a scaling factor of 1.5 was selected. Using this scaling factor, renal clearance was simulated for all 46 test drugs using all available in vitro permeability values (Figure 2.4, Table 2.3) resulting in acceptable renal clearance predictions with overall AFE of 0.76, overall AAFE of 1.59, and overall RMSE of 26.9 (Table 2.8). At least one measured permeability value predicted renal clearance within 2-fold of the observed renal clearance for 40 drugs (87%) and the mean simulated renal clearance was within 2-fold of the observed for 37 drugs (80%) (Table 2.8), demonstrating high predictive quality of the model. The AFE's for neutrals, bases, acids, and zwitterions, ranged from 0.59 to 0.93, and the AAFE's ranged from 1.37 to 1.83 (Table 2.8). The RMSE's varied between 8.27 and 38.3 (Table 2.8). For majority of the drugs the mean simulated renal clearance and at least one of the renal clearances predicted with individual in vitro permeability values were within 2-fold of the observed (Table 2.8), and

only one drug had predicted renal clearance outside 3-fold range (Table 2.8). In addition, the model performance was also evaluated based on net reabsorption ($CL_r<f_{u,p}$*GFR) and net secretion ($CL_r>f_{u,p}$*GFR) and the calculated AFE's AAFE's and RMSE's for these two groups (Table 2.8) generally showed a more accurate prediction for net reabsorbed drugs than net secreted drugs.

2.4.3 Incorporation of active secretion to simulate renal clearance

To explore whether active secretion could be incorporated into the developed model, PAH and cimetidine were selected based on published literature to predict renal clearance that incorporates active secretion and passive diffusion. Using literature in vitro transporter data, protein binding data, and in vitro permeability data, the model successfully predicted the renal clearance of PAH and cimetidine (Table 2.9), demonstrating the feasibility of the model to predict complex renal clearance scenarios with both passive diffusion and secretion clearance incorporated at both apical and basolateral sides of proximal tubule in the model. Notably, when the secretion clearance was incorporated only in one subsegment, the simulated renal clearance was consistently lower than when the secretion clearance was uniformly distributed across the tubular segments. As transporter localization data is not available, these simulations are only shown to illustrate the relevance of knowledge of transporter localization within the kidney tubules.

2.4.4 Simulation of urine pH-dependent renal clearance

Renal clearance can be affected by changes in urine flow and urine pH and therefore, any broadly useful kidney model must incorporate changes in ionization status and reabsorption clearance due to tubular pH and flow changes. To test the developed model, the renal clearance of memantine and salicylic acid were simulated under different urine pH conditions and with different urine flows (memantine). The effect of both urine pH and urine flow were accurately predicted by the

model for memantine (Figure 2.5 and Table 2.10) demonstrating robust validation of ionization processes, passive diffusion, and tubular flow. Similarly, the effect of urine pH on salicylic acid renal clearance was well predicted using five different in vitro permeability values (Figure 2.5). The overall simulation results for both substrates were acceptable based on the calculated 99% confidence interval and visual inspection of the urine pH-dependent renal clearance.

2.5 Discussion

Since the development of the well-stirred model of hepatic clearance, predictions of hepatic clearance from in vitro data have become commonplace and can typically predict human hepatic clearances within 2-fold of observed. In contrast, due to the sequential nature of renal clearance processes, and the challenges in predicting the fraction reabsorbed from the tubular lumen during the sojourn of the drug within the kidney, at present, renal clearance cannot be effectively predicted from in vitro data prior to human dosing. In addition, considerable uncertainty exists regarding the quantitative contribution of active transport processes in drug renal clearance. The goal of this work was to develop a mechanistic and dynamic physiologically-based kidney model that would consider spatiotemporal changes in concentrations, flows, pH, and effective permeability for renal clearance predictions, and allow true in vitro-to-in vivo predictions of renal clearance using plasma unbound fraction, permeability, and active transport data.

The developed method has clear advantages over QSAR, allometry, and static model approaches although these approaches have been successfully used to predict renal clearances. For example, static models assume that passive diffusion always reaches equilibrium and urine concentration is equal to unbound plasma concentration (Kunze *et al.*, 2014)(Scotcher *et al.*, 2016) an assumption readily violated with hydrophilic or low permeability drugs or when urine flow increases. Still, two static kidney models achieved 95% (Kunze *et al.*, 2014) and 87% (Scotcher *et al.*, 2016) success rates in predicting renal clearance within 3-fold error using 20 and 45 test compounds, respectively. The dynamic model developed here performed equally well or better, with 45 drugs (98%) having mean simulated renal clearance within 3-fold of the observed renal clearance and 37 drugs (80%) with mean simulated renal clearance within 2-fold of the observed renal clearance. The developed model also provides additional power to simulate temporal, urine flow and pH

dependent changes in renal clearance and to incorporate active apical and basolateral transport of drugs of interest.

This is the first study that examined the effect of different in vitro permeability values from multiple data sources on the accuracy of renal clearance predictions and systematically accounted for ionization status, tubular flow, and tubular pH gradients in renal clearance mechanisms. As few experimental data in humans exists for pH gradients in the kidney tubule at various urine pH values, further refinement of the pH gradients used in this study may be necessary as more data becomes available. Previous studies have relied on single source permeability values from LLC-PK (Kunze *et al.*, 2014) or Caco-2 (Scotcher *et al.*, 2016) cells although high variability in cell culture systems is well documented (Artursson *et al.*, 2001), potentially biasing overall predictions. As the in vitro determined permeability values can vary more than an order of magnitude between studies (Table 2.3), it is expected that some predicted renal clearances will fall outside of the 2-fold acceptance criteria. It is also likely that active secretion processes exist for some of the test drugs resulting in an under-prediction of renal clearance values. This hypothesis is supported by the overall under-prediction of the renal clearance values in this study and the distinct greater underprediction of renal clearances for drugs that were classified as net secreted when compared to net reabsorbed compounds (Table 2.8). Finally, inaccurate measurements of in vivo renal clearances and $f_{u,p}$'s may introduce error into comparisons of predicted and observed data. As such, the model performance in predicting renal clearances from in vitro data and the accurate simulation of pH and flow dependent changes in renal clearances can be considered excellent.

The developed model can feasibly incorporate a bottom-up prediction of renal clearance for transported drugs as shown with the renal clearance predictions with PAH, cimetidine, memantine, and salicylic acid. While several prior studies (Posada *et al.*, 2015; Burt *et al.*, 2016; Emami

Riedmaier *et al.*, 2016; Mori *et al.*, 2016; Scotcher *et al.*, 2017; Wang *et al.*, 2017) have used the Simcyp kidney model to simulate drug renal clearances, to our knowledge this is the first study to predict the renal clearance of a drug with active renal transport using solely in vitro-to-in vivo extrapolation methods. The prior studies relied on incorporating scaling factors based on observed in vivo data to either fit active secretion clearance (Posada *et al.*, 2015; Burt *et al.*, 2016; Emami Riedmaier *et al.*, 2016; Scotcher *et al.*, 2017; Wang *et al.*, 2017) or passive diffusion clearance (Mori *et al.*, 2016). The current study provides a model for bottom-up approach using plasma unbound fraction, in vitro permeability, and in vitro transporter uptake clearance to successfully simulate renal clearance. In addition, due to the incorporation of the verified passive diffusion process, an adjustment factor to account for the discrepancy of transporter expression between in vitro and in vivo can be applied with higher confidence than before. The developed model also provides a feasible approach to predict the impact of changes in urine pH on renal clearance.

Table 2.1. Physiological parameters of human kidney.

Tubular radius and length for each tubule are values for single nephron. Volume and surface area of the tubule are reported for total of two kidneys assuming 0.9 million nephrons per kidney. The method to calculate the surface area of the collecting duct was adapted from Scotcher et al 2016. Microvilli adjustment for the surface area is 30 of proximal tubule and 1 for all other tubule according to Brown et al 2010. All physiological parameters were calculated from literature values as described in materials and methods.

	Proximal Tubule	Loop of Henle	Distal Tubule	Collecting Duct
Tubule radius (mm)	0.03	0.009	0.025	0.1
Tubule length (mm)	18	12	5.5	21
Volume of tubule (L)	0.092	0.0055	0.019	1.19
Volume of each subsegment in the model (L)	0.0305	0.0027	0.0194	0.237
Surface area of tubule (dm^2)	611	122	156	33
Microvilli adjustment (dm^2)	18321	122	156	33
Each subsegment in the model (dm^2)	6107	61	156	6.7

Table 2.2. Physiological parameters of the mechanistic kidney model.

The tubular flow rate exiting each tubular subsegment is equal to the tubular flow rate entering the next tubular subsegment. The flow rate at the beginning of the first proximal tubule subsegment is equal to glomerular filtration rate (120 mL/min) and the exiting flow rate at the end of the last collecting duct subsegment (Collecting $duct_5$) is equal to normal urine formation rate (1 mL/min). The volumes, tubular surface areas, and flow rates are scaled to two kidneys with 0.9 million nephrons per kidney based on the physiological values with detailed calculation described in Table 2.1 and Methods section.

Segment	Volume (L)	Tubular surface area (dm^2)	Tubular flow rate entering each tubular subsegment (mL/min)	pH value
Proximal $tubule_1$	0.0305	6107	120	7.2
Proximal $tubule_2$	0.0305	6107	94	7.1
Proximal $tubule_3$	0.0305	6107	68	7
Loop of $henle_D$	0.0027	61	43	7
Loop of $henle_A$	0.0027	61	24	7
Distal tubule	0.0194	156	24	6.9
Collecting $duct_1$	0.009	6.7	11	6.8
Collecting $duct_2$	0.009	6.7	9	6.7
Collecting $duct_3$	0.009	6.7	7	6.6
Collecting $duct_4$	0.009	6.7	5	6.5
Collecting $duct_5$	0.009	6.7	3	6.5

Table 2.3. Summary of physicochemical and pharmacokinetic properties of 46 test drugs.

Drug	Chem	pKa (acid)	pKa (base)	fu,p	Observed CLr (mL/min)	Mean predicted CLr (mL/min)	Irvine 1998[f]	Irvine 1998	Di 2001[f]	Scotcher 2016	Alsenz 2003	Li 2007	Yazdanian 1998	Artursson 1991	Yee 1997	Gres 1998	Hovgaard 1995	Yamashita 2000
Acetaminophen	Neutral			0.81[a]	11.5[a]	14.11	35	100	-	-	-	-	-	-	-	-	-	23.7
Betamethasone	Neutral			0.36[a]	9.5[a]	9.42	-	-	-	26.5	-	-	-	-	-	-	-	-
Dapsone	Neutral			0.27[a]	5.5[a]	3.24	-	-	-	49.7	-	-	-	-	-	-	-	-
Dexamethasone	Neutral			0.32[b]	6.3[b]	13.37	20	40	-	-	-	12.5	12.2	12.50	23.40	-	-	12.1
Fluconazole	Neutral			0.86[a]	15.7[a]	17.29	-	-	-	36.3	-	-	-	-	29.80	-	-	-
Levetiracetam	Neutral			0.9[a]	39.4[a]	38.72	-	-	-	15.7	-	-	-	-		-	-	-
Linezolid	Neutral			0.78[a]	39.5[a]	13.85	-	-	-	36.1	-	-	-	-	-	-	-	-
Metronidazole	Neutral			0.98[a]	9.6[a]	8.04	-	-	-	64.7	-	-	-	-	-	-	-	-
Ribavirin	Neutral			1[a]	109.9[a]	106.44	-	-	-	1.55	-	-	-	-	-	-	-	-
Topiramate	Neutral			0.87[a]	15.1[a]	11.19	-	-	-	46.2	-	-	-	-	-	-	-	-
Voriconazole	Neutral			0.42[a]	1.57[a]	2.12	-	-	-	96.5	-	-	-	-	-	-	-	-
Atenolol	Base		9.67	0.97[a]	145.3[a]	114.33	1.8	3.3	1.31	0.256	1.73	1.6	0.53	0.20	-	1.16	-	0.4
Betaxolol	Base		9.67	0.45[a]	49.6[a]	26.31	-	-	-	20	-	-	-	-	-	-	48.50	-
Desipramine	Base		10.02	0.13[a]	28.6[a]	9.37	-	-	-	-	43	-	24.4	-	21.60	-		-
Imipramine	Base		9.17	0.13[a]	6.8[a]	5.41	-	-	-	33.4	-	-	-	-	14.10	-	-	-
Lamotrigine	Base		5.87	0.45[a]	2.5[a]	2.83	88	110	-	-	-	-	-	-	-	-	-	-
Metoprolol	Base		9.7	0.87[a]	109.6[a]	69.96	150	140	24.6	17	31.77	33.2	23.7	27.00	-	18.00	-	-
Midazolam	Base		6.57	0.05[d]	0.55[d]	0.79	-	-	-	-	-	-	-	-	-	-	-	69.9
Nadolol	Base		9.76	0.8[a]	126[b]	94.56	1.4	0.39	0.83	-	-	0.6	3.88	-	-	-	-	0.33
Ondansetron	Base		7.34	0.27[b]	20.7[b]	7.05	110	110	-	-	-	-	-	-	-	-	-	-
Oxprenolol	Base		9.67	0.14[a]	9.35[a]	6.71	130	160	-	30	-	-	-	-	-	-	65.50	-
Trimethoprim	Base		7.16	0.49[a]	78.2[a]	21.93	52	87	17.9	-	-	-	-	-	-	-	-	-
Verapamil	Base		9.68	0.16[a]	25.6[a]	9.58	-	-	7.48	20.9	44.67	45.7	-	-	-	-	-	-
Acetylsalicylic Acid	Acid	3.41		0.51[b]	9.1[b]	18.03	7.4	2.2	-	-	-	-	9.09	2.4	30.7	-	-	-
Cefuroxime	Acid	3.15		0.67[b]	127.4[b]	73.30	0.16	0.38	-	-	-	-	-	-	-	-	-	-
Chloramphenicol	Acid	7.49		0.34[b]	16.8[b]	11.70	-	-	-	-	-	-	-	-	20.60	-	-	-
Chlorpropamide	Acid	4.33		0.05[a]	0.6[a]	0.36	-	-	-	88.1	-	-	-	-	-	-	-	-
Ibuprofen	Acid	4.85		0.01[a]	0.574[a]	0.23	-	-	-	-	-	-	-	-	52.50	-	-	-
Probenecid	Acid	3.53		0.09[a]	0.5[a]	0.70	-	-	-	84.5	-	-	-	-	-	-	-	-
Propylthiouracil	Acid	8.09		0.16[a]	3.2[a]	1.15	41	96	-	80.8	-	-	-	-	-	-	-	-
Sulfamethoxazole	Acid	6.16		0.35[a]	4.5[a]	7.54	-	-	-	41.7	-	-	-	-	-	-	-	-
Theophylline	Acid	7.82		0.52[a]	5.5[a]	9.18	-	-	23.1	65.1	-	22.6	-	-	-	-	-	25
Amoxicillin	Zwitterion	3.23	7.43	0.83[a]	167[a]	97.75	0.24	0.021	-	-	0.01	-	-	-	-	0.33	-	-
Ampicillin	Zwitterion	3.24	7.44	0.8[a]	163.6[a]	95.03	-	-	-	-	-	-	-	-	-	-	-	0.081
Difloxacin	Zwitterion	5.81	7.39	0.62[a]	4.5[a]	3.32	-	-	-	74.6	-	-	-	-	-	-	-	-
Enalaprilat	Zwitterion	3.13	7.83	0.61[b]	112[b]	61.17	-	-	-	-	1.85	-	-	-	-	-	-	-
Gabapentin	Zwitterion	4.63	9.91	0.97[a]	95.1[a]	113.30	0.36	0.01	-	0.67	-	-	-	-	-	-	-	-
Labetalol	Zwitterion	8.1	9.8	0.49[b]	64.4[b]	43.06	25	76	7.34	-	-	-	9.31	-	-	-	-	-
Lisinopril	Zwitterion	3.17	10.2	0.99[b]	84[b]	114.55	0.18	0.22	0.23	-	1.27	-	-	-	-	-	-	-
Melagatran	Zwitterion	2.12	11.62	0.93[a]	113.7[a]	110.34	-	-	-	0.145	-	-	-	-	-	-	-	-
Methyldopa	Zwitterion	1.73	9.85	0.84[b]	147[b]	99.62	-	-	-	-	0.15	-	-	-	-	-	-	-
Oxytetracycline	Zwitterion	0.24	7.75	0.77[a]	90.8[a]	86.67	-	-	-	0.85	-	-	-	-	-	-	-	-
Pefloxacin	Zwitterion	5.66	6.47	0.75[a]	12.9[a]	6.34	-	-	-	63.7	-	-	-	-	-	-	-	-
Terbutaline	Zwitterion	8.86	9.76	0.74[b]	154[b]	87.86	1	0.41	-	-	1.71	0.8	0.47	0.38	-	1.04	-	0.12
Tetracycline	Zwitterion	-2.2	8.24	0.76[a]	86.4[a]	83.83	-	-	-	1.1	-	-	-	-	-	-	-	-
Trovafloxacin	Zwitterion	5.41	9.44	0.31[a]	12.6[a]	6.79	-	-	-	-	-	-	-	-	30.23	-	-	-

[a]CLr value is obtained from Scotcher 2016; [b]CLr value is obtained from Ito 2013; [c]CLr value is obtained from Gottlieb 1971; [d]CLr value is obtained from Bjelland 2012; [e]CLr value is obtained from Varma 2009; [g]Data is obtained from Zhang 2012; [h]Data value is obtained from McInnes 2013.

[f]Permeability value is obtained from MDCK cell line; otherwise Caco2 cell line

The permeability unit is 10^{-6} cm/s

Table 2.4. *In vitro* data used for prediction of *in vivo* renal clearance of PAH.

Prediction of in vivo PAH basolateral and apical secretion clearances based on in vitro transporter data (Hotchkiss et al. 2015, Uchino et al 2000, and Smeets 2004) assuming the transporter expression level per mg of in vitro system is equal to the transporter expression level per mg of human kidney and 300 grams of kidney per person.

	Jmax (pmol/min/mg protein)	Km (uM)	CL (ul/min/mg protein)	CL (L/hr)	Sum (L/hr)
OAT1	1095	22.3	49.1	884	884
NPT1	1880	2660	0.71	12.7	22.3
MRP2	160	5000	0.032	0.58	
MRP4	80	160	0.5	9	

Table 2.5. *In vitro* data used for prediction of *in vivo* renal clearance of cimetidine.

Prediction of in vivo cimetidine basolateral and apical secretion clearances based on in vitro transporter data (Burt et al. 2016) using scaling factor of 60 million proximal tubule cells per gram of kidney (Neuhoff et al 2013) and 300 grams of kidney per person. PTC, proximal tubule cells, Sum refers to the OCT2+OAT3 contribution and the combination of the two MATEs.

	J_{max} (pmol/min/ million PTC)	K_m (uM)	CL (ul/min/ million PTC)	CL (ul/min/mg kidney)	CL (L/hr)	Sum (L/hr)
OCT2	2170	72.6	29.9	1793	32.28	
OAT3	1232	161.5	7.6	458	8.24	40.5
MATE1	135.5	7.7	17.6	1056	19.01	
MATE2-K	216	18.2	11.9	712	12.82	31.8

Table 2.6.**Error! Reference source not found.** Tubular pH parameters used to predict renal clearance of memantine.

Setup of the pH gradient for the different subsegments of the model to simulate effects of altered urine pH on renal clearance of memantine. The pH assumed for each subsegment is reported for the four different urine pH values.

Segment	Uncontrolled urine pH	Urine pH 5.1	Urine pH 7.9	Urine pH 8.1
Proximal tubule$_1$	7.2	7.2	7.4	7.4
Proximal tubule$_2$	7.1	7	7.4	7.4
Proximal tubule$_3$	7	6.8	7.4	7.4
Loop of henle$_D$	7	6.8	7.4	7.4
Loop of henle$_A$	7	6.8	7.4	7.4
Distal tubule	6.9	6.4	7.5	7.5
Collecting duct$_1$	6.8	6	7.6	7.6
Collecting duct$_2$	6.7	5.8	7.7	7.7
Collecting duct$_3$	6.6	5.6	7.8	7.8
Collecting duct$_4$	6.5	5.4	7.9	7.9
Collecting duct$_5$	6.5	5.1	7.9	8.1

Table 2.7. Tubular pH parameters used to predict renal clearance of salicylic acid.

Setup of the pH gradient for the different subsegments of the model to simulate effects of altered urine pH on renal clearance of salicylic acid. The pH assumed for each subsegment is reported for the four different urine pH values.

Segment	Urine pH 5	Urine pH 6	Urine pH 7	Urine pH 8
Proximal $tubule_1$	7.2	7.2	7.2	7.4
Proximal $tubule_2$	7	7.1	7.1	7.4
Proximal $tubule_3$	6.8	6.9	7	7.4
Loop of $henle_D$	6.8	6.9	7	7.4
Loop of $henle_A$	6.8	6.9	7	7.4
Distal tubule	6.4	6.8	7	7.5
Collecting $duct_1$	6	6.7	7	7.6
Collecting $duct_2$	5.8	6.6	7	7.7
Collecting $duct_3$	5.6	6.4	7	7.8
Collecting $duct_4$	5.4	6.2	7	7.9
Collecting $duct_5$	5	6	7	8

Table 2.8. Summary of model performance for the different drug categories.

The performance parameters average fold error (AFE), absolute average fold error (AAFE), and root mean square error (RMSE) were calculated as described in Materials and Methods, and the values were obtained by comparing the predicted individual and mean values to the observed listed in Table 2.3.

	n	AFE	AAFE	RMSE	at least one simulated CL_r within 2 fold	mean simulated CL_r within 2-fold	mean simulated CL_r within 3-fold
Neutral	11	0.93	1.37	8.27	10 (91%)	9 (82%)	11 (100%)
Base	12	0.59	1.83	27.3	9 (75%)	8 (67%)	11 (92%)
Acid	9	0.87	1.82	18.4	8 (89%)	7 (78%)	9 (100%)
Zwitterion	14	0.74	1.46	38.3	13 (93%)	13 (93%)	14 (100%)
Net reabsorbed	32	0.87	1.51	9.67	28 (88%)	26 (81%)	32 (100%)
Net secreted	14	0.56	1.78	46.5	12 (86%)	11 (79%)	13 (93%)
Total	46	0.76	1.59	26.9	40 (87%)	37 (80%)	45 (98%)

Table 2.9. Simulation of renal clearance of para-aminohippuric acid (PAH) and cimetidine in the presence and absence of active secretion clearances.

The renal clearances were simulated as described in Methods sections using collected permeability data in Caco-2 cells, plasma unbound fraction ($f_{u,p}$,), active secretion clearance at apical side of each of the 3 subsegments of proximal tubule $CL_{api,scr}$, and active secretion clearance at basolateral side of each of the 3 subsegments of proximal tubule $CL_{bsl,scr}$. The tubular subsegment for secretion clearance indicated the specific subsegment in which the secretion clearance was incorporated. Secretion clearances were set as 0 in all other subsegments

fu,p	Caco-2 permeability (10-6 cm/s)	$CL_{api,scr}$ (L/hr)	$CL_{bsl,scr}$ (L/hr)	Tubular subsegment for secretion clearance	Observed CL_r (mL/min)	Simulated CL_r (mL/min)	S/O ratio
Para-aminohippuric acid							
1	0.72	0	0		550	93.9	0.17
		7.43	295	Each subsegment		812	1.48
		22.3	884	1st subsegment		734	1.33
		22.3	884	2nd subsegment		746	1.36
		22.3	884	3rd subsegment		770	1.40
Cimetidine							
0.8	1.37	0	0		543	90.6	0.17
		10.6	13.5	Each subsegment		427	0.79
		31.8	40.5	1st subsegment		383	0.71
		31.8	40.5	2nd subsegment		387	0.71
		31.8	40.5	3rd subsegment		393	0.72

Table 2.10. Simulation of urine pH-dependent renal clearance of memantine.

The observed data is shown for five different conditions (uncontrolled urine pH and flow; urine pH of 5.1, urine flow of 0.99 mL/min; urine pH of 5.1, urine flow of 2.72 mL/min; urine pH of 8.1, urine flow of 1.15 mL/min; urine pH of 7.9, urine flow of 2.6 mL/min). The pH dependent renal clearance of memantine was simulated under the same five conditions according to the process described in the Methods sections using in vitro permeability values reported in MDCK cells and Caco-2 cells, and the average permeability value from the two studies.

	Observed CL_r (mL/min)		Simulated CL_r (mL/min)		
Study group	Median (25%-75%)	99% Confidence Interval	MDCK	Caco-2	Average
Uncontrolled	149 (139-183)	64.8 - 233	155	121	136
pH=5.1 Qu=0.99mL/min	210 (183-220)	139 - 281	220	197	208
pH=5.1 Qu=2.72mL/min	219 (194-233)	144 - 294	220	197	208
pH=8.1 Qu=1.15mL/min	19.4 (17.2-24.4)	5.63 - 33.2	12.6	4.88	7.64
pH=7.9 Qu=2.60mL/min	30.5 (26.6-34.4)	15.6 - 45.4	23.2	10.1	15.0

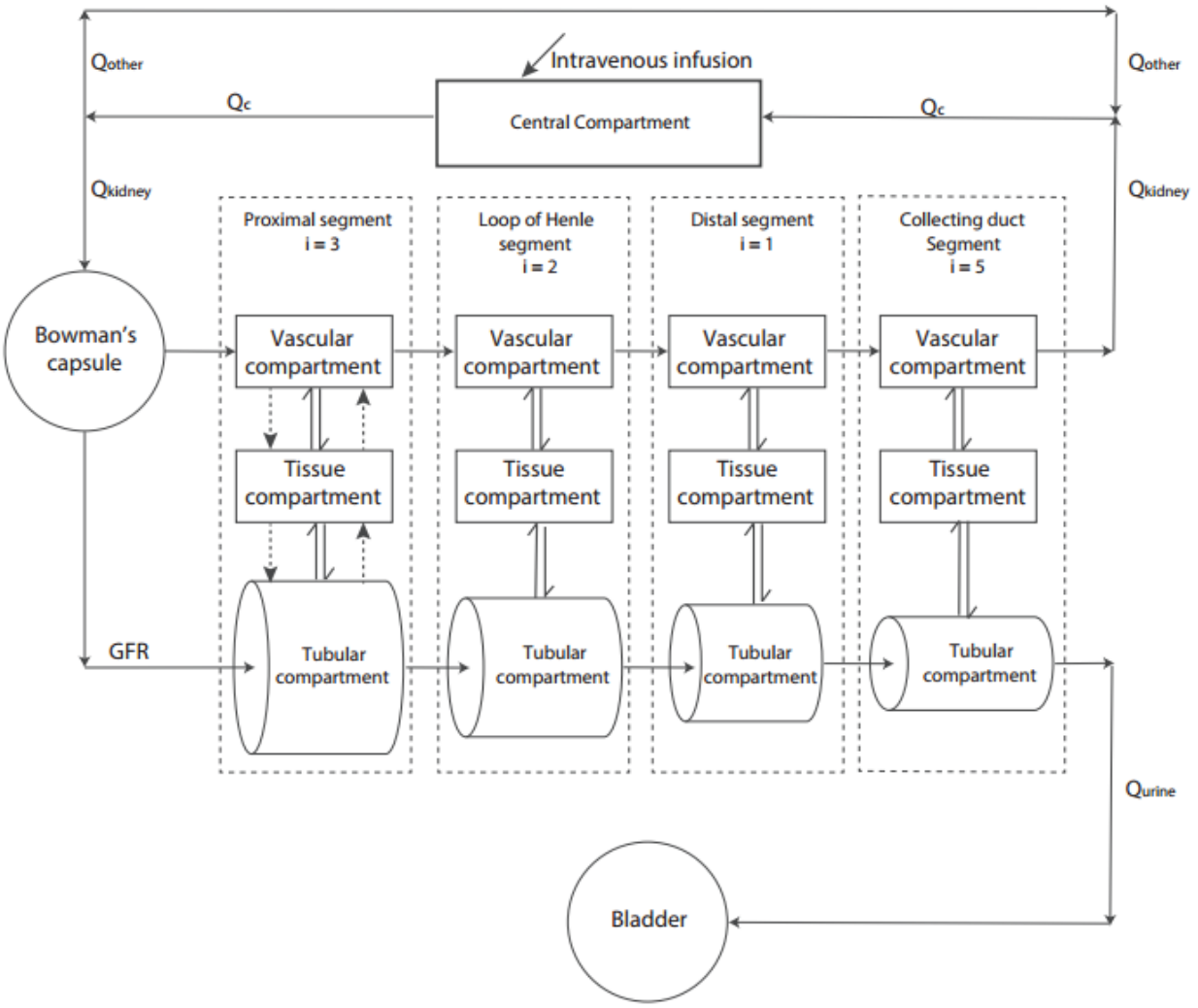

Figure 2.1. Schematic diagram of the mechanistic kidney model.

Q_c, blood flow in the central compartment; Q_{kidney}, blood flow in the kidney; Q_{other}, blood flow of all other organs in the body; Q_{urine}, urine formation flow; *GFR*, glomerular filtration rate; *i*, the amount of subcompartment each segment is divided into; *single solid arrow*, the fluid flow; *single dash arrow*, active secretion and active reabsorption; *double arrow*, bidirectional passive diffusion.

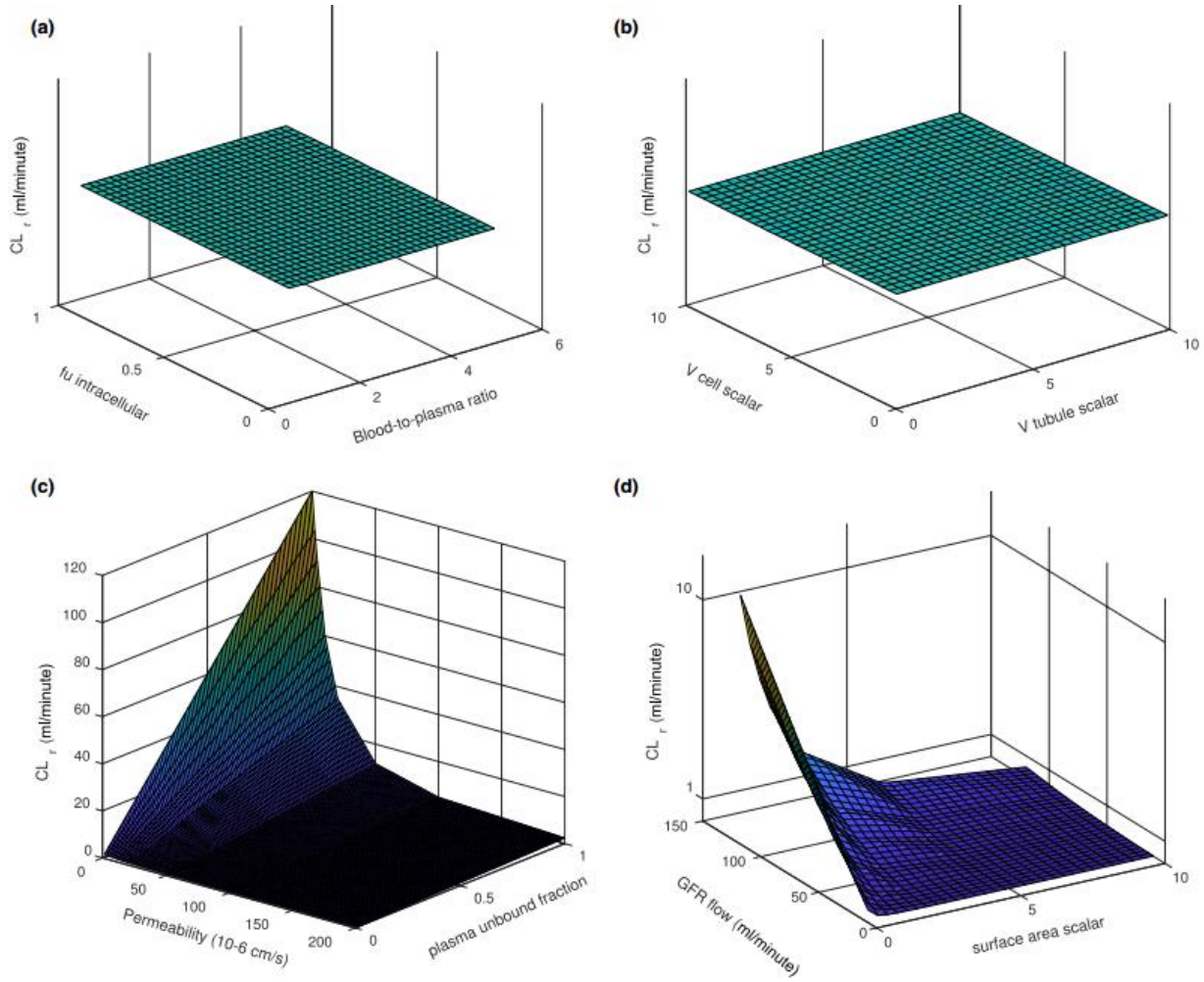
(a)
CL r (ml/minute)
1
0.5
0
fu intracellular
0
2
4
6
Blood-to-plasma ratio
(b)
CL r (ml/minute)
10
5
0
V cell scalar
0
5
10
V tubule scalar
(c)
CL r (ml/minute)
120
100
80
60
40
20
0
0
50
100
150
200
Permeability (10-6 cm/s)
0
0.5
1
plasma unbound fraction
(d)
CL r (ml/minute)
10
1
150
100
50
0
GFR flow (ml/minute)
0
5
10
surface area scalar

Figure 2.2. Sensitivity analysis of the developed kidney model.

The sensitivity analysis was conducted using a hypothetical neutral drug with permeability of 10 (10^{-6} cm/s) and plasma unbound fraction of 0.1 (unless stated otherwise). Panel (A) shows the effects of unbound fraction (0.1-1) inside the renal cell and blood-to-plasma ratio (0.5-5) on simulated renal clearance. Panel (B) shows the effects of tubular volume (0.1-10 fold) and renal cell volume (0.1-10 fold) on simulated renal clearance. Panel (C) shows the effects of in vitro permeability (0.1-200 (10^{-6} cm/s)) and plasma unbound fraction (0.1-1) on simulated renal clearance. Panel (D) shows the effects of glomerular filtration rate (15-120 mL/min) and tubular surface area (0.1-10 fold) on simulated renal clearance.

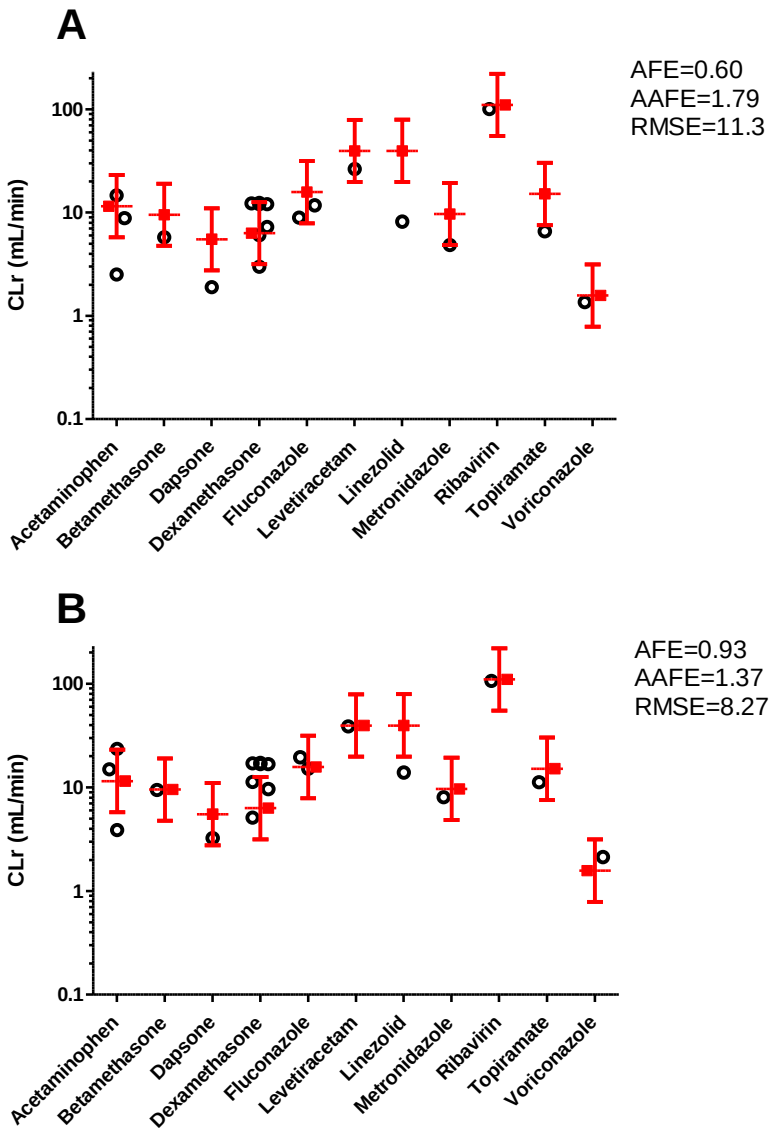
A
AFE=0.60
AAFE=1.79
RMSE=11.3
CLr (mL/min)
100
10
1
0.1
Acetaminophen
Betamethasone
Dapsone
Dexamethasone
Fluconazole
Levetiracetam
Linezolid
Metronidazole
Ribavirin
Topiramate
Voriconazole
B
AFE=0.93
AAFE=1.37
RMSE=8.27
CLr (mL/min)
100
10
1
0.1
Acetaminophen
Betamethasone
Dapsone
Dexamethasone
Fluconazole
Levetiracetam
Linezolid
Metronidazole
Ribavirin
Topiramate
Voriconazole

Figure 2.3. Simulation of renal clearance of 11 neutral test compounds before and after adjustment for microvilli expression level in the *in vitro* experimental system.

Red symbols represent the observed renal clearances of the 11 test compounds with 2-fold error range. Black symbols represent the simulated renal clearances using the available different in vitro permeability data. Panel (a) shows the comparison between simulated and observed renal clearance and the overall AFE, AAFE, and RMSE using the intrinsic permeability calculated under the assumption that microvilli expression is completely absent in the experimental system used to determine permeability values. Panel (b) shows the comparison of simulated and observed renal clearance and the overall AFE, AAFE, and RMSE for the same 11 neutral test compounds using the intrinsic permeability calculated under the assumption that microvilli expression in the in vitro system accounts for 1.5 fold higher measured permeability than would be expected from intrinsic permeability in the absence of microvilli.

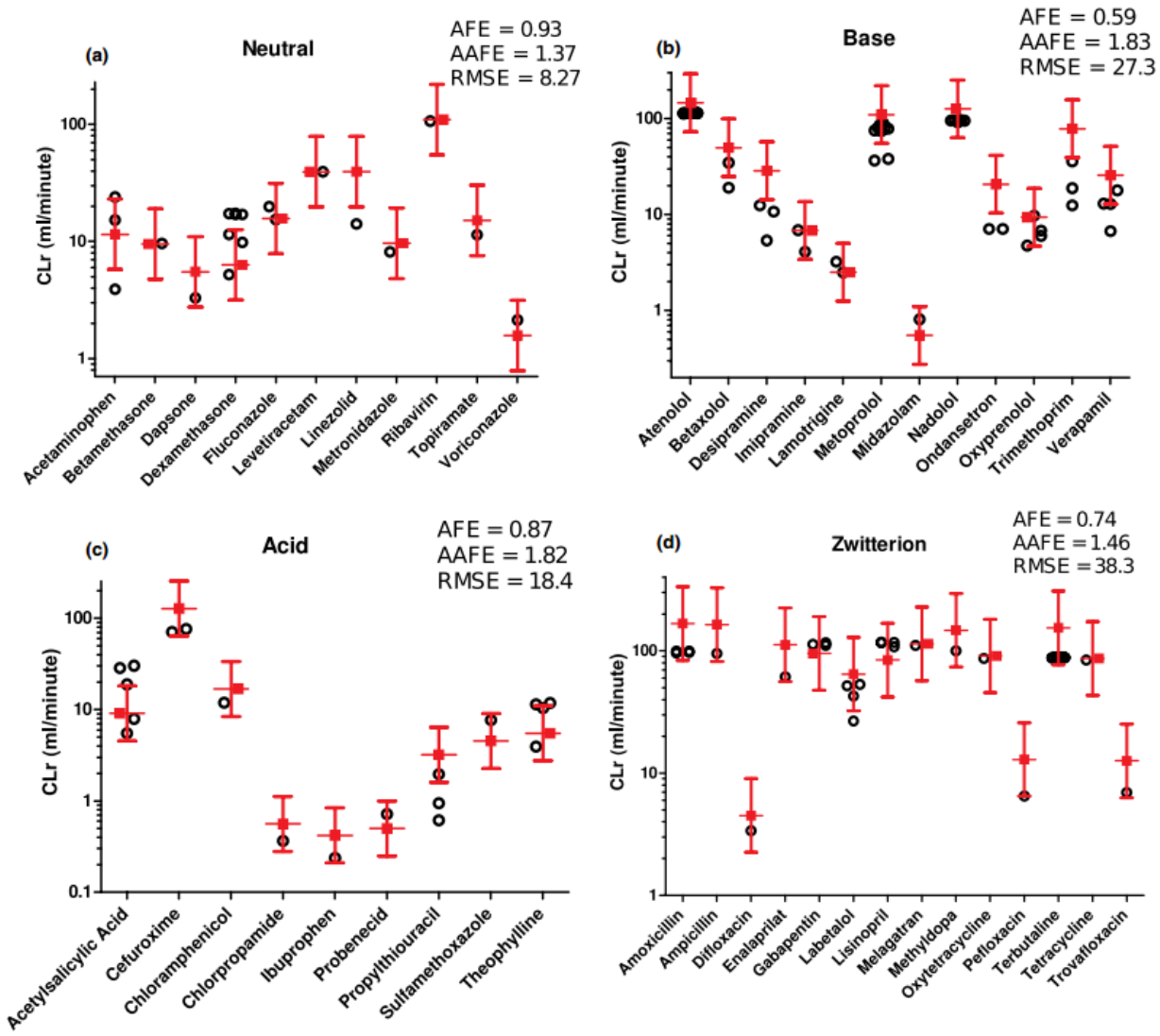

Figure 2.4. Simulation of renal clearances of 11 neutrals, 12 bases, 9 acids, and 14 zwitterions as verification of mechanistic kidney model.

Red symbols represent the observed renal clearances of the test compounds with 2-fold error range. Black symbols represent the simulated renal clearances using different in vitro permeability values. The comparisons between simulated versus observed renal clearances and the AFE and RMSE values for neutral (A), base (B), acid (C), and zwitterion (D) are shown.

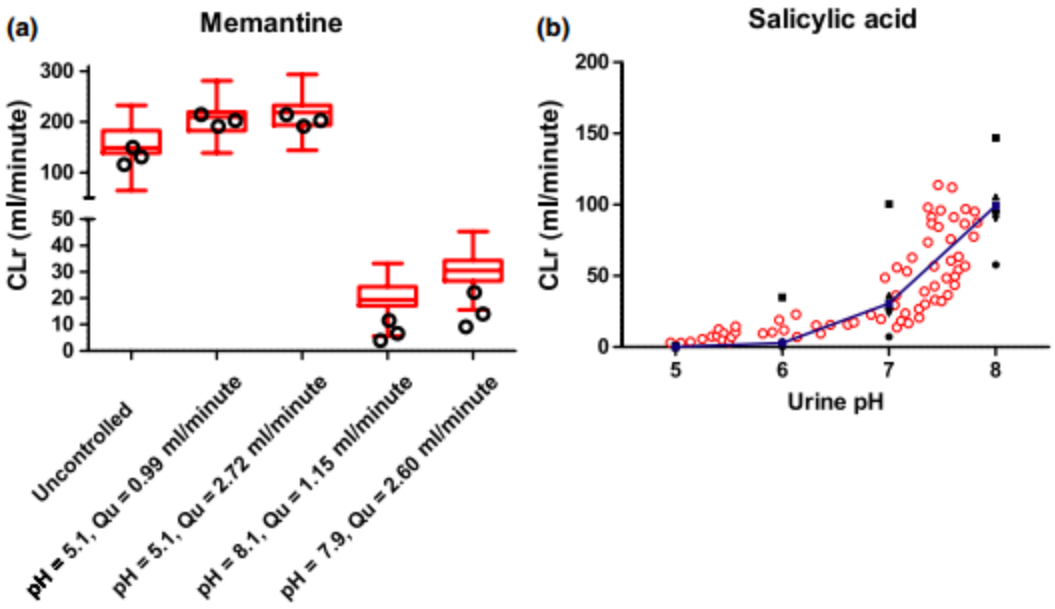
(a)
Memantine
CLr (ml/minute)
300
200
100
50
40
30
20
10
0
Uncontrolled
pH = 5.1, Qu = 0.99 ml/minute
pH = 5.1, Qu = 2.72 ml/minute
pH = 8.1, Qu = 1.15 ml/minute
pH = 7.9, Qu = 2.60 ml/minute
(b)
Salicylic acid
CLr (ml/minute)
200
150
100
50
0
5
6
7
8
Urine pH

Figure 2.5. Simulation of urine pH-dependent renal clearance of memantine and salicylic acid. (Panel A) The observed data is shown (red box plots) for five different conditions (uncontrolled urine pH and flow; urine pH of 5.1, urine flow of 0.99 mL/min; urine pH of 5.1, urine flow of 2.72 mL/min; urine pH of 8.1, urine flow of 1.15 mL/min; urine pH of 7.9, urine flow of 2.6 mL/min). The pH dependent renal clearance of memantine was simulated under the same five conditions (open black circles) according to the process described in the Methods sections using in vitro permeability values reported in MDCK cells and Caco-2 cells, and the average permeability value from the two studies.

(Panel B) Salicylic acid renal clearance was simulated at pH 5, 6, 7 and 8 using each individual permeability values from separate in vitro studies (black squares) and mean permeability values from five studies (blue squares) to explore the effect of altered ionization status of salicylic acid on renal clearance. The simulated values were compared to observed renal clearances (open red circles) of salicylic acid at different measured urine pH values. The observed data is from (Macpherson *et al.*, 1955).

Chapter 3. SAMPLING SITE HAS A CRITICAL IMPACT ON PBPK MODELING

This chapter was published in *Journal of Pharmacology and Experimental Therapeutics (2020) 372, 30-45*

3.1 Abstract

It has been shown that arterial (central) and venous (peripheral) plasma drug concentrations can be very different. While pharmacokinetic studies typically measure drug concentrations from peripheral vein such as the arm vein, physiologically-based pharmacokinetic (PBPK) models generally output simulated concentrations from central venous compartment that physiologically represents the right atrium, a merge of superior and inferior vena cava. In this study, a physiologically-based peripheral forearm sampling site model was developed and verified using nicotine, ketamine, lidocaine, and fentanyl. This verified model allows output of simulated peripheral venous concentrations that can be meaningfully compared to the observed pharmacokinetic data from arm vein. The generalized effect of PBPK model sampling site on simulation output was investigated. Drugs and metabolites with large volumes of distribution showed considerable concentration discrepancy between simulated central venous compartment and peripheral arm vein after intravenous or oral administration, resulting in significant differences in C_{max} and t_{max} values. In addition, the simulated central venous metabolite profile showed an unexpected profile that was not observed in peripheral arm vein. Using fentanyl as a model compound, we show that using the wrong sampling site in PBPK models can lead to biased model evaluation and subsequent erroneous model parameter optimization. Such error in model parameters along with the discrepant sampling site could dramatically mislead the pharmacokinetic prediction in unstudied clinical scenarios, affecting the assessment of drug safety and efficacy. Overall, this study shows that PBPK model publications should specify the model sampling sites and match with those employed in clinical studies.

Significance Statement

Our study shows that sampling from the central venous compartment (right atrium) during PBPK model development gives rise to biased model evaluation and erroneous model parameterization when observed data are collected from peripheral arm vein. This can lead to clinically significant error in predictions of plasma concentration-time profiles in unstudied scenarios. To address this error, we developed and verified a novel peripheral sampling site model to simulate arm vein drug concentrations that can be applied to different drug dosing scenarios.

3.2 Introduction

Physiologically-based pharmacokinetic (PBPK) modeling has been widely used to facilitate design of first-in-human dosing (Jones *et al.*, 2013; Offman and Edginton, 2015; Miller *et al.*, 2019), estimate magnitude of drug-drug interactions (DDIs) (Min and Bae, 2017; Grimstein *et al.*, 2018; Britz *et al.*, 2019), predict pharmacokinetic parameters (Huang and Isoherranen, 2018; Kaur *et al.*, 2018), and simulate drug disposition in specific populations (Khalil and Läer, 2011; Rowland Yeo *et al.*, 2011; Huang *et al.*, 2017). The underlying theory (Jones *et al.*, 2006b; Rowland *et al.*, 2011; Jones and Rowland-Yeo, 2013) and common applications (Jones *et al.*, 2012; Sager *et al.*, 2015; Jamei, 2016) of PBPK models have been extensively reviewed in the literature. Regulatory agencies also use PBPK modeling to facilitate decision making during drug approval process (Huang *et al.*, 2013; Luzon *et al.*, 2017; Shebley *et al.*, 2018). Surprisingly, the specific nature of the sampling site of the primary PBPK simulation outcome, drug concentration data, is rarely explicitly discussed. Simulation output is typically the drug concentration in the central venous compartment that drains blood from the tissue/organ compartments (Kuepfer *et al.*, 2016). This central venous compartment is built in the PBPK models as a mixed compartment that merges all the tissue/organ-specific veins. Physiologically this central venous compartment resembles the right atrium where superior and inferior vena cava merge together. However, in clinical practice and in pharmacokinetic studies, plasma samples (i.e. the observed data) are usually taken from a peripheral sampling site such as the median cubital vein (i.e. arm vein). This generates a concerning discrepancy between the modelled and observed data, as measured drug concentrations from arm artery, which are essentially equivalent to the drug concentrations in the right atrium (assuming lung distribution is not significant and distribution equilibrium in the lung is reached instantaneously) have been shown to differ from concentrations in peripheral vein for multiple

drugs (Chiou, 1989; Gourlay and Benowitz, 1997; Ericsson *et al.*, 2000; Rentsch *et al.*, 2001; Persson *et al.*, 2002; Darwish, Kirby, *et al.*, 2006; Olofsen *et al.*, 2010). This arteriovenous drug concentration difference has been shown to affect pharmacokinetic-pharmacodynamic (PK-PD) modeling when pharmacodynamic effect is empirically fitted to plasma drug concentrations. (Gumbleton *et al.*, 1994; Jacobs and Nath, 1995; Tuk *et al.*, 1997). Due to the observed discrepancy between arterial and arm vein concentrations, the derived PK-PD relationship using different concentrations as reference may differ. This may result in misspecified PK-PD models that fail to predict PD in other circumstances. Based on the observed arteriovenous drug concentration differences, we hypothesized that PBPK-model simulated concentration profiles, model parameterization, model acceptance and model extrapolation will be impacted by model sampling site.

Two previous studies that developed a virtual peripheral blood compartment to model drug concentrations at peripheral sampling site have shown differences in the simulated concentrations depending on the sampling site (Levitt, 2004; Musther *et al.*, 2015). However, neither study established a physiologically-based forearm compartment, which prevents capturing the unique forearm tissue distribution phenomenon at the sampling site. Instead, both studies employed empirical fitting strategy to estimate peripheral blood concentration. The first study (Levitt, 2004) mentioned that such fitting could not be conducted in a global manner and the verification of the fitted peripheral site using a different set of test drugs was unsuccessful. The second study (Musther *et al.*, 2015) modified Levitt's model but did not verify the model using arterial concentrations or arteriovenous difference. In addition, neither study addressed 1) the general impact of sampling site on different compounds with varying properties, 2) the arteriovenous difference after oral dosing, 3) the arteriovenous difference for drug metabolite,

and 4) the impact of model sampling site selection on PBPK model development, evaluation, and application. Hence, further studies are needed to understand the importance of sampling site selection in PBPK modeling. In this study, a physiologically-based forearm compartment was developed and verified as the peripheral sampling site in the PBPK model. The verified model was then used to explore the differences in the simulated concentrations between different PBPK model sampling sites after intravenous and oral dosing for drugs and metabolites with a wide spectrum of pharmacokinetic properties. Finally, the model was applied to simulate central arterial and peripheral arm vein concentrations after fentanyl buccal administration to demonstrate the impact of discrepant sampling site on model evaluation, parameter optimization, and prediction in unstudied scenarios during model application and extrapolation.

3.3 Materials and methods

3.3.1 Development of full body PBPK parent-metabolite structural model with peripheral forearm sampling site

A 32-compartment parent-metabolite full-body PBPK model (Figure 3.1) was developed using MATLAB and Simulink platform (R2018a; MathWorks, Natick, MA). A central venous (i.e. physiologically analogous to right atrium) compartment was included to merge all organ/tissue-specific emergent veins before encountering the lung compartment. A central arterial compartment was built to receive blood from the lungs and distribute blood flows to all tissue compartments. Similar to conventional full PBPK models (Rowland *et al.*, 2011; Jones and Rowland-Yeo, 2013), 12 physiologically important tissues and organs (adipose, bone, brain, gut, heart, kidney, liver, lung, muscle, skin, spleen, and pancreas) were included in the model (Table 3.1). Except liver, all other tissue/organ compartments including forearm were modeled as perfusion-limited compartments where drug distribution was assumed to reach equilibrium instantaneously between tissue mass and tissue blood, with a total drug concentration gradient defined by tissue-to-plasma partition coefficient (K_p). For the liver, a permeability-limited model including two compartments, the hepatocytes and the sinusoidal blood, was built. In this study, the exchange of drug between the two compartments was determined by passive diffusion which was set to be sufficiently high to reflect perfusion-limited hepatic distribution. The hepatic metabolism of drug and metabolite, and the formation of metabolite in the liver were modeled to occur within the hepatocyte compartment (Figure 3.1).

A forearm compartment was incorporated in parallel with other distribution organs based on known physiology to capture drug distribution to the peripheral sampling site (Figure 3.1). Since the median cubital vein is a superficial vein that mostly drains from adipose, muscle, and skin

tissues of the forearm, the forearm compartment only included these three tissue types and neglected bone that is believed to be drained only by the deep vein. The model parameters of volumes (Cooper *et al.*, 1955) and blood flows (Elia and Kurpad, 1993) of the forearm adipose, muscle, and skin are physiological values in humans and are summarized in Table 3.1. Each of the forearm tissues was assumed to share the same K_p value as the respective tissues in the rest of the body. Structurally, the forearm compartment was modeled as a perfusion-limited tissue with anastomoses taken into account as a blood flow shunt directly from arm artery into arm vein. A previously applied fit-for-purpose anastomoses fraction of 10% (Musther *et al.*, 2015) was used in the arm model in the current study. Sensitivity analyses were conducted (Figure 3.2 and 3.3) to examine the potential impact of parameter uncertainty on central venous compartment (right atrium) and peripheral arm vein drug concentrations. Specifically, the influence of K_p values of muscle, adipose, and skin tissues and anastomoses fraction were tested. For the sensitivity analysis, the baseline condition was set with K_p values for all tissues equal to 3 (V_{ss} = 200 L) and anastomoses fraction equal to 10%. Overall, 2 sets of scenarios were tested after iv administration. For the first set of scenarios, K_p values of muscle, adipose or skin were either increased from 3 to 5 or decreased from 3 to 1. In all scenarios, K_p values for other untested tissues were adjusted uniformly such that the V_{ss} remained at 200 L to avoid the impact of total volume changes on drug disposition and the simulated plasma concentration curves. In addition, the impact of the anastomoses fraction was examined by increasing anastomoses fraction from 10% to 30% and decreasing anastomoses fraction from 10% to 0%. For the second set of scenarios, K_p values of muscle, adipose or skin were either increased from 3 to 10 or decreased from 3 to 1 without controlling for the V_{ss}, so that only one parameter was changed at a time and a wider range of K_p values could be tested. For sampling in the simulations, plasma drug concentrations were sampled

from the central venous compartment (right atrium), central artery compartment, and peripheral forearm vein (Figure 3.1). The model file and code script are provided in Supplementary Material.

3.3.2 Verification of the peripheral forearm sampling site model

To verify our developed physiologically-based forearm model as the peripheral sampling site, six observed pharmacokinetic studies conducted with nicotine, ketamine, lidocaine, and fentanyl after intravenous administration were used (Tucker and Boas, 1971; Gourlay and Benowitz, 1997; Persson *et al.*, 2002; Isohanni *et al.*, 2005; Macleod *et al.*, 2012; Ziesenitz *et al.*, 2015). Plasma concentration-time curves from these studies were digitized using WebPlotDigitizer (version 4.2, https://automeris.io/WebPlotDigitizer). To simulate the plasma concentration-time profile for nicotine, ketamine, lidocaine, and fentanyl, drug-specific models for individual compounds were built and detailed drug parameters are shown in Table 3.2. The physicochemical properties, plasma unbound fraction, and blood-to-plasma ratios were collected from literature for each compound (Rodgers and Rowland, 2007). Tissue-specific K_p values that have been experimentally determined in the rat were used for each drug (Edwards and Mather, 2001; Rodgers *et al.*, 2005). For the tissues/organs that did not have experimentally determined K_p data for a given drug, a value of 1 was used. The systemic plasma clearances that were reported in each of the corresponding human studies used for verification were used in the model (Persson *et al.*, 2002; Pitsiu *et al.*, 2002; Isohanni *et al.*, 2005; Macleod *et al.*, 2012; Ziesenitz *et al.*, 2015). One study (Tucker and Boas, 1971) did not report the observed clearance value, and therefore a secondary source (Goodman *et al.*, 2006) was used for lidocaine clearance. The hepatic intrinsic clearance was calculated assuming well-stirred model and the systemic clearances were all attributed to hepatic clearance. All simulations used the same dosage, route of administration, and infusion

length as described in the original clinical studies (Tucker and Boas, 1971; Gourlay and Benowitz, 1997; Persson *et al.*, 2002; Isohanni *et al.*, 2005; Macleod *et al.*, 2012; Ziesenitz *et al.*, 2015). A representative virtual subject was used in all simulations with typical physiological values without variability. The simulated plasma drug concentrations were sampled from the central venous compartment (right atrium), which is essentially equal to arterial compartment, and from the developed peripheral arm vein compartment to compare to the observed arterial and arm vein concentrations, respectively.

For quantitative evaluation and model verification, absolute average fold error (AAFE, equation 1) between observed and simulated data was calculated. The model was considered acceptable if the AAFE was within the 1.5-fold criteria.

$$AAFE = 10^{\frac{1}{n}\Sigma\left|log_{10}\frac{Simulated}{Observed}\right|} \quad (1)$$

3.3.3 Sampling site effect on PBPK model-simulated plasma drug concentrations after intravenous administration

The verified model was used to investigate whether the effect of PBPK model sampling site on simulated plasma drug concentration-time profiles and PK parameters could be generalized for a wide range of compounds that have not been experimentally studied for arteriovenous drug concentration difference. A matrix of 9 hypothetical drugs with a range of clearance and distribution characteristics was produced for generalization purposes. The simulated hypothetical drugs had clearances that ranged from low (metabolic intrinsic clearance, CL_{int}=10 L/hr, extraction ratio, ER=0.1) to medium (CL_{int}=100 L/hr, ER=0.53) and high (CL_{int}=1000 L/hr, ER=0.92) clearance and distribution characteristics that varied from volume of distribution at steady state (V_{ss}) of 66 L (K_p =1 for all organs) to V_{ss} of 189 L (K_p =3 for all organs) and V_{ss} of 619 L (K_p =10

for all organs). The blood-to-plasma ratio and plasma unbound fraction were 1 for all simulations and renal and biliary clearances were set as 0. All simulations were run for 240 hrs after dosing. The AUCs were calculated from t=0-240 hrs using trapezoidal method in MATLAB, and the C_{last} value was the drug concentration at t=240 hrs. To simulate intravenous dosing, 1,000 mg drug was infused at a constant rate into the central venous compartment (right atrium). First, iv infusion times of 1 min, 5 min, 10 min, 20 min, and 30 min were tested (Figure 3.4). Based on these simulations, a 1 min infusion time was selected and used for all subsequent simulations of iv bolus dosing.

3.3.4 Verification of the fentanyl model after buccal administration

To explore the arteriovenous differences for route of administration other than iv, the fentanyl drug model verified for iv administration was used and expanded to capture arteriovenous differences after buccal administration. A PK study that reported both arterial and peripheral arm vein fentanyl concentrations after buccal administration was used as the training dataset for model development (Darwish, Kirby, *et al.*, 2006). Plasma concentration-time curves were digitized using WebPlotDigitizer (version 4.2, https://automeris.io/WebPlotDigitizer). To simulate the fentanyl buccal administration, 50% of the dose was absorbed through buccal and the other 50% was absorbed through gut based on the drug label (FDA, 2011). The absorption was assumed to be complete from both buccal and the GI routes (i.e. F_a=1). Intestinal metabolism was assumed to be zero (i.e. F_g=1). The buccal absorption rate constant ($k_{a,buccal}$) and gut absorption rate constant ($k_{a,gut}$) were optimized to be 1 hr^{-1} and 3 hr^{-1}, respectively, based on the training dataset (Darwish, Kirby, *et al.*, 2006). To verify the optimized absorption rate parameters, three independent datasets (Darwish, Tempero, *et al.*, 2006; Darwish *et al.*, 2010)

that reported only peripheral arm vein concentrations were used as the test dataset. During the verification, the simulated plasma drug concentrations sampled from the developed forearm vein compartment were compared to the observed peripheral arm vein concentrations. For quantitative evaluation and model verification, AAFE and C_{max} ratio were calculated. The model was considered acceptable if the AAFE was within the conventional 2-fold criteria and the C_{max} ratio was within the 0.8-to-1.25-fold range.

3.3.5 Sampling site effect on PBPK model-simulated plasma drug concentrations after oral administration

After the verification of fentanyl buccal administration, the model was used to investigate the effect of PBPK model sampling site on simulated plasma drug concentration-time profiles for a set of hypothetical drugs with a wide range of PK characteristics after oral administration. A matrix of 15 hypothetical drugs with a range of clearance and distribution parameters was generated. The simulated hypothetical drugs had clearances that ranged from low (CL_{int}=10 L/hr, ER=0.1) to medium (CL_{int}=100 L/hr, ER=0.53) and high (CL_{int}=1000 L/hr, ER=0.92) clearance, and distribution characteristics that varied from V_{ss} = 66 L (K_p =1 for all organs), V_{ss} = 189 L (K_p =3 for all organs), V_{ss} = 619 L (K_p =10 for all organs), V_{ss} = 209 L (K_p =1 for adipose, muscle, and skin and K_p =10 for all other organs), and V_{ss} = 477 L (K_p =10 for adipose, muscle, and skin and K_p =1 for all other organs). The blood-to-plasma ratio and plasma unbound fraction were 1 for all simulations and renal and biliary clearances were set as 0. All simulations were run for 240 hours after dosing, the AUCs from t=0-240 hrs were calculated using trapezoidal method in MATLAB and the C_{last} value was the drug concentration at t=240 hrs. To simulate po dosing, 1,000 mg drug was introduced into the gut lumen followed by immediate complete dissolution and homogeneous

distribution inside the lumen. The drug absorption from gut lumen into intestinal blood was described by a single first order rate constant k_a. Drug appearance in the portal vein was driven by both k_a and the blood flow of the gut. Fraction absorbed (F_a) was assumed to be one and no intestinal metabolism occurred. First, k_a values of 0.2, 0.5, 1, 2, and 5 hr^{-1} were simulated (Figure 3.5), and based on these simulations, k_a value of 1 hr^{-1} was selected for the matrix of oral dosing simulations unless otherwise stated.

3.3.6 Sampling site effect on PBPK model evaluation, parameter optimization, and model extrapolation

To explore the potential impact of the use of a discrepant sampling site between PBPK model simulations and observed studies on model evaluation during top-down model development, fentanyl disposition after buccal administration was used as a representative scenario. Three observed datasets of fentanyl buccal administration (Darwish, Tempero, *et al.*, 2006; Darwish *et al.*, 2010) that reported only peripheral arm vein sampling were used and the simulated central venous compartment (right atrium) fentanyl concentrations were compared to the observed arm vein data. The model evaluations were considered acceptable if the C_{max} ratio met the 0.8-to-1.25-fold criterion and if the AAFE was within the conventional 2-fold criterion. The k_a values in the fentanyl model were then optimized using central venous compartment (right atrium) as the sampling site (Darwish *et al.*, 2010) so that the simulated central venous compartment concentrations met the model verification criteria when compared to the observed arm vein data.

The collective impact of the choice of sampling site on PBPK model development and the rigor in predicting unstudied situations was evaluated in a hypothetical scenario where a new buccal formulation of fentanyl was created with an estimated 400% increase in the buccal absorption rate.

Both arm vein model with verified k_a values and the central venous compartment sampling model with k_a values optimized using discrepant sampling site were used to simulate fentanyl PK in this unstudied clinical scenario. The predicted C_{max} change for the new formulation was calculated based on the arm vein model and the central venous compartment sampling model.

3.3.7 Sampling site effect on PBPK model simulated plasma metabolite concentrations

The impact of sampling site on simulated metabolite kinetics was studied via simulations of plasma concentration-time curves of metabolites with a matrix of different drug and metabolite characteristics. Three scenarios of hypothetical drug (CL_{int}) and metabolite ($CL_{int,m}$) intrinsic clearance combinations were simulated: 1) CL_{int}=10 L/hr, $CL_{int,m}$=20 L/hr, 2) CL_{int}=1000 L/hr, $CL_{int,m}$=20 L/hr, 3) CL_{int}=10 L/hr, $CL_{int,m}$=2000 L/hr. For each combination of drug and metabolite intrinsic clearances, different distribution kinetics of the metabolite were simulated: 1) metabolite K_p ($K_{p,m}$)=1, 2) $K_{p,m}$=3, and 3) $K_{p,m}$=10 for all organs, with the drug K_p values of all organs =3. For the simulations, the drug was administered either as a 1,000 mg iv bolus over 1 min into the central venous compartment or as a 1,000 mg oral dose into the gut lumen as described above. The k_a and F_a were as described above and no metabolite was formed in the gut tissue.

3.4 Results

3.4.1 Development and verification of the full body PBPK structural model with peripheral forearm sampling site

A full physiologically-based pharmacokinetic (PBPK) model with a novel peripheral forearm sampling site was developed using conventional PBPK model structure and incorporating both peripheral and central sampling sites (Figure 3.1). A forearm compartment consisting of forearm muscle, forearm skin, and forearm adipose with human physiology-based volumes and blood flows for each tissue was included in the model to allow arm vein sampling (Table 3.1). To evaluate the impact of parameter uncertainty on central venous compartment (right atrium) and peripheral arm vein concentrations, sensitivity analyses were conducted. The results (Figure 3.2 and 3.3) show that the K_p of muscle is the most sensitive parameter, which would be expected as the forearm predominantly consists of muscle tissue and the blood perfusion rate for muscle is the lowest among all forearm tissues (Table 3.1). In addition, an optimized anastomoses fraction of 10% (Musther *et al.*, 2015) was used in the present model, and the sensitivity analyses show that this parameter is not critically sensitive (Figure 3.2). The sensitivity analyses also show that while the arm vein concentration profile is sensitive to the K_p values or arm tissues and anastomoses fraction, the arterial and central venous compartment (right atrium) concentrations are relatively insensitive to these parameters.

To verify the developed model, nicotine, ketamine, lidocaine, and fentanyl pharmacokinetic (PK) data collected from arm artery and vein after iv administration were used (Figure 3.6). These drugs

were chosen after an extensive literature search, based on data availability of arterial and arm vein concentrations and experimentally measured K_p values in animal. PK data from six clinical studies where arterial or arm vein drug concentrations were reported after intravenous administration were collected (Tucker and Boas, 1971; Gourlay and Benowitz, 1997; Persson *et al.*, 2002; Isohanni *et al.*, 2005; Macleod *et al.*, 2012; Ziesenitz *et al.*, 2015). Notably, nicotine and ketamine studies reported simultaneous arterial and arm vein drug concentration-time profiles during and after iv infusion. The average fold difference between the observed arterial and arm vein data across all analyzed time points was 1.7 for nicotine (Figure 3.6a) and 1.6 for ketamine (Figure 3.6b), illustrating the considerable differences between arterial and arm vein drug concentrations during and after iv infusion.

To simulate the observed PK data and to verify the developed model, drug-specific models for nicotine, ketamine, lidocaine, and fentanyl were developed (Table 3.2), both central venous compartment (right atrium) and peripheral arm vein concentrations were simulated, and the simulations were compared to the observed arterial and arm vein data, respectively. Overall, both arterial and arm vein concentrations were successfully recapitulated for all four drugs in all seven studies with AAFE values within 1.5-fold (Figure 3.6), verifying the developed forearm structural model. The simulated drug concentration-time profiles sampled from the central venous compartment (right atrium) superimposed with the simulated drug concentration-time profiles sampled from artery compartment (Figure 3.6a, b, c, and e), confirming that the central venous compartment (right atrium) sampling accurately represents the arterial data when lung distribution is not significant and distribution equilibrium is reached instantaneously. For nicotine and ketamine, two drugs for which observed simultaneous arterial and arm vein concentrations after iv administration are available, the simulated drug concentration-time profiles successfully

captured the observed arteriovenous difference (Figure 3.6). For these studies, the arm vein concentrations were consistently lower than the arterial concentrations before pseudo-equilibrium was reached. This difference is likely due to forearm tissue distribution (dilution) effect, resulting in a lower C_{max} in the arm vein compared to the arterial concentration. For lidocaine and fentanyl, for which observed simultaneous arterial and arm vein concentrations were not available, separate studies that reported either arterial or arm vein concentration data were used for model verification. The independent recapitulation of either arterial or arm vein observed concentration data was successful based on the AAFE values that were within 1.5-fold (1.16 to 1.35). Importantly, none of these simulations of iv dosing applied any scalar or implemented any optimization besides top down incorporation of CL and prediction of V_{ss} based on observed rat K_p values. This further supports the confidence in the forearm structural model verification. As such, this work establishes the first physiologically-based peripheral sampling site model that has been verified using simultaneous arterial and arm vein concentration data. The verification results suggest that our model accurately captures the arterial concentration-time profile, arm vein concentration-time profile, and the arteriovenous difference and that the forearm structural model is sufficiently robust to be applied to simulate drug disposition for other unstudied compounds and scenarios.

3.4.2 Sampling site effect on PBPK model-simulated plasma drug concentrations after intravenous administration

To investigate whether certain drug specific PK characteristics contribute to the magnitude of arteriovenous concentration difference after iv administration, the central venous compartment (right atrium), central artery and peripheral forearm vein concentrations were simulated after iv administration for a matrix of hypothetical drugs (Figure 3.7). The pharmacokinetic analyses of

the simulation data from each site are shown in Table 3.3. The simulations unequivocally show that selection of PBPK model sampling site affects the simulated distribution kinetics and the plasma concentration-time profile of the drug, and the differences between sampling sites can be considerable. However, the areas under plasma concentration-time curves (AUCs) and clearances (CLs) were equal among all sampling sites (Table 3.3). As expected, the simulated central venous compartment (right atrium) concentrations and central artery concentrations were superimposable (lung distribution is not significant and distribution equilibrium in lung is reached instantaneously). In contrast, similar to the observed studies (Figure 3.6a and b), the arm vein concentrations during the initial distribution phase and arm vein C_{max} were much lower than central venous compartment (right atrium) concentrations after iv dosing (Figure 3.7). In addition, slower iv infusion rate or longer duration of infusion did not eliminate the discrepancy in the concentrations between sampling sites (Figure 3.4). The simulations with a matrix of hypothetical drugs showed that the impact of sampling site on the PK characteristics was more pronounced for drugs with high volumes of distribution (Figure 3.7). Drugs with large volume of distribution showed an appreciable concentration difference during the distribution phase where arm vein drug concentrations were consistently lower than central venous compartment (right atrium) drug concentrations. Lastly, after distribution pseudo-equilibrium was reached (i.e. terminal elimination phase), the simulated peripheral arm vein concentrations were consistently higher than those collected from the central venous compartment, with drugs with higher clearances showing greater differences between the sampling sites. Taken together, these data show that special attention to the choice of experimental and simulation sampling site should be paid for drugs with large volumes of distribution or high clearances.

3.4.3 Sampling site effect on PBPK model-simulated plasma drug concentrations after oral administration

Reported clinical studies investigating arteriovenous differences are almost exclusively conducted after iv administration. However, we hypothesized that significant sampling site effect would also be observed after oral administration. Indeed, significant arteriovenous drug concentration differences were shown for fentanyl after buccal administration (Darwish, Kirby, *et al.*, 2006). To explore this difference, the fentanyl model verified after iv dosing (Figure 3.6) was further developed and verified for buccal administration (Figure 3.8). To simulate buccal administration, buccal absorption rate constant ($k_{a,buccal}$) and gut absorption rate constant ($k_{a,gut}$) were incorporated into the model and optimized to be 1 hr^{-1} and 3 hr^{-1}, respectively, based on observed fentanyl arteriovenous difference (Figure 3.8a). To verify the optimized buccal absorption rate constant ($k_{a,buccal}$) and gut absorption rate constant ($k_{a,gut}$), three independent studies were used as test datasets (Figure 3.8b-d). As shown in Figure 3.8, the optimized absorption rate parameters successfully recapitulated all independent test datasets sampled from arm vein with all AAFE values < 2 and all simulated C_{max} values within the 0.8-to-1.25-fold range of observed C_{max} values (Figure 3.8b-d). Hence, the optimized absorption rate constants were considered successfully verified. Such verification substantiates the validity of our forearm structural model and the applicability of our model to simulate arteriovenous differences after oral administration. The data with fentanyl after buccal administration (Darwish, Kirby, *et al.*, 2006) also strongly suggest that importance of arteriovenous differences is not limited to iv administration.

To investigate the overall effect of sampling site on arteriovenous concentration difference after oral administration, the verified model was used to simulate arterial and arm vein drug concentrations after oral dosing for a matrix of drugs with a variety of PK parameters (Figure 3.9).

Similar to the iv dosing, the simulations of oral administration show that selection of the PBPK model sampling site affects the simulated drug distribution kinetics and the plasma drug concentration-time profile, but not AUCs (Table 3.4). Specifically, the arm vein concentrations during the initial distribution phase were lower than the central venous compartment (right atrium) concentrations, and slower oral absorption rates did not eliminate this discrepancy (Supplementary Figure 3.8). This impact of sampling site during the initial distribution phase was more pronounced for drugs with large volumes of distribution. Especially, the K_p values of skin, adipose, and muscle, which directly affect the forearm distribution kinetics had a sizable effect on the concentration difference between arm vein and central venous compartment (right atrium) (Figure 3.9j-o). As a result, the values of C_{max} and t_{max} were substantially affected. The simulated C_{max} value obtained by sampling from central venous compartment was higher than the C_{max} obtained from peripheral arm vein, with a C_{max} ratio between the two sites ranging from 1.07 to 4.25 (Figure 3.9). The simulated t_{max} value for the drug based on central venous sampling was consistently shorter (0.12-0.72-fold) than the t_{max} from peripheral arm vein sampling (Figure 3.9). Similar to the iv dosing, during the terminal elimination phase, the simulated arm vein concentrations of the drug were higher than those collected from the central venous compartment, and drugs with higher clearances showed greater differences (Table 3.4). Taken together, these simulations show that the choice of sampling site has quantitatively important effect also after oral administration on clinically significant measures of drug exposure and accumulation such as C_{max} and C_{trough}.

3.4.4 Sampling site effect on PBPK model evaluation, parameter optimization, and model extrapolation

During PBPK model development, simulated central venous compartment (right atrium) concentrations are usually compared to observed PK data that are almost exclusively obtained from peripheral arm vein, and the PK parameters are optimized to achieve concordance between simulated and observed data. Due to the true differences between central venous compartment (right atrium) and peripheral arm vein concentrations, we hypothesized that the use of simulated central venous compartment concentration-time profile and observed arm vein concentrations may result in biased model evaluation despite the use of verified "true" parameters. This hypothesis was tested using the verified fentanyl buccal and iv administration model (Figure 3.10). While the verified absorption rate parameters correctly simulated peripheral and arterial fentanyl concentrations (Figure 3.8), the use of central venous compartment (right atrium) sampling site as the PBPK model output with observed arm vein data rendered all simulations unacceptable with AAFE values > 2 and C_{max} ratios outside the 0.8-to-1.25-fold range (Figure 3.10). As a result, when discrepant sampling site is used, the true drug parameters are likely not selected for the PBPK model under development (Figure 3.11a). Instead, false model parameters will be obtained through erroneous model optimization until the simulated central venous profile conforms to the observed arm vein data (Figure 3.11b). The difference between the "true" and "false" parameter estimates can be considerable as illustrated by the fentanyl example. While the verified "true" parameters for $k_{a,buccal}$ and $k_{a,gut}$ were 1 hr^{-1} and 3 hr^{-1}, respectively (Figure 3.8), the erroneously optimized $k_{a,buccal}$ and $k_{a,gut}$ for central venous sampling were 0.35 hr^{-1} and 0.7 hr^{-1} respectively (Figure 3.11b). This illustrates that parameter optimization using simulated central venous profile and observed arm vein sampling may result in confounded drug models that do not accurately reflect the true pharmacokinetic properties.

To test whether the erroneous parameter optimization has an impact in model application and whether the use of discrepant sampling sites between simulation and observation can result in biased prediction in unstudied clinical scenarios, a hypothetical case with increased $k_{a,buccal}$ (new formulation) for fentanyl was simulated using the model optimized based on arm vein ("true") (Figure 3.11c) and central venous sampling ("false") (Figure 3.11d). The C_{max} in the arm vein due to new formulation was predicted to increase by 40% (Figure 3.11c) using the verified arm model and verified absorption parameters, while the C_{max} using central venous sampling and erroneous parameters was predicted to increase by 119% (Figure 3.11d). This shows an approximately 3-fold difference in the predicted magnitude of formulation effect on C_{max} which would be considered clinically significant. The simulations show that PBPK models developed and optimized using central venous sampling can erroneously predict the impact of new formulation on pharmacokinetics and drug disposition, and lead to wrong conclusions that have clinical significance.

3.4.5 Sampling site effect on simulated plasma metabolite concentration using PBPK model

An aspect that has not been clinically tested in humans is whether sampling site has an impact on metabolite plasma concentration profile. To investigate the overall sampling site effect on plasma metabolite concentration, the central venous compartment (right atrium) and peripheral forearm vein were sampled for simulated metabolite concentrations after iv (Figure 3.12) and oral (Figure 3.13) administration of the parent drug. The simulation data show that selection of the sampling site affects the simulated distribution kinetics and the plasma concentration-time profile of the metabolite as well, but not the metabolite AUC. Similar to the parent drug, the impact of sampling

site on metabolite simulation was more pronounced with metabolites with high volumes of distribution (high $K_{p,m}$, Figures 3.12 and 3.13). The simulated metabolite C_{max} value obtained by sampling from central venous compartment was in general higher than the metabolite C_{max} obtained from arm vein, with a C_{max} ratio between the two sites ranging from 1.00 to 4.62 (Figures 3.12 and 3.13).

Intriguingly, the choice of the sampling site in PBPK simulations of metabolites had some unexpected effects. A metabolite plasma concentration-time profile is expected to follow a biphasic curve of increasing and decreasing plasma concentrations. However, metabolite concentrations sampled from the central venous compartment (right atrium) showed a unique profile with a spike in the metabolite concentrations during the distribution phase of the parent drug after iv dosing (Figure 3.12a, d, and g) followed by a second peak of the plasma concentrations corresponding to the metabolite C_{max} expected from arm vein sampling. The presence of the spike could also be observed after po dosing when the drug had a low clearance (Figure 3.13d and g) but was less pronounced compared to iv dosing. Further, the spike observed from central venous (right atrium) profile was hardly observed from arm vein profile, which agrees with observed metabolite profile from common clinical studies.

3.5 Discussion

It has been shown that arterial drug concentrations can be remarkably different from peripheral venous drug concentrations in animals and humans (Chiou, 1989; Gourlay and Benowitz, 1997; Ericsson *et al.*, 2000; Rentsch *et al.*, 2001; Persson *et al.*, 2002; Darwish, Kirby, *et al.*, 2006; Olofsen *et al.*, 2010). The physiologically-based simulations presented here reproduced the observed phenomenon of arteriovenous drug concentration differences. To our knowledge, our peripheral sampling model is the first physiologically-based model that is verified using both arterial and arm vein drug concentrations simultaneously. Our analysis is also the first to systematically evaluate drug PK characteristics that drive arteriovenous drug concentration differences after both iv and oral administration. Consistent with previous theory (Chiou, 1989), the simulations show that arteriovenous differences during the initial distribution phase are most pronounced for compounds with large volumes of distribution since the arteriovenous difference during initial phase is due to drug distribution into the forearm tissue. During the terminal elimination phase, the arteriovenous differences are only significant for compounds with high clearances, as the arteriovenous difference during terminal phase is a result of the blood emerging from the eliminating organ diluting the drug concentration measured in the central venous compartment (right atrium). The simulations also show that arteriovenous differences in drug concentrations can be significant following oral administration. This is important as minimal clinical studies have been done to explore arteriovenous differences after oral administration in humans. Yet, PBPK modeling is frequently used to simulate oral dosing scenarios and to specifically explore the C_{max}. Based on our simulations and the existing data (Gourlay and Benowitz, 1997; Moksnes *et al.*, 2008), it is highly likely that arteriovenous differences are also important following other routes of administration such as intranasal or inhalation and should be

considered in PBPK modeling of these routes of administration. In addition, our PBPK modeling approach could also be extended to preclinical species in which experimental studies with various sampling sites and routes of administration are feasible.

Based on the observed arteriovenous differences, we hypothesized that this difference would be crucial for PBPK modeling when the model does not output simulations from the same site as the observed study. As one of the key advantages of PBPK models is that they allow simulation of complete plasma concentration-time curves and especially C_{max} for drugs with narrow therapeutic indexes that have concerns of concentration-dependent adverse effects, it is important to address whether correct simulated concentrations are sampled from PBPK models to reflect the concentrations driving pharmacological or toxicological effects. Our findings highlight the need for either sampling from arm artery in experimental PK studies and comparing to PBPK model-simulated arterial concentrations, or sampling from the arm vein in studies and comparing to simulated peripheral sampling compartment concentrations. For the latter, our results suggest that a peripheral sampling compartment that specifically addresses distribution at a peripheral sampling site needs to be developed and incorporated into PBPK models to allow meaningful comparisons between simulated and observed drug concentrations.

In this study, we developed an *in silico* peripheral sampling compartment using human forearm physiology to replicate peripheral sampling site. In contrast, previous models (Levitt, 2004; Musther *et al.*, 2015) used optimized hybrid of emergent veins from total body skin, adipose and muscle tissue without constructing a physiologically-based peripheral sampling compartment. Comparing to the previous hybrid models, the physiologically-based model developed here performed better, showing successful simulations of all verification datasets (AAFE 1.16-1.35) without extensive drug parameter optimization. The first study (Levitt, 2004) used optimized

hybrid approach and could not generate a standardized arm model. Different arm model parameters were needed to recapitulate disposition for different chemicals. The second study (Musther *et al.*, 2015) modified the Levitt's model and used the simulated/observed C_{max} ratio as the evaluation criteria. Only 6 of 15 test datasets had a simulated/observed C_{max} ratio within 0.8-to-1.25-fold and the model was not validated using arterial and arm vein concentration data simultaneously. One uncertain parameter in all these models is the anastomoses fraction. Due to incomplete physiological information of anastomoses in human, a 10% fraction was estimated previously and used here. This is likely an acceptable parameter as the sensitivity analysis (Figure 3.2) showed that it is not a critically sensitive parameter. Commercial PBPK software such as Simcyp also provides the option to sample from a peripheral site, using the published model (Musther *et al.*, 2015). However, whether Simcyp users employ this during modeling is unclear. Although our forearm sampling model is distinctly different from the Simcyp model, the discrepancy between simulated central and peripheral concentrations for both drug and metabolite after iv and po dosing was qualitatively replicated using Simcyp version 17 (Figure 3.14). Therefore, this phenomenon appears to be a general consideration for all PBPK models. More attention should be payed to specifying and reporting the sampling site in PBPK modeling regardless of the modeling platform used. For establishing compound-specific drug models, it is advisable to experimentally determine the K_p values for muscle (most sensitive), skin, and adipose to capture sampling site distribution. If not possible, the K_p values can be refined via fitting approach together with observed arterial and arm vein concentrations.

The critical importance of the choice of the sampling site in PBPK models is further emphasized by the impact on model verification, parameter optimization, and model extrapolation. A common practice of top-down PBPK model development is to optimize experimentally undetermined

parameters until the observed data are captured by the simulation. Therefore, the choice of simulation output is critical. Choosing a PBPK model sampling site that is different from the actual site used to collect observed PK data is likely to specifically lead to erroneous parameter optimization and rejection of true model parameters due to the inherent differences between arterial and arm vein concentrations. This observation is particularly important for parameters that are poorly experimentally characterized and therefore typically empirically optimized, such as tissue-to-plasma partition coefficient and absorption rate constant. This concept is illustrated in the simulations of fentanyl disposition after buccal administration using fentanyl model verified for both arterial and arm vein sampling. When concentrations were sampled from central venous compartment (right atrium) in the simulations but compared to the observed arm vein concentrations, the verified fentanyl model with the true parameters failed to meet model acceptance criteria. As a result, fentanyl absorption parameters were optimized erroneously to compensate for the inherent sampling site-dependent discrepancy. Importantly, these erroneously optimized model parameters mispredicted the impact of changes in formulation and absorption rate on C_{max} by 3-fold, leading to wrong conclusions of drug safety and efficacy.

A similar issue of misfitting or model misspecification has been discussed previously regarding how arteriovenous differences affect the accurate derivation of PK-PD relationships and therefore the prediction of PD (Gumbleton *et al.*, 1994; Jacobs and Nath, 1995; Tuk *et al.*, 1997). Previous PK-PD communications regarding arteriovenous differences have mainly used empirically fitted compartmental models, and hence cannot be directly compared to mechanistic PBPK models. It has been proposed that coupling PBPK model to PK-PD model can provide a mechanistic prediction of therapeutic effect given the capacity of the PBPK modeling to simulate tissue drug concentrations where the drug effects occur (Kuepfer *et al.*, 2016; Pichardo-Almarza and Diaz-

Zuccarini, 2016; Boger and Fridén, 2019). Since PK-PD models often assess the time course of pharmacological effect and how the onset of effect relates to plasma concentrations during the initial distribution phase, strong scrutiny to correct sampling site is necessitated during model development.

Finally, our study extends the PBPK model application to explore the unstudied scenario of arteriovenous concentration differences for metabolites after iv and oral administration. Using simulations, we discovered an atypical metabolite profile resulting from central venous compartment (right atrium) sampling showing a spike during the early distribution phase of the parent drug. This unique phenomenon is caused by initial high concentrations of parent drug during its distribution phase and rapid appearance of metabolite in central venous compartment (right atrium) due to unrestricted passive diffusion across sinusoidal membrane for metabolite formed in the liver. This atypical metabolite spike observed from simulated central venous metabolite profile was hardly observed from the simulated peripheral arm vein metabolite profile due to tissue distribution and dilution at sampling site. The simulated peripheral arm vein metabolite profiles shown here agree with commonly observed metabolite profiles from clinical studies.

In conclusion, this study shows that the developed PBPK model with peripheral sampling compartment can successfully recapitulate arteriovenous drug concentration differences and it is critically important to match the PBPK model sampling site with the experimental sampling site used in clinical studies, especially for drugs with large volumes of distribution or high clearances. We also show that arteriovenous differences can be considerable following oral dosing and for drug metabolites. The use of discrepant sampling site may lead to biased model evaluation, erroneous parameter optimization, and clinically significant mispredictions of plasma concentration-time curves. As PBPK-PD models are being developed, attention needs to be

payed to assessing arteriovenous differences and using comparable sampling site between simulations and observations.

Table 3.1. Physiological parameters used for the developed PBPK model.

Except for the forearm tissues and blood flows, all the data are from (Brown *et al.*, 1997) and are based on a 70kg man. The physical volumes for the forearm tissues are from (Cooper *et al.*, 1955), forearm blood flow value is from (Elia and Kurpad, 1993), and anastomoses flow value is from (Musther *et al.*, 2015).

Tissue	Blood Flow (L/hr)	Physiological Volume (L)
Central vein	300	1.67
Central artery	300	3.33
Adipose	15.6	15
Bone	12.6	10
Brain	34.2	1.4
Gut	45.0	1.2
Heart	12.0	0.33
Kidney	60.0	0.31
Liver	90.0	1.8
Lung	300	0.53
Muscle	57.3	28
Pancreas	3.0	0.098
Skin	17.4	2.6
Spleen	6.0	0.18
Forearm	0.6430	0.3380
Forearm adipose	0.0709	0.0338
Forearm muscle	0.2900	0.2680
Forearm skin	0.2180	0.0363
Forearm anastomoses	0.0643	-

Table 3.2. Physicochemical and pharmacokinetic parameters of drugs used for structural model verification

Parameter	Nicotine[1]	Ketamine[2]	Lidocaine[1]	Fentanyl[1]
Physicochemical parameters[3]				
Molecular weight (g/mol)	162.23	237.73	234.34	336.47
pK_a	7.80	7.50	8.01	8.99
LogP	1.17	2.65	2.44	4.05
$f_{u,p}$	0.84	0.77	0.35	0.16
B/P	0.80	1.24	0.87	1.00
Distribution				
$K_{p,adipose}$	0.50	2.8	1.0	26.7
$K_{p,bone}$	1.0	1.0	1.0	1.0
$K_{p,brain}$	2.8	6.0	3.2	3.5
$K_{p,gastrointestinal\ tract}$	1.0	5.8	3.1	8.4
$K_{p,heart}$	1.9	6.8	2.7	4.5
$K_{p,kidney}$	13.3	11.3	17.2	12.1
$K_{p,liver}$	3.5	5.3	11.5	3.8
$K_{p,lung}$	2.1	7.6	3.8	13.5
$K_{p,muscle}$	1.6	2.0	1.7	3.1
$K_{p,pancreas}$	1.0	1.0	1.0	21.3
$K_{p,skin}$	1.1	1.0	2.6	2.1
$K_{p,spleen}$	1.0	1.0	4.8	27.6
Metabolism and Excretion				
CL_{total} (L/hr)	89	102	38.6(a); 56.3(v)	71.4(a); 83.3(v); 83.5(b)

$f_{u,p}$, fraction unbound in plasma; B/P, blood-to-plasma ratio; K_p, tissue-to-plasma partition coefficient for specific organ/tissue; CL_{total}, observed clearance for each study; (a), clinical studies used for model verification that report arterial data; (v), clinical studies used for model verification that report venous data; (b), clinical study that uses buccal administration;
[1]K_p data collected from (Rodgers *et al.*, 2005)
[2]K_p data collected from (Edwards and Mather, 2001)
[3]Physicochemical data collected from (Rodgers and Rowland, 2007)

Table 3.3. Simulation results for the PK characteristics of parent drug after iv.

Pharmacokinetic characteristics for parent drug corresponding to the simulation scenarios shown in Figure 3.7 for IV dosing. The pharmacokinetic measures obtained based on sampling from the vena cava or arm vein are listed. C_{end} is measured at 40 hrs to ensure pseudo-equilibrium is reached. AUC was calculated using trapezoidal rule from 0 to 400 hrs to capture the $AUC_{0\text{-infinity}}$.

Figure Panel	CL_{int} (L/hr)	K_p for skin, muscle, adipose	K_p for other organs	C_{max} vena cava (mg/L)	C_{max} arm vein (mg/L)	t_{max} vena cava (hr)	t_{max} arm vein (hr)	C_{end} vena cava (mg/L)	C_{end} arm vein (mg/L)	C_{end} ratio	AUC vena cava (mg*hr/L)	AUC arm vein (mg*hr/L)	AUC central artery (mg*hr/L)	V_{ss} (L)
a	10	1	1	161.2	16.9	0.017	0.025	0.083	0.090	0.93	111.2	111.2	111.2	66
b	100	1	1	161.0	16.9	0.017	0.025	1.19×10^{-8}	1.74×10^{-8}	0.68	21.1	21.1	21.1	66
c	1000	1	1	160.3	16.8	0.017	0.024	1.12×10^{-11}	2.18×10^{-11}	0.51	12.1	12.1	12.1	66
d	10	3	3	155.7	12.4	0.017	0.025	0.774	0.835	0.93	111.2	111.2	111.2	189
e	100	3	3	155.7	12.4	0.017	0.025	0.0023	0.0034	0.67	21.1	21.1	21.1	189
f	1000	3	3	155.6	12.4	0.017	0.025	0.0001	0.0002	0.51	12.1	12.1	12.1	189
g	10	10	10	153.9	7.8	0.017	0.031	0.804	0.866	0.93	111.2	111.2	111.2	619
h	100	10	10	153.9	7.8	0.017	0.031	0.087	0.129	0.68	21.1	21.1	21.1	619
i	1000	10	10	153.9	7.8	0.017	0.031	0.023	0.044	0.52	12.1	12.1	12.1	619

Table 3.4. Simulation results for the PK characteristics of parent drug after oral dosing. Pharmacokinetic characteristics for parent drug corresponding to the simulation scenarios shown in Figure 3.9 for po dosing. C_{end} is measured at 40 hrs to ensure pseudo-equilibrium is reached. AUC was calculated using trapezoidal rule from 0 to 400 hrs to capture the $AUC_{0\text{-infinity}}$.

Figure Panel	CL_{int} (L/hr)	K_p for skin, muscle, adipose	K_p for other organs	C_{max} vena cava (mg/L)	C_{max} arm vein (mg/L)	C_{max} ratio	t_{max} vena cava (hr)	t_{max} arm vein (hr)	C_{end} vena cava (mg/L)	C_{end} arm vein (mg/L)	C_{end} ratio	AUC central vein (mg*hr/L)	AUC arm vein (mg*hr/L)	AUC central artery (mg*hr/L)
a	10	1	1	9.97	9.28	1.07	1.51	2.37	0.086	0.093	0.93	100.1	100.1	100.1
b	100	1	1	3.19	2.54	1.26	0.51	1.23	1.16×10^{-8}	1.7×10^{-8}	0.68	10.0	10.0	10.0
c	1000	1	1	0.43	0.32	1.36	0.32	0.97	3.17×10^{-12}	6.16×10^{-12}	0.51	1.0	1.0	1.0
d	10	3	3	5.88	3.83	1.54	0.75	2.54	0.732	0.790	0.93	100.1	100.1	100.1
e	100	3	3	2.40	1.32	1.83	0.49	1.54	0.0014	0.0020	0.67	10.0	10.0	10.0
f	1000	3	3	0.35	0.18	1.99	0.36	1.31	0.00001	0.00002	0.51	1.0	1.0	1.0
g	10	10	10	3.58	1.47	2.44	1.15	3.06	0.737	0.794	0.93	99.6	99.6	99.6
h	100	10	10	1.64	0.57	2.86	0.82	2.33	0.044	0.065	0.68	10.0	10.0	10.0
i	1000	10	10	0.25	0.08	3.11	0.64	1.93	0.002	0.004	0.53	1.0	1.0	1.0
j	10	1	10	5.74	5.34	1.07	1.99	2.77	0.719	0.734	0.98	100.0	100.0	100.0
k	100	1	10	2.25	1.92	1.17	1.18	1.81	0.007	0.007	0.95	10.0	10.0	10.0
l	1000	1	10	0.32	0.26	1.23	0.86	1.40	0.00025	0.00027	0.94	1.0	1.0	1.0
m	10	10	1	6.21	1.82	3.42	0.33	2.20	0.787	0.865	0.91	99.9	99.9	99.9
n	100	10	1	2.58	0.65	3.95	0.23	1.75	0.033	0.054	0.62	10.0	10.0	10.0
o	1000	10	1	0.38	0.09	4.25	0.18	1.51	0.0015	0.0032	0.45	1.0	1.0	1.0

(a)

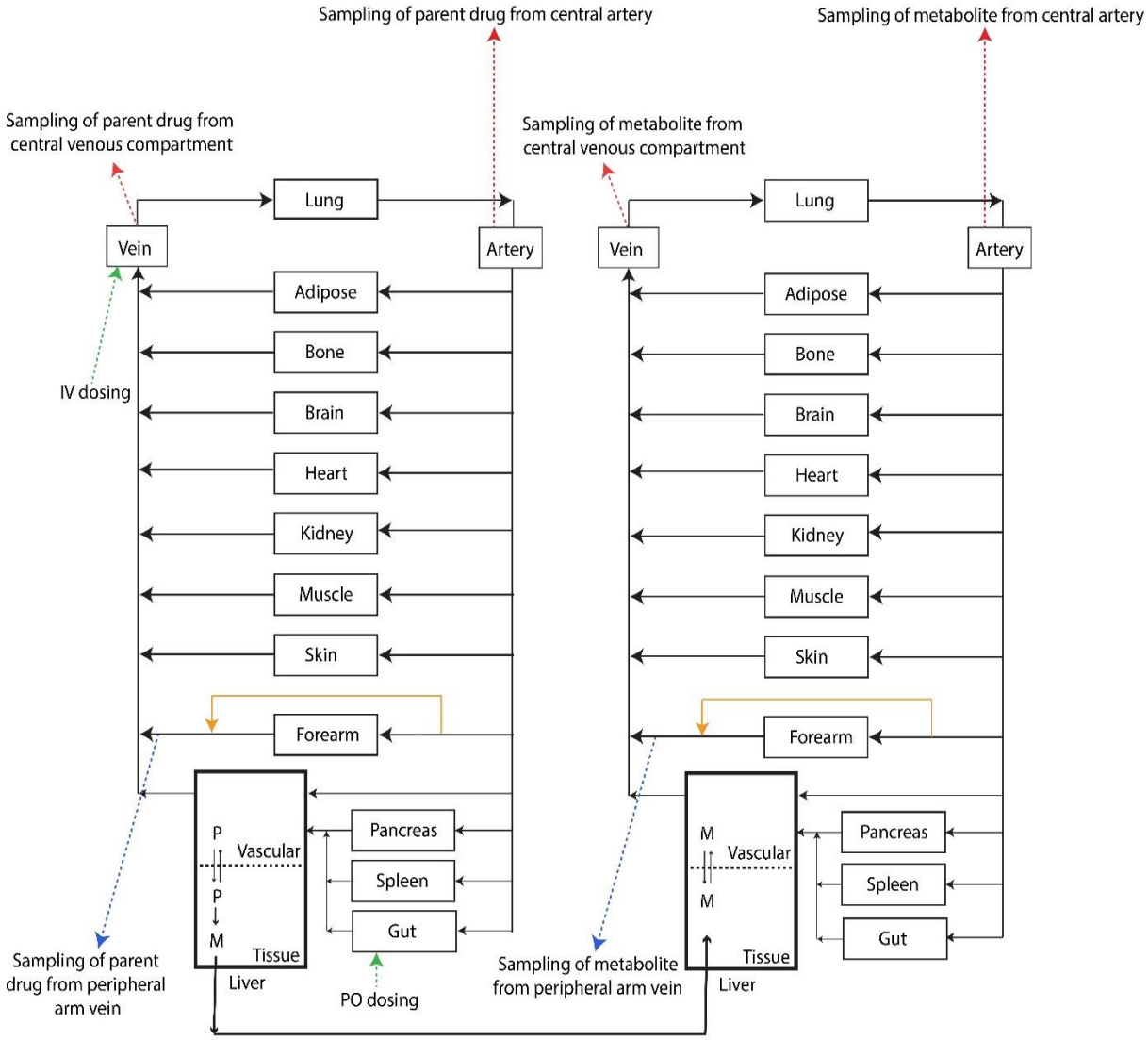
Sampling of parent drug from central artery
Sampling of metabolite from central artery
Sampling of parent drug from central venous compartment
Sampling of metabolite from central venous compartment
Lung
Vein
Artery
Adipose
Bone
Brain
Heart
Kidney
Muscle
Skin
Forearm
IV dosing
P
Vascular
P
M
Tissue
Liver
Pancreas
Spleen
Gut
PO dosing
Sampling of parent drug from peripheral arm vein
M
Vascular
M
Tissue
Liver
Sampling of metabolite from peripheral arm vein

(b)

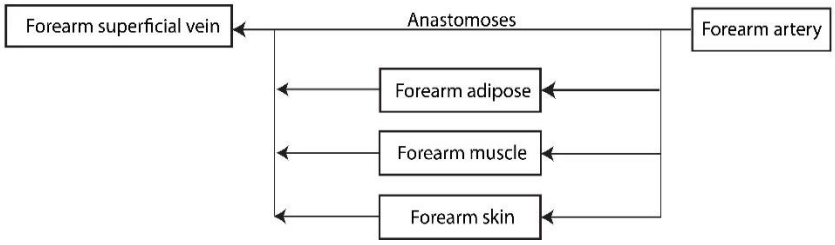
Forearm superficial vein
Anastomoses
Forearm artery
Forearm adipose
Forearm muscle
Forearm skin

Figure 3.1. Structure of the PBPK model and the forearm sampling site developed.
(a) Schematic diagram of the full body physiologically based parent-metabolite pharmacokinetic model with forearm compartment incorporated. Three different sampling sites of drug and metabolite are shown. Sampling from central venous compartment (right atrium) and central artery compartment are shown with red dashed lines and sampling from the peripheral arm vein is shown with blue dashed lines. The intravenous and oral dosing sites are shown with green dashed lines. The forearm anastomoses shunt is shown by orange line. (b) The detailed structural model of the forearm compartment.

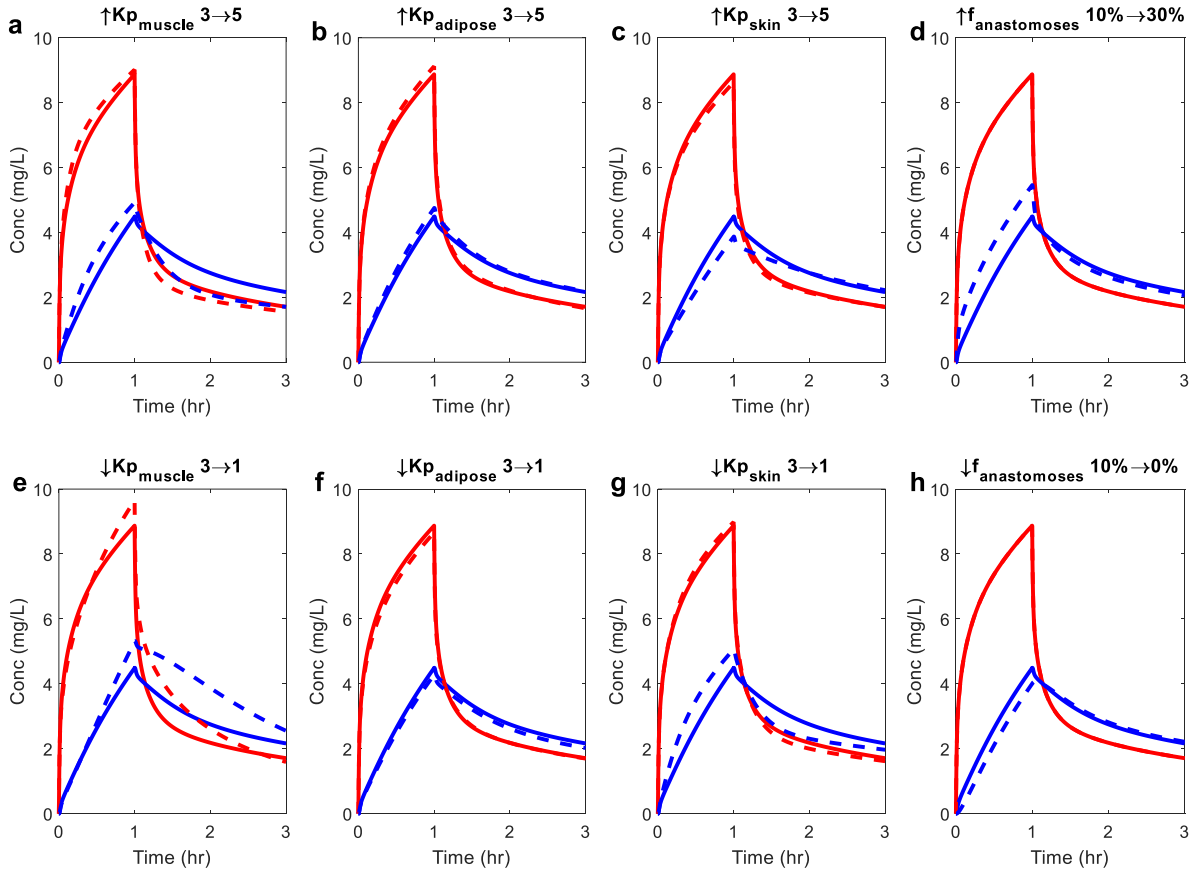
a
↑Kp muscle 3→5
b
↑Kp adipose 3→5
c
↑Kp skin 3→5
d
↑f anastomoses 10%→30%
e
↓Kp muscle 3→1
f
↓Kp adipose 3→1
g
↓Kp skin 3→1
h
↓f anastomoses 10%→0%
Conc (mg/L)
Time (hr)

Figure 3.2. Sensitivity analysis of the effect of tissue partition coefficients (K_p's) assignment and anastomoses fraction on arteriovenous concentration differences.

All simulations were conducted for a 1-hour iv infusion of 1000 mg/hr into the vena cava. Red curves represent the simulated drug concentrations sampled from vena cava. Blue curves represent the simulated drug concentrations sampled from arm vein. Solid curves represent the baseline simulation condition where K_p for all tissues is equal to 3 (V_{ss} = 200 L) and anastomoses fraction is 10%. Dashed curves represent the conditions of interest for the sensitivity tests. Panel a-c: K_p value of muscle, adipose, and skin was increased from 3 (solid line) to 5 (dashed line) while other organ K_p values were decreased to maintain V_{ss} unchanged. Panel d-f: K_p value of muscle, adipose, and skin was decreased from 3 (solid line) to 1 (dashed line) while other organ K_p values were increased to maintain V_{ss} unchanged. Panel d: anastomoses fraction increased from 10% to 30%. Panel h: anastomoses fraction decreased from 10% to 0%.

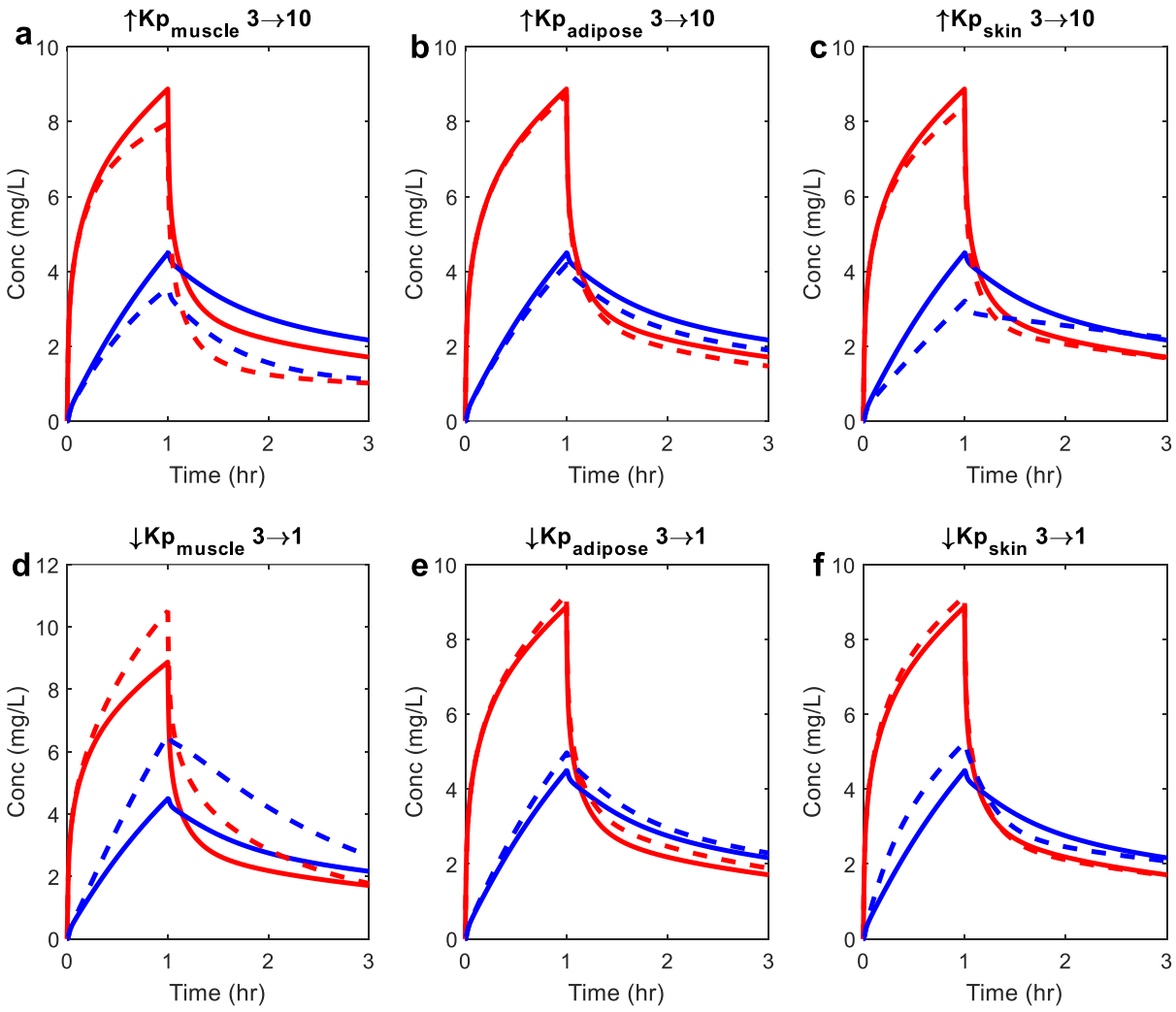
a
↑Kp muscle 3→10
b
↑Kp adipose 3→10
c
↑Kp skin 3→10
d
↓Kp muscle 3→1
e
↓Kp adipose 3→1
f
↓Kp skin 3→1
Conc (mg/L)
Time (hr)

Figure 3.3. One-way sensitivity analysis of the effect of specific tissue partition coefficients (K_p's) on arteriovenous concentration differences.

All simulations were conducted for a 1-hour iv infusion of 1000 mg/hr into the vena cava. Red curves represent the simulated drug concentrations sampled from vena cava. Blue curves represent the simulated drug concentrations sampled from arm vein. Solid curves represent the baseline simulation condition where K_p for all tissues is equal to 3 (V_{ss} = 200 L) and anastomoses fraction is 10%. Dashed curves represent the conditions of interest for the sensitivity tests. Panel a-c: K_p value of muscle, adipose, and skin was increased from 3 (solid line) to 10 (dashed line). Panel d-f: K_p value of muscle, adipose, and skin was decreased from 3 (solid line) to 1 (dashed line). All other parameters remain unchanged.

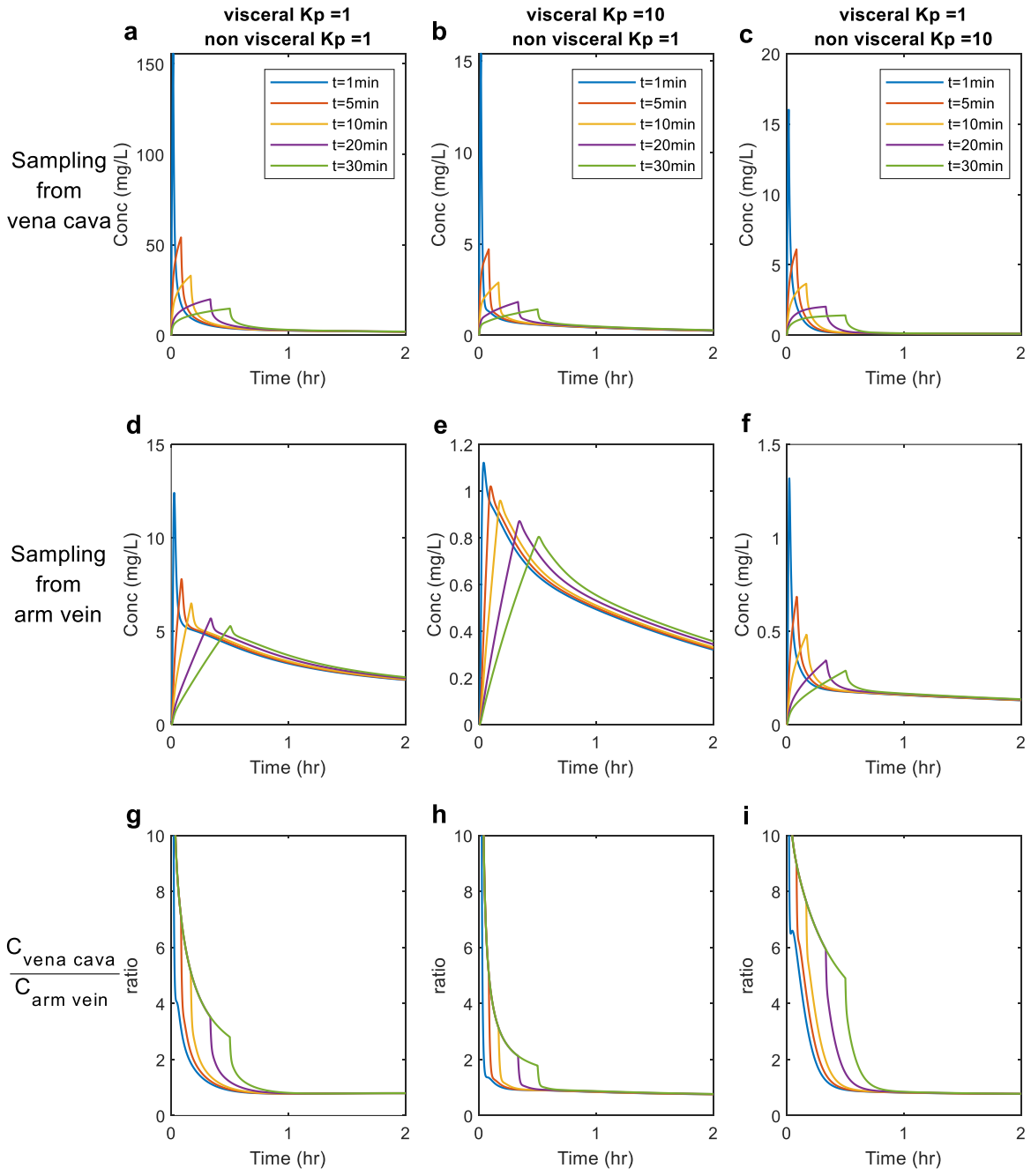
a
visceral Kp =1
non visceral Kp =1
b
visceral Kp =10
non visceral Kp =1
c
visceral Kp =1
non visceral Kp =10
t=1min
t=5min
t=10min
t=20min
t=30min
Sampling from vena cava
Conc (mg/L)
Time (hr)
d
e
f
Sampling from arm vein
g
h
i
C vena cava / C arm vein
ratio

Figure 3.4. Simulated plasma concentration-time profiles of parent drug sampled from central and peripheral sampling site after intravenous infusion.

The concentration profiles of parent drug after intravenous infusion of 1000mg drug with different infusion times (t=1min, 5mins, 10mins, 20mins, and 30mins) sampled from vena cava and arm vein. The bottom three panels show that the ratio of vena cava concentration and arm vein concentration does not equal to 1 for the majority of the time regardless of intravenous infusion times.

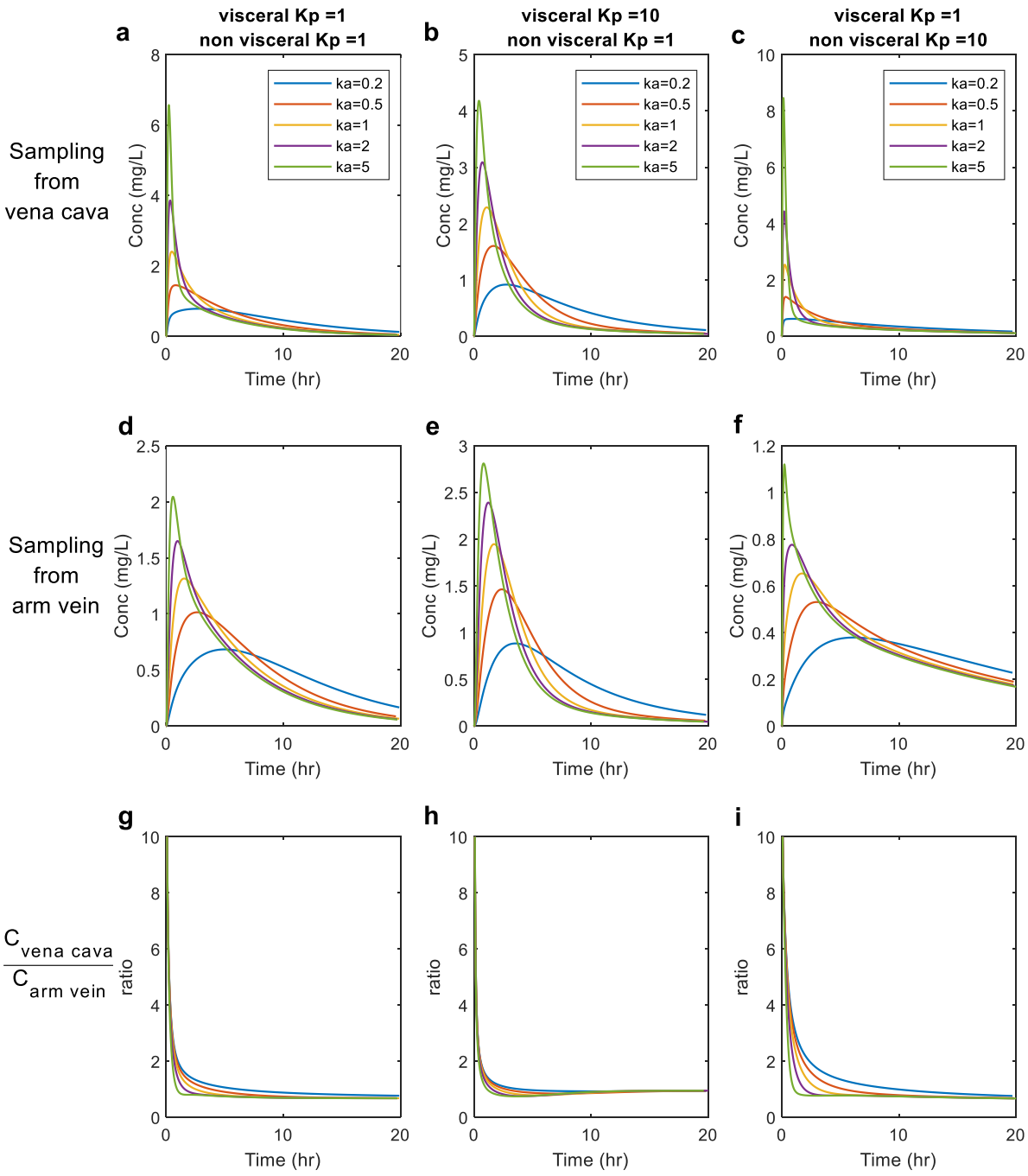
a
visceral Kp =1
non visceral Kp =1
b
visceral Kp =10
non visceral Kp =1
c
visceral Kp =1
non visceral Kp =10
ka=0.2
ka=0.5
ka=1
ka=2
ka=5
Sampling from vena cava
Sampling from arm vein
Conc (mg/L)
Time (hr)
d
e
f
g
h
i
ratio
C vena cava / C arm vein

Figure 3.5. Simulated plasma concentration-time profiles of parent drug sampled from central and peripheral sampling site after oral dosing.

The concentration profiles of parent drug after oral dosing of 1000mg drug with different absorption rate constant (k_a=0.2, 0.5, 1, 2, and 5 hr^{-1}) sampled from vena cava and arm vein. The bottom three panels show that the ratio of vena cava concentration and arm vein concentration does not equal to 1 for the majority of the time regardless of absorption rate constant.

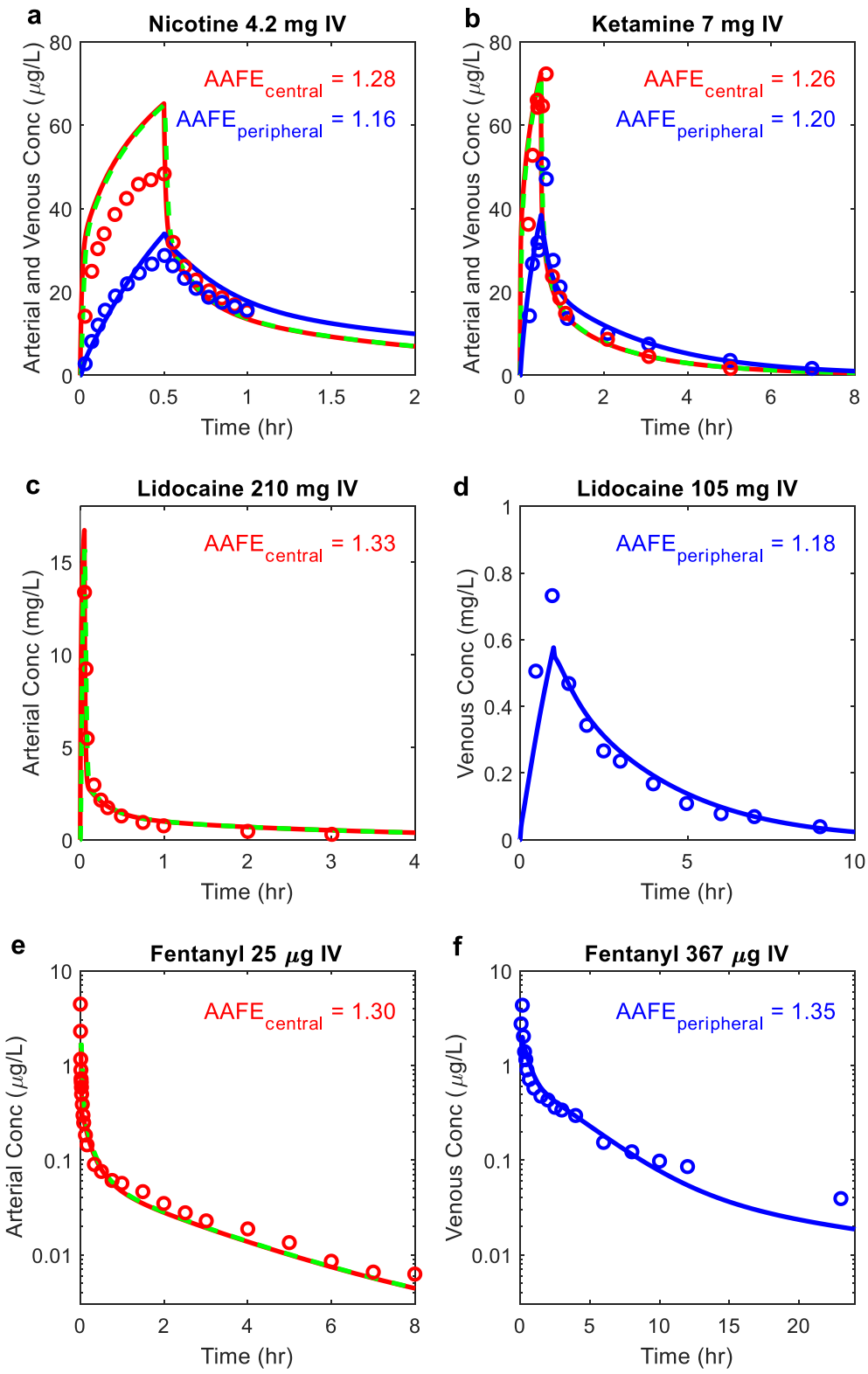
a
Nicotine 4.2 mg IV
AAFE central = 1.28
AAFE peripheral = 1.16
Arterial and Venous Conc (μg/L)
Time (hr)
b
Ketamine 7 mg IV
AAFE central = 1.26
AAFE peripheral = 1.20
Arterial and Venous Conc (μg/L)
Time (hr)
c
Lidocaine 210 mg IV
AAFE central = 1.33
Arterial Conc (mg/L)
Time (hr)
d
Lidocaine 105 mg IV
AAFE peripheral = 1.18
Venous Conc (mg/L)
Time (hr)
e
Fentanyl 25 μg IV
AAFE central = 1.30
Arterial Conc (μg/L)
Time (hr)
f
Fentanyl 367 μg IV
AAFE peripheral = 1.35
Venous Conc (μg/L)
Time (hr)

Figure 3.6. Model verification using arterial and arm vein concentration profiles after intravenous administration of four test drugs.

Simulated plasma drug concentration time curves and observed data are shown. (a) nicotine sampled from central venous compartment (right atrium), artery, and peripheral arm vein after 4.2 mg iv infusion over 30 min, (b) ketamine sampled from central venous compartment, artery, and peripheral arm vein after 7 mg iv infusion over 30 min, (c) lidocaine sampled from central venous compartment and artery after 210 mg iv infusion over 3 min, (d) lidocaine sampled from peripheral arm vein after 105 mg iv infusion over 1 hour, (e) fentanyl sampled from central venous compartment and artery after 25 μg iv bolus over 5 seconds, and (f) fentanyl sampled from peripheral arm vein after 367 μg infusion over 10 min. Red, green, and blue curves represent simulated plasma drug concentration time curves sampled from central venous compartment (right atrium), artery, and peripheral arm vein, respectively. Red and blue circles represent observed plasma drug concentration data sampled from artery and arm vein, respectively. $AAFE_{central}$ represents the calculated AAFE comparing simulated central venous compartment (right atrium) drug concentration profile with observed arterial concentration data. $AAFE_{peripheral}$ represents the calculated AAFE comparing simulated peripheral arm vein drug concentration profile with observed arm vein concentration data. The observed data are from (Tucker and Boas, 1971; Gourlay and Benowitz, 1997; Persson *et al.*, 2002; Isohanni *et al.*, 2005; Macleod *et al.*, 2012; Ziesenitz *et al.*, 2015).

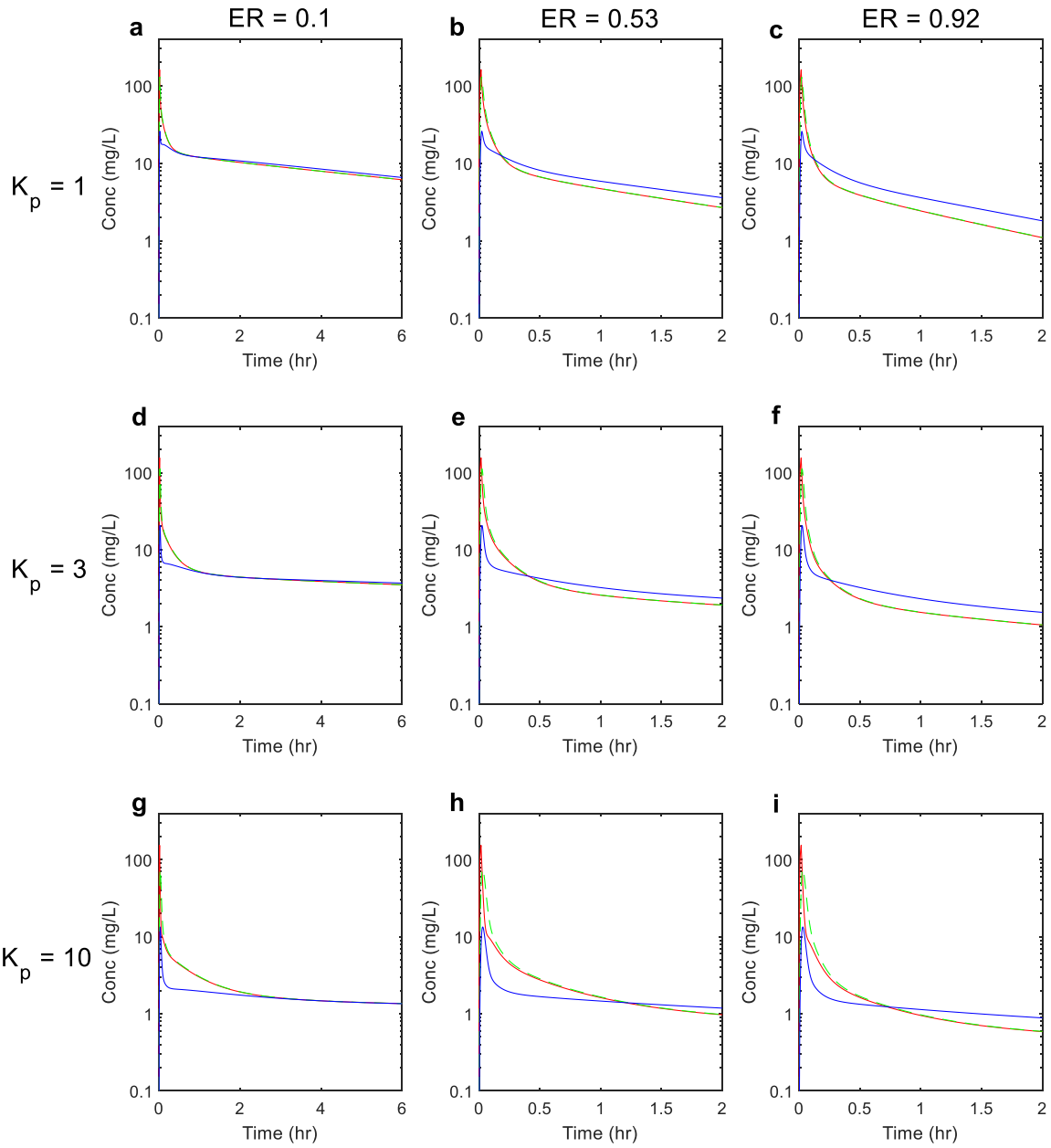
a
ER = 0.1
b
ER = 0.53
c
ER = 0.92
K_p = 1
K_p = 3
K_p = 10
d
e
f
g
h
i
Conc (mg/L)
Time (hr)
100
10
1
0.1
0
2
4
6
0.5
1
1.5
2

Figure 3.7. Simulation of plasma drug concentration-versus time curves after iv administration sampled from different sites in PBPK model for hypothetical drugs with different clearance and distribution characteristics.

In panels a-c K_p =1, panels d-f K_p =3, and panels g-i K_p =10. Panels a, d and g show drugs with ER=0.1, panels b, e and h show drugs with ER=0.53, and panels c, f and i show drugs with ER=0.92. All other drug parameters are as described in methods. In all panels blue lines represent drug concentrations in the peripheral arm vein, red lines represent drug concentrations in the central venous compartment (right atrium) and green dashed lines represent drug concentrations in the artery. ER indicates the extraction ratio of the model drug and K_p indicates the tissue-to-plasma partition coefficient value of all tissues. All simulations were conducted as described in Materials and Methods section.

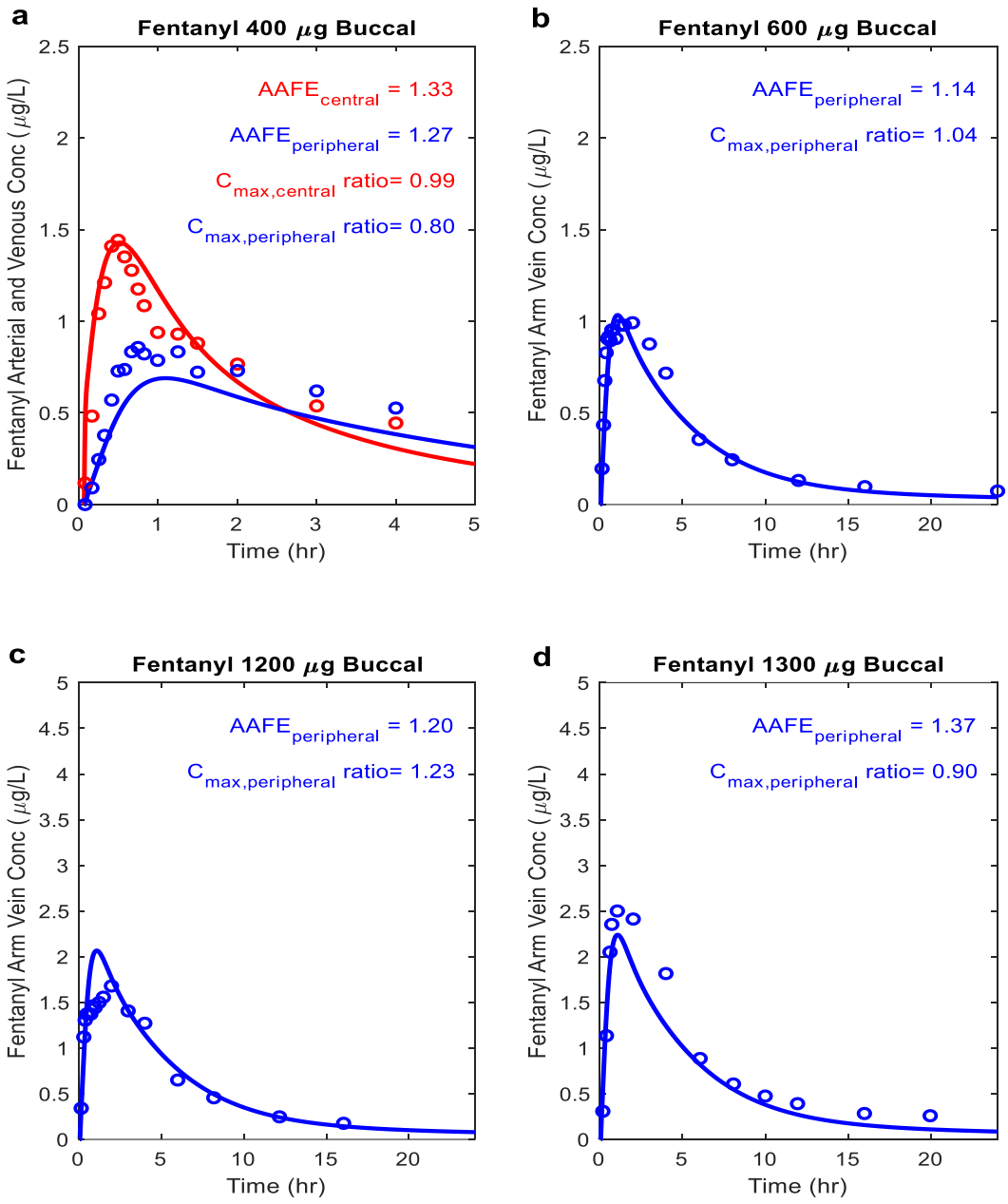
a
Fentanyl 400 μg Buccal
AAFE central = 1.33
AAFE peripheral = 1.27
C max,central ratio= 0.99
C max,peripheral ratio= 0.80
Fentanyl Arterial and Venous Conc (μg/L)
Time (hr)
b
Fentanyl 600 μg Buccal
AAFE peripheral = 1.14
C max,peripheral ratio= 1.04
Fentanyl Arm Vein Conc (μg/L)
Time (hr)
c
Fentanyl 1200 μg Buccal
AAFE peripheral = 1.20
C max,peripheral ratio= 1.23
Fentanyl Arm Vein Conc (μg/L)
Time (hr)
d
Fentanyl 1300 μg Buccal
AAFE peripheral = 1.37
C max,peripheral ratio= 0.90
Fentanyl Arm Vein Conc (μg/L)
Time (hr)

Figure 3.8. Development and verification of fentanyl buccal model using arterial and arm vein fentanyl concentration data.

Panel a shows the development of the fentanyl buccal administration model by comparing the simulated drug concentration time profiles from central venous compartment (red curves) and peripheral arm vein (blue curves) to the observed arterial data (red circles) and observed venous data (blue circles) respectively after 400µg buccal tablet administration. Panels b, c, and d show the verification of the developed fentanyl buccal model by comparing the simulated arm vein fentanyl concentration time profiles (blue curves) to the observed arm vein fentanyl data (blue circles) after 600µg (Darwish *et al.*, 2010), 1200µg (Darwish, Tempero, *et al.*, 2006), and 1300µg (Darwish *et al.*, 2010) buccal tablet administration respectively. $AAFE_{peripheral}$ represents the calculated AAFE comparing simulated arm vein drug concentration profile with observed arm vein concentration data. $C_{max,\ peripheral}$ ratio represents the ratio between simulated maximum arm vein drug concentration and the observed maximum arm vein concentration. $AAFE_{central}$ represents the calculated AAFE comparing simulated central venous compartment (right atrium) drug concentration profile with observed arterial concentration data. $C_{max,\ central}$ ratio represents the ratio between simulated maximum central venous compartment drug concentration and the observed maximum arterial concentration.

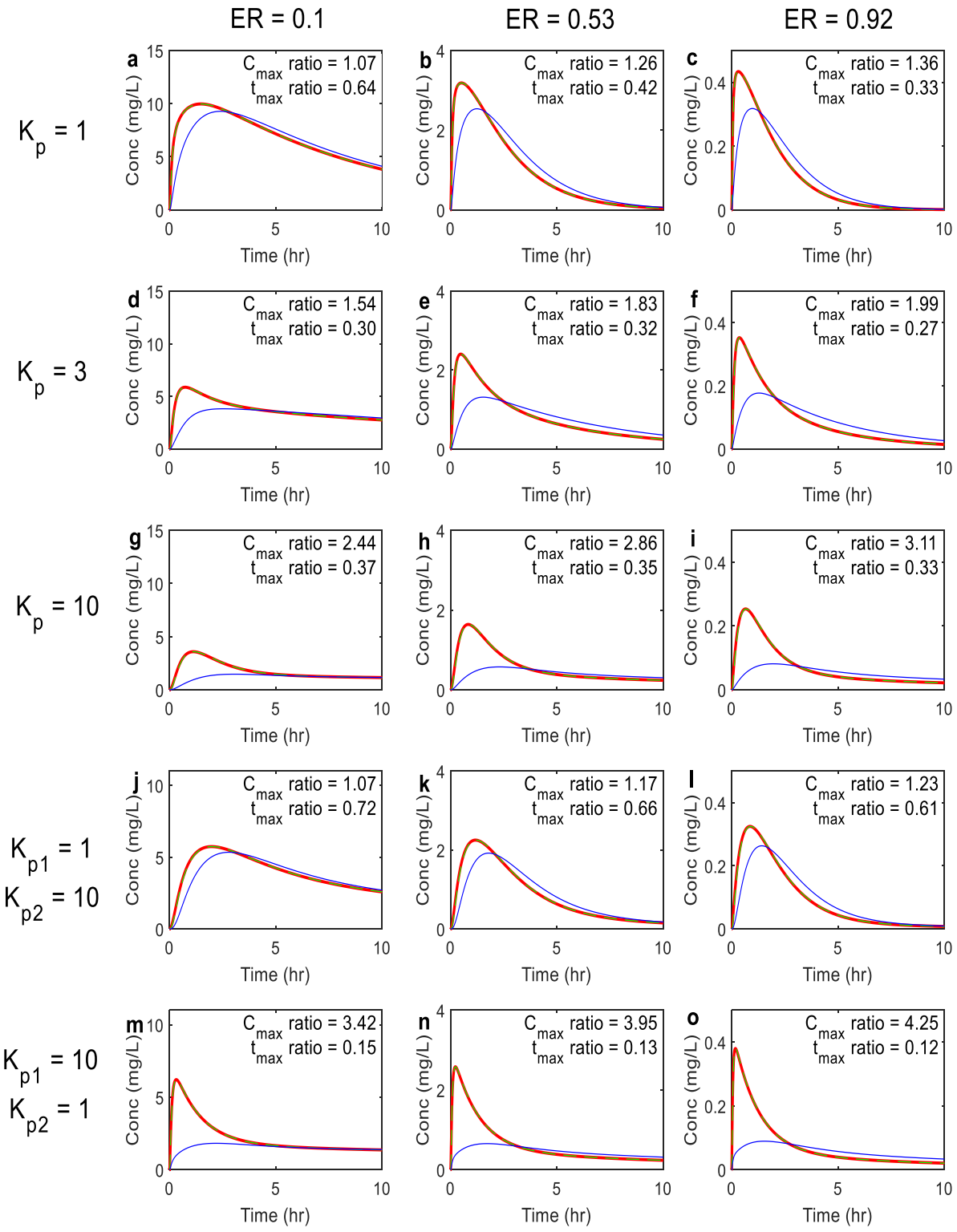
ER = 0.1
ER = 0.53
ER = 0.92
Kp = 1
Kp = 3
Kp = 10
Kp1 = 1
Kp2 = 10
Kp1 = 10
Kp2 = 1
a
b
c
d
e
f
g
h
i
j
k
l
m
n
o
Cmax ratio = 1.07
tmax ratio = 0.64
Cmax ratio = 1.26
tmax ratio = 0.42
Cmax ratio = 1.36
tmax ratio = 0.33
Cmax ratio = 1.54
tmax ratio = 0.30
Cmax ratio = 1.83
tmax ratio = 0.32
Cmax ratio = 1.99
tmax ratio = 0.27
Cmax ratio = 2.44
tmax ratio = 0.37
Cmax ratio = 2.86
tmax ratio = 0.35
Cmax ratio = 3.11
tmax ratio = 0.33
Cmax ratio = 1.07
tmax ratio = 0.72
Cmax ratio = 1.17
tmax ratio = 0.66
Cmax ratio = 1.23
tmax ratio = 0.61
Cmax ratio = 3.42
tmax ratio = 0.15
Cmax ratio = 3.95
tmax ratio = 0.13
Cmax ratio = 4.25
tmax ratio = 0.12
Conc (mg/L)
Time (hr)

Figure 3.9. Simulation of plasma drug concentration-versus time curves after oral administration sampled from different sites in PBPK model for hypothetical drugs with different clearance and distribution characteristics.

In panels a-c K_p =1, panels d-f K_p =3, panels g-i K_p =10, panels j-l K_p value of adipose, skin, and muscle (K_{p1}) = 1 and K_p value of other organs (K_{p2}) = 10 and panels m-o K_p value of adipose, skin, and muscle (K_{p1}) = 10 and K_p value of other organs (K_{p2}) = 1. Panels a, d, g, j and m show drugs with ER=0.1, panels b, e, h, k and n show drugs with ER=0.53, and panels c, f, i, l and o show drugs with ER=0.92. All other drug parameters are as described in methods. In all panels blue lines represent drug concentrations in the peripheral arm vein, red lines represent drug concentrations in the central venous compartment (right atrium) and green dashed lines represent drug concentrations in the artery. ER indicates the extraction ratio of the model drug. The C_{max} ratio in the insets is calculated as the ratio of the C_{max} of simulated central venous compartment (right atrium) concentrations and C_{max} of simulated peripheral arm vein concentrations. The t_{max} ratio is calculated from the t_{max} of simulated central venous compartment concentrations and t_{max} of simulated arm vein concentrations.

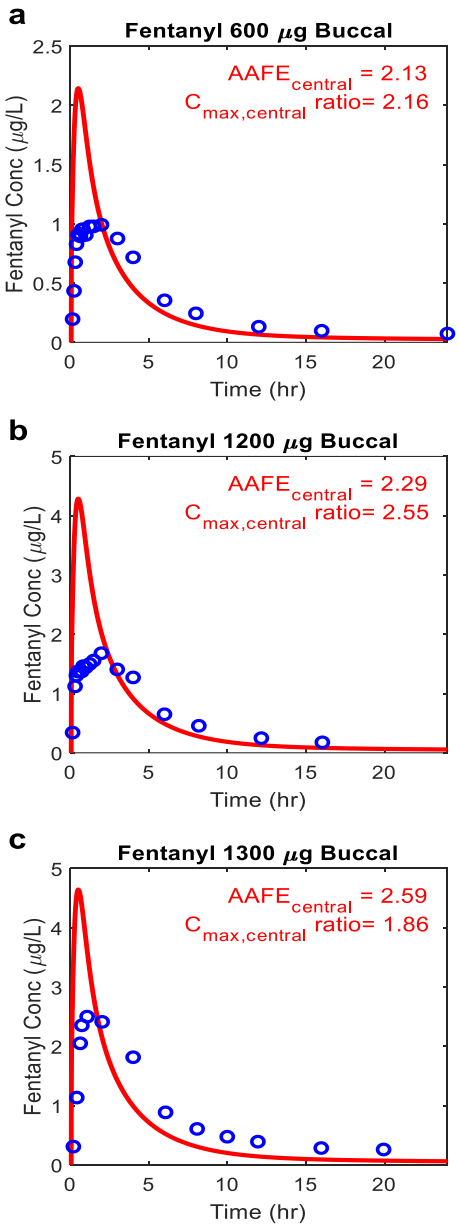
a
Fentanyl 600 μg Buccal
AAFE central = 2.13
C max,central ratio= 2.16
Fentanyl Conc (μg/L)
Time (hr)
b
Fentanyl 1200 μg Buccal
AAFE central = 2.29
C max,central ratio= 2.55
Fentanyl Conc (μg/L)
Time (hr)
c
Fentanyl 1300 μg Buccal
AAFE central = 2.59
C max,central ratio= 1.86
Fentanyl Conc (μg/L)
Time (hr)

Figure 3.10. Impact of choice of the sampling site on PBPK model evaluation.

Panels a, b, and c show the impact of discrepant sampling site between observed and simulated data on model performance evaluation. The simulated drug concentration time profiles (red curves) are conventional PBPK simulation outputs sampled from central venous compartment (right atrium) and the observed data are from commonly used arm vein sampling (blue circles) after (a) 600 μg (Darwish *et al.*, 2010), (b) 1200 μg (Darwish, Tempero, *et al.*, 2006), and (c) 1300 μg (Darwish *et al.*, 2010) buccal tablet administration of fentanyl, respectively. The observed data shown and the model used here are the same as the ones shown and used in Figure 3.8. The $AAFE_{central}$ represents the calculated AAFE comparing simulated central venous compartment (right atrium) drug concentration profile with observed arm vein concentration data. The $C_{max,\ central}$ ratio represents the ratio between simulated maximum central venous compartment (right atrium) drug concentration and the observed maximum arm vein concentration.

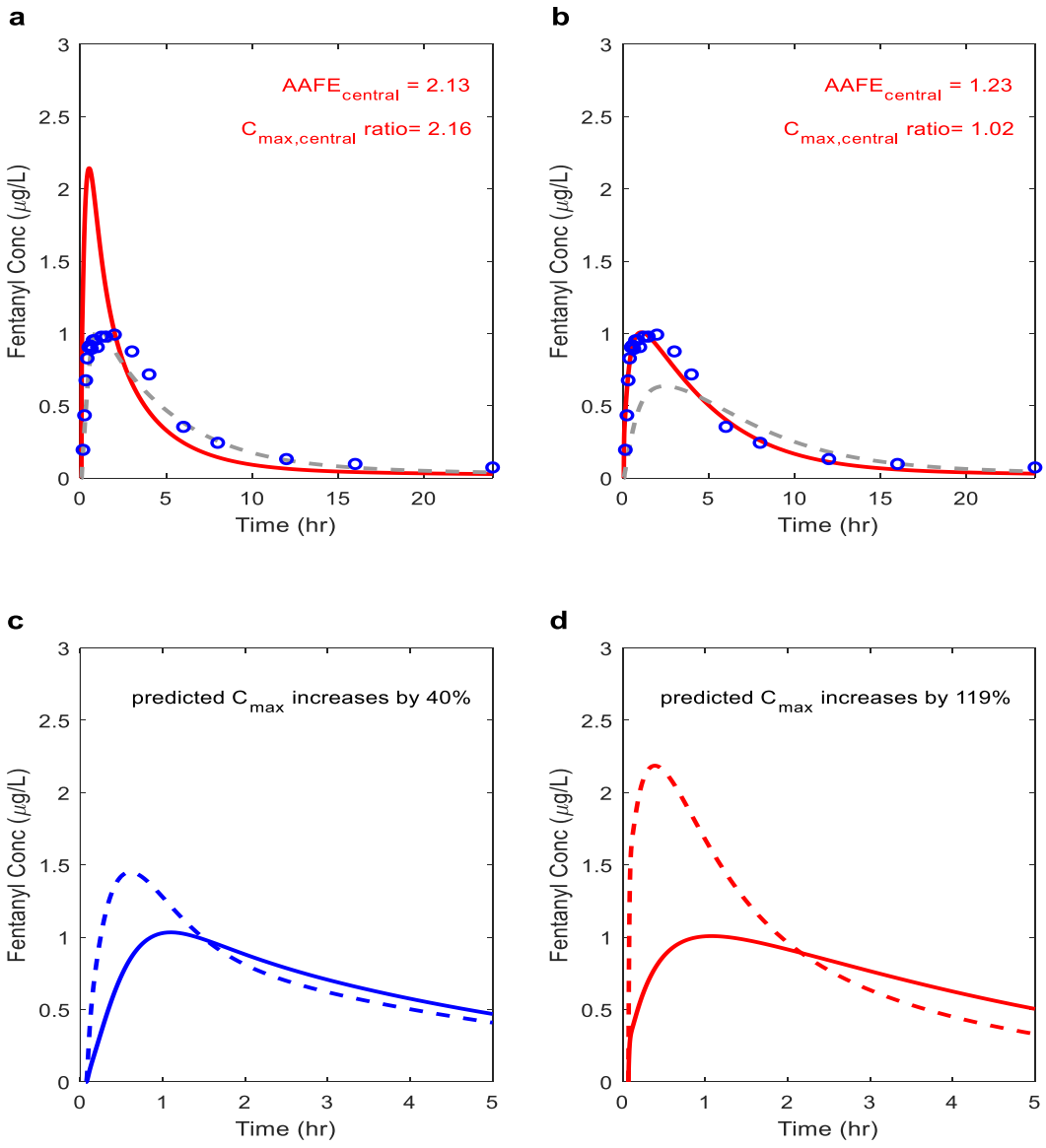
a
AAFE central = 2.13
C max,central ratio= 2.16
Fentanyl Conc (μg/L)
Time (hr)
b
AAFE central = 1.23
C max,central ratio= 1.02
Fentanyl Conc (μg/L)
Time (hr)
c
predicted C max increases by 40%
Fentanyl Conc (μg/L)
Time (hr)
d
predicted C max increases by 119%
Fentanyl Conc (μg/L)
Time (hr)

Figure 3.11. Impact of choice of the sampling site on PBPK model parameter optimization and extrapolation to unstudied clinical scenarios.

Panel a shows a scenario where the modeler uses the PBPK model-simulated central venous compartment (right atrium) concentrations (red curve) to compare to the observed data from peripheral arm vein (blue circles), rather than using the simulated peripheral sampling site concentrations (gray curve shown for comparison). In this case both AAFE and C_{max} ratio suggest model rejection although true parameters were used ($k_{a,buccal}$ = 1 hr^{-1} and $k_{a,gut}$ = 3 hr^{-1}). Panel b shows the fentanyl simulation with $k_{a,buccal}$ = 0.35 hr^{-1} and $k_{a,gut}$ = 0.7 hr^{-1} based on erroneous parameter optimization to adapt simulated central venous concentrations to conform to observed data collected from arm vein. The gray line shows the simulated arm vein concentrations using the same "false" parameters. Panel c shows the simulation of the impact of a new formulation with 400% increase in $k_{a,buccal}$ (dashed blue curve) on the plasma-concentration curve sampled from the arm vein in comparison to baseline $k_{a,buccal}$ (solid blue curve) using verified peripheral sampling site model with true parameters, predicting a 40% increase in arm vein C_{max}. Panel d shows the simulation of the same new formulation as in panel c with 400% increase in $k_{a,buccal}$ (dashed red curve) in comparison to baseline $k_{a,buccal}$ (solid red curve) using central venous compartment sampling with the erroneously optimized parameters from panel b. The central venous compartment sampling predicts a 119% increase in C_{max}.

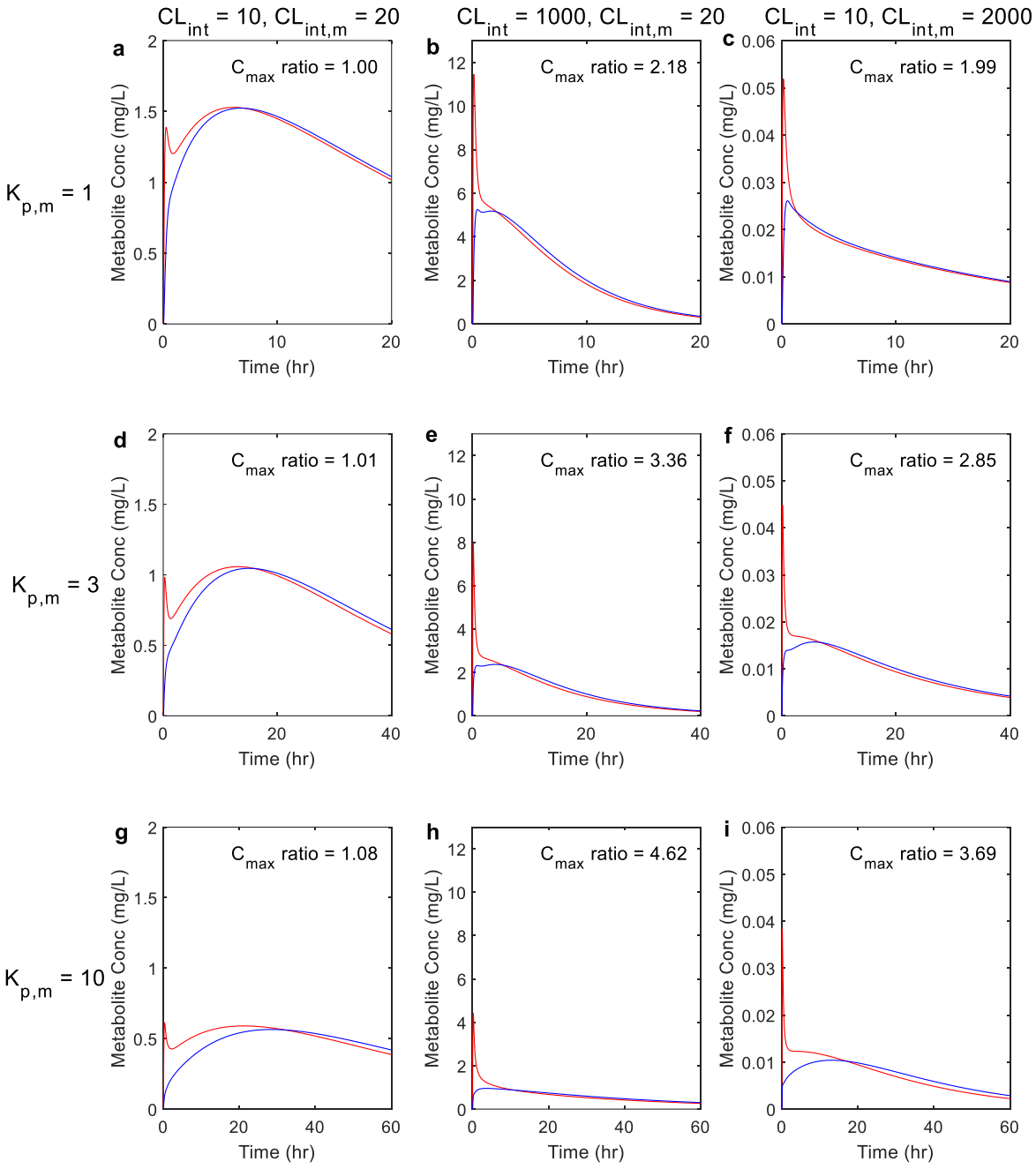
CL_int = 10, CL_int,m = 20
CL_int = 1000, CL_int,m = 20
CL_int = 10, CL_int,m = 2000
K_p,m = 1
K_p,m = 3
K_p,m = 10
a
b
c
d
e
f
g
h
i
C_max ratio = 1.00
C_max ratio = 2.18
C_max ratio = 1.99
C_max ratio = 1.01
C_max ratio = 3.36
C_max ratio = 2.85
C_max ratio = 1.08
C_max ratio = 4.62
C_max ratio = 3.69
Metabolite Conc (mg/L)
Time (hr)

Figure 3.12. Simulated plasma metabolite concentration-versus time curves after iv administration of parent drug sampled from different sites in PBPK model for metabolites with different clearance and distribution characteristics.

In panels a-c metabolite Kp (Kp,m) =1, panels d-f Kp,m =3, and panels g-i Kp,m =10. Panels a, d and g show metabolite concentration curves when drug has an intrinsic clearance (CLint) of 10 L/hr and the metabolite intrinsic clearance (CLint,m) is 20 L/hr, panels b, e and h show metabolite concentration curves when drug CLint=1000 L/hr and the CLint,m is 20 L/hr, and panels c, f and i show metabolite concentration curves when drug CLint=10 L/hr and the CLint,m is 2000 L/hr. The drug Kp value of all organs =3 in all panels. In all panels blue lines represent metabolite concentrations in the peripheral arm vein, and red lines represent metabolite concentrations in the central venous compartment (right atrium). The Cmax ratio in each panel is calculated using the Cmax of simulated central venous compartment (right atrium) metabolite concentration divided by Cmax of simulated arm vein metabolite concentration.

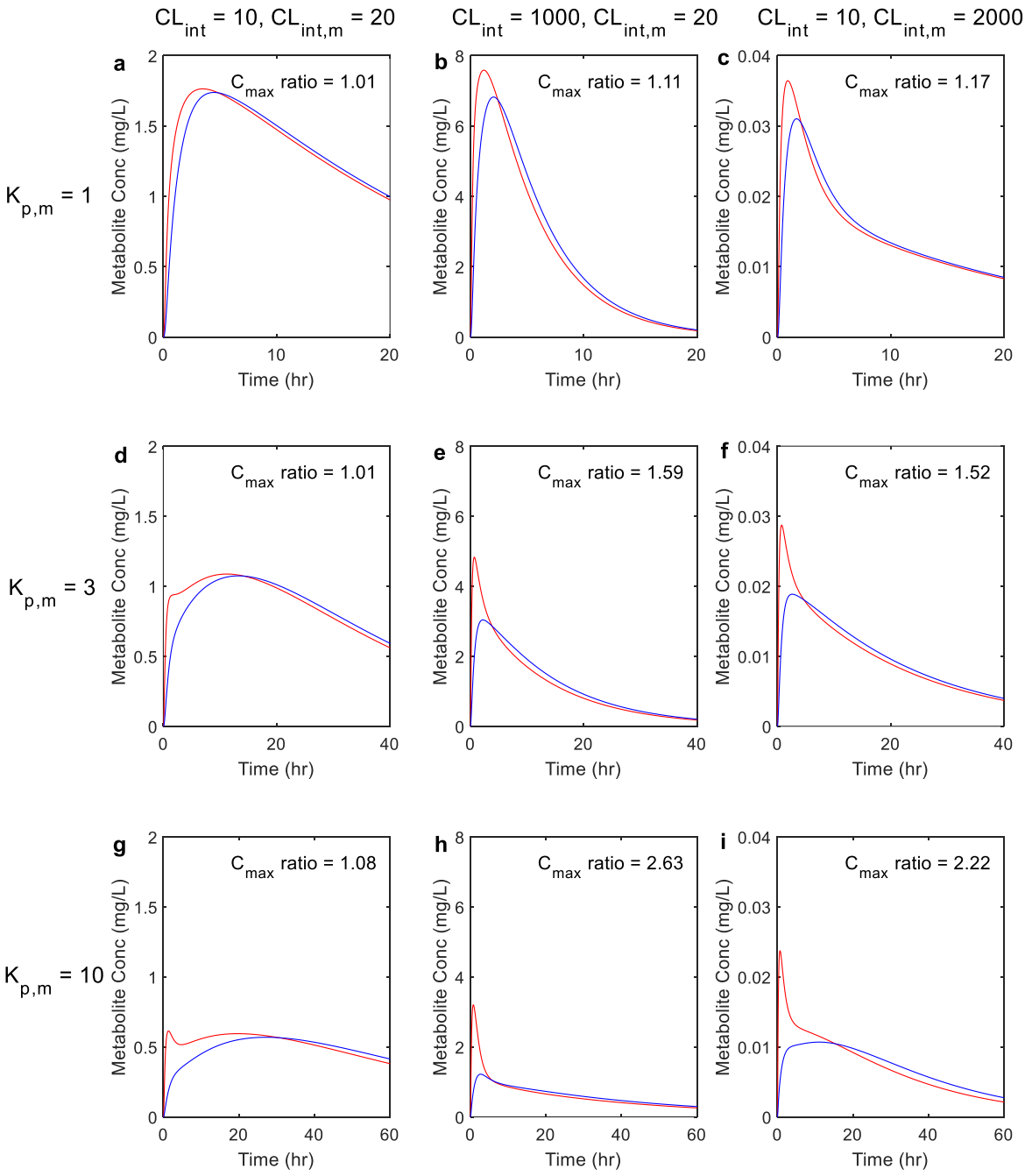
CL_int = 10, CL_int,m = 20
CL_int = 1000, CL_int,m = 20
CL_int = 10, CL_int,m = 2000
K_p,m = 1
K_p,m = 3
K_p,m = 10
a
b
c
d
e
f
g
h
i
C_max ratio = 1.01
C_max ratio = 1.11
C_max ratio = 1.17
C_max ratio = 1.01
C_max ratio = 1.59
C_max ratio = 1.52
C_max ratio = 1.08
C_max ratio = 2.63
C_max ratio = 2.22
Metabolite Conc (mg/L)
Time (hr)

Figure 3.13. Simulated plasma metabolite concentration-versus time curves after oral administration of drug with PBPK models for metabolites with different clearance and distribution characteristics.

In panels a-c metabolite K_p ($K_{p,m}$) =1, panels d-f $K_{p,m}$ =3, and panels g-i $K_{p,m}$ =10. Panels a, d and g show metabolite concentration curves when drug has an intrinsic clearance (CL_{int}) of 10 L/hr and the metabolite intrinsic clearance ($CL_{int,m}$) is 20 L/hr, panels b, e and h show metabolite concentration curves when drug CL_{int}=1000 L/hr and the $CL_{int,m}$ is 20 L/hr, and panels c, f and i show metabolite concentration curves when drug CL_{int}=10 L/hr and the $CL_{int,m}$ is 2000 L/hr. The drug K_p value of all organs =3 in all panels. In all panels blue lines represent metabolite concentrations in the arm vein, and red lines represent metabolite concentrations in the central venous compartment (right atrium). The C_{max} ratio in each panel is calculated using the C_{max} of simulated central venous compartment (right atrium) metabolite concentration divided by C_{max} of simulated arm vein metabolite concentration.

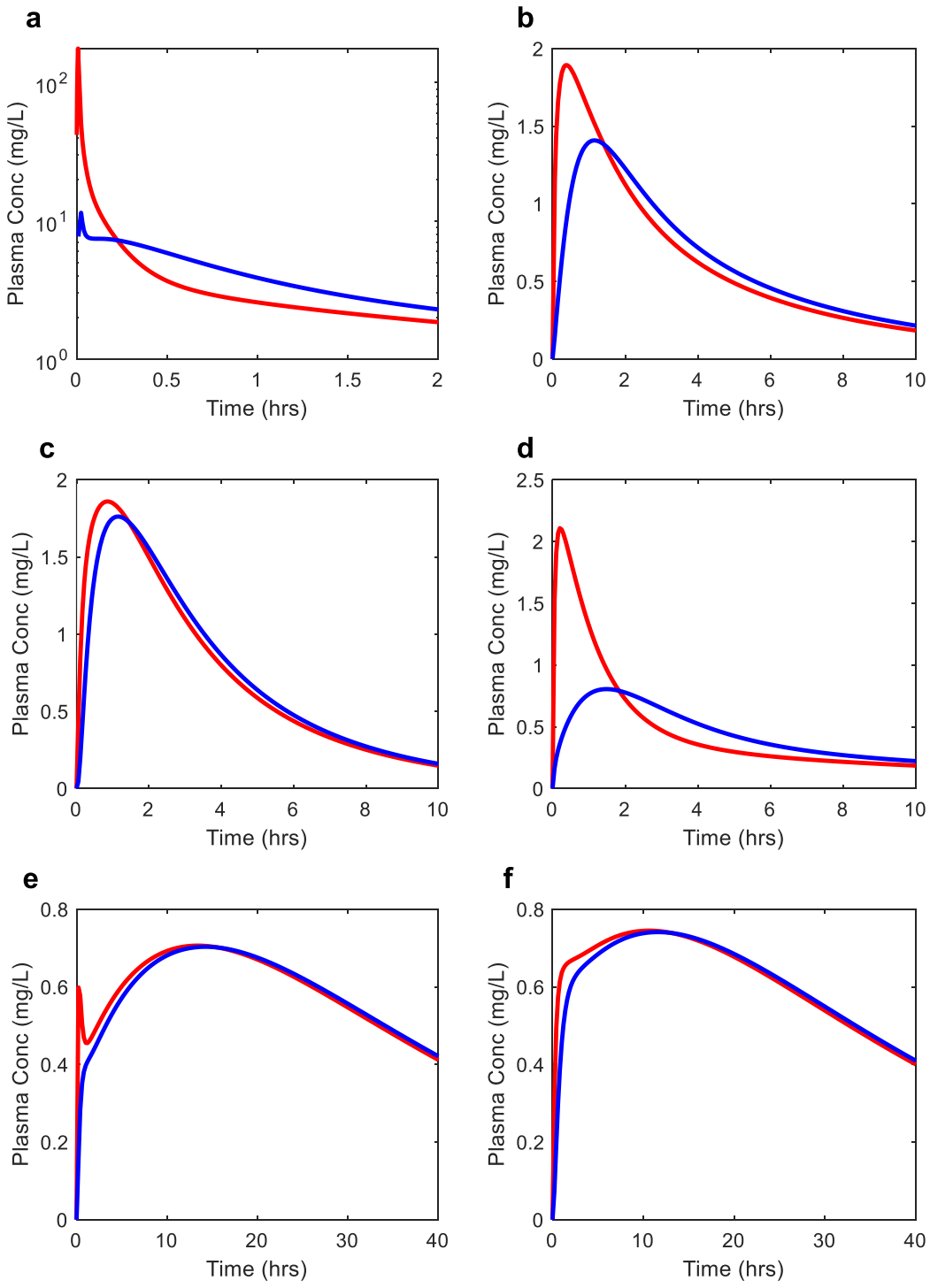
a
b
c
d
e
f
Plasma Conc (mg/L)
Time (hrs)

Figure 3.14. The simulated vena cava and peripheral sampling site concentrations of drug and metabolite with different pharmacokinetic properties using Simcyp.

Red curves represent the simulated concentration sampling from vena cava. Blue curves represent the simulated concentrations sampling from peripheral sampling site. Simulated drug concentrations were shown in panel a-d, simulated metabolite concentrations were shown in panel e and f. Panel a: 1000 mg drug (K_p for all tissues = 3, CL_{int} = 100 L/hr) was intravenously infused into vena cava within 1 minute. Panel b: 1000 mg drug (K_p for all tissues = 3, CL_{int} = 100 L/hr) was administered orally with k_a = 1. Panel c: 1000 mg drug (K_{p1} for muscle, skin, and adipose = 1, K_{p2} for all other organs and tissues = 10, CL_{int} = 100 L/hr) was administered orally with k_a = 1. Panel d: 1000 mg drug (K_{p1} for muscle, skin, and adipose = 10, K_{p2} for all other organs and tissues = 1, CL_{int} = 100 L/hr) was administered orally with k_a = 1. Panel e: 1000 mg drug (K_p for all tissues = 3, $K_{p,m}$ for all tissues = 3, CL_{int} = 10 L/hr, $CL_{int,m}$ = 20 L/hr) was intravenously infused into vena cava within 1 minute. Panel f: 1000 mg drug (K_p for all tissues = 3, $K_{p,m}$ for all tissues = 3, CL_{int} = 10 L/hr, $CL_{int,m}$ = 20 L/hr) was administered orally with k_a = 1.

Chapter 4. MECHANISTIC PBPK MODELING OF URINE PH EFFECT ON RENAL AND SYSTEMIC DISPOSITION OF METHAMPHETAMINE AND AMPHETAMINE

This chapter was published in *Journal of Pharmacology and Experimental Therapeutics (2020) 373, 488-501*

4.1 Abstract

The effect of urine pH on renal drug excretion and systemic drug disposition has been observed for many drugs. When urine pH is altered, tubular drug ionization, passive reabsorption, renal clearance, and systemic exposure may all change dramatically, raising clinically significant concerns. Surprisingly, the urine pH effect on drug disposition is not routinely explored in humans, and regulatory agencies have neither developed guidance on this issue nor required industry to conduct pertinent human trials. In this study, we hypothesized that PBPK modeling can be used as a cost-effective method to examine potential urine pH effect on drug and metabolite disposition. Our previously developed and verified mechanistic kidney model was integrated with a full body PBPK model to simulate renal clearance and systemic AUC with varying urine pH statuses, using methamphetamine and amphetamine as model compounds. We first developed and verified drug models for methamphetamine and amphetamine under normal urine pH condition (absolute-average-fold-error (AAFE) < 1.25 at study level). Then, acidic and alkaline urine scenarios were simulated. Our simulation results show that the renal excretion and plasma concentration-time profiles for methamphetamine and amphetamine could be recapitulated under different urine pH (AAFE < 2 at individual level). The methamphetamine-amphetamine parent-metabolite full body PBPK model also successfully simulated amphetamine plasma concentration-time profile (AAFE < 1.25 at study level) and amphetamine/methamphetamine urinary concentration ratio (AAFE < 2 at individual level) after dosing methamphetamine. This demonstrates that our mechanistic PBPK model can predict urine pH effect on systemic and urinary disposition of drugs and metabolites.

Significance Statement

Our study shows that integrating mechanistic kidney model with full body PBPK model can predict the magnitude of alteration in renal excretion and systemic AUC of drugs when urine pH is changed. This provides a cost-effective method to evaluate the likelihood of renal and systemic disposition changes due to varying urine pH. This is important as multiple drugs and diseases can alter urine pH, leading to quantitatively and clinically significant changes in drug and metabolite disposition that may require adjustment of therapy.

4.2 Introduction

The effect of urine pH on renal clearance of weak acids and bases was discovered more than half a century ago in studies with salicylic acid (Macpherson *et al.*, 1955) and methamphetamine (Beckett and Rowland, 1965c). The mechanism behind this phenomenon is believed to be the altered ionization status of weak acids and bases with changes in renal tubular filtrate pH, and the subsequent alterations in renal passive reabsorption of unionized drugs (Milne *et al.*, 1958; Tucker, 1981). Changes in renal passive reabsorption can have a drastic impact on renal clearance. For example, when urine pH decreased from alkaline (pH ≈ 7.5-8.5) to acidic (pH ≈ 4.5-5.5), the amount of drug excreted unchanged in urine for weak bases such as pethidine, methamphetamine, and mexiletine increased up to 21-fold (Chan, 1979), 48-fold (Beckett and Rowland, 1965c), and 87-fold (Kiddie *et al.*, 1974), respectively, while the renal clearance of weak acids such as chlorpropamide (Neuvonen and Kärkkäinen, 1983) and salicylic acid (Macpherson *et al.*, 1955) decreased by 99% and 97%, respectively. Also, after dosing of imipramine, methamphetamine, and amitriptyline, their respective metabolites desipramine, amphetamine, and nortriptyline have been shown up to 5-fold (Gram *et al.*, 1971), 11-fold (Beckett and Rowland, 1965b), and 93-fold (Kärkkäinen and Neuvonen, 1986) increases in urinary excretion, respectively, in acidic urine condition in comparison to alkaline urine condition. These findings demonstrate the pronounced and broad significance of the urine pH effect on both drugs and metabolites.

Overall, approximately 31% of marketed drugs are significantly excreted unchanged via the kidney (Varma *et al.*, 20s09), and 70% of marketed drugs are either monoprotic weak acids or monoprotic weak bases (Manallack, 2007) that may have varying ionization statuses in the tubular lumen. In addition, the mean logP of patented compounds across 18 pharmaceutical

companies ranged from 3.5 to 4.5 (Leeson and St-Gallay, 2011), suggesting that the majority of drugs have a moderate to high intrinsic lipophilicity and therefore transcellular permeability. Together, these data suggest that many drugs are potentially subject to significant renal clearance and effective renal passive reabsorption that can be altered due to urine pH changes. As such, the variability of renal clearance with urine pH can be surprisingly common. Indeed, more than a dozen drugs have been shown to have urine pH-dependent renal excretion (Macpherson *et al.*, 1955; Beckett and Rowland, 1965a; c; Sharpstone, 1969; Sjöqvist *et al.*, 1969; Gerhardt *et al.*, 1969; Gram *et al.*, 1971; Kiddie *et al.*, 1974; Chan, 1979; Neuvonen and Kärkkäinen, 1983; Muhiddin *et al.*, 1984; Benowitz and Jacob, 1985; Aoki and Sitar, 1988; Freudenthaler *et al.*, 1998). If renal excretion is an important elimination pathway for the drug of interest, the systemic drug disposition will also be affected by altered urine pH. For example, for weak bases memantine and flecainide, the area under the plasma drug concentration-time curve ($AUC_{0\text{-}inf}$) increased by 5.3-fold (Freudenthaler *et al.*, 1998) and 3.6-fold (Muhiddin *et al.*, 1984), respectively, while for weak acids cinoxacin and chlorpropamide, the plasma $AUC_{0\text{-}inf}$ decreased by 67% (Barbhaiya *et al.*, 1982) and 81% (Neuvonen and Kärkkäinen, 1983), respectively, in alkaline urine condition in comparison to acidic urine condition. This demonstrates that the magnitude of urine pH effect on plasma AUC could be as significant as drug-drug interactions resulting from co-administration with a strong inhibitor or inducer (i.e. AUC increased by 5-fold or decreased by 80%).

Given the number of known drugs affected by urine pH and the substantial magnitude of observed urine pH effects on drug and metabolite disposition, it is striking that urine pH effects on drug and metabolite renal and systemic disposition are not routinely examined for weak acids and bases in clinical studies, and regulatory agencies have not developed guidelines to assess

drug safety under different urine pHs. In contrast, characterization of drug-drug interactions, food effects and disease effects on drug disposition are required by regulatory agencies as essential components of drug approval process, and these interactions and effects have been explored extensively in human subjects and simulated by models (Shebley *et al.*, 2018) to support regulatory decision making.

In this study, we hypothesized that modeling techniques could be leveraged to understand and predict urine pH effect on drug and metabolite disposition. To test this hypothesis, a recently developed and verified dynamic physiologically-based mechanistic kidney model (Huang and Isoherranen, 2018) was integrated into a parent-metabolite full body physiologically based pharmacokinetic (PBPK) model (Huang and Isoherranen, 2020) to simulate urine pH dependent parent-metabolite systemic disposition and urinary excretion using methamphetamine and amphetamine as model compounds.

4.3 Materials and methods

4.3.1 Development of parent-metabolite full body PBPK model with mechanistic kidney model and peripheral arm vein sampling site

A 104-compartment parent-metabolite (52 compartments for each) full-body PBPK model was developed using MATLAB and Simulink platform (R2018a; MathWorks, Natick, MA) by merging our previously published mechanistic kidney model (Huang and Isoherranen, 2018) with the parent-metabolite full-body PBPK model (Huang and Isoherranen, 2020), as shown in Figure 4.1. This model contains ten physiologically important tissue/organ compartments modeled as perfusion-rate limited organs, two blood circulation compartments (i.e. central venous compartment and central arterial compartment), a peripheral arm vein sampling site as previously described (Huang and Isoherranen, 2020), a 2-compartment permeability-rate limited liver model, and a 35-compartment mechanistic kidney model (Huang and Isoherranen, 2018). The mechanistic kidney model was incorporated to replace the conventional perfusion-rate limited kidney compartment, to capture the unbound filtration, active secretion, and tubular filtrate/urine pH-dependent passive reabsorption. The mechanistic kidney model was merged with the PBPK model by connecting the central arterial compartment to the glomerulus to create the renal inflow and connecting the vascular compartment of the last subsegment of collecting duct to the central venous compartment to create the renal outflow. The model file and the code script are provided as Supplementary Material.

4.3.2 Physicochemical parameters for methamphetamine and amphetamine

In this study, only dextrorotary isomers of methamphetamine and amphetamine (i.e. S(+)-methamphetamine and S(+)-amphetamine) are discussed due to their greater psychoactive activity compared to the levorotatory isomers. The molecular weight, pK_a, and LogP values of methamphetamine (Meth) and amphetamine (Amph) were collected from www.drugbank.ca. The plasma unbound fractions ($f_{u,p}$) of methamphetamine and amphetamine were determined in pooled human plasma by ultracentrifugation as previously described (Shirasaka *et al.*, 2013). In brief, pooled human plasma was spiked with methamphetamine and amphetamine to a final concentration of 0.2 µM. Three 200 µL aliquots were centrifuged in 435,000 g for 90 min at 37 °C and another three 200 µL aliquots were incubated at 37 °C for 90 min. The supernatant (50 µL) from the ultracentrifugation and the incubated samples (50 µL) were then quenched with 250 µL of 3:1 (v/v) acetonitrile:methanol containing 100 nM methamphetamine-d_{11} and amphetamine-d_{11} as internal standards and analyzed by LC-MS/MS as previously described (Wagner *et al.*, 2017). The experiments were conducted in triplicate on two separate days. The plasma unbound fraction for each day was calculated as the ratio of mean free concentration (C_u) in supernatant (after ultracentrifugation) over mean total concentration (C) in plasma (after incubation). The average value of the two experiments was used as the final plasma unbound fraction ($f_{u,p}$).

The blood-to-plasma ratio (B/P) of methamphetamine and amphetamine were experimentally determined as described previously (Sager *et al.*, 2016). Methamphetamine and amphetamine were spiked into 3 mL of fresh human blood to a final concentration of 0.2 µM. Three 700 µL aliquots were collected and incubated for 2 hours at 37 °C to equilibrate blood partitioning. Blood samples (60 µL) were collected after incubation to measure blood concentration, remaining samples were centrifuged in 1,000 g for 10 min to separate plasma and a plasma sample (60 µL) was collected

to measure plasma concentration. Both blood and plasma samples (60 µL) were then quenched with 120 µL of methanol containing 100 nM methamphetamine-d_{11} and amphetamine-d_{11} as internal standards and analyzed by LC-MS/MS as previously described (Wagner *et al.*, 2017). The experiments were conducted in triplicate on two separate days and the blood-to-plasma ratio was calculated as the ratio of concentration in blood sample over concentration in plasma sample. The average value of the two experiments was used as the final blood-to-plasma ratio.

The cellular permeabilities of methamphetamine and amphetamine were measured using Madin-Darby canine kidney (MDCK) cells (ATCC CCL-34 passage 10 to 15). The cells were cultured in Dulbecco's modified Eagle's medium (DMEM) supplemented with 10% fetal bovine serum (FBS), 4.5 g/L glucose, and 1% penicillin/streptomycin, at 37°C with 5% CO_2 in a humidified atmosphere. Cells were seeded at a density of approximately 6.5×10^4 cells/cm^2 on 24-well Transwell plates with 0.4 µm pore size inserts. Ninety-six hours after seeding, cells were used for permeability assays. For the preincubation, the apical and basolateral chambers were first rinsed twice with warm Hank's Balanced Salt Solution (HBSS) pH 7.2, followed by acclimation to HBSS for 15 minutes. Membrane integrity was confirmed by transepithelial electrical resistance (TEER) measurements and monolayers with values below 200 $\Omega\times cm^2$ were excluded from the study. Transport assay was initiated by replacing the buffer on either apical or basolateral side with test solutions (200 µL apical, 800 µL basolateral donor chambers) containing 1 µM of methamphetamine or amphetamine in HBSS (pH 7.2). Samples of 100 µL medium from the receiver chamber were collected at 0, 20, 40, 60, 90, and 120 minutes for analysis by LC-MS/MS using a previously published method (Wagner *et al.*, 2017). The apparent permeability (P_{app}) of methamphetamine and amphetamine across cell monolayers was calculated using eq. 1:

$$P_{app} = \frac{dQ/dt}{A\times C_0} \quad (1)$$

where A is the membrane surface area (cm^2) of the insert filter, C_0 is the initial concentration of compound in the donor chamber (μM), and dQ/dt (μmol/s) is the slope of the linear regression line of measured drug amount in receiver chamber (Q) as a function of time (t), and represents the amount of methamphetamine or amphetamine that crossed the monolayer per unit time. The experiments were conducted for both apical-to-basolateral (A-to-B) and basolateral-to-apical (B-to-A) directions in duplicates on three separate days. The average value of P_{app} measured in both directions in three experiments was used as the final apparent permeability. Detailed results are shown in Figure 4.2 and 4.3.

4.3.3 PBPK model development for methamphetamine and amphetamine

The overall workflow for model development and verification is shown in Figure 4.4. For the drug model development, the clinical pharmacokinetic data of methamphetamine and amphetamine in humans were collected from the National Center for Biotechnology Information database (http://www.ncbi.nlm.nih.gov/pubmed) accessed on January 1st, 2019. Search keywords were "methamphetamine OR amphetamine AND pharmacokinetics". One iv (Li *et al.*, 2010) and two po (Rowland, 1969; CDER, 2001) datasets were used as training sets for methamphetamine and amphetamine model development, respectively. Seven (six iv and one po) and two (both po) datasets published in 6 studies (Perez-Reyes *et al.*, 1991; Cook *et al.*, 1993; Mendelson *et al.*, 1995, 2006; CDER, 2002; Harris *et al.*, 2003) were used as test sets to verify the developed PBPK models for methamphetamine and amphetamine, respectively. The detailed information of study populations and study designs for all the datasets used are summarized in Table 4.1. Plasma concentration-time curves and urinary excretion profiles from these studies were digitized using WebPlotDigitizer (version 4.2, https://automeris.io/WebPlotDigitizer).

For oral drug absorption of both methamphetamine and amphetamine, compounds in the gastrointestinal lumen were assumed to be completely dissolved and evenly distributed inside the lumen compartment immediately upon oral administration. The drug absorption from lumen into intestinal blood was assumed to be governed by a single absorption rate constant k_a, which was set to be a sufficiently high value such that the overall absorption was intestinal blood flow limited. This was based on the high aqueous solubility (928 mg/L and 1740 mg/L (www.drugbank.ca)) and high permeability of methamphetamine and amphetamine. The gut metabolism of methamphetamine and amphetamine was assumed to be negligible as both drugs have low extraction ratios in the liver primarily mediated by CYP2D6, and CYP2D6 is not highly expressed in the intestine (Paine *et al.*, 2006). As such, the fraction absorbed (F_a) and fraction escaping gut clearance (F_g) were assumed to be 1.

For the physiological model, the system-specific parameters including the physical volume and the blood flow to each organ/tissue were collected from literature (Brown *et al.*, 1997). The tissue-to-plasma partition coefficients (K_p) for brain, gastrointestinal tract, heart, kidney, liver, lung, pancreas, and spleen for methamphetamine were calculated based on a published human positron emission tomography (PET) study (Volkow *et al.*, 2010), while the K_p values for adipose, bone, muscle, and skin were optimized as K_p=3 based on observed methamphetamine volume of distribution at steady state (V_{ss}) of 4.02 L/kg (Harris *et al.*, 2003). Due to the structural similarity between methamphetamine and amphetamine, the visceral organ-specific K_p values (i.e. K_p for brain, gastrointestinal tract, heart, kidney, liver, lung, pancreas, and spleen) for amphetamine were set the same as methamphetamine. Based on the higher polarity of amphetamine in comparison to methamphetamine, the tissue-specific K_p values of adipose, bone, muscle, and skin were set as 2

for amphetamine, resulting in a predicted V_{ss} of 3.14 L/kg, versus an observed apparent V_{ss} ranging from 3.2 L/kg to 5.6 L/kg after oral dosing (Randall, 2004).

The hepatic clearances of methamphetamine and amphetamine were modeled based on *in vivo* human data. Methamphetamine has an observed systemic clearance of 18.0 L/hr (Li *et al.*, 2010) and an observed renal clearance of 8.09 L/hr (Li *et al.*, 2010) after intravenous administration. Amphetamine has an observed oral clearance of 15.8 L/hr (CDER, 2001) and an observed renal clearance of 7.14 L/hr (Rowland, 1969). As a result, the hepatic clearances of methamphetamine and amphetamine were calculated as 9.91 L/hr and 7.41 L/hr, respectively, based on the assumption that F_a and F_g are equal to 1 for amphetamine. The intrinsic metabolic clearances of methamphetamine and amphetamine were back-calculated as 14.4 and 9.87 L/hr respectively based on measured plasma unbound fraction, blood-to-plasma ratio, and the well-stirred hepatic clearance model (Wilkinson and Shand, 1975).

The mechanistic kidney model was used to simulate the renal clearance of methamphetamine and amphetamine. The experimentally determined human plasma unbound fraction ($f_{u,p}$) and the permeability in the MDCK cells were used as model inputs to simulate unbound filtration and passive reabsorption processes as previously described (Huang and Isoherranen, 2018). Without incorporating active secretion, the mechanistic kidney model predicted CL_r values of 2.9 L/hr and 3.2 L/hr for methamphetamine and amphetamine, respectively, which are significantly below the observed values (8.09 L/hr for methamphetamine (Li *et al.*, 2010) and 7.14 L/hr for amphetamine (Rowland, 1969)). Therefore, an active secretion component was added to the mechanistic kidney model to simulate methamphetamine and amphetamine renal clearances based on the previous characterization of methamphetamine and amphetamine as OCT2 and MATE substrates (Wagner *et al.*, 2017). Due to the low confidence of *in vitro* and *in vivo* renal transporter quantification and

expression, the active secretion clearances of methamphetamine and amphetamine were optimized with respect to the observed renal clearance (i.e. 8.09 L/hr for methamphetamine (Li *et al.*, 2010) and 7.14 L/hr for amphetamine (Rowland, 1969)) assuming equal apical and basolateral secretion and uniform distribution of active secretion among the three subsegments of proximal tubule in the model. All the detailed physicochemical and pharmacokinetic values used in the models are listed in Table 4.2.

4.3.4 Verification of methamphetamine and amphetamine PBPK models

All simulations were performed using MATLAB and Simulink platform (R2018a; MathWorks, Natick, MA) with the same route of administration and the same dosage regimen as reported in the corresponding clinical studies (Table 4.1), assuming a representative population with average physiology. The renal tubular filtrate pH gradient for a representative population is shown in Table 4.3 with a urine pH value of 6.5 under uncontrolled (i.e. normal) condition. The overall model development and verification workflow was adapted from previous studies (Huang *et al.*, 2017; Cheong *et al.*, 2019), and is shown schematically in Figure 4.4. To verify the methamphetamine model, methamphetamine plasma concentration-time profiles were simulated after intravenous and oral dosing and compared to the observed data from 7 test sets (6 iv and 1 po dosing) published in 5 studies (Perez-Reyes *et al.*, 1991; Cook *et al.*, 1993; Mendelson *et al.*, 1995, 2006; Harris *et al.*, 2003). These studies were not used in model development. For amphetamine model verification, the amphetamine plasma concentration-time profiles were simulated after oral dosing and compared to the observed data from 2 test datasets (CDER, 2002) that were not used in model development. All simulated plasma concentrations were sampled from peripheral arm vein sampling site which was developed and verified previously (Huang and Isoherranen, 2020) to

match with the sampling site in the observed PK studies. To assess model performance, absolute average fold error (AAFE) was calculated according to equation 2. Furthermore, the area under the simulated plasma concentration-time curve (AUC) was calculated using trapezoidal method and compared to the observed AUC. The ratio between the simulated and observed AUC was calculated to assess the fold-difference between the two. The calculated AAFE and AUC ratio had to be within 0.8-to-1.25-fold (model acceptance criterion) for the simulation to be considered successful.

$$AAFE = 10^{\frac{1}{n}\sum\left|log_{10}\frac{Simulated}{Observed}\right|} \quad (2)$$

4.3.5 Simulation and verification of urine pH effect on renal excretion and systemic disposition of methamphetamine and amphetamine

To evaluate whether the verified full body PBPK model could be applied to predict urine pH effect on plasma concentration-time profile and urinary drug excretion of methamphetamine and amphetamine, methamphetamine disposition was simulated under two different urine pH conditions in contrast to the default uncontrolled urine pH (i.e. urine pH = 6.5). For acidic urine pH, the tubular filtrate pH was set to decrease in a stepwise manner from 7.2 at the first proximal tubule subsegment to 5.0 at the last collecting duct subsegment. For alkaline urine pH, the tubular filtrate pH was set to increase in a stepwise manner from 7.4 at the first proximal tubule subsegment to 8.0 at the last collecting duct subsegment. Detailed renal tubular filtrate pH gradient setups used in the modeling are shown in Table 4.3.

The amount of drug excreted in urine with time and the plasma concentration-time profile for methamphetamine were simulated at each of the three urine pH conditions after oral dosing of 11 mg methamphetamine base. The simulated urinary excretion versus time profiles were compared

to observed data from three test sets corresponding to the three urine pH conditions (Beckett and Rowland, 1965c). Due to the limited number of subjects in the observed data (n=1), a 2-fold acceptance criterion of AAFE was used as the acceptance criterion when the simulated population representative was compared to the individual observed data. The 2-fold criterion was selected given the reported inter-individual variability (coefficient of variance: 56%) in methamphetamine renal clearance (Kim *et al.*, 2004). The 2-fold range is a conservative criterion provided renal clearance follows log-normal distribution, where 95% of individuals have a renal clearance within 2.53-19.5 L/hr, yielding a 2.77-fold difference between the upper/lower limit and the geometric mean. The simulation results of the urine pH effect on methamphetamine urinary excretion were also compared to another clinical study (Beckett and Rowland, 1965b) as a second set of verification. Because the observed plasma concentration-time data for methamphetamine were not available under the basic and acidic urine pH conditions, simulated and observed plasma concentrations were not compared.

The urinary excretion and plasma concentration-time profile for amphetamine were simulated similarly under uncontrolled, acidic, and alkaline urine conditions after oral dosing of 11 mg amphetamine base. The percentage of amphetamine dose excreted into urine was calculated by dividing the cumulative amount excreted into urine by dose. The amount excreted into urine was considered over 48 hours for uncontrolled urine pH and 16 hours for acidic and alkaline urine pH as described in the observed study, and compared to observed data from respective test datasets (Beckett and Rowland, 1965a). The effect of altered urine pH on amphetamine urinary excretion was evaluated based on the percent change in urinary excretion (amount of amphetamine excreted) under either acidic or alkaline urine in comparison to the urinary excretion when urine pH was not controlled (simulated urine pH = 6.5). The ratio of the predicted to observed percent change in

urinary excretion with altered urine pH was calculated. A 2-fold acceptance criterion, similar to what has been used for drug-drug interaction studies (Sager *et al.*, 2015), was applied to this ratio to determine whether the simulation was successful. Additionally, simulated plasma concentration-time profile for amphetamine under uncontrolled and acidic urine conditions was compared to the observed data from four test datasets (Beckett *et al.*, 1969). Due to the limited number of subjects in the observed data (n=2), a 2-fold acceptance criterion of AAFE was used when comparing the simulated population mean results to the individual observed data.

4.3.6 Verification of methamphetamine-amphetamine parent-metabolite model

The methamphetamine-amphetamine parent-metabolite model was established based on the individual compound models using previously developed PBPK model (Huang and Isoherranen, 2020). Amphetamine formation from methamphetamine was modeled to occur within the liver compartment. The hepatic formation clearance of amphetamine from methamphetamine was calculated as 3.29 L/hr using the data from a clinical study reporting the AUC ratio of amphetamine to methamphetamine (ratio = 0.208) after iv dosing of methamphetamine (Newton *et al.*, 2005) and observed amphetamine oral clearance of 15.8 L/hr (CDER, 2001) based on a previous method (Lane and Levy, 1980).

To verify the methamphetamine-amphetamine parent-metabolite kinetic model, amphetamine plasma concentration-time profiles as a metabolite of methamphetamine after intravenous administration of methamphetamine were simulated and compared to the observed data from 4 test sets (Cook *et al.*, 1993; Harris *et al.*, 2003; Mendelson *et al.*, 2006). To evaluate the model, a 0.8-to-1.25-fold acceptance criterion was applied to the AAFE to determine whether the simulation was successful. All simulations were performed with the same route of administration and same

dosage as reported in the corresponding studies (Table 4.1) and all simulated plasma concentrations were sampled from the peripheral arm vein sampling site.

To test whether the verified parent-metabolite model can capture the methamphetamine-amphetamine urinary kinetics under different urine pH conditions, simulation results were compared to observed urinary concentration ratio (Oyler *et al.*, 2002) and excretion data (Kim *et al.*, 2004). First, the urinary concentration of methamphetamine and amphetamine were simulated under uncontrolled urine pH (urine pH = 6.5) after 4 consecutive oral doses of 10 or 20 mg methamphetamine. The urinary metabolite/parent concentration ratio was calculated as the ratio of amphetamine to methamphetamine urinary concentration, and the ratio was compared to the observed data (Oyler *et al.*, 2002). Since the observed data were reported only from a single subject after 10 or 20 mg doses, a 2-fold acceptance criterion for the calculated AAFE was used to determine whether the simulation was successful. For extrapolation, we also simulated the urinary metabolite/parent concentration ratio under acidic and alkaline urine conditions. As the observed urinary metabolite/parent ratio data were not available under the acidic and alkaline urine pH conditions, no comparisons between simulated and observed urinary concentrations were done for these two conditions. Second, the amount of methamphetamine and amphetamine excreted in urine was simulated under uncontrolled urine pH (urine pH = 6.5) after 4 consecutive doses of 10 mg methamphetamine. The percentage of methamphetamine dose excreted into urine as methamphetamine or amphetamine was calculated by dividing cumulative amount of methamphetamine and amphetamine excreted into urine over 16 days by methamphetamine dose. The urinary metabolite/parent excretion ratio was calculated by dividing the urinary excretion of amphetamine with the urinary excretion of methamphetamine. The simulated percentage of

urinary excretion of methamphetamine and amphetamine, and the metabolite/parent ratio were compared to observed data from 13 individuals (Kim *et al.*, 2004).

4.4 Results

4.4.1 Verification of methamphetamine and amphetamine drug models

Human plasma unbound fraction, blood-to-plasma ratio, and MDCK cellular permeability were experimentally determined for methamphetamine and amphetamine and used in the PBPK model. The $f_{u,p}$ value was 0.77 (±0.03) for methamphetamine and 0.82 (±0.09) for amphetamine. The blood-to-plasma ratio was 1.04 (±0.07) for methamphetamine and 1.04 (±0.06) for amphetamine, suggesting some distribution into the red blood cells. The MDCK cellular permeability was 29.1×10^{-6} (±5.75) cm/s for methamphetamine and 26.9×10^{-6} (±4.42) cm/s for amphetamine (Figure 4.2 and 4.3), indicating a high permeability for both compounds.

The methamphetamine (Figure 4.5) and amphetamine (Figure 4.6) drug models were independently verified using the observed plasma concentration-time data from seven methamphetamine test sets (six iv dosing and one oral dosing) (Perez-Reyes *et al.*, 1991; Cook *et al.*, 1993; Mendelson *et al.*, 1995, 2006; Harris *et al.*, 2003) and two amphetamine oral dosing test sets (CDER, 2002), respectively. The AAFE values for methamphetamine (Figure 4.5) and amphetamine (Figure 4.6) plasma concentration-time data in the test sets ranged from 1.04 to 1.19 and the predicted over observed AUC ratios ranged from 0.87 to 1.11 (Table 4.1 and Figure 4.7). Both evaluation metrics met the stringent 0.8-to-1.25-fold model acceptance criterion demonstrating successful model verification and high confidence on the model parameter inputs for both methamphetamine and amphetamine.

4.4.2 Simulation and verification of urine pH effect on renal excretion and systemic disposition of methamphetamine and amphetamine

After the successful verification of the methamphetamine systemic model, methamphetamine urinary excretion was simulated as a function of time under different urine pH conditions. The goal of these simulations was to test whether the effect of urine pH on methamphetamine excretion could be simulated using the full body PBPK model coupled with the mechanistic kidney model. Our simulations show that methamphetamine urinary excretion when urine is acidic (Figure 4.8a red dashed curve) significantly exceeds the excretion when urine is alkaline (Figure 4.8a blue dotted curve), and that the simulated urinary excretion profile of methamphetamine under alkaline or acidic urine agrees with the observed data in human (Beckett and Rowland, 1965c). The simulated excretion of methamphetamine with urine pH of 6.5 (Figure 4.8a black solid curve) is in between the acidic and alkaline urine conditions (Figure 4.8a red and blue). The urine pH of 6.5 was selected to represent the estimated urine pH in individuals when urine pH is not controlled. The calculated AAFE values met the 2-fold model acceptance criterion under all three urine pH conditions (Figure 4.8a). The urine pH effect on urinary excretion was also simulated and compared to a second observed study, shown in Figure 4.9. The percent dose excreted in urine as methamphetamine was successfully captured under all three urine pH conditions, with all calculated AAFE values meeting the 2-fold model acceptance criterion (Figure 4.9).

The urine pH effect on methamphetamine systemic disposition was also simulated (Figure 4.8b) to explore the effect of changes in urine pH on methamphetamine exposure and half-life. The calculated plasma methamphetamine $AUC_{0\text{-}inf}$ values under alkaline, uncontrolled, and acidic urine conditions were 970, 542, and 284 μg×hr/L, respectively, after an oral dose of 11 mg methamphetamine base, illustrating a dramatic impact of urine pH on methamphetamine systemic exposure. The simulated plasma concentrations of methamphetamine were highest when urine was

alkaline, followed by uncontrolled urine pH (urine pH = 6.5), and the plasma concentrations of methamphetamine were the lowest when urine was acidic (Figure 4.8b).

Similar to methamphetamine, urine pH also plays a significant role in amphetamine urinary excretion (Beckett and Rowland, 1965a). To recapitulate the urine pH effect on amphetamine renal disposition, the urinary excretion of amphetamine was simulated under three different urine pH conditions (Figure 4.10a). Compared to uncontrolled urine pH condition (urine pH = 6.5), alkaline urine condition was predicted to result in a 97% decrease of urinary excretion of amphetamine, while the observed decrease was 91%, resulting in a predicted over observed ratio of 1.07-fold meeting the acceptance criterion of 2-fold. On the other hand, urine acidification was predicted to result in a 48% increase of urinary excretion of amphetamine when compared to uncontrolled urine pH condition, while the observed increase was 75%, resulting in a predicted over observed ratio of 0.64-fold meeting the acceptance criterion of 2-fold.

The urine pH effect on amphetamine systemic disposition was also simulated (Figure 4.10b and c) and compared to the observed data (Beckett *et al.*, 1969). The AAFE values for the simulations of acidic and uncontrolled urine pH met the 2-fold model acceptance criterion (Figure 4.10b and c). The 2-fold criterion was used due to the small sample size in the observed studies (n=2). Unfortunately, clinical data regarding the alkaline urine pH effect on amphetamine systemic disposition were not available, and hence no verification was conducted for this condition. Based on the simulations using the verified amphetamine model, the plasma amphetamine $AUC_{0\text{-}inf}$ values under alkaline, uncontrolled, and acidic urine conditions were 1325, 692, and 361 μg×hr/L, respectively, after an oral dose of 11 mg amphetamine base, demonstrating a dramatic impact of urine pH on amphetamine systemic exposure.

4.4.3 Simulation and verification of plasma and urinary methamphetamine-amphetamine parent-metabolite kinetics

After the successful verification of methamphetamine (Figure 4.5) and amphetamine (Figure 4.6) models, the parent-metabolite link was established to allow for simulation of amphetamine disposition as a metabolite of methamphetamine. To verify the methamphetamine-amphetamine parent-metabolite model, amphetamine plasma concentration-time profiles were simulated as a metabolite after iv dosing of methamphetamine and compared to observed data. As shown in Figure 4.11, all AAFE values were within the 0.8-to-1.25-fold acceptance criterion, indicating the parent-metabolite linkage between methamphetamine and amphetamine was successfully established and verified.

To evaluate the applicability of the verified parent-metabolite model to capture the methamphetamine-amphetamine urinary kinetics, the urinary metabolite/parent concentration ratio was simulated under uncontrolled urine pH (urine pH=6.5) and compared to the observed data (Oyler *et al.*, 2002) from a single subject after 4 consecutive doses of 10 mg or 20 mg methamphetamine (Figure 4.12). The AAFE values for these simulations were within the 2-fold acceptance criterion, which was used due to the small sample size (n=1). The urinary metabolite/parent concentration ratio was also simulated under acidic and alkaline urine conditions to explore the impact of varying urine pH on this measure. The simulation results show that the urinary metabolite/parent concentration ratio can be affected by urine pH. Particularly, alkaline urine resulted in a higher urinary Amph/Meth ratio. In addition, the percent dose excreted in urine as methamphetamine and amphetamine was also simulated under uncontrolled urine pH (urine pH = 6.5) and compared to the observed data (Figure 4.13). The observed mean percent dose excreted in urine as methamphetamine and amphetamine were

41.3% and 9.8%, respectively, while the predicted values were 40.6% and 8.2% respectively. The observed amphetamine/methamphetamine ratio in urine was 0.26 while the predicted ratio was 0.20. The predicted/observed values were all within the 2-fold acceptance criterion. Together, these data suggest successful application of the model to simulate systemic and urinary parent-metabolite kinetics.

4.5 Discussion

The effect of urine pH on renal excretion of drugs has been observed for a multitude of drugs in humans (Macpherson *et al.*, 1955; Beckett and Rowland, 1965a; c; Sharpstone, 1969; Sjöqvist *et al.*, 1969; Gerhardt *et al.*, 1969; Gram *et al.*, 1971; Kiddie *et al.*, 1974; Chan, 1979; Muhiddin *et al.*, 1984; Benowitz and Jacob, 1985; Aoki and Sitar, 1988; Freudenthaler *et al.*, 1998). In addition, a plethora of medications and disease states have been reported to cause changes in urine pH (Cook *et al.*, 2007). For example, acetazolamide which was indicated for glaucoma and edema has been shown to increase urinary pH in humans from 5.5 to 7.6 (Moviat *et al.*, 2006). In contrast, cholestyramine, indicated for hypercholesterolemia, was shown to induce metabolic acidosis and therefore can decrease urinary pH to as low as 4.8 (Eaves and Korman, 1984). Further, urine acidification is observed with diabetes, obesity, and chronic kidney disease (Maalouf *et al.*, 2004, 2010; Nakanishi *et al.*, 2012), and urine alkalinization is observed with vomiting and urinary tract infection (Yi *et al.*, 2012; Lai *et al.*, 2019). Therefore, the potential impact of co-medications and comorbidities on urine pH and consequently renal drug clearance can be commonplace and profound. Nonetheless, the overall effect of altered urine pH on urinary drug concentrations, excretion profiles, systemic exposure, and the subsequent clinical consequences has been underappreciated. In this study, we hypothesized that *in silico* modeling could be used to understand and predict the effects of altered urine pH on drug and metabolite renal and systemic disposition. The goal of this study was to integrate the verified mechanistic kidney model (Huang and Isoherranen, 2018) with a parent-metabolite full body PBPK model (Huang and Isoherranen, 2020) to examine the applicability of the final model to predict the effect of varying urine pH on renal clearance and systemic exposure to assess the potential clinical consequences, using methamphetamine and amphetamine as model compounds.

Currently, the urine pH effect on renal clearance and systemic disposition have rarely been considered when using *in silico* techniques to simulate drug and metabolite disposition. For studies that specifically explore urinary excretion as a function of time, the urinary excretion profiles were mostly simulated using simple first order urinary kinetics (Ortiz *et al.*, 2014; Phillips *et al.*, 2014; Adachi *et al.*, 2015; Marchand *et al.*, 2015; Yang *et al.*, 2015) governed by a fixed observed value such as elimination rate constant. Although these models may have successfully recapitulated the observed data, they cannot be extrapolated to untested or altered scenarios due to their non-mechanistic nature when simulating urinary kinetics. In contrast, mechanistic modeling can be used to extrapolate drug disposition from known settings to unstudied scenarios such as unstudied populations and unstudied drug co-administration (Wagner *et al.*, 2015b; Huang *et al.*, 2017; Zhang *et al.*, 2017; Hanke *et al.*, 2018), and likely to unstudied urine pH conditions.

Recently, the MechKiM model embedded in the Simcyp platform was used to predict renal clearance and urine pH effects on renal clearance (Matsuzaki *et al.*, 2019). In that study, seven compounds were used as the test set to examine model performance, and the simulations were conducted assuming uniform renal tubular filtrate pH throughout all renal segments. The overall simulation results under the uncontrolled urine pH condition showed AAFE values ranging from 2.87 (assuming uniform tubular filtrate pH = 6.2) to 3.62 (assuming uniform tubular filtrate pH = 7.4). In comparison, our mechanistic kidney model which assumes a tubular pH gradient across different tubular segments showed superior performance for a set of 35 non-neutral test compounds with AAFE values of 1.83, 1.82, and 1.46 for weak bases, weak acids, and zwitterions, respectively (Huang and Isoherranen, 2018). This better performance could be due to our strategy to use a stepwise gradient for renal tubular filtrate pH to account for the naturally

continuous acidification process of tubular filtrate, although other differences such as microvilli consideration and a larger number (11 vs 7) of tubular compartments in our model may also contribute to our better performance. Further, the previous study (Matsuzaki *et al.*, 2019) showed a relatively insensitive response of simulated renal clearance to urine pH changes. For example, their simulated amphetamine renal clearance did not change with urine pH between 5 and 8, which is inconsistent with the observed dramatic changes (Beckett and Rowland, 1965a; Beckett *et al.*, 1969). Conversely, our model accurately recapitulated the renal excretion of methamphetamine and amphetamine under acidic (urine pH = 5.0), uncontrolled (urine pH = 6.5), and alkaline (urine pH = 8.0) urine conditions (Figure 4.10), and was previously shown to capture the varying renal clearance of salicylic acid and memantine as a function of urine pH (Huang and Isoherranen, 2018). We confirmed the importance of the stepwise gradient via an in-house head-to-head comparison of the urinary methamphetamine excretion using our stepwise pH gradients and the previously published (Matsuzaki *et al.*, 2019) constant pH value. The constant pH value approach failed to recapitulate the observed data under uncontrolled (AAFE = 2.2 or 6.5) and alkaline urine condition (AAFE = 13.6) (Figure 4.14) while the stepwise pH gradient approach successfully (AAFE < 2) simulated methamphetamine urinary excretion (Figure 4.9). Together, these results support that our PBPK model and strategy can capture the mathematical relationship between urine pH and the corresponding apparent permeability, passive reabsorption, and renal clearance successfully. More examination using additional dataset is warranted for further validation of the full model.

Altered urine pH may also affect the systemic exposure of drugs and their metabolites if renal clearance is an important elimination pathway. For example, amphetamine plasma AUC was decreased by approximately 50% under acidic urine pH condition compared to uncontrolled

urine pH condition (Beckett *et al.*, 1969), and as urine pH is known to affect the renal clearance for many drugs, such effects on drug AUC can be common. The modeling and simulation workflow presented here offers a feasible approach to predict whether the drug exposure is sensitive to changes in urine pH. To do this, it is important to construct both urine pH-sensitive mechanistic kidney model and a full body PBPK model that captures drug absorption, distribution, and other pathways of elimination such as hepatic metabolism and biliary excretion. In this study, we first verified the full body PBPK model for methamphetamine (Figure 4.5) and amphetamine (Figure 4.6), and then verified the urine pH effect on renal excretion (Figure 4.8a and 4.10a), to ultimately simulate the urine pH effect on plasma AUC for methamphetamine (Figure 4.8b) and amphetamine (Figure 4.10b and c). Based on the simulations, we also predicted that urine alkalinization can increase plasma AUC of methamphetamine and amphetamine by about 100% in comparison to uncontrolled urine pH due to increased passive reabsorption and decreased renal clearance (Figures 4.8 and 4.10). Collectively, we showed a modeling workflow that can serve as a robust and cost-effective method to assess how drug AUC is altered when urine pH is changed due to co-medications or disease states.

The urine pH effect also impacts the interpretation of urinary concentration data. At present, the urinary concentrations of drugs and metabolites have been widely used for understanding drug pharmacokinetics, for phenotyping human subjects for certain metabolizing enzymes (Wedlund *et al.*, 1984; Chládek *et al.*, 2000; Vogl *et al.*, 2015), and for testing and screening for illicit drug use (Fabbri, 2003; Moeller *et al.*, 2017). As shown in Figures 4.8 and 4.10, the changes in urine pH will change the renal excretion and therefore urinary concentration-time profile. Further, simulations in Figure 4.12 suggest that urinary metabolite/parent ratio can also be influenced by urine pH changes. Currently, urine samples collected at a single time point often serve as the

direct proxy for data interpretation, without the quantitative consideration of the confounding effect of different urine pHs on urinary disposition. As such, analysis of drug concentrations in the collected urine samples may lead to misinterpretation and suboptimal decision making. The modeling and simulation approach described here, together with the measurement of urine pH values, can aid in interpreting urinary excretion data and help to minimize false negative and false positive readings.

In conclusion, this study shows that the previously developed and verified mechanistic kidney model together with the full body parent-metabolite PBPK model can accurately predict the effect of urine pH on methamphetamine and amphetamine renal clearance, plasma concentration-time profile and systemic and urinary parent-metabolite kinetics. These results suggest that mechanistic PBPK models can be generally applied to predict the potential impact of co-medications and comorbidities on parent-metabolite renal and systemic disposition due to altered urine pH. The modeling workflow and approach established here is likely to be useful in assessing the sensitivity of new compounds' disposition to changes in urine pH, especially for weak acids and bases that have substantial permeability.

Table 4.1. Clinical studies used for model development and verification of methamphetamine and amphetamine

Study	Drug	n	Dose of drug Base (mg)	Route	Infusion length	Observed Meth $AUC_{0\text{-}inf}$ (ng×hr/mL)	Predicted Meth $AUC_{0\text{-}inf}$ (ng×hr/mL)	Predicted/Observed Meth AUC ratio	Observed Amph $AUC_{0\text{-}inf}$ (ng×hr/mL)	Predicted Amph $AUC_{0\text{-}inf}$ (ng×hr/mL)	Predicted/Observed Amph AUC ratio	Observed CL_r (L/hr)
Training set												
Li et al., 2010	Meth	12	17.8	i.v.	1 minute	1023	959.0	0.94	-	-	-	8.09
CDER 21-303 trial 371.404	Amph	8	4.7	p.o.	-	-	-	-	300	295	1.02	-
Rowland 1969	Amph	3	7.3	p.o.	-	-	-	-	-	-	-	7.14
Test set for systemic disposition												
Cook et al., 1993	Meth	6	12.4	i.v.	1 minute	787	685	0.87	157	131	1.20	-
Mendelson et al., 1995	Meth	8	24.1	i.v.	1 minute	1330	1328	1.00	-	-	-	-
Harris et al., 2003	Meth	4	5	i.v.	15 minutes	248	276	1.11	-	-	-	-
Harris et al., 2003	Meth	8	10	i.v.	15 minutes	514	551	1.07	94.1	106	0.89	-
Mendelson et al., 2006	Meth	12	18.4	i.v.	1 minute	1010	1013	1.00	173	194	0.89	-
Mendelson et al., 2006	Meth	12	36.8	i.v.	1 minute	1978	2026	1.02	353	389	0.91	-
Perez-Reyes et al., 1991	Meth	6	8	p.o.	-	-	-	-	-	-	-	-
CDER 11-522 trial 371.101	Amph	-	14.1	p.o.	-	-	-	-	884	886	1.00	-
CDER 11-522 trial 371.102	Amph	-	4.7	p.o.	-	-	-	-	290	295	0.98	-

Table 4.2. Physicochemical and pharmacokinetic parameters of methamphetamine and amphetamine used in the full body parent-metabolite PBPK model with the integrated mechanistic kidney model and peripheral arm vein sampling site.

Parameter	Methamphetamine	Amphetamine
Physicochemical		
Molecular weight (g/mol)	149.23[a]	135.21[a]
Compound type	Base[a]	Base[a]
pK_a	10.21[a]	10.01[a]
LogP	2.23[a]	1.85[a]
$f_{u,p}$	0.77[b]	0.82[b]
B/P	1.04[b]	1.04[b]
MDCK cellular permeability (10^{-6} cm/s)	29.1[b]	26.9[b]
Absorption		
k_a (hr^{-1})	5[c]	5[c]
F_a	1[c]	1[c]
F_g	1[c]	1[c]
Distribution		
$K_{p,adipose}$	3[d]	2[d]
$K_{p,bone}$	3[d]	2[d]
$K_{p,brain}$	9.67[e]	9.67[e]
$K_{p,gastrointestinal\ tract}$	25.2[e]	25.2[e]
$K_{p,heart}$	5.21[e]	5.21[e]
$K_{p,kidney}$	14.5[e]	14.5[e]
$K_{p,liver}$	25[e]	25[e]
$K_{p,lung}$	6.94[e]	6.94[e]
$K_{p,muscle}$	3[d]	2[d]
$K_{p,pancreas}$	12.7[e]	12.7[e]
$K_{p,skin}$	3[d]	2[d]
$K_{p,spleen}$	11[e]	11[e]
Metabolism		
CL_{total} (L/hr)	18.0[f] (i.v.)	15.8[g] (p.o.)
CL_h (L/hr)	9.91[h]	7.41[h]
$CL_{intrinsic}$ (L/hr)	14.4[h]	9.87[h]
CL_f (L/hr)	-	3.29[i]
Excretion		
CL_r (L/hr)	8.09[f]	7.14[j]
$CL_{section}$ (L/hr)	48[k] (16×3)	30[k] (10×3)

$f_{u,p}$, fraction unbound in plasma; B/P, blood-to-plasma ratio; MDCK, Madin-Darby canine kidney; k_a, absorption rate constant from gut lumen to blood; F_a, fraction absorbed; F_g, fraction passed the enterocyte; K_p, tissue-to-plasma partition coefficient for specific organ/tissue; CL_{total}, total body clearance (intravenous administration for methamphetamine; oral administration for amphetamine); CL_h, hepatic clearance; $CL_{intrinsic}$, metabolic intrinsic clearance; CL_f, formation clearance; CL_r, renal clearance; $CL_{section}$, renal active secretion clearance at proximal tubule (clearance value of each proximal subsegment S1, S2, and S3) [a]Collected from www.drugbank.ca, [b]Measured from experiments, [c]Assumed as described in Materials and Methods, [d]Optimized as described in Materials and Methods, [e](Volkow *et al.*, 2010), [f](Li *et al.*, 2010), [g](CDER, 2001), [h]Derived as described in Materials and Methods, [i]Derived based on (Lane and Levy, 1980; CDER, 2001; Newton *et al.*, 2005), [j](Rowland, 1969), [k]Optimized as described in Materials and Methods

Table 4.3. Setup of the pH gradient for the different sub-segments of the model used to simulate the effect of altered urine pH on renal clearance.

Segment	Uncontrolled urine pH	Controlled acidic urine pH	Controlled alkaline urine pH
Proximal $tubule_1$	7.2	7.2	7.4
Proximal $tubule_2$	7.1	6.8	7.4
Proximal $tubule_3$	7	6.4	7.4
Loop of $henle_D$	7	6.0	7.4
Loop of $henle_A$	7	6.0	7.4
Distal tubule	6.9	5.8	7.4
Collecting $duct_1$	6.8	5.6	7.4
Collecting $duct_2$	6.7	5.4	7.4
Collecting $duct_3$	6.6	5.2	7.6
Collecting $duct_4$	6.5	5.0	7.8
Collecting $duct_5$	6.5	5.0	8.0

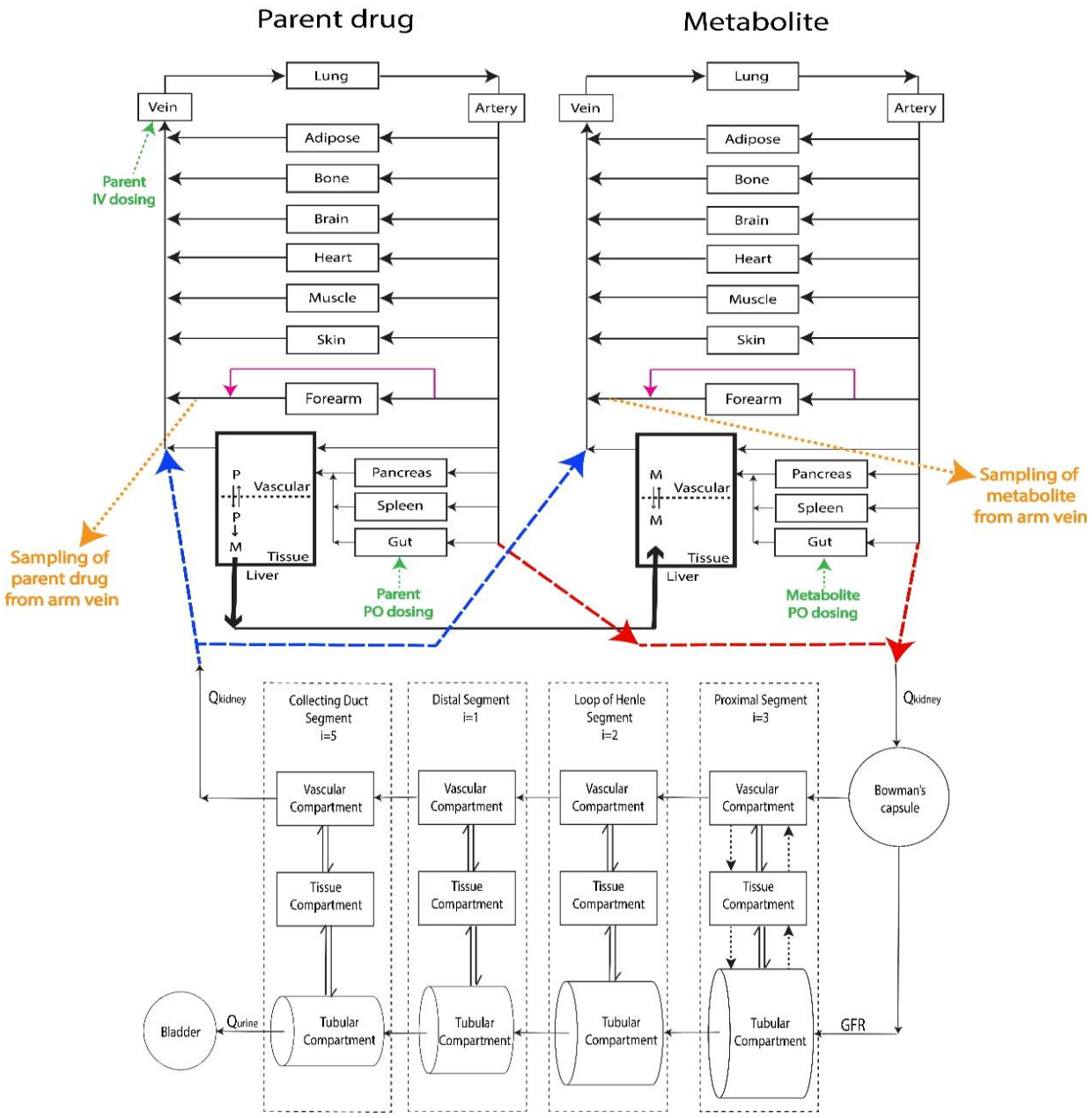
Parent drug
Metabolite
Lung
Vein
Artery
Adipose
Bone
Brain
Heart
Muscle
Skin
Forearm
Pancreas
Spleen
Gut
Liver
Tissue
Vascular
Parent IV dosing
Sampling of parent drug from arm vein
Parent PO dosing
Metabolite PO dosing
Sampling of metabolite from arm vein
Qkidney
Collecting Duct Segment i=5
Distal Segment i=1
Loop of Henle Segment i=2
Proximal Segment i=3
Vascular Compartment
Tissue Compartment
Tubular Compartment
Bowman's capsule
Bladder
Qurine
GFR

Figure 4.1. Structure of the developed mechanistic kidney-integrated parent-metabolite full body PBPK model.

Schematic presentation of the physiologically based parent-metabolite pharmacokinetic model with a mechanistic kidney model and peripheral arm vein sampling site incorporated. The renal artery that connects central artery to the entrance of the mechanistic kidney model is shown in red dashed lines. The renal vein that connects the exit of mechanistic kidney model to the central venous compartment is shown in blue dashed lines. The transporter-mediated active secretion or active reabsorption is shown in black dotted arrows. The bidirectional pH-dependent passive diffusion is shown in double arrows. The peripheral arm vein sampling sites are shown in orange with forearm anastomoses shown in magenta. The intravenous and oral dosing are shown in green. Q_{kidney}, renal blood flow; Q_{urine}, urine formation flow; GFR, glomerular filtration rate; i, the number of subsegment each segment is divided into.

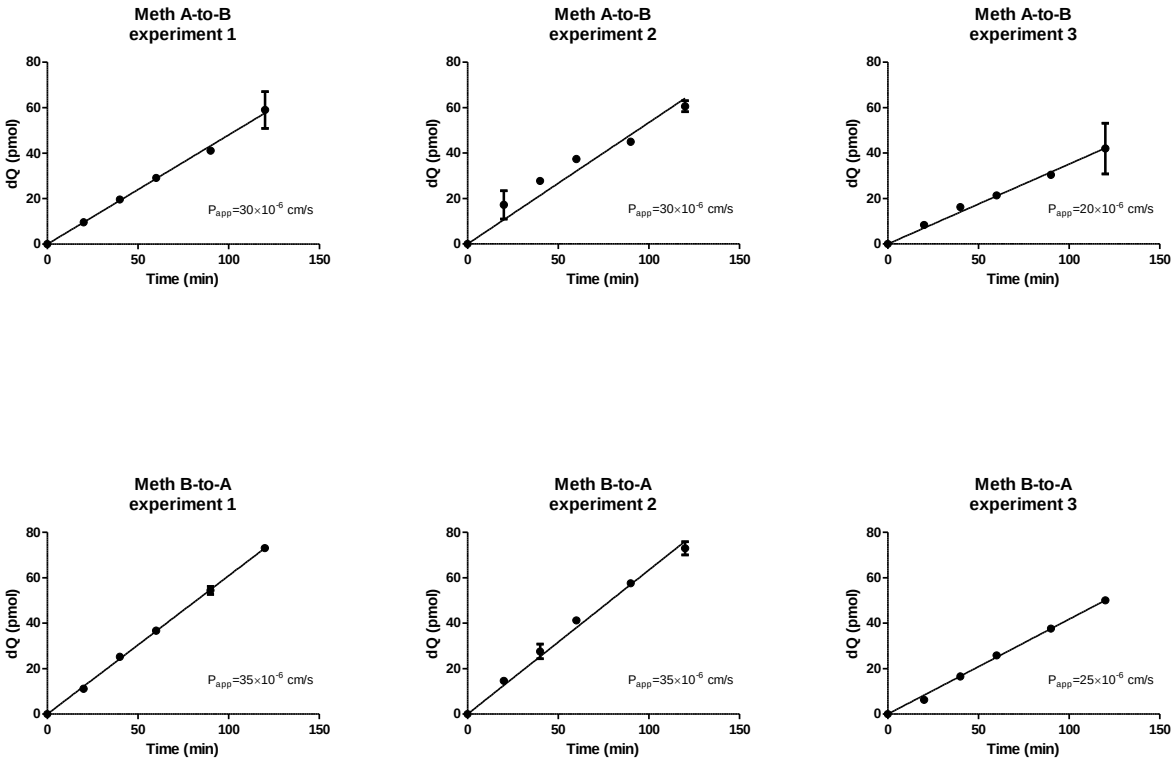

Figure 4.2. MDCK permeability for methamphetamine measured from both A-to-B side and B-to-A side on three different days.

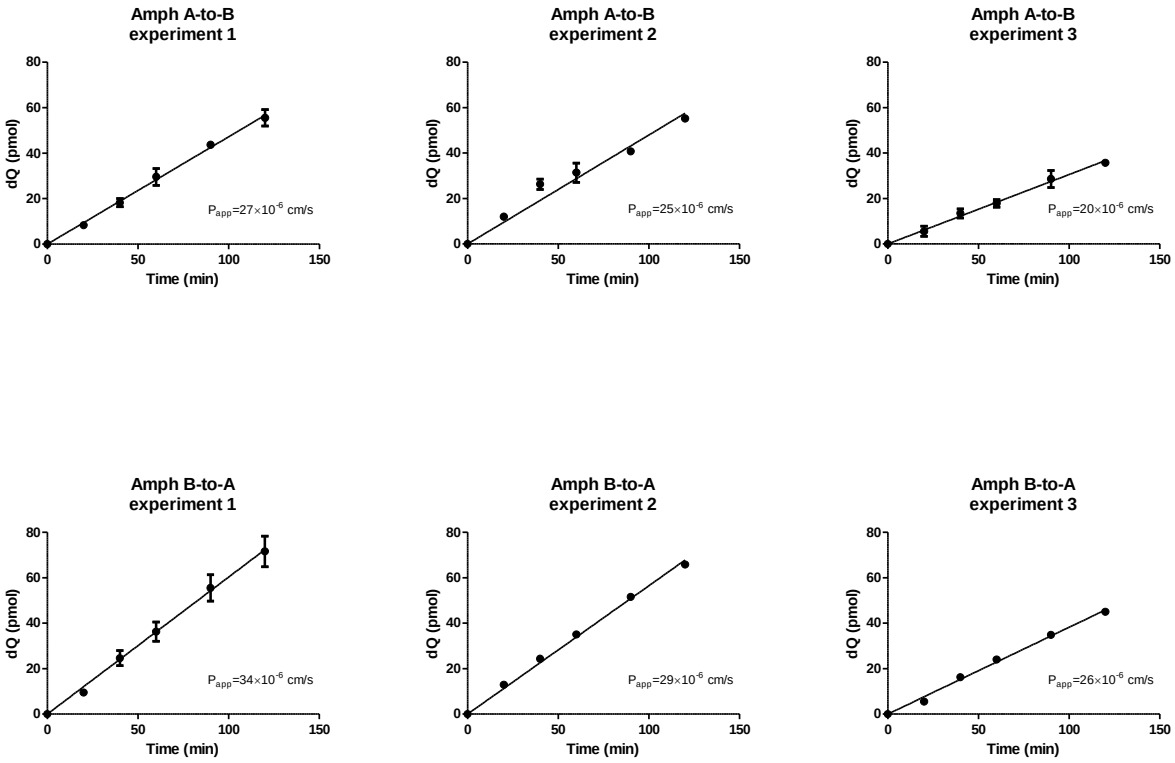

Figure 4.3. MDCK permeability for amphetamine measured from both A-to-B side and B-to-A side on three different days.

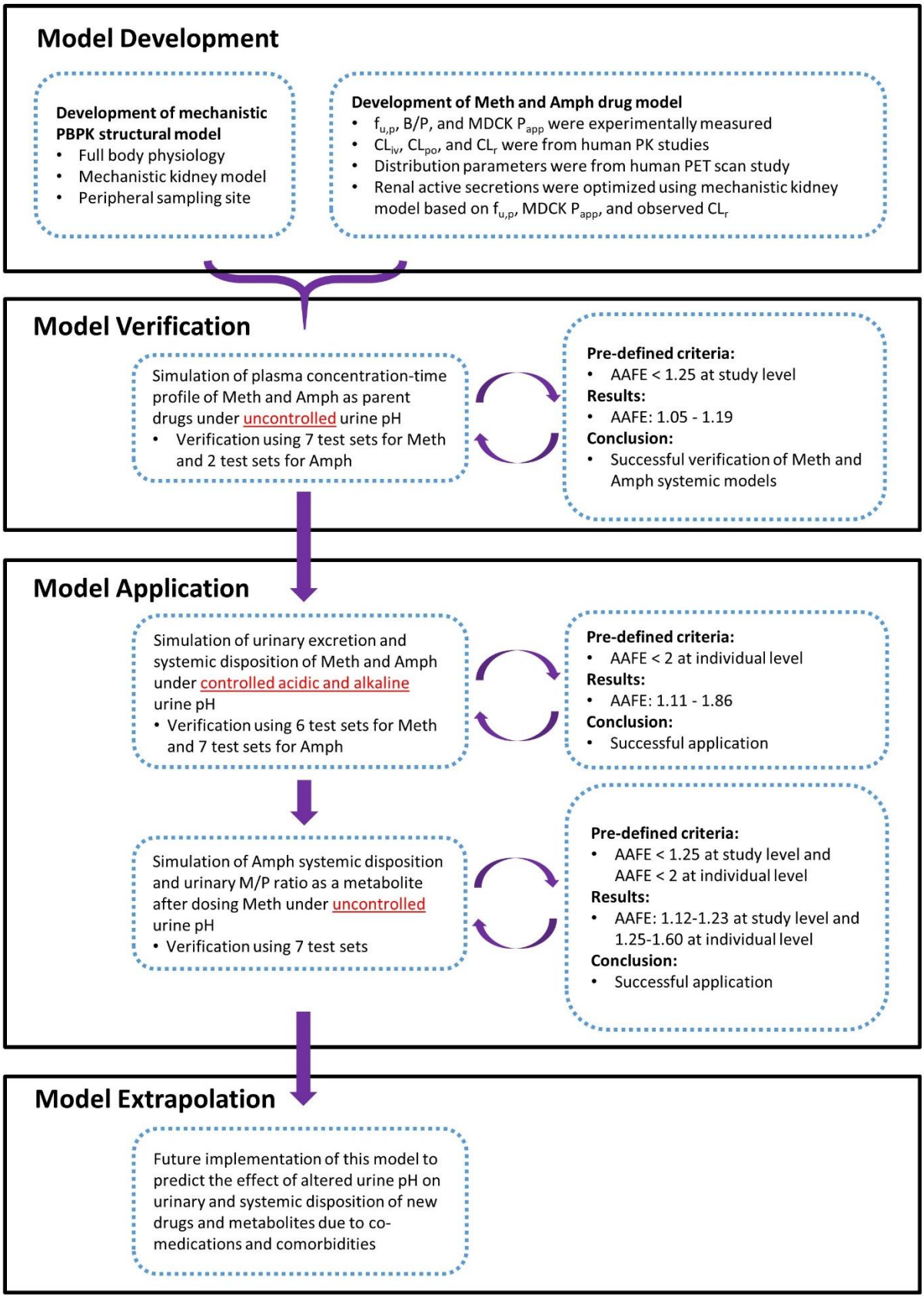
Model Development
Development of mechanistic PBPK structural model
• Full body physiology
• Mechanistic kidney model
• Peripheral sampling site
Development of Meth and Amph drug model
• $f_{u,p}$, B/P, and MDCK P_{app} were experimentally measured
• CL_{iv}, CL_{po}, and CL_r were from human PK studies
• Distribution parameters were from human PET scan study
• Renal active secretions were optimized using mechanistic kidney model based on $f_{u,p}$, MDCK P_{app}, and observed CL_r
Model Verification
Simulation of plasma concentration-time profile of Meth and Amph as parent drugs under uncontrolled urine pH
• Verification using 7 test sets for Meth and 2 test sets for Amph
Pre-defined criteria:
• AAFE < 1.25 at study level
Results:
• AAFE: 1.05 - 1.19
Conclusion:
• Successful verification of Meth and Amph systemic models
Model Application
Simulation of urinary excretion and systemic disposition of Meth and Amph under controlled acidic and alkaline urine pH
• Verification using 6 test sets for Meth and 7 test sets for Amph
Pre-defined criteria:
• AAFE < 2 at individual level
Results:
• AAFE: 1.11 - 1.86
Conclusion:
• Successful application
Simulation of Amph systemic disposition and urinary M/P ratio as a metabolite after dosing Meth under uncontrolled urine pH
• Verification using 7 test sets
Pre-defined criteria:
• AAFE < 1.25 at study level and AAFE < 2 at individual level
Results:
• AAFE: 1.12-1.23 at study level and 1.25-1.60 at individual level
Conclusion:
• Successful application
Model Extrapolation
Future implementation of this model to predict the effect of altered urine pH on urinary and systemic disposition of new drugs and metabolites due to co-medications and comorbidities

Figure 4.4. The overall workflow for developing and verifying the full body parent-metabolite PBPK model of methamphetamine and amphetamine for the simulation of urine pH-dependent systemic disposition and urinary excretion.

Meth, methamphetamine. Amph, amphetamine. fu,p, unbound fraction in plasma. B/P, blood-to-plasma ratio. MDCK, Madin-Darby canine kidney. Papp, experimentally determined apparent cellular permeability. CLiv, total body clearance measured after intravenous dosing. CLpo, total body clearance measured after oral dosing. CLr, renal clearance. PET, positron emission tomography. AAFE, absolute average fold error. M/P, metabolite-to-parent ratio.

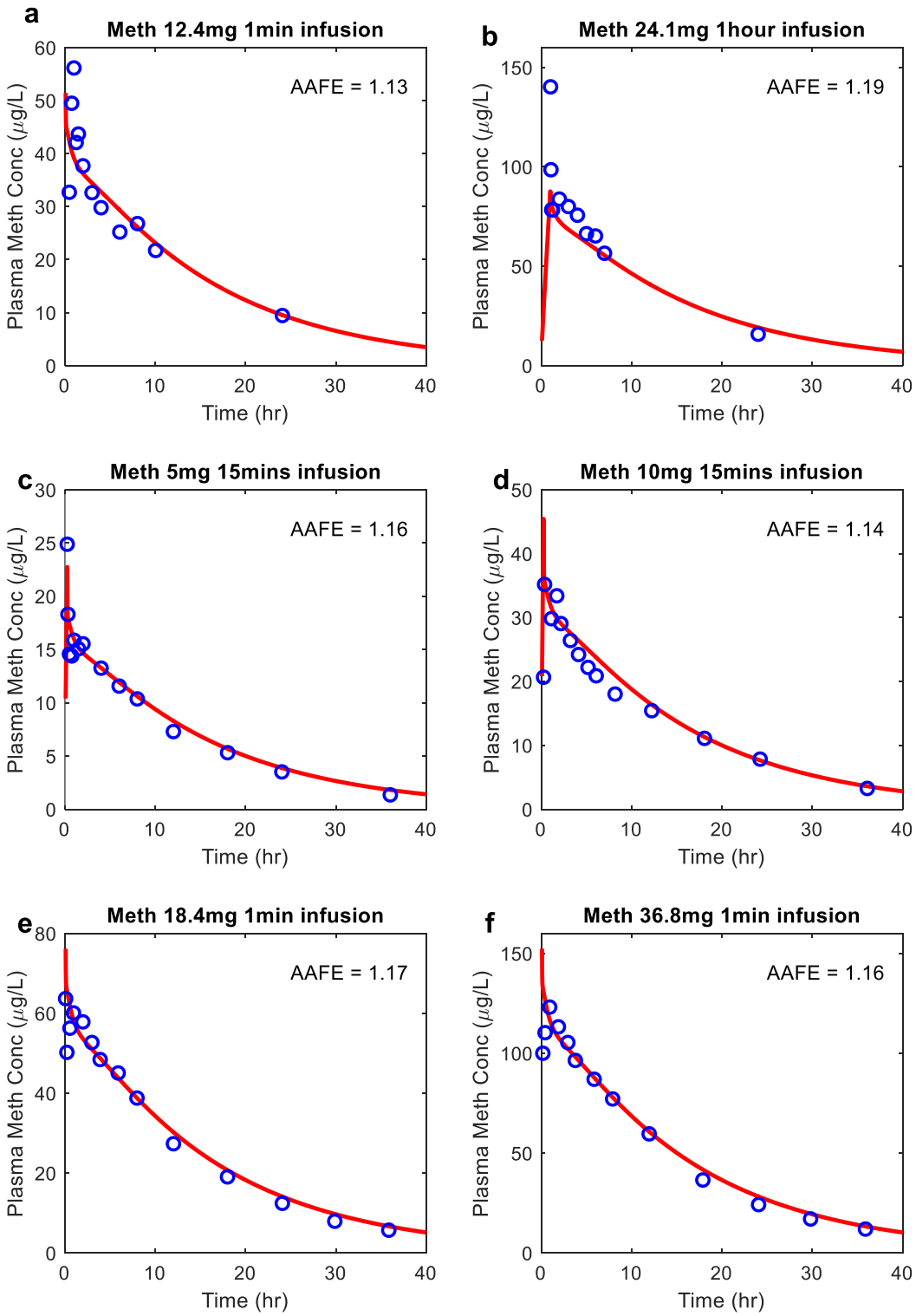
a
Meth 12.4mg 1min infusion
AAFE = 1.13
b
Meth 24.1mg 1hour infusion
AAFE = 1.19
c
Meth 5mg 15mins infusion
AAFE = 1.16
d
Meth 10mg 15mins infusion
AAFE = 1.14
e
Meth 18.4mg 1min infusion
AAFE = 1.17
f
Meth 36.8mg 1min infusion
AAFE = 1.16
Plasma Meth Conc (μg/L)
Time (hr)

Figure 4.5. Simulation of methamphetamine (Meth) plasma concentration-time profile after iv dosing.

Methamphetamine plasma concentration-time profiles were simulated after intravenous dosing and the simulated plasma concentrations (shown in red) were compared to the observed data (shown in blue) from 6 different test sets. The calculated AAFE value for each dataset is shown in each panel. The observed data for methamphetamine are from (a) (Cook *et al.*, 1993), (b) (Mendelson *et al.*, 1995), (c) (Harris *et al.*, 2003), (d) (Harris *et al.*, 2003), (e) (Mendelson *et al.*, 2006), and (f) (Mendelson *et al.*, 2006).

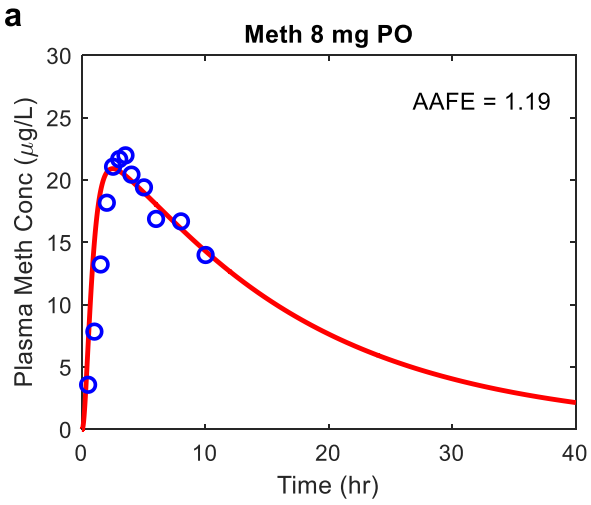
a
Meth 8 mg PO
AAFE = 1.19
Plasma Meth Conc (μg/L)
Time (hr)
0
5
10
15
20
25
30
0
10
20
30
40

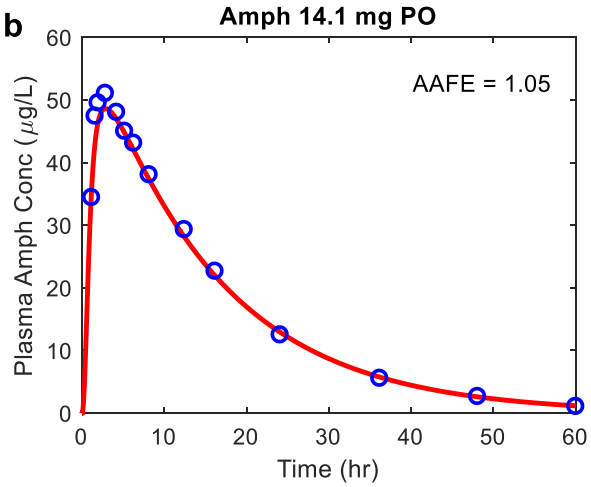
b
Amph 14.1 mg PO
AAFE = 1.05
Plasma Amph Conc (μg/L)
Time (hr)
0
10
20
30
40
50
60
0
10
20
30
40
50
60

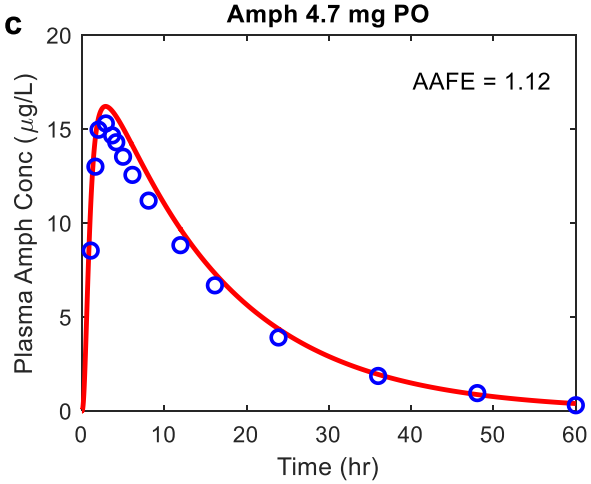
c
Amph 4.7 mg PO
AAFE = 1.12
Plasma Amph Conc (μg/L)
Time (hr)
0
5
10
15
20
0
10
20
30
40
50
60

Figure 4.6. Simulation of methamphetamine (Meth) and amphetamine (Amph) plasma concentration-time profiles after oral dosing.

Methamphetamine and amphetamine plasma concentration-time profiles were simulated after oral dosing and the simulated plasma concentrations (red lines) were compared to the observed data (blue circles) from 3 different test sets. The calculated AAFE value for each dataset is shown in each panel. The observed data for methamphetamine (a) are from (Perez-Reyes *et al.*, 1991), and the observed data for amphetamine (b and c) are from (CDER, 2002).

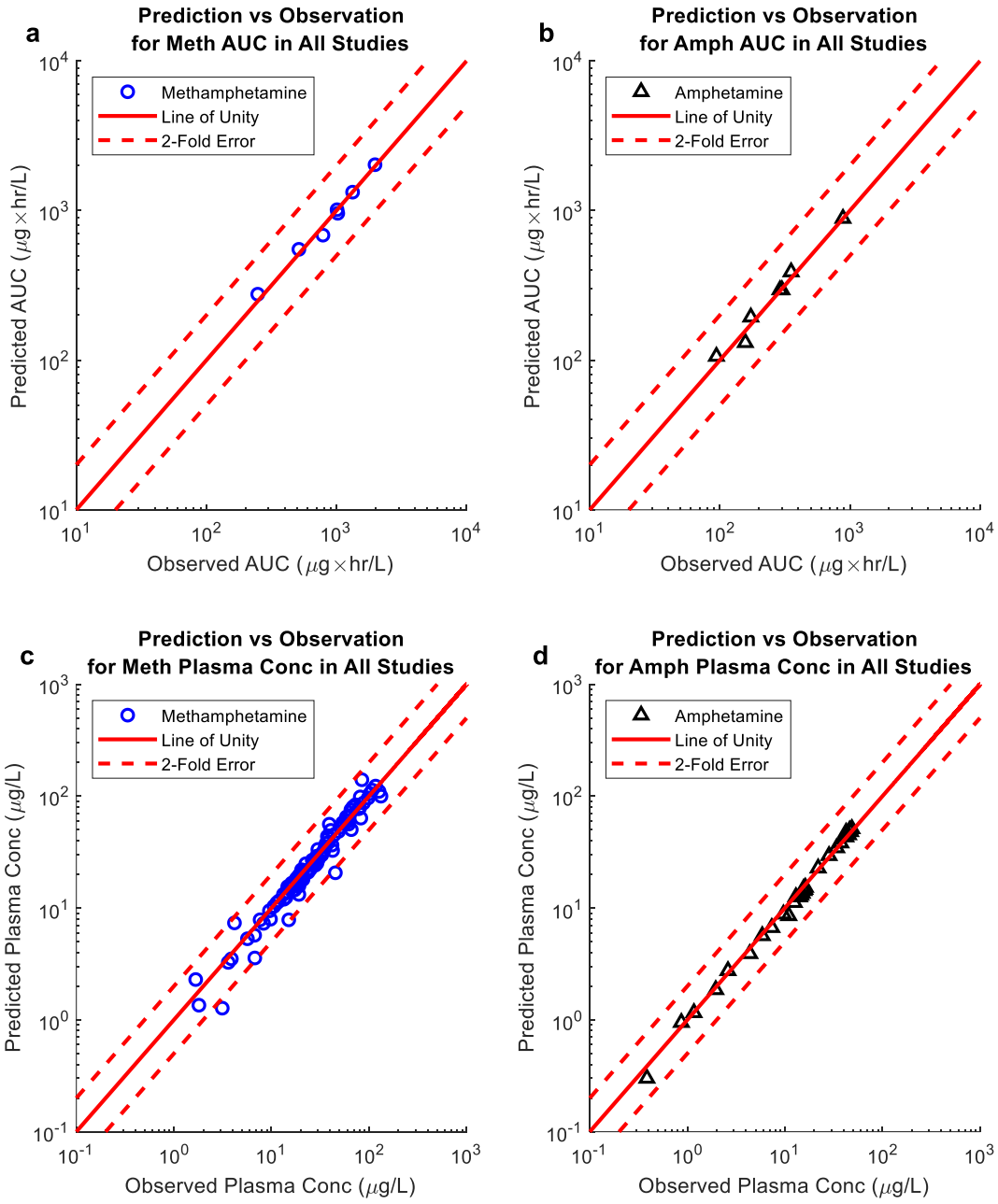
a
Prediction vs Observation
for Meth AUC in All Studies
Methamphetamine
Line of Unity
2-Fold Error
Predicted AUC (μg×hr/L)
Observed AUC (μg×hr/L)
b
Prediction vs Observation
for Amph AUC in All Studies
Amphetamine
Line of Unity
2-Fold Error
Predicted AUC (μg×hr/L)
Observed AUC (μg×hr/L)
c
Prediction vs Observation
for Meth Plasma Conc in All Studies
Methamphetamine
Line of Unity
2-Fold Error
Predicted Plasma Conc (μg/L)
Observed Plasma Conc (μg/L)
d
Prediction vs Observation
for Amph Plasma Conc in All Studies
Amphetamine
Line of Unity
2-Fold Error
Predicted Plasma Conc (μg/L)
Observed Plasma Conc (μg/L)

Figure 4.7. Comprehensive verification plot.

Plot of predicted versus observed plasma AUC (panel a and b) and plasma concentration (panel c and d) for methamphetamine (panel a and c) and amphetamine (panel b and d). Panels c and d contain all the mean plasma concentration data from clinical studies used in the model development and model verification, and include observed data points and simulation results from Figures 4.5 and 4.6.

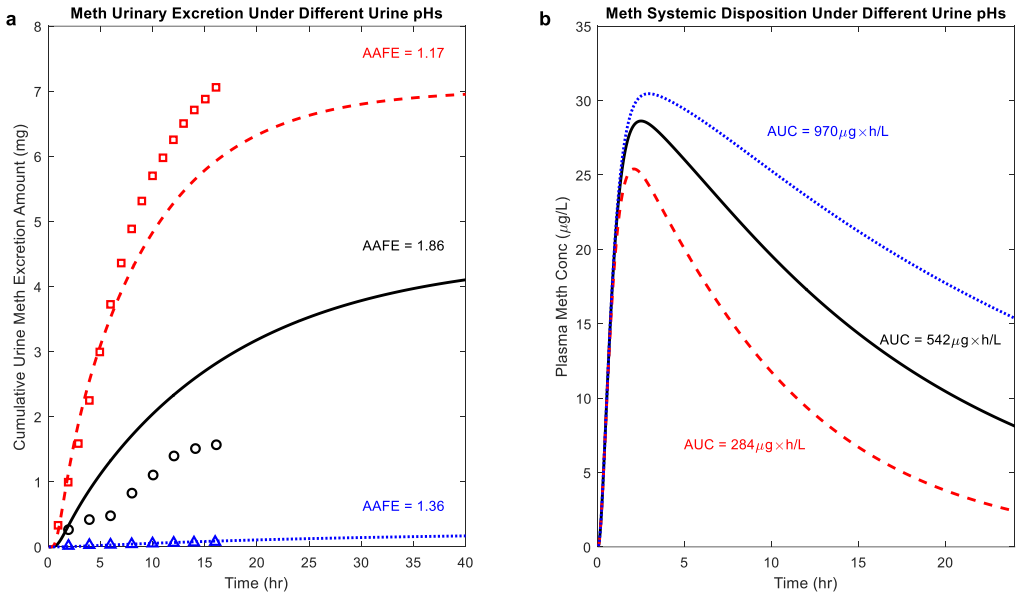

Figure 4.8. Simulation of the urine pH effect on methamphetamine urinary excretion and plasma concentration-time profile of methamphetamine (Meth).

Methamphetamine urinary excretion profiles (a) and plasma concentration-time profiles (b) were simulated after 11 mg methamphetamine oral administration under acidic urine pH condition (red dashed curves), uncontrolled urine pH condition (black solid curves), and alkaline urine pH condition (blue dotted curves). Simulated methamphetamine urinary excretion as a function of time was compared to observed data (N=1) under 3 different urine conditions (Beckett and Rowland, 1965c) shown in red squares (acidic urine), black circles (uncontrolled pH urine), and blue triangles (alkaline urine). The calculated AAFE values for all three urine conditions are shown in the insets.

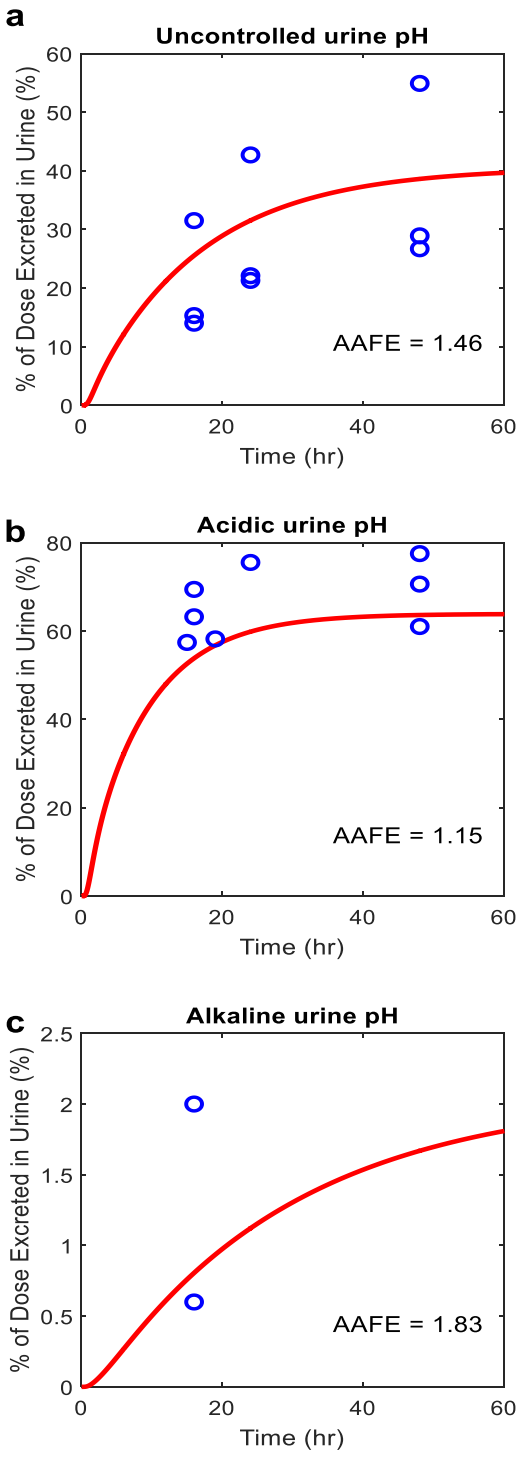
a
Uncontrolled urine pH
% of Dose Excreted in Urine (%)
Time (hr)
AAFE = 1.46
b
Acidic urine pH
% of Dose Excreted in Urine (%)
Time (hr)
AAFE = 1.15
c
Alkaline urine pH
% of Dose Excreted in Urine (%)
Time (hr)
AAFE = 1.83

Figure 4.9. Simulation of the urine pH effect on methamphetamine urinary excretion profile using stepwise pH gradient strategy (Table 4.3).

Cumulative percent dose excreted in urine as methamphetamine as a function of time was simulated after 11 mg methamphetamine oral administration under uncontrolled urine pH condition (panel a), acid urine pH condition (panel b), and alkaline urine pH condition (panel c), and compared to observed data (Beckett and Rowland, 1965) shown in the blue circles. The calculated AAFE values for each dataset are shown in the insets.

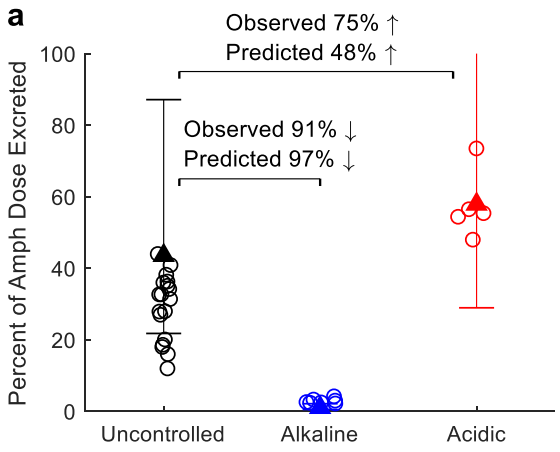
a
Observed 75% ↑
Predicted 48% ↑
Observed 91% ↓
Predicted 97% ↓
Percent of Amph Dose Excreted
100
80
60
40
20
0
Uncontrolled
Alkaline
Acidic

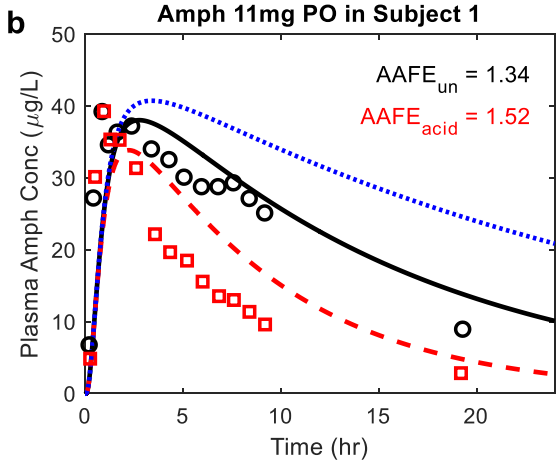
b
Amph 11mg PO in Subject 1
AAFE$_{un}$ = 1.34
AAFE$_{acid}$ = 1.52
Plasma Amph Conc (μg/L)
50
40
30
20
10
0
0
5
10
15
20
Time (hr)

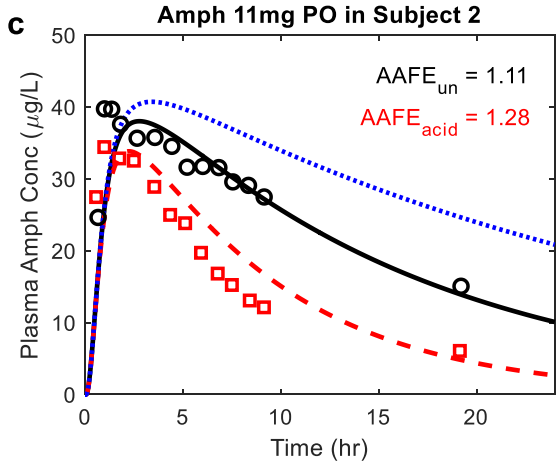
c
Amph 11mg PO in Subject 2
AAFE$_{un}$ = 1.11
AAFE$_{acid}$ = 1.28
Plasma Amph Conc (μg/L)
50
40
30
20
10
0
0
5
10
15
20
Time (hr)

Figure 4.10. Simulation of the effect of urine pH on the urinary excretion and plasma concentration-time profile of amphetamine.

Amphetamine urinary excretion over 48 hours (uncontrolled urine pH shown in black), 16 hours (alkaline urine pH shown in blue), and 16 hours (acidic urine pH shown in red) was simulated after 11 mg amphetamine oral administration (a). The observed individual data of amphetamine excretion are shown in circles (Beckett and Rowland, 1965a). The mean simulated amount (as percent of dose) of amphetamine excreted in urine under each urine pH condition is shown in triangles with 2-fold error bars. Simulated (curves) amphetamine plasma concentration-time profiles (b and c) are shown in comparison to the observed (open symbols, (Beckett *et al.*, 1969)) data in two individual subjects under uncontrolled urine pH (black symbols and solid curve), acidic urine pH (red symbols and dashed curve), and alkaline urine pH (blue dotted curve) after 11 mg oral administration of amphetamine. The calculated AAFE values for each individual subject are shown. $AAFE_{un}$ represents the calculated AAFE comparing simulated and observed amphetamine plasma concentrations under uncontrolled urine pH. $AAFE_{acid}$ represents the calculated AAFE comparing simulated and observed amphetamine plasma concentrations under acidic urine pH.

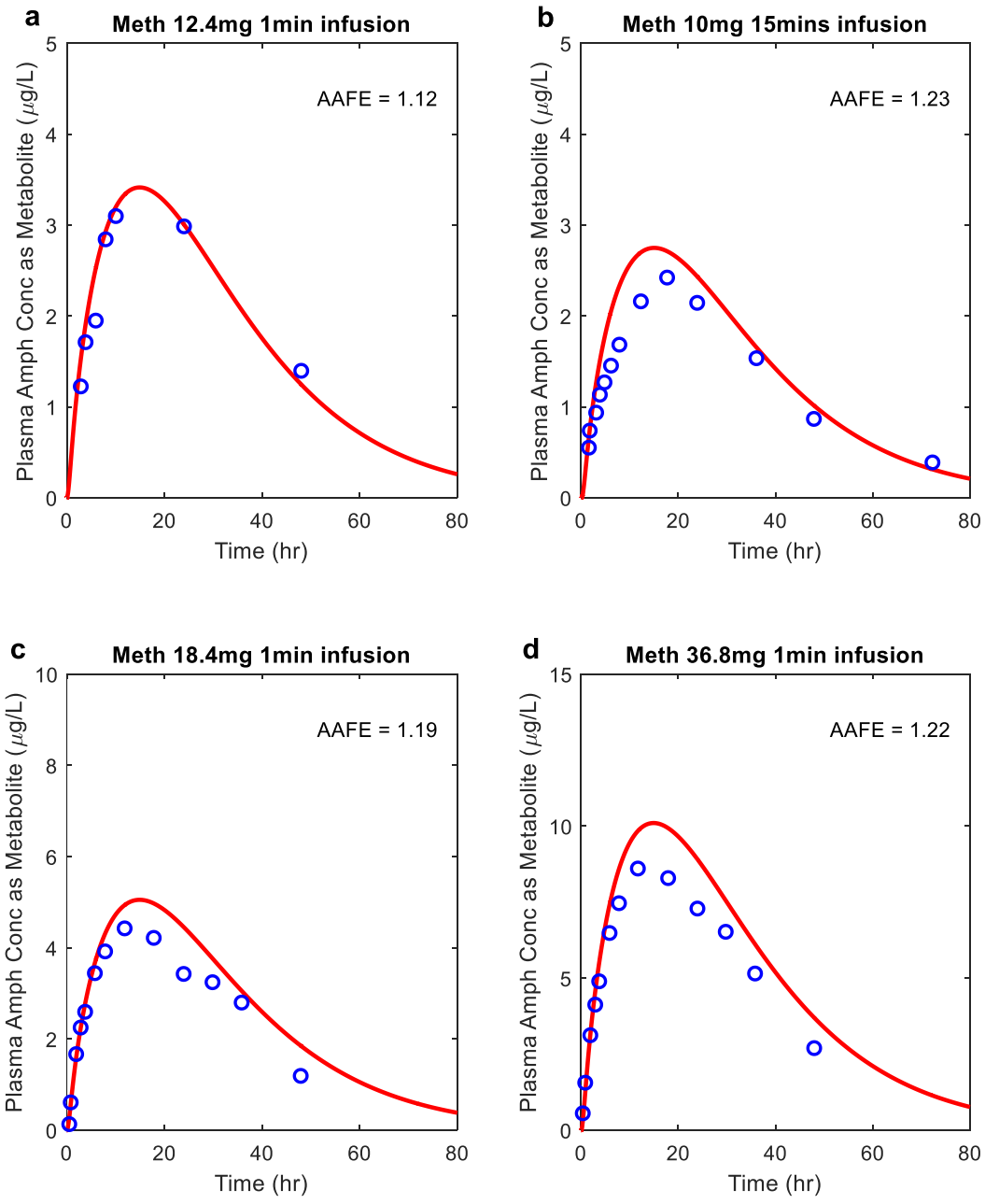
a
Meth 12.4mg 1min infusion
AAFE = 1.12
Plasma Amph Conc as Metabolite (μg/L)
Time (hr)
b
Meth 10mg 15mins infusion
AAFE = 1.23
Plasma Amph Conc as Metabolite (μg/L)
Time (hr)
c
Meth 18.4mg 1min infusion
AAFE = 1.19
Plasma Amph Conc as Metabolite (μg/L)
Time (hr)
d
Meth 36.8mg 1min infusion
AAFE = 1.22
Plasma Amph Conc as Metabolite (μg/L)
Time (hr)

Figure 4.11. Simulation of plasma amphetamine concentration-time profile as a metabolite after iv dosing of methamphetamine.

Amphetamine plasma concentration-time profiles were simulated (shown in red curves) as the metabolite of methamphetamine after iv dosing of methamphetamine and compared to the observed data (shown in blue circles) from 4 test sets. The calculated AAFE values were all within the 0.8-to-1.25-fold range. The observed data of amphetamine are from (a) (Cook *et al.*, 1993), (b) (Harris *et al.*, 2003), (c) (Mendelson *et al.*, 2006), (d) (Mendelson *et al.*, 2006).

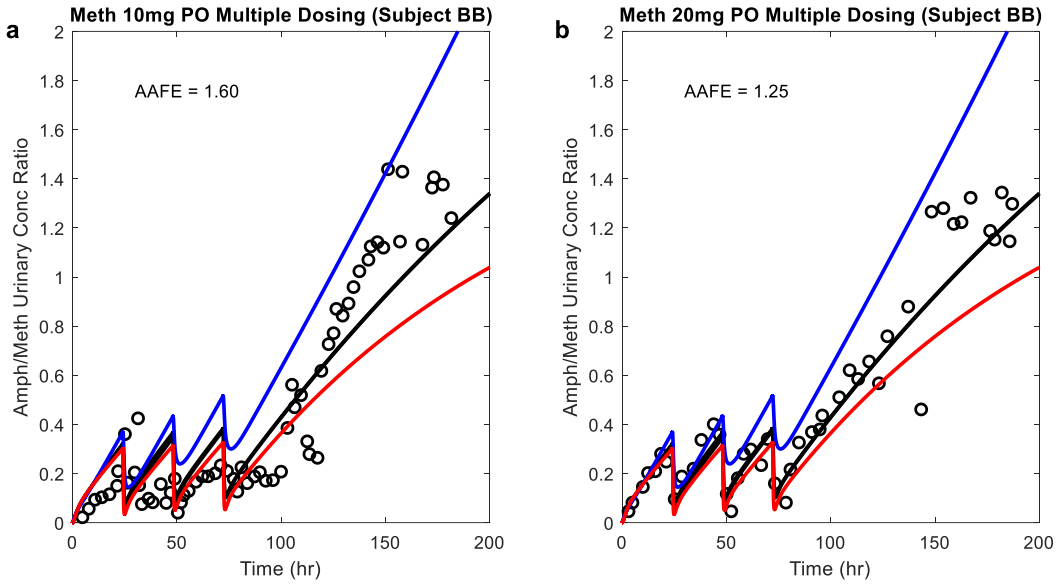

Figure 4.12. Simulation of the time course of metabolite to parent (amphetamine/methamphetamine) urinary concentration ratio after multiple oral doses of methamphetamine.

Amphetamine/methamphetamine urinary ratio was simulated under acidic urine pH condition (red curves), uncontrolled urine pH condition (black curve), and alkaline urine pH condition (blue curve) after 4 consecutive oral doses of methamphetamine and compared to the observed urinary ratio (black circles) from 2 test sets (Oyler *et al.*, 2002) with 10 mg dose (panel a) and 20 mg dose (panel b) under uncontrolled urine pH condition. The calculated AAFE values comparing simulation and observation under uncontrolled urine pH condition are shown in insets.

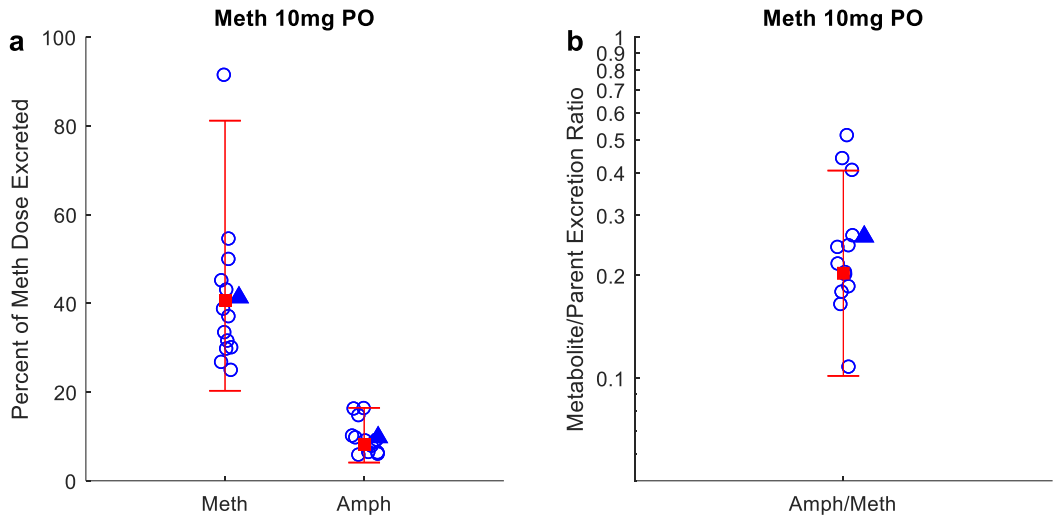

Figure 4.13. Simulation of the amount of methamphetamine and its metabolite amphetamine excretion into urine (as a percent of methamphetamine dose) after multiple oral dosing of methamphetamine.

Panel (a) shows the simulated fraction (in red square with two-fold error bars) of methamphetamine dose excreted into urine as methamphetamine and amphetamine (expressed as a percent of methamphetamine dose) after 4 oral doses of 10 mg methamphetamine and assuming urine pH of 6.5 to mimic uncontrolled urine pH. The simulated Amph/Meth urinary excretion ratio (in red square with two-fold error bars) based on the data presented in (a) is shown in panel (b). The observed data (Kim *et al.*, 2004) for individual subjects are shown in blue circles and observed means are shown in blue triangles.

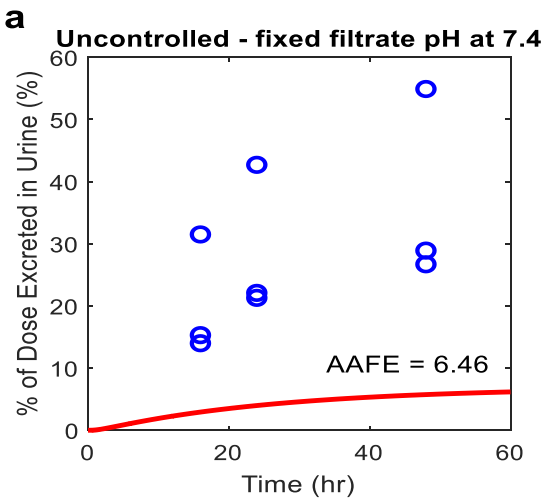
a
Uncontrolled - fixed filtrate pH at 7.4
% of Dose Excreted in Urine (%)
Time (hr)
AAFE = 6.46

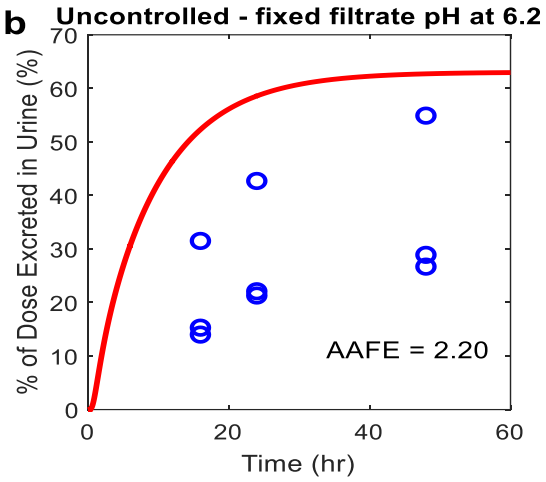
b
Uncontrolled - fixed filtrate pH at 6.2
% of Dose Excreted in Urine (%)
Time (hr)
AAFE = 2.20

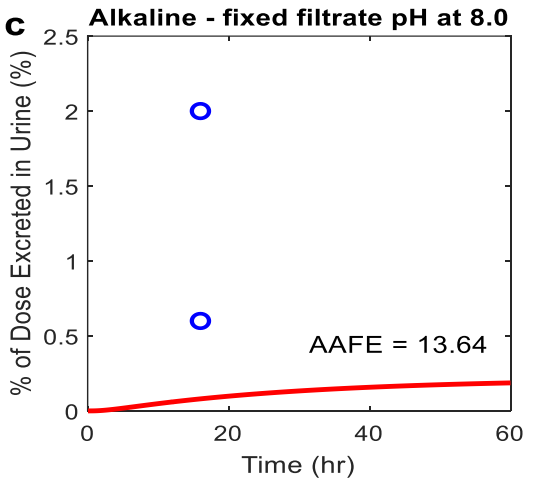
c
Alkaline - fixed filtrate pH at 8.0
% of Dose Excreted in Urine (%)
Time (hr)
AAFE = 13.64

Figure 4.14. Simulation of the urine pH effect on methamphetamine urinary excretion profile using previously published fixed pH strategy (Matsuzaki *et al.*, 2019).

Cumulative percent sdose excreted in urine as methamphetamine as a function of time was simulated after 11 mg methamphetamine oral administration under uncontrolled urine pH condition (panel a and b) using a fixed tubular filtrate pH value of 7.4 (panel a), a fixed tubular filtrate pH value of 6.2 (panel b), and alkaline urine pH condition using a fixed tubular filtrate pH value of 8.0 (panel c), and compared to observed data (Beckett and Rowland, 1965) shown in the blue circles. The calculated AAFE values for each dataset are shown in the insets. Except for the pH gradient all other parameters are identical to Figure 4.9.

Chapter 5. NOVEL MECHANISTIC PBPK MODEL TO PREDICT RENAL CLEARANCE IN VARYING STAGES OF CKD BY INCORPORATING TUBULAR ADAPTATION AND DYNAMIC PASSIVE REABSORPTION

This chapter was submitted to *CPT: Pharmacometrics & Systems Pharmacology on May 15th 2020*

5.1 Abstract

Chronic kidney disease (CKD) exhibits significant effects on the renal clearance (CL_r) of drugs. Physiologically-based pharmacokinetic (PBPK) models were recently used to specifically predict CKD effects on transporter-mediated renal active secretion and CL_r for hydrophilic nonpermeable compounds. However, no study has shown systematic PBPK modeling of renal passive reabsorption or CL_r for hydrophobic permeable drugs in CKD. Our analyses unequivocally show a dramatic nonlinear effect of CKD on renal passive reabsorption for permeable drugs, resulting in an over 7-fold error if using a proportional GFR scaling/reduction approach to predict CL_r in CKD. Thus, our goal was to expand our previously developed and verified mechanistic kidney model to incorporate the physiologically-based tubular changes of reduced water reabsorption/increased tubular filtrate flow per remaining functional nephron in CKD, and use the final adaptive kidney model to predict renal passive reabsorption and CL_r across varying degrees of renal impairment. Our results show that this adaptive kidney model successfully (absolute-fold-error (AFE) all<2) predicted CL_r of 20 permeable and nonpermeable test compounds with differing physicochemical properties in all stages of CKD without any optimization/empirical scaling. In contrast, proportional GFR reduction approach generated unacceptable CL_r predictions (AFE=2.61-7.35) in severe CKD. Finally, the adaptive kidney model accurately predicted CL_r of PAH and memantine (two secreted compounds) in CKD, suggesting successful integration of active secretion into the model, along with passive reabsorption. Together, our novel adaptive kidney model captures physiologically-based tubular changes in CKD, enabling successful translation from *in vitro* plasma unbound fraction and permeability estimates into *in vivo* CL_r throughout CKD progression.

5.2 Introduction

Chronic kidney disease (CKD) is a progressive illness that is pathologically heterogeneous (Levey and Coresh, 2012) and systemic (Zoccali *et al.*, 2017). It is mainly characterized by declining functional nephron mass and glomerular filtration rate (GFR) (Bricker *et al.*, 1960). As such, GFR is a critical index for CKD diagnosis, progression, and classification (KDIGO, 2013). Clinically, patients with severe (stage 4, GFR~15-29 mL/min) and end stage (stage 5, GFR<15 mL/min) CKD are at high risk for comorbidities, polypharmacy, and adverse drug reactions (Thomas *et al.*, 2008; Chapin *et al.*, 2010; Secora *et al.*, 2018; Schmidt *et al.*, 2019), necessitating careful medication management due to dramatically altered pharmacokinetics (PK) associated with CKD. As a result, clinical characterization of drug disposition in CKD patients is critically important. Prior to dedicated renal impairment studies during drug development, predicting the disease effects on drug PK and estimating the optimal dosing regimen is challenging and often unreliable. Empirically, for highly renally eliminated drugs, the optimal regimen can be estimated by reducing the dosage proportionally with the estimated (Cockcroft and Gault, 1976; Levey *et al.*, 2009) GFR lost in target patient population. This assumes all renal drug handling pathways and therefore renal clearance (CL_r) decrease proportionally with filtration. Indeed, this proportional assumption is supported by clinical data for multiple predominantly filtered drugs (Blair *et al.*, 1981; Blum *et al.*, 1994) without significant secretion or reabsorption.

However, for highly renally secreted drugs, CL_r may decrease more than proportionally with GFR in stage 4/5 CKD (Hsueh *et al.*, 2016; Chapron *et al.*, 2017), possibly due to inhibition of renal transporters by accumulated uremic solutes. Further, for highly renally reabsorbed drugs, CL_r can decrease less than proportionally with GFR in stage 4/5 CKD (Welling *et al.*, 1975;

Houghton *et al.*, 1985; Montay *et al.*, 1985). Together, observed clinical data consistently show that empirical/proportional GFR scaling approach may not accurately predict CL_r in severe CKD due to the multiplicity and convoluted interaction of disease effects on renal drug handling. To overcome this challenge, physiologically-based pharmacokinetic (PBPK) models that capture the disease-specific characteristics are potentially able to predict CKD effects on drug PK, although such practice is currently considered as low-confidence application by regulatory agencies (Grimstein *et al.*, 2019; US Food and Drug Administration (FDA)., 2019). Recently, PBPK modeling has been used to specifically predict the CKD effect on renal active secretion (Hsu *et al.*, 2014; Hsueh *et al.*, 2018; Yee *et al.*, 2018), but the test drugs used for model verification all lack significant permeability and hence passive reabsorption. At present, no PBPK model could quantitatively predict the alterations in renal passive reabsorption or CL_r for highly reabsorbed drugs in CKD, let alone systematically capture the diverse effects of CKD on renal elimination. Physiologically, CKD patients showed reduced water reabsorption/increased tubular filtrate flows per remaining functional nephron (Lindberg *et al.*, 1966; Sharpstone, 1969; Welling *et al.*, 1973, 1975; Yeh *et al.*, 1975; Fukuda *et al.*, 2006; Nechita *et al.*, 2015) as an adaptation mechanism. This is to adjust for the reduced number of functional nephrons and reduced GFR, to maintain critical homeostasis such as extracellular fluid volume and plasma sodium concentration (Biber *et al.*, 1968; McNay and Miyazaki, 1973; Yeh *et al.*, 1975; Pennell and Bourgoignie, 1981; Fukuda *et al.*, 2006). We hypothesized that such physiological adaptation in renal tubular water reabsorption and tubular filtrate flow will dramatically decrease the drug concentration gradient between intratubular filtrate and peritubular blood, leading to reduced passive reabsorption and higher CL_r than expected from residual GFR alone in CKD. Indeed, this hypothesis is supported by observed data (Welling *et al.*, 1975; Houghton *et al.*, 1985; Montay *et*

al., 1985) for various permeable drugs such as pefloxacin, metronidazole, and minocycline. For these drugs, the observed CL_r in CKD patients were reduced to 30-37% of healthy when residual GFR were only 4-9% of healthy (Welling *et al.*, 1975; Houghton *et al.*, 1985; Montay *et al.*, 1985), demonstrating an over 7-fold disproportionality between resulting CL_r and GFR.

To simulate the CKD effect on tubular passive reabsorption, we expand our previously developed and verified mechanistic kidney model (Huang and Isoherranen, 2018) to incorporate the physiologically-based tubular changes of reduced water reabsorption/increased tubular filtrate flow per remaining functional nephron for each renal subsegment across varying CKD stages. The final adaptive kidney model enables the translation from *in vitro* drug permeability into degree of passive reabsorption and renal clearance value and was validated using a set of 20 compounds with differing properties without any optimization or empirical scaling throughout the progression of CKD from healthy to the end stage.

5.3 Methods

5.3.1 Development and sensitivity analyses of proportional model and novel adaptive kidney model for CKD

Two distinct kidney disease models were built using MATLAB and Simulink platform (R2018a; MathWorks, Natick, MA) to predict CL_r in patients with different stages of CKD. Both models were established based on our previously published and verified physiologically-based mechanistic kidney model(Huang and Isoherranen, 2018) for healthy humans, but with modified system parameters to reflect physiological changes in CKD. The first model, a proportional model, was built assuming all functions of the nephron, all pathways of renal drug handling, and therefore the values of CL_r decline proportionately with GFR. The second model, an adaptive model, was built by accounting for the tubular adaptation of reducing water reabsorption/increasing water excretion per remaining functional nephron, as observed in many CKD patients (Lindberg *et al.*, 1966; Sharpstone, 1969; Welling *et al.*, 1973, 1975; Yeh *et al.*, 1975; Fukuda *et al.*, 2006; Nechita *et al.*, 2015). In both models, all of the volume (n=33), surface area (n=22), peritubular renal blood flow (n=12), basolateral uptake clearance (n=3) and apical efflux clearance (n=3) parameters were reduced proportionally with GFR by multiplying the baseline parameters in healthy subjects by the fraction of GFR remaining (ratio of GFR_i in a specific CKD $stage_i$ over 120 mL/min, the healthy GFR). The major distinction between the proportional and adaptive models is the parameterization of renal tubular filtrate flow (TFF) in CKD patients. In the proportional model, all TFF parameters were decreased proportionally with GFR, as for other model parameters. In contrast, the adaptive model incorporates the physiologically-based adaptation of tubular water reabsorption in CKD patients to parameterize TFF and therefore TFF decreases less than proportionally in relation to GFR. Quantitatively, a set of tubular subsegment-specific adaptation

factor (AF_i) was calculated based on reported mean urine formation of 0.62 mL/min (62% of healthy urine flow) in CKD patients (n=216) with a mean GFR of 10 mL/min (8.3% of healthy GFR) (Nechita *et al.*, 2015). Physiologically and mathematically, the magnitude of adaptation of TFF in CKD patients must be different in different tubular subsegments. The inflow of the first subsegment of the proximal tubule must equal GFR and as such must decline proportionally with GFR. Similarly, the outflow of the last subsegment of the collecting duct must match the observed urine flow in CKD patients and hence decline much less than GFR. For example, at a GFR of 10 mL/min, the observed urine flow is 7.5-fold higher than what would be expected from the change in GFR (Nechita *et al.*, 2015). Based on these boundaries, the tubular subsegment-specific AF (AF_i) for each TFF was calculated using Equation 1:

$$Adaptation\ Factor_i\ (AF_i) = min + \frac{max - min}{1+10^{n(Log_{10}TFF_{i,H}-1)}} \quad (1)$$

where min represents the minimum adaptation capacity of 0, max represents the maximum adaptation capacity of 0.57, n is analogous to Hill coefficient which was set at 1.80. $TFF_{i,H}$ represents the individual value of renal tubular filtrate flow entering each tubular subsegment (including bladder) in healthy subjects (i.e. GFR = 120 mL/min) where i ranges from 1 to 12 and H stands for healthy state.

To incorporate the calculated AF_i into the subsegment-specific TFF at a given GFR (GFR_j), a scalar was defined using Equation 2:

$$Scalar_{ij} = 1 - (1 - \frac{GFR_j}{120}) \times (1 - AF_i) \quad (2)$$

where GFR_j represents the specific GFR value (mL/min) of CKD patients of interest (j ranges from 5 to 120 mL/min), $GFR_j/120$ represents the remaining renal function in specific CKD patients, and AF_i is the subsegment-dependent adaptation factor as defined by Equation 1.

Finally, the $TFF_{ij,CKD}$ for each tubular subsegment (i ranges from 1 to 12) at different stages of CKD (j ranges from 5 mL/min to 120 mL/min) was calculated using Equation 3:

$$TFF_{ij,CKD} = TFF_{i,H} \times Scalar_{ij} \quad (3)$$

where $TFF_{i,H}$ represents renal tubular filtrate flow entering each tubular subsegment (including bladder) in healthy subjects and the $Scalar_{ij}$ is defined by Equation 2. The full set of calculated AF values and representative TFF values are shown in Table 5.1 and Table 5.2. Each GFR input value results in a different set of TFF values for all 12 subsegments, producing a unique CKD stage-specific kidney model that describes the diseased renal tubular system at that level of renal impairment.

To ensure model integrity and evaluate sensitivities of CL_r to drug properties and physiological parameters, five sets of local sensitivity analyses were conducted to evaluate the impact of drug permeability (P_{app} = 1-100×10^{-6} cm/s), plasma unbound fraction ($f_{u,p}$=0.1-1), peritubular renal blood flow (300-1000 mL/min), unbound intrinsic basolateral uptake transport clearance (CL_{uptake} = 10-3000 mL/min), and unbound intrinsic apical efflux transport clearance (CL_{efflux} = 10-3000 mL/min) on simulated CL_r using both proportional and adaptive models across varying levels of renal impairment.

5.3.2 Prediction of CL_r for 20 test compounds in varying stages of CKD using proportional model and novel adaptive kidney model

To assess the performance of the proportional and adaptive models in predicting CL_r with declining GFR, the CL_r of 20 test compounds were simulated and compared to the observed values. The 20 test compounds included three parent-metabolite pairs, six nonpermeable drugs, six highly permeable drugs, all of which lacked significant secretion (CL_r < 1.25×$f_{u,p}$GFR, Table 5.3) and

two renally secreted compounds. All the permeable non-secreted drugs are highly renally reabsorbed ($1-CL_r/(f_{u,p}\times GFR)$ ~ 72% to 97%, Table 5.3). The collected pK_a values, *in vitro* permeability data, $f_{u,p}$, and observed CL_r values in healthy subjects and stage4/5 CKD patients are summarized in Table 5.3. Overall, the 20 test compounds had a wide range of pK_a values (2.9-11.5), *in vitro* permeabilities ($0.1\text{-}120\times10^{-6}$ cm/s), $f_{u,p}$ (0.05-1), and CL_r in healthy subjects (0.42-599 mL/min) and in patients with CKD stage 4/5 (0.19-76.4 mL/min), providing a robust dataset to verify the new adaptive model and to differentiate the performance of the adaptive and proportional models.

Renal clearances of all 20 test compounds were simulated as described before (Huang and Isoherranen, 2018) using both proportional and adaptive models with GFR input value decreasing from 120 mL/min to 5 mL/min with a decrement of 1 mL/min. Plasma unbound fraction and permeability were compound-specific input parameters and uptake/efflux transport clearances were set as 0 for all test compounds except para-aminohippuric acid (PAH) and memantine, for which previously published transport clearance values(Huang and Isoherranen, 2018) were used. The simulated CL_r using both proportional and adaptive models were compared to the observed values at different stages of CKD. To quantitatively evaluate the performance of proportional and adaptive models, absolute fold error (AFE) (Equation 4) between the simulated and observed mean CL_r in severe/end stage (i.e. stage 4/5) of CKD patients along with a 2-fold acceptance criterion was used.

$$AFE = 10^{\left|log_{10}\frac{Simulated\ Mean}{Observed\ Mean}\right|} \quad (4)$$

5.4 Results

5.4.1 Development of proportional model and novel adaptive kidney model for CKD

To predict CL_r of drugs in CKD patients, the proportional and adaptive models were developed and tested. In the proportional model, all TFF are reduced proportionally with GFR (Figure 5.1) resulting in a predicted urine flow that is reduced by same percentage as GFR. For a GFR of 10 mL/min (91.7% decrease from 120 mL/min), the proportional model predicts a urine flow of 0.083 mL/min, which is 87% lower than the observed urine flow of 0.6 mL/min (Nechita *et al.*, 2015). In contrast, in the adaptive model, the TFF values are reduced (Equation 3) by scalars (Equation 2) defined by the remaining GFR and the adaptation factors (Equation 1), resulting in a urine flow of 0.6 mL/min (Figure 5.1) when GFR = 10 mL/min, better matching the observed data (Nechita *et al.*, 2015). This suggests that the adaptive model successfully captures the physiological changes in renal tubules of remaining functional nephrons in CKD patients. Table 5.1 summarizes the representative TFF predicted using both adaptive and proportional models at GFRs of 80 mL/min, 40 mL/min, 20 mL/min, and 5 mL/min. At mild CKD (GFR = 80 mL/min), the difference of TFF values between proportional and adaptive models was small, with a maximum of 28% difference in the final urine flow. However, the difference in urine flow between proportional and adaptive models increased with declining GFR reaching a ~200% difference in moderate CKD (GFR = 40 mL/min), ~400% difference in severe CKD (GFR = 20 mL/min), and ~1,400% difference in the end stage CKD (GFR = 5 mL/min).

5.4.2 Sensitivity analyses of proportional model and novel adaptive kidney model for CKD

To further test which drug- or system-specific parameters impact the CL_r predictions across varying levels of renal impairment, sensitivity analyses were conducted to examine the effects of drug permeability, $f_{u,p}$ and peritubular renal blood flow. For the proportional model, the decrease in CL_r with decreasing GFR was unaffected by drug permebility (Figure 5.2a), while for the adaptive model the decrease in CL_r with decreasing GFR was highly sensitive to drug premeability (Figure 5.2b). Using the adaptive model, when GFR decreased by 96% to 5 mL/min, the simulated CL_r for drugs with low permeability (e.g. 1×10^{-6} cm/s) also decreased by 96%, while the simulated CL_r for drugs with high permeability (e.g. 100×10^{-6} cm/s) only decreased by 32%, resulting in dramatic difference in the predicted effect of CKD on CL_r (Figure 5.2b). Overall, the adaptive model predicts dramatically different effects of CKD on CL_r than the proportional model for drugs with moderate to high permeability ($>10\times10^{-6}$ cm/s) in severe/end stage CKD (GFR<30 mL/min) (Figure 5.2c). As expected, $f_{u,p}$ correlated negatively with simulated CL_r (Figure 5.2d and e), and had no impact on the difference in simulated CL_r between proportional and adaptive models (Figure 5.2f). Further, peritubular renal blood flow had no effect on simulated CL_r regardless of CKD stage in both proportional and adaptive models for non-secreted drugs (Figure 5.2g-i).

5.4.3 Prediction of CL_r for non-secreted compounds in varying stages of CKD and verification of adaptive kidney model

To verify the adaptive model for different stages of CKD, the CL_r of 18 non-secreted compounds at different stages of CKD (GFR 120 mL/min to 5 mL/min) were predicted and compared to observed CL_r. First, the CL_r of all compounds were simulated in healthy subjects (GFR=120mL/min) based on reported $f_{u,p}$ and *in vitro* permeability (experimentally determined or optimized in healthy subjects) and all predicted CL_r values were within 2-fold of the observed

(Table 5.3), confirming satisfactory baseline simulation in healthy subjects and appropriate model parameterization. In healthy subjects, the adaptation was 0, therefore, both adaptive and proportional models resulted in identical simulation results (Figures 5.3-5.5) when GFR input was 120 mL/min.

To evaluate the performance of adaptive and proportional models with decreasing GFR (advancing CKD), three pairs of permeable drugs and their respective nonpermeable glucuronide metabolites studied concomitantly were used as the first test set. For all three permeable drugs, the adaptive model successfully predicted the CL_r across the entire range of GFRs considered (Figure 5.3a-c) while the proportional model only predicted the CL_r acceptably in mild CKD where physiological changes are not drastic. As shown in stage 4/5 CKD (Figure 5.3d-f), the calculated AFE_A ranged from 1.03 to 1.28 using adaptive model while the calculated AFE_P were all > 2 using proportional model. This suggests successful verification of the adaptive model in predicting CL_r at all stages of CKD, and inadequate performance of the proportional model for severe/end stage of CKD. For the nonpermeable glucuronide metabolites measured in the same studies, both adaptive and proportional models successfully predicted the CL_r (Figure 5.3g-i) across varying levels of renal impairment including CKD stage 4/5 (AFE 1.14-1.38, all < 2) (Figure 5.3j-l).

For further verification, the adaptive and proportional models were evaluated using six nonpermeable drugs that are predominantly filtered without significant reabsorption or secretion (Figure 5.4) and six permeable drugs that are significantly renally reabsorbed (Figure 5.5). Both adaptive and proportional models successfully predicted the CL_r for all six nonpermeable drugs across varying levels of renal impairment including CKD stage 4/5 (Figure 5.4a-c and g-i), with calculated AFE_A of 1.00-1.76 and AFE_P of 1.02-1.65, all < 2 (Figure 5.4d-f and j-l). In addition, the ratio between AFE_A and AFE_P for each individual drug was within the 0.8-to-1.25 range for

all non-permeable test drugs, suggesting an equivalent performance between adaptive and proportional models for CL_r prediction for non-permeable and non-secreted compounds. In contrast, the performance of the adaptive model was considerably better than the proportional model (Figure 5.5) for advanced CKD stages for permeable compounds that undergo significant renal reabsorption (83% to 97%) (Table 5.3). The adaptive model successfully (AFE_A = 1.05-1.73, all < 2) predicted the CL_r across varying levels of renal impairment, including stage 4/5 CKD (Figure 5.5), suggesting high confidence in the use of the adaptive model to predict CL_r in CKD patients. In contrast, discrepancy between the proportional model-simulated CL_r and observed CL_r was pronounced as the GFR decreased (Figure 5.5). At stage 4/5 CKD, the proportional model dramatically underpredicted the CL_r (AFE_P = 2.61-7.35, all > 2) with 83% of drugs having AFE_P > 3 (Figure 5.5). This demonstrates alarming inappropriateness of applying a proportional model (or proportional GFR scaling of CL_r) in CKD patients for drugs with medium-to-high permeability.

5.4.4 Prediction of renal clearance for secreted compounds in varying stages of CKD

To test whether the adaptive model could incorporate tubular secretion and predict the impact of CKD on the CL_r of secreted drugs, two sets of local sensitivity analyses were first conducted for uptake and efflux transport clearance after their incorporations as described in our previously published model (Huang and Isoherranen, 2018). The simulated CL_r showed a strong positive association with CL_{uptake} at all stages of CKD, with gradually lessened sensitivity as increasing CL_{uptake} surpassed 1,000 mL/min, the average renal blood flow of healthy human subjects (Figure 5.6a). Conversely, the simulated CL_r showed weak sensitivity with CL_{efflux} at all stages of CKD, suggesting that apical efflux is not the rate-determining step for CL_r (Figure 5.6b). The adaptive model was then used to predict CL_r of two secreted compounds, PAH and memantine,

across a range of GFRs (5-120 mL/min) and compared to the observed data. Overall, the simulation results for PAH and memantine agreed with the observed CL_r for all stages of CKD (Figure 5.5) with high accuracy (AFE 1.10-1.12, CKD stage 4/5). This suggests that the adaptive model can be used to predict CL_r of secreted compounds as well in varying stages of CKD in addition to non-secreted drugs.

5.5 Discussion

PBPK modeling has been proposed as a promising tool to predict drug disposition in complicated and unknown scenarios (Rowland Yeo *et al.*, 2011; Grillo *et al.*, 2012; Zhao *et al.*, 2012; Sayama *et al.*, 2014) due to its mechanistic capability of integrating multiple complex interactions. Indeed, great progress has been made in PBPK modeling of CKD effects on drug disposition, with special attention focused on altered hepatic metabolism (Zhao *et al.*, 2012; Yeung *et al.*, 2014; Huang *et al.*, 2017; Tan *et al.*, 2018) and renal active secretion (Hsu *et al.*, 2014; Hsueh *et al.*, 2018; Yee *et al.*, 2018) In contrast, the effect of CKD on renal passive reabsorption has not been considered in existing CKD models. This study is the first to systematically explore the observed effects of CKD on highly renally reabsorbed drugs, and to investigate the adaptive physiological changes in CKD in order to establish a PBPK modeling framework to predict CL_r throughout CKD progression. We expanded our previously developed and verified mechanistic kidney model (Huang and Isoherranen, 2018) to incorporate the physiologically-based tubular changes of reduced water reabsorption/increased tubular filtrate flow per remaining functional nephron for each renal subsegment across varying CKD stages. The final adaptive model was used to predict passive reabsorption and CL_r of a wide variety of compounds at different stages of CKD using *in vitro* $f_{u,p}$ and permeability without any optimization or empirical scaling. Using 20 test compounds representing different degrees of permeability and extent of passive renal reabsorption, our analyses unequivocally show that passive reabsorption and hence renal clearance may not decrease proportionally with GFR in CKD (Figures 5.3-5.5). Instead, the permeable and renally reabsorbed drugs had much lower (by 261% ~ 735%) reduction of CL_r than the reduction of GFR (Figure 5.5), while nonpermeable and predominantly filtered drugs did not show such disproportionality (Figure 5.4). Our model which considers physiologically-

based tubular surface area and dynamic tubular flow allows prediction of the extent of passive reabsorption based on drug permeability, conferring appropriate model sensitivity to drug permeability that reflects the observed CL_r in human. Further, only the adaptive model shown here that accounts for the tubular flow adaptation (decreased water reabsorption/increased tubular flow per remaining functional nephron) due to CKD could successfully simulate the decrease in drug concentration gradient between intratubular filtrate and peritubular blood, and subsequently reduced passive reabsorption, and confer higher CL_r than expected from residual GFR alone, as a result of CKD. The proportional model or the empirical GFR scaling approach that assumes all renal handling pathways are reduced proportionally with GFR was shown to be remarkably inappropriate for drugs with moderate-to-high permeability (Figure 5.5) and thus only applicable to low permeability, non-reabsorbed drugs (Figure 5.4).

Over the recent decade, PBPK modeling has been used to model CKD effects on renal elimination, primarily for highly secreted drugs that do not have significant permeability or passive reabsorption.(Hsu *et al.*, 2014; Hsueh *et al.*, 2018; Yee *et al.*, 2018; Bergman *et al.*, 2019; You *et al.*, 2020) While these models recover drug disposition in CKD, inconsistent scalars have been applied to a relative activity factor (RAF, scalars ranging from 0.28 (You *et al.*, 2020) to 3 (Bergman *et al.*, 2019)) and proximal tubular cells per gram kidney (PTCPGK, scalars up to 15(Hsu *et al.*, 2014)) that do not allow the model to recover the observed data in both healthy subjects and CKD patients. This suggests low confidence on both IVIVE of renal transport and understanding of CKD effect on renal drug handling. This is concerning, as many renally secreted drugs such as amphetamine, also have considerable permeability and reabsorption (Huang *et al.*, 2020). For such drugs, the empirical practice of optimizing active secretion using data from healthy subjects and extrapolating to CKD patients may result in

erroneous parameter optimization and misleading prediction of unstudied scenarios, as recently demonstrated in the context of full-body PBPK modeling (Huang and Isoherranen, 2020). As such, the adaptive system model shown here was entirely developed based on physiological knowledge independent of drug molecules, and was collectively verified against 20 test compounds with differing permeabilities throughout CKD stages without any optimization or empirical scaling for any of the test compounds. Our work demonstrates successful simulations of CL_r in CKD for a wide variety of drugs, establishing confidence of disease effect on renal passive reabsorption and laying a foundation for incorporating the CKD impact on renal active secretion.

It is well established that transporter-mediated renal active secretion is reduced in CKD due to declined number of functional nephrons and accumulating uremic solutes that may inhibit OAT1/3 activity (Hsueh *et al.*, 2016). In this study we used the developed and verified adaptive model to simulate CL_r for the two secreted test compounds, PAH and memantine, and showed successful CL_r prediction (AFE = 1.10 ~ 1.12, Figure 5.6) in varying stages of CKD. We demonstrated that our adaptive model can effectively incorporate specific transporter (OAT1/3 and OCT2) mediated renal secretion into CL_r prediction. Based on the simulation results, the novel adaptive model, together with proportional decline in transporter clearance, adequately captures the changes in CL_r with progression of CKD for PAH and memantine. This is likely because the CL_r (and the vectorial secretion) of PAH is renal plasma flow limited and memantine is a substrate of OCT2 where data suggest accumulating uremic solutes mainly inhibit OAT1/3-mediated renal uptake (Hsueh *et al.*, 2016) but have no effect on OCT2 (Cheung *et al.*, 2017). Further studies on OAT1/3 and OCT2 activity and expression in CKD are warranted for future model refinement. All other test compounds in this study lacked significant active secretion.

In this study, a disease effect on the $f_{u,p}$ was assumed to be insignificant, as the plasma albumin concentration in mild and severe CKD is only 7% and 16% lower than healthy subjects (Rowland Yeo *et al.*, 2011) and alterations in $f_{u,p}$ due to uremic solute displacement likely only apply to acidic (Brater, 2009) compounds with a reported median (n=16) increase (Sayama *et al.*, 2014) of 35% in $f_{u,p}$ in severe CKD. For a total of 20 test compounds included here, only 3 are highly protein bound (Table 5.3) and digitoxin is the only acid, where clinical study has showed unchanged $f_{u,p}$ of digitoxin in CKD patients (Kirch *et al.*, 1986). As illustrated by the sensitivity analyses (Figure 5.2), the potentially small changes in $f_{u,p}$ in CKD cannot explain the dramatic (mean = 458% (261% ~ 735%)) discrepancy between the observed CL_r and the expected CL_r from proportional model for permeable drugs (Figure 5.5). Yet, the modeling framework established here using MATLAB Simulink could readily incorporate changes in $f_{u,p}$ during CKD if observed/expected.

In conclusion, we have developed and successfully verified a novel adaptive model that describes physiological changes in renal tubules and enables accurate prediction of passive reabsorption and CL_r for a wide variety of compounds using *in vitro* $f_{u,p}$ and permeability across multiple CKD stages without any optimization or empirical scaling. The developed model can serve as a foundation to incorporate/explore the CKD impact on renal transporter expression and uremic solute inhibition, and can also be integrated into a full-body PBPK model (Huang *et al.*, 2020) to simulate the systemic disposition of drugs and metabolites in CKD.

Table 5.1. Representative renal tubular filtrate flows (TFF) for the proportional and adaptive models at different stages of CKD (set 1).

The tubular subsegment-dependent adaptation factors (AF_i) were calculated according to Equation 1 and implemented for the adaptive model. The renal tubular filtrate flows (TFF) were calculated using either proportional model (TFF_P) by direct scaling to GFR as described in Methods, or using the adaptive model (TFF_A) according to Equation 3. The renal tubular filtrate flow (TFF) (mL/min) shown here indicates the inflow rate of entering each renal subsegment, which equals to the outflow rate exiting from the previous renal subsegment. The inflow rate of the first proximal tubule subsegment always equals to the GFR. The outflow rate of the last subsegment of collecting duct always equals to the inflow rate of bladder and the urine formation rate (as no reabsorption occurs within bladder). All flows are presented in mL/min.

	Healthy (Stage 1) GFR = 120 mL/min		Mild Stage CKD (Stage 2) GFR = 80 mL/min		Moderate Stage CKD (Stage 3) GFR = 40 mL/min		Severe Stage CKD (Stage 4) GFR = 20 mL/min		End Stage CKD (Stage 5) GFR = 5 mL/min	
Model Subsegment	TFF	Adaptation Factor	TFF_P	TFF_A	TFF_P	TFF_A	TFF_P	TFF_A	TFF_P	TFF_A
Proximal $Tubule_1$	120	0	80.00	80.00	40.00	40.00	20.00	20.00	5.00	5.00
Proximal $Tubule_2$	94	0.0099	62.67	62.98	31.33	31.96	15.67	16.44	3.92	4.81
Proximal $Tubule_3$	68	0.018	45.33	45.73	22.67	23.46	11.33	12.33	2.83	3.98
Loop of $Henle_D$	43	0.038	28.67	29.22	14.33	15.44	7.17	8.55	1.79	3.38
Loop of $Henle_A$	24	0.098	16.00	16.78	8.00	9.56	4.00	5.95	1.00	3.25
Distal Tubule	24	0.098	16.00	16.78	8.00	9.56	4.00	5.95	1.00	3.25
Collecting $Duct_1$	11	0.26	7.33	8.29	3.67	5.58	1.83	4.22	0.46	3.21
Collecting $Duct_2$	9	0.31	6.00	6.94	3.00	4.87	1.50	3.84	0.38	3.07
Collecting $Duct_3$	7	0.37	4.67	5.54	2.33	4.08	1.17	3.35	0.29	2.80
Collecting $Duct_4$	5	0.44	3.33	4.07	1.67	3.14	0.83	2.68	0.21	2.33
Collecting $Duct_5$	3	0.51	2.00	2.51	1.00	2.02	0.50	1.78	0.13	1.60
Bladder (Urine)	1	0.56	0.67	0.85	0.33	0.71	0.17	0.63	0.04	0.58

Table 5.2. Representative tubular filtrate flows (TFF) for the proportional and adaptive models at different stages of CKD (set 2).

The tubular subsegment-dependent adaptation factors (AF_i) were calculated according to Equation 1 and implemented for the adaptive model. The renal tubular filtrate flows (TFF) were calculated using either proportional model (TFF_P) by direct scaling to GFR as described in Methods, or using the adaptive model (TFF_A) according to Equations 2 and 3. The renal tubular filtrate flow (TFF) (mL/min) shown here indicates the inflow rate of entering each renal subsegment, which equals to the outflow rate exiting from the previous renal subsegment. The inflow rate of the first proximal tubule subsegment always equals to the GFR. The outflow rate of the last subsegment of collecting duct always equals to the inflow rate of bladder and the urine formation rate (as no reabsorption occurs within bladder). All flows are presented in mL/min.

	Healthy (Stage 1) GFR = 120 mL/min		Mild Stage CKD (Stage 1/2) GFR = 90 mL/min		Moderate Stage CKD (Stage 2/3) GFR = 60 mL/min		Severe Stage CKD (Stage 3/4) GFR = 30 mL/min		End Stage CKD (Stage 4/5) GFR = 15 mL/min	
Model Subsegment	TFF	Adaptation Factor	TFF_P	TFF_A	TFF_P	TFF_A	TFF_P	TFF_A	TFF_P	TFF_A
Proximal $Tubule_1$	120	0	90.00	90.00	60.00	60.00	30.00	30.00	15.00	15.00
Proximal $Tubule_2$	94	0.0099	70.50	70.73	47.00	47.47	23.50	24.20	11.75	12.57
Proximal $Tubule_3$	68	0.018	51.00	51.30	34.00	34.60	17.00	17.89	8.50	9.54
Loop of $Henle_D$	43	0.038	32.25	32.66	21.50	22.33	10.75	11.99	5.38	6.82
Loop of $Henle_A$	24	0.098	18.00	18.59	12.00	13.17	6.00	7.76	3.00	5.05
Distal Tubule	24	0.098	18.00	18.59	12.00	13.17	6.00	7.76	3.00	5.05
Collecting $Duct_1$	11	0.26	8.25	8.97	5.50	6.93	2.75	4.90	1.38	3.88
Collecting $Duct_2$	9	0.31	6.75	7.45	4.50	5.90	2.25	4.36	1.13	3.58
Collecting $Duct_3$	7	0.37	5.25	5.90	3.50	4.81	1.75	3.71	0.88	3.16
Collecting $Duct_4$	5	0.44	3.75	4.30	2.50	3.61	1.25	2.91	0.63	2.56
Collecting $Duct_5$	3	0.51	2.25	2.63	1.50	2.27	0.75	1.90	0.38	1.72
Bladder (Urine)	1	0.56	0.75	0.89	0.50	0.78	0.25	0.67	0.13	0.62

Table 5.3. Summary of the physicochemical and pharmacokinetic properties for the 20 test compounds used for adaptive model verification and comparison of the simulated and observed renal clearances for all test compounds used for model verification (Figures 5.3 to 5.6).

Drug	pK_a (acid)[a]	pK_a (base)[a]	$f_{u,p}$	Permeability (10^{-6} cm/s)	Observed Mean CL_r in Healthy (mL/min)	Simulated Mean CL_r in Healthy (mL/min)	Sim/Obs Ratio of CL_r in Healthy	Observed Mean CL_r in CKD4/5 (mL/min)	Simulated Mean CL_r in CKD4/5 (mL/min)	Sim/Obs Ratio of CL_r in CKD4/5
Parent-Metabolite Test Compounds in Figure 5.3										
Rotigotine	-	10.97	0.11	19.5	3.7	4.8	1.30	1.8	1.9	1.03
Acetaminophen	-	-	0.8	35	13	15	1.15	7.1	5.5	0.78
Lamotrigine	-	5.87	0.44	88	3.4	3.1	0.92	1.9	2.1	1.13
Rotigotine Glucuronide	-	-	1[b]	0.1[b]	110	119	1.08	27	22	0.82
Acetaminophen Glucuronide	-	-	1[b]	0.1[b]	108	119	1.10	17	15	0.88
Lamotrigine Glucuronide	-	-	1[b]	0.1[b]	114	119	1.04	13	18	1.37
Nonpermeable Test Compounds in Figure 5.4										
Melagatran	3.2	11.5	0.93	0.145	94	110	1.17	12	12	0.97
Sotalol	-	9.43	0.83	0.26	107	99	0.92	19	16	0.81
Gabapentin	4.63	9.91	0.97	0.67	99	110	1.12	12	16	1.30
Nadolol	-	9.76	0.8	1.4	82	94	1.15	8.0	8.0	1.00
Ribavirin	-	-	1	1.55	107	106	0.99	10	18	1.76
Doxycycline	3.27	8.33	0.1	1.8	15	10	0.71	2.0	2.0	0.98
Permeable Test Compounds in Figure 5.5										
Pefloxacin	5.66	6.47	0.75	63.7	7.5	6.4	0.86	2.9	3.1	1.05
Metronidazole	-	-	0.89	64.7	6.8	7.3	1.08	2.6	4.4	1.73
Minocycline	2.9	7.9	0.24	76	1.5	1.1	0.70	0.98	0.85	0.87
Digitoxin	7.18	-	0.05	30[c]	0.85	1.2	1.37	0.62	0.38	0.62
Cicletanine	-	-	0.07	95[c]	0.42	0.36	0.86	0.19	0.29	1.52
Pirfenidone	-	-	0.42	120[c]	1.7	1.7	0.99	0.96	1.5	1.53
Secreted Test Compounds in Figure 5.6										
Para-aminohippuric Acid (PAH)	3.83	4.24	1	0.72	599	500	0.84	76	86	1.12
Memantine	-	10.7	0.55	25	70	77	1.10	16	17	1.10

[a]pK_a values are obtained from https://www.drugbank.ca/
[b]experimentally determined metabolite data are not available, therefore these values are assumed based on physicochemical properties.
[c]experimentally determined data are not available, therefore permeability values were optimized using previously published and verified mechanistic kidney model with reported $f_{u,p}$ and observed CL_r in healthy subjects.

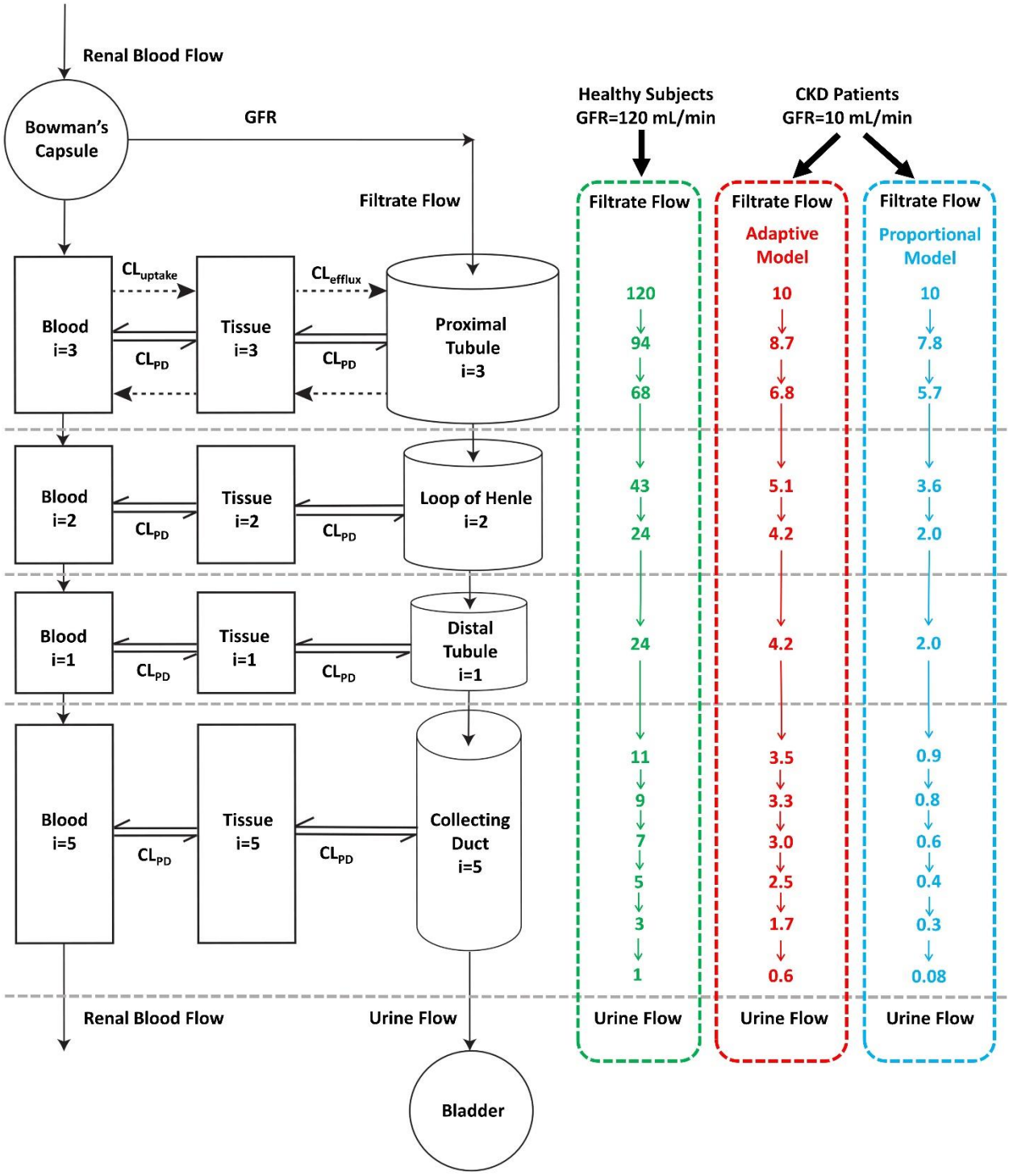
Renal Blood Flow
Bowman's Capsule
GFR
Filtrate Flow
Blood i=3
Tissue i=3
Proximal Tubule i=3
CL_uptake
CL_efflux
CL_PD
Blood i=2
Tissue i=2
Loop of Henle i=2
Blood i=1
Tissue i=1
Distal Tubule i=1
Blood i=5
Tissue i=5
Collecting Duct i=5
Renal Blood Flow
Urine Flow
Bladder
Healthy Subjects GFR=120 mL/min
CKD Patients GFR=10 mL/min
Filtrate Flow
Adaptive Model
Proportional Model
120 94 68 43 24 24 11 9 7 5 3 1
10 8.7 6.8 5.1 4.2 4.2 3.5 3.3 3.0 2.5 1.7 0.6
10 7.8 5.7 3.6 2.0 2.0 0.9 0.8 0.6 0.4 0.3 0.08
Urine Flow

Figure 5.1. Schematic presentation of the mechanistic kidney model structure, together with the corresponding renal tubular filtrate flow (TFF, in mL/min) for each individual subsegment of the model (a total of 12).

Three sets of physiologically-based TFF shown here are for healthy subjects (GFR 120 mL/min, in green) and for the representative CKD patients who have residual GFR of 10 mL/min using the adaptive model (in red) and the proportional model (in blue). The dynamic physiologically-based mechanistic kidney model shown here is parameterized by 33 volume parameters, 22 surface area parameters, 12 peritubular renal blood flow parameters, 12 renal tubular filtrate flow (TFF) parameters, 3 basolateral uptake clearance parameters and 3 apical efflux clearance parameters to fully capture the disposition of drugs/metabolites between renal tubules, cells, and vasculature.

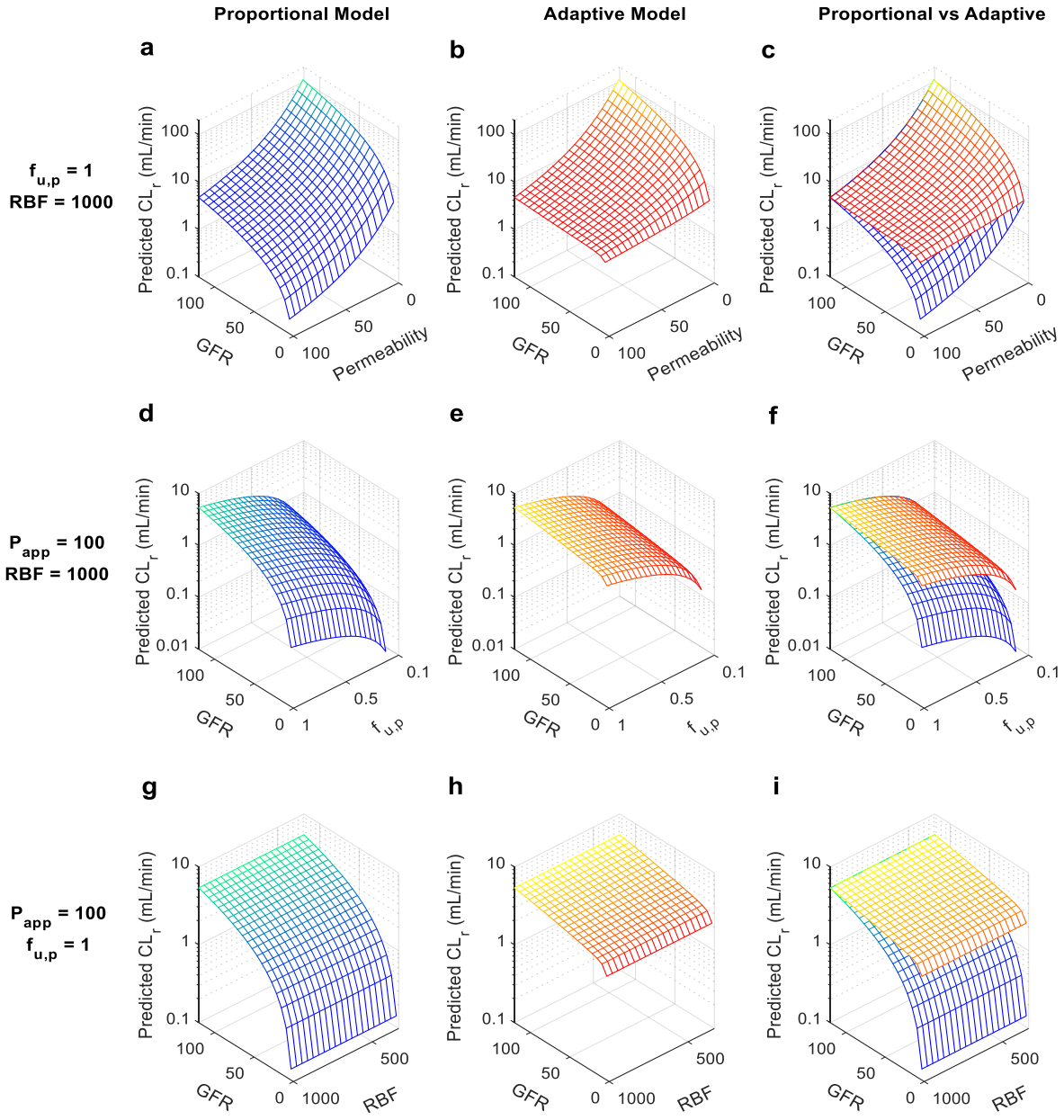
Proportional Model
Adaptive Model
Proportional vs Adaptive
a
b
c
d
e
f
g
h
i
$f_{u,p}$ = 1
RBF = 1000
P_{app} = 100
RBF = 1000
P_{app} = 100
$f_{u,p}$ = 1
Predicted CL_r (mL/min)
GFR
Permeability
$f_{u,p}$
RBF

Figure 5.2. Sensitivity analyses of simulated renal clearance (CL_r, in mL/min) at multiple stages of chronic kidney disease (CKD) reflected as varying glomerular filtration rate (GFR, in mL/min) using proportional model (shown in blue-green) versus adaptive model (shown in yellow-red).

Three sets of sensitivity analyses were conducted: 1) CL_r of neutral drugs with varying permeability values (P_{app} = 1-100×10^{-6} cm/s, all values shown are in 10^{-6} cm/s) but a constant plasma unbound fraction ($f_{u,p}$ = 1) and peritubular renal blood flow (RBF = 1000 mL/min, the average of healthy human subjects) were simulated using proportional model (panel a), adaptive model (panel b), and both models (panel c) across a wide range of GFR values from 5 mL/min to 120 mL/min; 2) renal clearances of highly permeable neutral drugs (P_{app} = 100×10^{-6} cm/s) with varying plasma unbound fraction ($f_{u,p}$ = 0.1-1) but a constant peritubular renal blood flow (RBF = 1000 mL/min) were simulated using proportional model (panel d), adaptive model (panel e), and both models (panel f) across a range of GFR from 5 mL/min to 120 mL/min; and 3) CL_r of a highly permeable neutral drugs (Papp = 100×10^{-6} cm/s) with varying peritubular renal blood flow (RBF = 300-1000 mL/min) but a constant plasma unbound fraction ($f_{u,p}$ = 1) were simulated using proportional model (panel g), adaptive model (panel h), and both models (panel i) across a range of GFR from 5 mL/min to 120 mL/min.

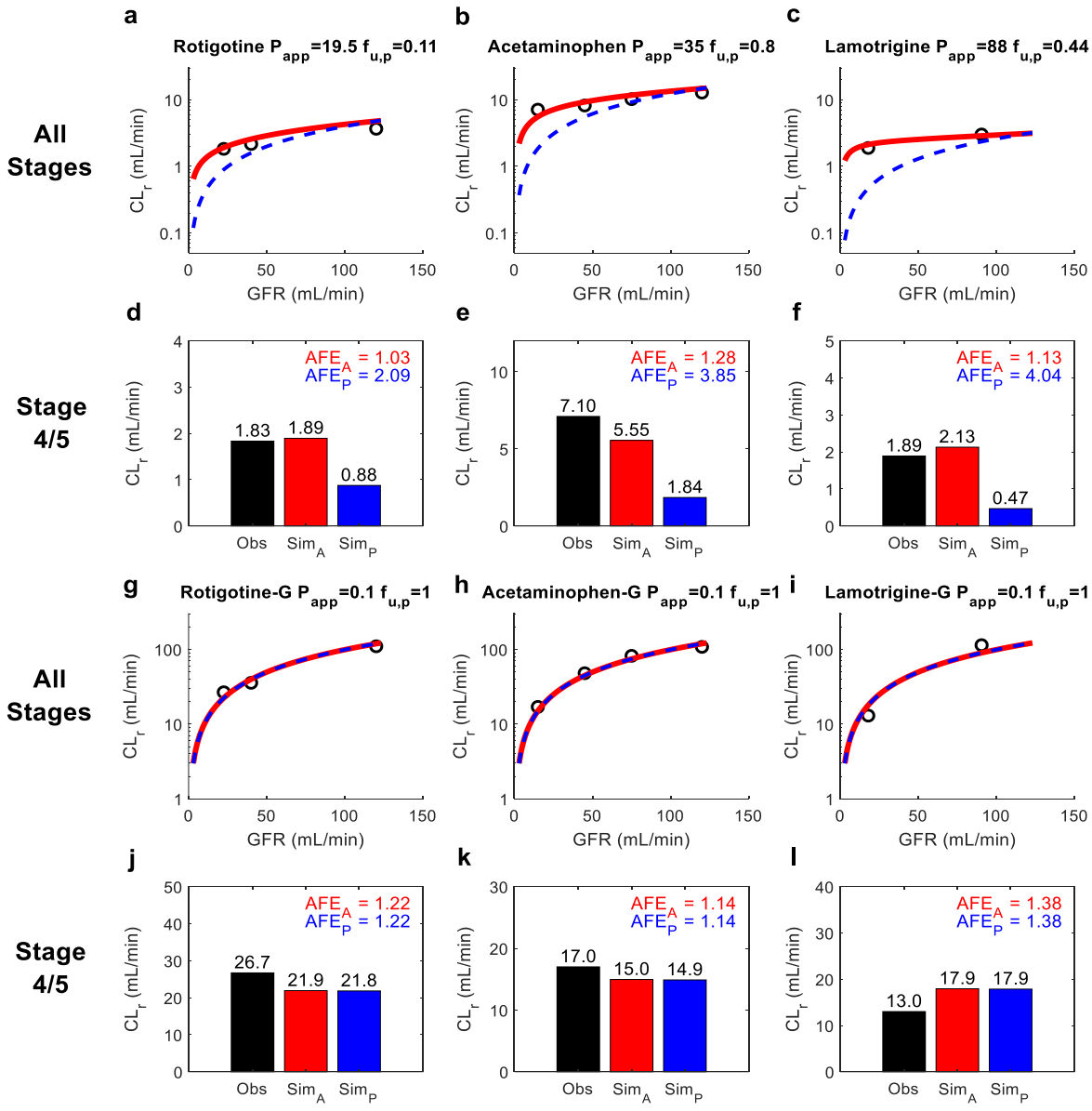
All Stages
Stage 4/5
All Stages
Stage 4/5
a
Rotigotine P_app=19.5 f_u,p=0.11
b
Acetaminophen P_app=35 f_u,p=0.8
c
Lamotrigine P_app=88 f_u,p=0.44
d
AFE_A = 1.03
AFE_P = 2.09
1.83
1.89
0.88
e
AFE_A = 1.28
AFE_P = 3.85
7.10
5.55
1.84
f
AFE_A = 1.13
AFE_P = 4.04
1.89
2.13
0.47
g
Rotigotine-G P_app=0.1 f_u,p=1
h
Acetaminophen-G P_app=0.1 f_u,p=1
i
Lamotrigine-G P_app=0.1 f_u,p=1
j
AFE_A = 1.22
AFE_P = 1.22
26.7
21.9
21.8
k
AFE_A = 1.14
AFE_P = 1.14
17.0
15.0
14.9
l
AFE_A = 1.38
AFE_P = 1.38
13.0
17.9
17.9
CL_r (mL/min)
GFR (mL/min)
Obs
Sim_A
Sim_P

Figure 5.3. Simulation and verification of renal clearance (CL_r) of three drugs and their corresponding glucuronide metabolites at multiple stages of chronic kidney diseases (CKD) reflected by varying glomerular filtration rate (GFR).

Black open circles represent observed CL_r of the test compounds. The simulated CL_r of different test compounds at varying stages of CKD are shown with red curves for the adaptive model and blue dashed curves for the proportional model (panel a-c and g-i). The performance of the adaptive and proportional models was evaluated at CKD stage 4/5 where GFR $\leq$ 30 mL/min using calculated AFE_A (shown in red) and AFE_P (shown in blue), respectively (panel d-f and j-l). The experimentally determined apparent permeability (P_{app}), plasma unbound fraction ($f_{u,p}$), and observed CL_r data of rotigotine (panel a and d), acetaminophen (panel b and e), and lamotrigine (panel c and f) were collected from literature and summarized in Table 5.3. The P_{app} and $f_{u,p}$ values of all glucuronide metabolites (panel g-l) were assumed to be 0.1×10^{-6} cm/s and 1, respectively, based on their physicochemical properties. The observed renal clearance (CL_r) data of all metabolites were from the same subjects in the same studies of their respective parent drugs (Table 5.3).

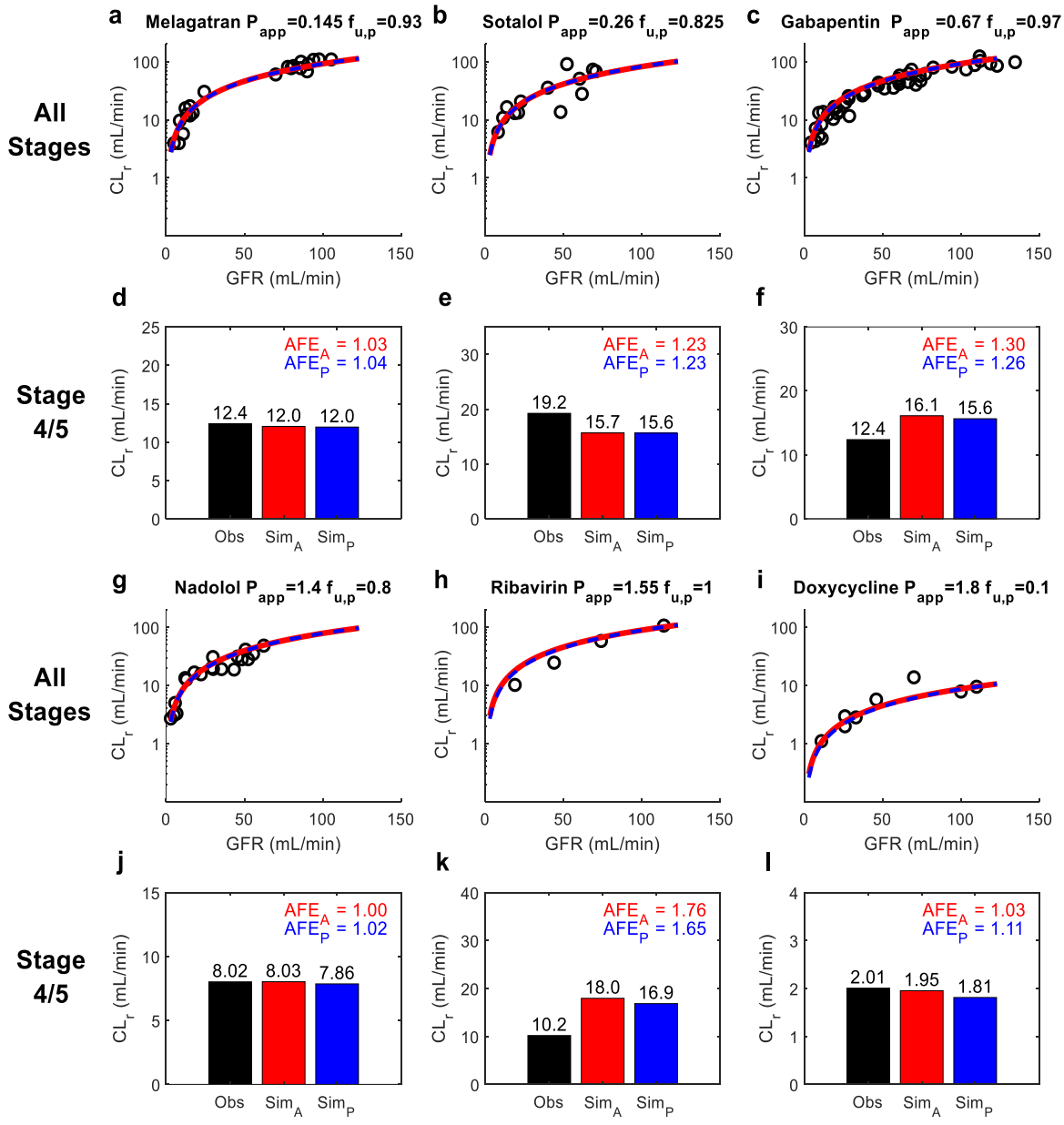
All Stages
Stage 4/5
All Stages
Stage 4/5
a
Melagatran P_app=0.145 f_u,p=0.93
b
Sotalol P_app=0.26 f_u,p=0.825
c
Gabapentin P_app=0.67 f_u,p=0.97
d
AFE_A = 1.03
AFE_P = 1.04
12.4
12.0
12.0
e
AFE_A = 1.23
AFE_P = 1.23
19.2
15.7
15.6
f
AFE_A = 1.30
AFE_P = 1.26
12.4
16.1
15.6
g
Nadolol P_app=1.4 f_u,p=0.8
h
Ribavirin P_app=1.55 f_u,p=1
i
Doxycycline P_app=1.8 f_u,p=0.1
j
AFE_A = 1.00
AFE_P = 1.02
8.02
8.03
7.86
k
AFE_A = 1.76
AFE_P = 1.65
10.2
18.0
16.9
l
AFE_A = 1.03
AFE_P = 1.11
2.01
1.95
1.81
CL_r (mL/min)
GFR (mL/min)
Obs
Sim_A
Sim_P

Figure 5.4. Simulation and verification of renal clearance (CL_r) of six non-permeable compounds at multiple stages of chronic kidney diseases (CKD) reflected by varying glomerular filtration rate (GFR).

Black circles represent observed renal clearance (CL_r) of six non-permeable test compounds. The simulated CL_r of different test compounds at varying stages of CKD are shown with red curves for the adaptive model and blue dashed curves for the proportional model (panel a-c and g-i). The performance of the adaptive model and proportional model was evaluated at CKD stage 4/5 ($GFR \leq 30$ mL/min) using calculated AFE_A (shown in red) and AFE_P (shown in blue), respectively (panel d-f and j-l). The experimentally determined apparent permeability (P_{app}), plasma unbound fraction ($f_{u,p}$), and observed CL_r data of melagatran (panel a and d), sotalol (panel b and e), gabapentin (panel c and f), nadolol (panel g and j), ribavirin (panel h and k), and doxycycline (panel i and l) were collected from literature and summarized in Table 5.3.

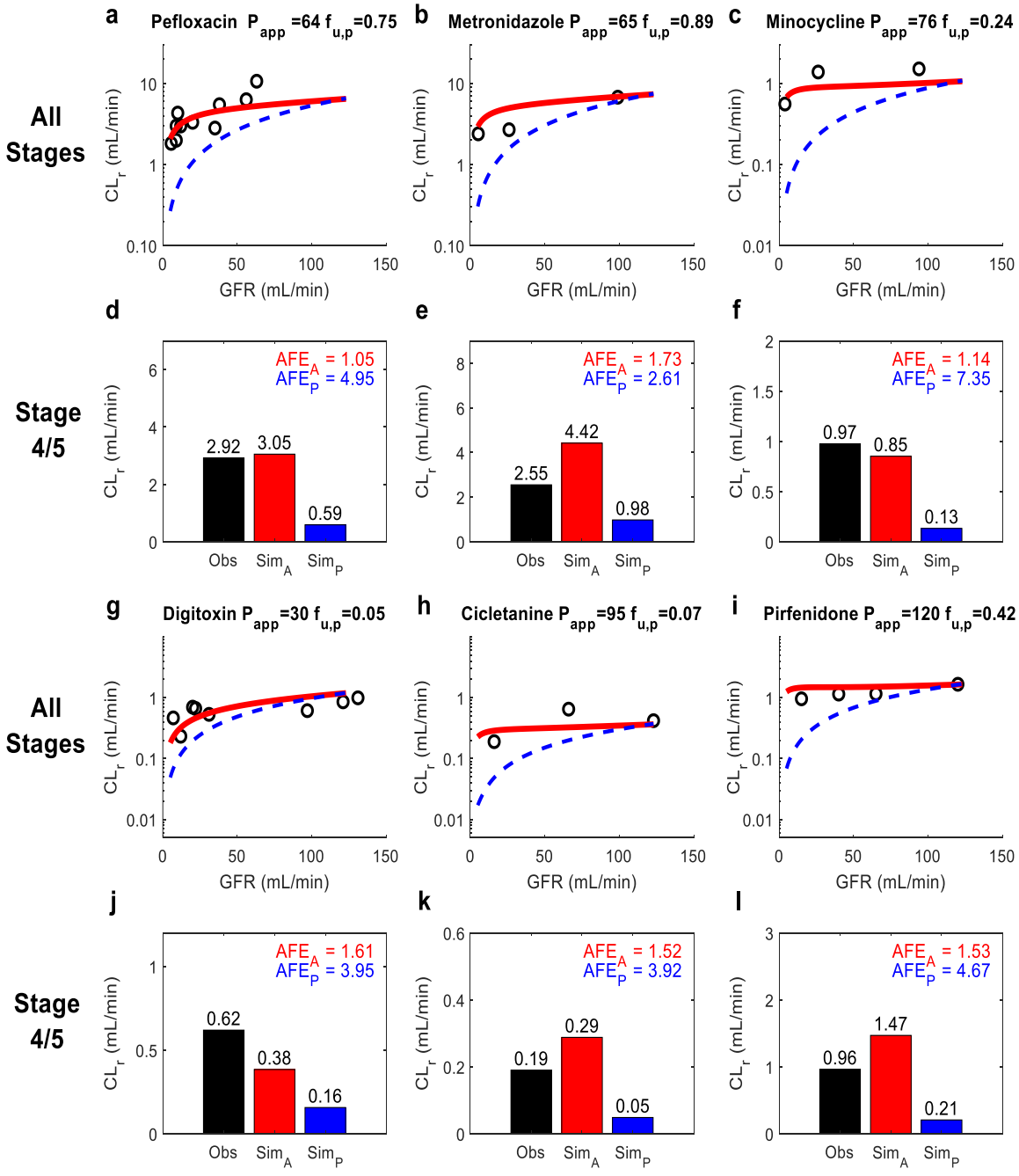
All Stages
Stage 4/5
All Stages
Stage 4/5
a
Pefloxacin P_app=64 f_u,p=0.75
b
Metronidazole P_app=65 f_u,p=0.89
c
Minocycline P_app=76 f_u,p=0.24
d
AFE_A = 1.05
AFE_P = 4.95
2.92
3.05
0.59
e
AFE_A = 1.73
AFE_P = 2.61
2.55
4.42
0.98
f
AFE_A = 1.14
AFE_P = 7.35
0.97
0.85
0.13
g
Digitoxin P_app=30 f_u,p=0.05
h
Cicletanine P_app=95 f_u,p=0.07
i
Pirfenidone P_app=120 f_u,p=0.42
j
AFE_A = 1.61
AFE_P = 3.95
0.62
0.38
0.16
k
AFE_A = 1.52
AFE_P = 3.92
0.19
0.29
0.05
l
AFE_A = 1.53
AFE_P = 4.67
0.96
1.47
0.21
CL_r (mL/min)
GFR (mL/min)
Obs
Sim_A
Sim_P

Figure 5.5. Simulation and verification of renal drug clearance (CL_r) of six permeable and highly renally reabsorbed compounds at multiple stages of chronic kidney diseases (CKD) reflected by varying glomerular filtration rate (GFR).

Black circles represent observed CL_r of six permeable test compounds. The simulated CL_r of different test compounds at varying stages of CKD are shown with red curves for the adaptive model and blue dashed curves for the proportional model (panel a-c and g-i). The performance of adaptive and proportional model was evaluated at CKD stage 4/5 (GFR ≤ 30 mL/min) using calculated AFE_A (shown in red) and AFE_P (shown in blue), respectively (panel d-f and j-l). The plasma unbound fraction ($f_{u,p}$) and observed CL_r data of pefloxacin (panel a and d), metronidazole (panel b and e), and minocycline (panel c and f), digitoxin (panel g and j), cicletanine (panel h and k), and pirfenidone (panel i and l) were collected from literature and summarized in Table 5.3. The apparent permeability (P_{app}) values of pefloxacin, metronidazole, and minocycline were experimentally determined, while the P_{app} values of other drugs were optimized using the $f_{u,p}$ and observed CL_r in healthy subjects, assuming no active secretion. The same optimized P_{app} values were used for extrapolated simulations at varying stages of chronic kidney diseases.

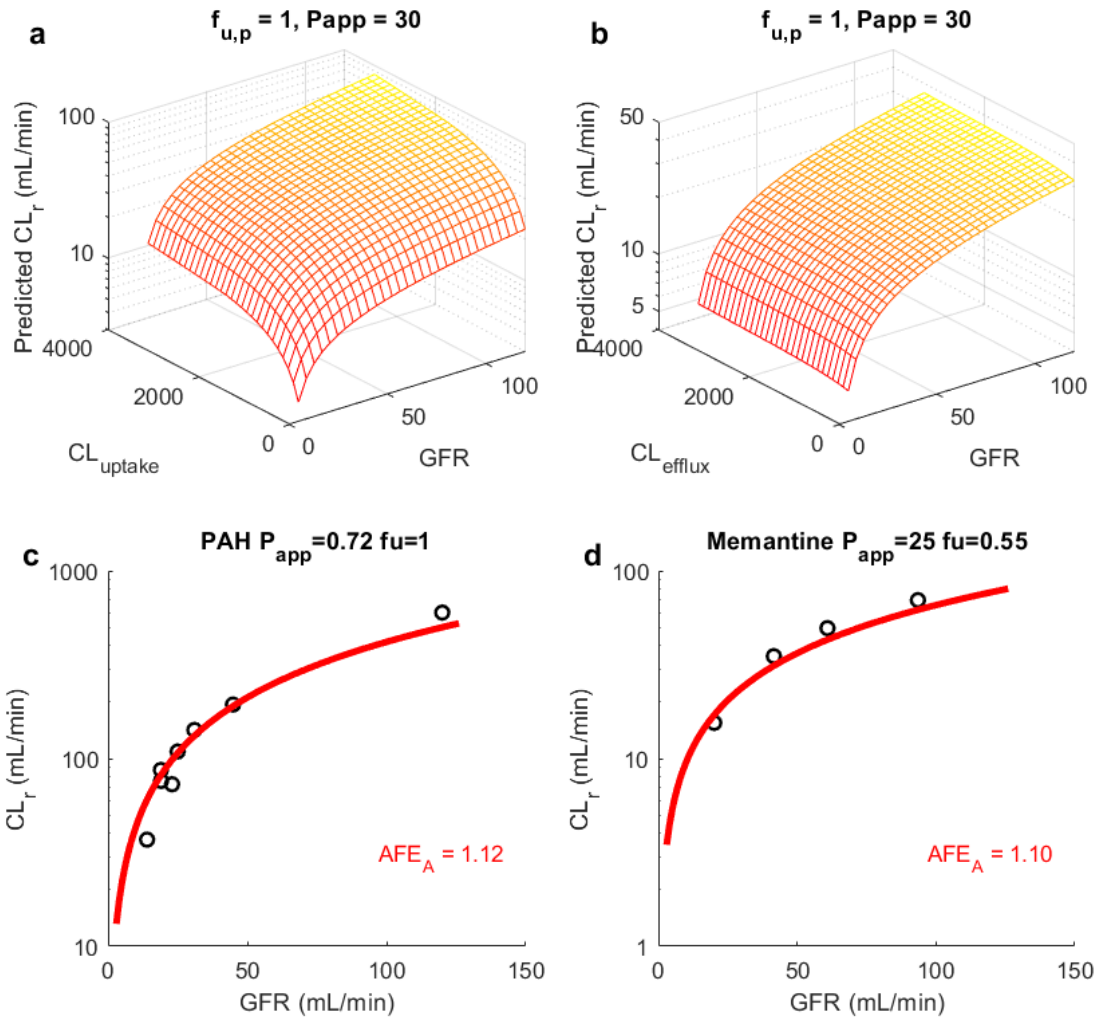
a
$f_{u,p}$ = 1, Papp = 30
Predicted CL_r (mL/min)
100
10
4000
2000
0
CL_{uptake}
0
50
100
GFR
b
$f_{u,p}$ = 1, Papp = 30
Predicted CL_r (mL/min)
50
10
5
4000
2000
0
CL_{efflux}
0
50
100
GFR
c
PAH P_{app}=0.72 fu=1
CL_r (mL/min)
1000
100
10
AFE_A = 1.12
0
50
100
150
GFR (mL/min)
d
Memantine P_{app}=25 fu=0.55
CL_r (mL/min)
100
10
1
AFE_A = 1.10
0
50
100
150
GFR (mL/min)

Figure 5.6. Sensitivity analyses of simulated renal clearance (CL_r in mL/min) at multiple stages of chronic kidney disease (CKD) and simulation results of PAH and memantine in CKD patients. Sensitivity analyses of simulated renal clearance (CL_r in mL/min) at multiple stages of chronic kidney disease (CKD) reflected by varying glomerular filtration rates (GFR in mL/min) using adaptive model (shown in yellow-red). Panel a shows the sensitivity analyses of adaptive model-simulated CL_r of neutral unbound permeable drugs ($f_{u,p}$ = 1, P_{app} = 30×10^{-6} cm/s) with a constant unbound intrinsic apical efflux transport clearance (CL_{efflux} = 150 mL/min) and different unbound intrinsic basolateral uptake transport clearances (CL_{uptake} = 10-3000 mL/min) across a range of GFRs (5-120 mL/min). Panel b shows the sensitivity analyses of adaptive model-simulated CL_r of neutral unbound permeable drugs ($f_{u,p}$ = 1, P_{app} = 30×10^{-6} cm/s) with a constant unbound intrinsic basolateral uptake transport clearance (CL_{uptake} = 150 mL/min) and different unbound intrinsic apical efflux transport clearances (CL_{efflux} = 10-3000 mL/min) across a range of GFRs (5-120 mL/min). Panels c and d show the simulations of CL_r of PAH and memantine in red curves, respectively, using adaptive model, at multiple stages of chronic kidney diseases (CKD), and comparison to the observed data (Table 5.3) shown in black open circles with calculated AFE_A shown in the insets.

Chapter 6. CONCLUSIONS

6 Conclusions

Physiologically-based pharmacokinetic (PBPK) models integrate population- or system-specific physiological features with drug-specific physicochemical and pharmacokinetic properties to predict drug disposition in the populations/systems of interest. Such integration allows different items (e.g. drug entities, proteins, membranes), events (e.g. drug-protein binding, catalytic reaction), processes (e.g. blood flow, drug movement and permeation), and pathways (e.g. cascade signaling, enzyme-mediated sequential metabolism, transporter-mediated vectorial uptake and efflux) to communicate and influence each other mechanistically. This provides predictive and instrumental insights on how human body handles drugs when items, events, processes, and pathways are altered. As such, a multitude of valuable applications of PBPK modeling have been realized and successfully demonstrated (Jones *et al.*, 2006a, 2013; Rowland *et al.*, 2011; Huang and Rowland, 2012; Wagner *et al.*, 2015a). Specifically, these applications range from estimating optimal PK characteristics during drug discovery (Agoram *et al.*, 2001; Jamei *et al.*, 2009; Kaur *et al.*, 2018), to optimizing first-in-human (FIH) dose for better clinical trial design (Offman and Edginton, 2015; Miller *et al.*, 2019), and predicting drug disposition in specific patient populations during drug development or even post-marketing (Johnson *et al.*, 2010; Zhao *et al.*, 2011; Grillo *et al.*, 2012; Zhang *et al.*, 2017).

Despite the great potential and variety of applications of PBPK modeling, knowledge gaps remain in model development, verification, and application. Specifically, system models that can sufficiently capture kidney physiological characteristics and can be used to understand and predict renal drug handling processes are lacking. Advanced model applications such as prediction of alteration in renal and systemic disposition when urine pH is changed or when the kidney is impaired remain low-confidence. Therefore, the overarching hypothesis of this thesis

was that mechanistic physiologically-based kidney modeling can be developed and used to predict renal clearance of drugs and metabolites with variety of physicochemical properties and under different clinical conditions such as altered urine pH and chronic kidney disease. The mechanistic kidney model can be further integrated into full body PBPK models to simulate both renal and systemic disposition in a multitude of scenarios.

In Chapter 2, I developed a dynamic physiologically-based 35-compartment mechanistic kidney model that addresses the impact of dynamic tubular flow, tubular pH, microvilli, and multi-source permeability on effective passive diffusion and subsequent renal clearance simulation. The model was successfully verified with 46 test compounds including neutrals, acids, bases, and zwitterions, and demonstrated the feasibility of incorporating active secretion and pH-dependent bidirectional passive diffusion.

In Chapter 3, I developed a physiologically-based peripheral forearm sampling site model that was integrated with a full body PBPK to allow the output of simulated peripheral venous concentrations to be meaningfully compared to the observed pharmacokinetic data collected from arm vein sampling. The model was successfully verified using arterial and venous concentrations of nicotine, ketamine, lidocaine, and fentanyl simultaneously. Further, I demonstrated that use of a discrepant sampling site in PBPK modeling than observed clinical studies may lead to biased model evaluation, erroneous model parameterization, and misleading prediction in unstudied clinical scenarios.

In Chapter 4, I integrated the mechanistic kidney model from Chapter 2 with peripheral arm sampling and full body PBPK model from Chapter 3, to predict the altered renal excretion and systemic AUC of drug and metabolite when urine pH is changed. The model was successfully verified with methamphetamine and amphetamine under varying urine pH statuses, and showed

feasibility for predicting quantitatively and clinically significant changes in drug and metabolite disposition under comedications and diseases that can alter urine pH.

In Chapter 5, I incorporated relevant physiological changes observed in chronic kidney disease patients into the mechanistic kidney model from Chapter 2, including adaptive renal tubular filtrate flows that decrease disproportionately with glomerular filtration rate. The model was successfully verified with three parent-metabolite pairs, six non-permeable drugs, six permeable drugs, and two secreted drugs. The simulation results demonstrated a sizable impact of physiologically-based adaptive changes in tubular filtrate flow on renal clearance prediction for reabsorbed, non-reabsorbed, secreted, and non-secreted compounds in chronic kidney disease patients.

In conclusion, the results of this thesis show that anatomical and physiological characteristics of kidney can be integrated into an *in silico* model to translate drug properties such as plasma protein binding, transcellular permeability, and intrinsic active transport rate into renal clearance of drugs and metabolites. Further, this model allows prediction of alterations in renal clearance of drugs and metabolites upon changes in urine pH and renal functions, and can be incorporated into a full-body PBPK model to predict alterations in systemic disposition of drugs and metabolites.

BIBLIOGRAPHY

Adachi K, Suemizu H, Murayama N, Shimizu M, and Yamazaki H (2015) Human biofluid concentrations of mono(2-ethylhexyl)phthalate extrapolated from pharmacokinetics in chimeric mice with humanized liver administered with di(2-ethylhexyl)phthalate and physiologically based pharmacokinetic modeling. *Environ Toxicol Pharmacol* **39**:1067–1073, Elsevier B.V.

Agoram B, Woltosz WS, and Bolger MB (2001) Predicting the impact of physiological and biochemical processes on oral drug bioavailability. *Adv Drug Deliv Rev* **50**.

Alsenz J, and Haenel E (2003) Development of a 7-Day, 96-Well Caco-2 Permeability Assay with High-Throughput Direct UV Compound Analysis. *Pharm Res* **20**:1961–1969.

Andersen ME, Clewell HJ, Gargas ML, MacNaughton MG, Reitz RH, Nolan RJ, and McKenna MJ (1991) Physiologically based pharmacokinetic modeling with dichloromethane, its metabolite, carbon monoxide, and blood carboxyhemoglobin in rats and humans. *Toxicol Appl Pharmacol* **108**:14–27.

Andersen ME, Clewell HJ, Gargas ML, Smith FA, and Reitz RH (1987) Physiologically based pharmacokinetics and the risk assessment process for methylene chloride. *Toxicol Appl Pharmacol* **87**:185–205.

Aoki FY, and Sitar DS (1988) Clinical pharmacokinetics of amantadine hydrochloride. *Clin Pharmacokinet* **14**:35–51.

Artursson P, and Karlsson J (1991) Correlation between oral drug absorption in humans and apparent drug permeability coefficients in human intestinal epithelial (Caco-2) cells. *Biochem Biophys Res Commun* **175**:880–885.

Artursson P, Palm K, and Luthman K (2001) Caco-2 monolayers in experimental and theoretical

predictions of drug transport. *Adv Drug Deliv Rev* **46**:27–43.

Barbhaiya RH, Gerber AU, Craig WA, and Welling PG (1982) Influence of urinary pH on the pharmacokinetics of cinoxacin in humans and on antibacterial activity in vitro. *Antimicrob Agents Chemother* **21**:472–480.

Beckett AH, and Rowland M (1965a) Urinary excretion kinetics of amphetamine in man. *J Pharm Pharmacol* **17**:628–39.

Beckett AH, and Rowland M (1965b) Urinary excretion kinetics of methylamphetamine in man. *J Pharm Pharmacol* **17**:109S-114S.

Beckett AH, and Rowland M (1965c) Urinary excretion of methylamphetamine in man. *Nature* **206**:1260–1261.

Beckett AH, Salmon JA, and Mitchard M (1969) The relation between blood levels and urinary excretion of amphetamine under controlled acidic and under fluctuating urinary pH values using [14C] amphetamine. *J Pharm Pharmacol* **21**:251–8.

Beconi MG, Howland D, Park L, Lyons K, Giuliano J, Dominguez C, Munoz-Sanjuan I, and Pacifici R (2012) Pharmacokinetics of memantine in rats and mice. *PLoS Curr*, doi: 10.1371/currents.RRN1291.

Benowitz N, Forsyth RP, Melmon KL, and Rowland M (1974) Lidocaine disposition kinetics in monkey and man I. Prediction by a perfusion model. *Clin Pharmacol Ther*, doi: 10.1002/cpt1974161part187.

Benowitz NL, and Jacob P (1985) Nicotine renal excretion rate influences nicotine intake during cigarette smoking. *J Pharmacol Exp Ther* **234**:153–5.

Bergman A, Bi Y an, Mathialagan S, Litchfield J, Kazierad DJ, Pfefferkorn JA, and Varma MVS (2019) Effect of Hepatic Organic Anion-Transporting Polypeptide 1B Inhibition and

Chronic Kidney Disease on the Pharmacokinetics of a Liver-Targeted Glucokinase Activator: A Model-Based Evaluation. *Clin Pharmacol Ther* **106**:792–802.

Biber TUL, Mylle M, Baines AD, Gottschalk CW, Oliver JR, and MacDowell MC (1968) A study by micropuncture and microdissection of acute renal damage in rats. *Am J Med* **44**:664–705.

Bischoff KB (1967) Applications of a Mathematical Model for Drug Distribution in Mammals, in *Chemical Engineering in Medicine and Biology* pp 417–446, Springer US, Boston, MA.

Bischoff KB, and Dedrick RL (1968) Thiopental pharmacokinetics. *J Pharm Sci*, doi: 10.1002/jps.2600570814.

Bjelland TW, Klepstad P, Haugen BO, Nilsen T, and Dale O (2013) Effects of hypothermia on the disposition of morphine, midazolam, fentanyl, and propofol in intensive care unit patients. *Drug Metab Dispos* **41**:214–223.

Blair AD, Burgess ED, Maxwell BM, and Cutler RE (1981) Sotalol kinetics in renal insufficiency. *Clin Pharmacol Ther* **29**:457–463.

Blum RA, Comstock TJ, Sica DA, Schultz RW, Keller E, Reetze P, Bockbrader H, Tuerck D, Busch JA, Reece PA, and Sedman AJ (1994) Pharmacokinetics of gabapentin in subjects with various degrees of renal function. *Clin Pharmacol Ther* **56**:154–159.

Boger E, and Fridén M (2019) Physiologically Based Pharmacokinetic/Pharmacodynamic Modeling Accurately Predicts the Better Bronchodilatory Effect of Inhaled Versus Oral Salbutamol Dosage Forms. *J Aerosol Med Pulm Drug Deliv* **32**:1–12.

Bois FY, Woodruff TJ, and Spear RC (1991) Comparison of three physiologically based pharmacokinetic models of benzene disposition. *Toxicol Appl Pharmacol* **110**:79–88.

Boxenbaum HG, Riegelman S, and Elashoff RM (1974) Statistical estimations in

pharmacokinetics. *J Pharmacokinet Biopharm* **2**:123–148.

Brater DC (2009) Drug dosing in patients with impaired renal function. *Clin Pharmacol Ther* **86**:483–489, Nature Publishing Group.

Bricker NS, Morrin PAF, and Kime SW (1960) The pathologic physiology of chronic bright's disease. *Am J Med* **28**:77–98.

Britz H, Hanke N, Volz A-K, Spigset O, Schwab M, Eissing T, Wendl T, Frechen S, and Lehr T (2019) PBPK models for CYP1A2 DDI prediction: a modelling network of fluvoxamine, theophylline, caffeine, rifampicin and midazolam. *CPT pharmacometrics Syst Pharmacol*, doi: 10.1002/psp4.12397.

Brown JW, and McKnight CJ (2010) Molecular model of the microvillar cytoskeleton and organization of the brush border. *PLoS One* **5**:e9406, Public Library of Science.

Brown RP, Delp MD, Lindstedt SL, Rhomberg LR, and Beliles RP (1997) Physiological parameter values for physiologically based pharmacokinetic models. *Toxicol Ind Health* **13**:407–84.

Burt HJ, Neuhoff S, Almond L, Gaohua L, Harwood MD, Jamei M, Rostami-Hodjegan A, Tucker GT, and Rowland-Yeo K (2016) Metformin and cimetidine: Physiologically based pharmacokinetic modelling to investigate transporter mediated drug-drug interactions. *Eur J Pharm Sci* **88**:70–82, Simcyp Limited.

Butler TC (1958) Introduction; termination of drug action by elimination of unchanged drug. *Fed Proc* **17**:1158–74.

Butler TC, MAHAFFEE C, and WADDELL WJ (1954) Phenobarbital: studies of elimination, accumulation, tolerance, and dosage schedules. *J Pharmacol Exp Ther* **111**:425–35.

CDER (2002) Application number 11-522. Clinical Pharmacology and biopharmaceutics

review(s).

CDER (2001) Application number 21-303. Clinical Pharmacology and biopharmaceutics review(s).

Chan K (1979) The effects of physiocochemical properties of pethidine and its basic metabolites on their buccal absorption and renal elimination. *J Pharm Pharmacol* **31**:672–5.

Chapin E, Zhan M, Hsu VD, Seliger SL, Walker LD, and Fink JC (2010) Adverse safety events in chronic kidney disease: The frequency of "Multiple Hits." *Clin J Am Soc Nephrol* **5**:95–101.

Chapron A, Shen DD, Kestenbaum BR, Robinson-Cohen C, Himmelfarb J, and Yeung CK (2017) Does Secretory Clearance Follow Glomerular Filtration Rate in Chronic Kidney Diseases? Reconsidering the Intact Nephron Hypothesis. *Clin Transl Sci* **10**:395–403.

Cheong EJY, Teo DWX, Chua DXY, and Chan ECY (2019) Systematic Development and Verification of A Physiologically-Based Pharmacokinetic Model of Rivaroxaban. *Drug Metab Dispos* dmd.119.086918.

Cheung KWK, Hsueh CH, Zhao P, Meyer TW, Zhang L, Huang SM, and Giacomini KM (2017) The Effect of Uremic Solutes on the Organic Cation Transporter 2. *J Pharm Sci* **106**:2551–2557, Elsevier Ltd.

Chiou WL (1989) The phenomenon and rationale of marked dependence of drug concentration on blood sampling site. Implications in pharmacokinetics, pharmacodynamics, toxicology and therapeutics (Part I). *Clin Pharmacokinet* **17**:175–99.

Chládek J, Zimová G, Beránek M, and Martínková J (2000) In-vivo indices of CYP2D6 activity: Comparison of dextromethorphan metabolic ratios in 4-h urine and 3-h plasma. *Eur J Clin Pharmacol* **56**:651–657.

Cockcroft DW, and Gault MH (1976) Prediction of creatinine clearance from serum creatinine. *Nephron* **16**:31–41.

Cook CE, Jeffcoat AR, Hill JM, Pugh DE, Patetta PK, Sadler BM, White WR, and Perez-Reyes M (1993) Pharmacokinetics of methamphetamine self-administered to human subjects by smoking S-(+)-methamphetamine hydrochloride. *Drug Metab Dispos* **21**:717–23.

Cook JD, Strauss KA, Caplan YH, LoDico CP, and Bush DM (2007) Urine pH: The effects of time and temperature after collection. *J Anal Toxicol* **31**:486–496.

Cooper KE, Edholm OG, and Mottram RF (1955) The blood flow in skin and muscle of the human forearm. *J Physiol* **128**:258–67.

Darwish M, Kirby M, Robertson P, Hellriegel E, and Jiang JG (2006) Comparison of equivalent doses of fentanyl buccal tablets and arteriovenous differences in fentanyl pharmacokinetics. *Clin Pharmacokinet* **45**:843–50.

Darwish M, Kirby M, Robertson P, Tracewell W, and Xie F (2010) Dose Proportionality of Fentanyl Buccal Tablet in Doses Ranging from 600 to 1300 μg in Healthy Adult Subjects. *Clin Drug Investig* **30**:1.

Darwish M, Tempero K, Kirby M, and Thompson J (2006) Relative bioavailability of the fentanyl effervescent buccal tablet (FEBT) 1080 pg versus Oral transmucosal fentanyl citrate 1600 pg and dose proportionality of FEBT 270 to 1300 μg: A single-dose, randomized, open-label, three-period study in healthy adul. *Clin Ther* **28**:715–724.

Dedrick RL, Zaharko DS, and Lutz RJ (1973) Transport and binding of methotrexate in vivo. *J Pharm Sci*, doi: 10.1002/jps.2600620603.

Di L, Whitney-Pickett C, Umland JP, Zhang H, Zhang X, Gebhard DF, Lai Y, Federico JJ, Davidson RE, Smith R, Reyner EL, Lee C, Feng B, Rotter C, Varma M V, Kempshall S,

Fenner K, El-Kattan AF, Liston TE, and Troutman MD (2011) Development of a new permeability assay using low-efflux MDCKII cells. *J Pharm Sci* **100**:4974–85.

Doddareddy MR, Cho YS, Koh HY, Kim DH, and Pae AN (2006) In silico renal clearance model using classical Volsurf approach. *J Chem Inf Model* **46**:1312–20.

Eaves ER, and Korman MG (1984) Cholestyramine induced hyperchloremic metabolic acidosis. *Aust N Z J Med* **14**:670–2.

Edwards SR, and Mather LE (2001) Tissue uptake of ketamine and norketamine enantiomers in the rat: indirect evidence for extrahepatic metabolic inversion. *Life Sci* **69**:2051–66.

Elia M, and Kurpad A (1993) What is the blood flow to resting human muscle? *Clin Sci (Lond)* **84**:559–63.

Emami Riedmaier A, Burt H, Abduljalil K, and Neuhoff S (2016) More Power to OATP1B1: An Evaluation of Sample Size in Pharmacogenetic Studies Using a Rosuvastatin PBPK Model for Intestinal, Hepatic, and Renal Transporter-Mediated Clearances. *J Clin Pharmacol* **56 Suppl 7**:S132-42.

Ericsson H, Bredberg U, Eriksson U, Jolin-Mellgård A, Nordlander M, and Regårdh CG (2000) Pharmacokinetics and arteriovenous differences in clevidipine concentration following a short- and a long-term intravenous infusion in healthy volunteers. *Anesthesiology* **92**:993–1001.

Fabbri A (2003) Comprehensive drug screening in decision making of patients attending the emergency department for suspected drug overdose. *Emerg Med J* **20**:25–28.

FDA (2011) Fentanyl (FENTORA): US prescribing information.

FDA (2010) Memantine (Namenda): US prescribing information. 1–21.

Freudenthaler S, Meineke I, Schreeb KH, Boakye E, Gundert-Remy U, and Gleiter CH (1998)

Influence of urine pH and urinary flow on the renal excretion of memantine. *Br J Clin Pharmacol* **46**:541–546.

Fukuda M, Motokawa M, Miyagi S, Sengo K, Muramatsu W, Kato N, Usami T, Yoshida A, and Kimura G (2006) Polynocturia in chronic kidney disease is related to natriuresis rather than to water diuresis. *Nephrol Dial Transplant* **21**:2172–2177.

Furst DE, Tozer TN, and Melmon KL (1979) Salicylate clearance, the resultant of protein binding and metabolism. *Clin Pharmacol Ther* **26**:380–389.

Gerhardt RE, Knouss RF, Thyrum PT, Luchi RJ, and Morris JJ (1969) Quinidine excretion in aciduria and alkaluria. *Ann Intern Med* **71**:927–33.

Goodman LS, Gilman A, Brunton LL, Lazo JS, and Parker KL (2006) Goodman & Gilman's the pharmacological basis of therapeutics (11th ed.), New York: McGraw-Hill.

Gourlay SG, and Benowitz NL (1997) Arteriovenous differences in plasma concentration of nicotine and catecholamines and related cardiovascular effects after smoking, nicotine nasal spray, and intravenous nicotine. *Clin Pharmacol Ther* **62**:453–463.

Gram LF, Kofod B, Christiansen J, and Rafaelsen OJ (1971) Imipramine metabolism: PH-Dependent distribution and urinary excretion. *Clin Pharmacol Ther* **12**:239–244.

Grès M, Julian J, Bourriè M, Meunier V., Roques C., Berger M., Boulenc X., Berger Y, and Fabre G (1998) Correlation Between Oral Drug Absorption in Humans, and Apparent Drug Permeability in TC-7 Cells, A Human Epithelial Intestinal Cell Line: Comparsion with the Parental Caco-2 Cell line. *Pharm Res* **15**:726–733.

Grillo JA, Zhao P, Bullock J, Booth BP, Lu M, Robie-suh K, and Gil E (2012) Utility of a physiologically – based pharmacokinetic (PBPK) modeling approach to quantitatively predict a complex drug – drug – disease interaction scenario for rivaroxaban during the drug

review process : implications for clinical practice. *Biopharm Drug Dispos* **33**:99–110.

Grimstein M, Yang Y, Zhang X, Grillo J, Huang S-M, Zineh I, and Wang Y (2018) Physiologically-based Pharmacokinetic (PBPK) Modeling in Regulatory Science: An Update from the US Food and Drug Administration's Office of Clinical Pharmacology. *J Pharm Sci* **108**:21–25, Elsevier Ltd.

Grimstein M, Yang Y, Zhang X, Grillo J, Huang SM, Zineh I, and Wang Y (2019) Physiologically Based Pharmacokinetic Modeling in Regulatory Science: An Update From the U.S. Food and Drug Administration's Office of Clinical Pharmacology. *J Pharm Sci* **108**:21–25, Elsevier Ltd.

Gumbleton M, Oie S, and Verotta D (1994) Pharmacokinetic-pharmacodynamic (PK-PD) modelling in non-steady-state studies and arterio-venous drug concentration differences. *Br J Clin Pharmacol* **38**:389–400.

Hamilton WF, Moore JW, Kinsman JM, and Spurling RG (1932) STUDIES ON THE CIRCULATION. *Am J Physiol Content* **99**:534–551.

Hanke N, Frechen S, Moj D, Britz H, Eissing T, Wendl T, and Lehr T (2018) PBPK Models for CYP3A4 and P-gp DDI Prediction: A Modeling Network of Rifampicin, Itraconazole, Clarithromycin, Midazolam, Alfentanil, and Digoxin. *CPT pharmacometrics Syst Pharmacol* **7**:647–659.

Harris DS, Boxenbaum H, Everhart ET, Sequeira G, Mendelson JE, and Jones RT (2003) The bioavailability of intranasal and smoked methamphetamine. *Clin Pharmacol Ther* **74**:475–486.

Harrison LI, and Gibaldi M (1977) Physiologically based pharmacokinetic model for digoxin disposition in dogs and its preliminary application to humans. *J Pharm Sci*, doi:

10.1002/jps.2600661206.

Himmelstein KJ, and Lutz RJ (1979) A review of the applications of physiologically based pharmacokinetic modeling. *J Pharmacokinet Biopharm* **7**:127–145.

Hotchkiss AG, Gao T, Khan U, Berrigan L, Li M, Ingraham L, and Pelis RM (2015) Organic anion transporter 1 is inhibited by multiple mechanisms and shows a transport mode independent of exchanges. *Drug Metab Dispos* **43**:1847–1854.

Houghton G, Dennis M, and Gabriel R (1985) Pharmacokinetics of metronidazole in patients with varying degrees of renal failure. *Br J Clin Pharmacol* **19**:203–209.

Hovgaard L, Brøndsted H, Buur A, and Bundgaard H (1995) Drug delivery studies in Caco-2 monolayers. Synthesis, hydrolysis, and transport of O-cyclopropane carboxylic acid ester prodrugs of various beta-blocking agents. *Pharm Res* **12**:387–92.

Hsu V, Vieira MDLT, Zhao P, Zhang L, Zheng JH, Nordmark A, Berglund EG, Giacomini KM, and Huang SM (2014) Towards quantitation of the effects of renal impairment and probenecid inhibition on kidney uptake and efflux transporters, using physiologically based pharmacokinetic modelling and simulations. *Clin Pharmacokinet* **53**:283–293.

Hsueh CH, Hsu V, Zhao P, Zhang L, Giacomini KM, and Huang SM (2018) PBPK Modeling of the Effect of Reduced Kidney Function on the Pharmacokinetics of Drugs Excreted Renally by Organic Anion Transporters. *Clin Pharmacol Ther* **103**:485–492.

Hsueh CH, Yoshida K, Zhao P, Meyer TW, Zhang L, Huang SM, and Giacomini KM (2016) Identification and quantitative assessment of uremic solutes as inhibitors of renal organic anion transporters, OAT1 and OAT3. *Mol Pharm* **13**:3130–3140.

Huang Q, and Riviere JE (2014) The application of allometric scaling principles to predict pharmacokinetic parameters across species. *Expert Opin Drug Metab Toxicol* **10**:1241–

1253.

Huang SM, Abernethy DR, Wang Y, Zhao P, and Zineh I (2013) The utility of modeling and simulation in drug development and regulatory review. *J Pharm Sci* **102**:2912–2923.

Huang SM, and Rowland M (2012) The Role of Physiologically Based Pharmacokinetic Modeling in Regulatory Review. *Clin Pharmacol Ther* **91**:542–549.

Huang SM, Zhang L, and Giacomini KM (2010) The international transporter consortium: A collaborative group of scientists from academia, industry, and the FDA. *Clin Pharmacol Ther* **87**:32–36, Nature Publishing Group.

Huang W, Czuba LC, and Isoherranen N (2020) Mechanistic PBPK Modeling of Urine pH Effect on Renal and Systemic Disposition of Methamphetamine and Amphetamine. *J Pharmacol Exp Ther* **373**:488–501.

Huang W, and Isoherranen N (2018) Development of a Dynamic Physiologically Based Mechanistic Kidney Model to Predict Renal Clearance. *CPT Pharmacometrics Syst Pharmacol* **7**:593–602.

Huang W, and Isoherranen N (2020) Sampling Site Has a Critical Impact on Physiologically Based Pharmacokinetic Modeling. *J Pharmacol Exp Ther* **372**:30–45.

Huang W, Nakano M, Sager J, Ragueneau-Majlessi I, and Isoherranen N (2017) Physiologically Based Pharmacokinetic Model of the CYP2D6 Probe Atomoxetine: Extrapolation to Special Populations and Drug-Drug Interactions. *Drug Metab Dispos* **45**:1156–1165.

Huh Y, Smith DE, and Rose Feng M (2011) Interspecies scaling and prediction of human clearance: Comparison of small- and macro-molecule drugs. *Xenobiotica* **41**:972–987.

Irvine JD, Takahashi L, Lockhart K, Cheong J, Tolan JW, Selick HE, Grove JR, and Rove JRUG (1999) MDCK (Madin − Darby Canine Kidney) Cells: A Tool for Membrane Permeability

Screening. *J Pharm Sci* **88**:28–33.

Isohanni MH, Ahonen J, Neuvonen PJ, and Olkkola KT (2005) Effect of ciprofloxin on the pharmacokinetics of intravenous lidocaine. *Eur J Anaesthesiol* **22**:795–9.

Ito S, Ando H, Ose A, Kitamura Y, Ando T, Kusuhara H, and Sugiyama Y (2013) Relationship between the urinary excretion mechanisms of drugs and their physicochemical properties. *J Pharm Sci* **102**:3294–3301, Elsevier Masson SAS.

Jacobs JR, and Nath PA (1995) Compartment model to describe peripheral arterial-venous drug concentration gradients with drug elimination from the venous sampling compartment. *J Pharm Sci* **84**:370–5.

Jamei M (2016) Recent Advances in Development and Application of Physiologically-Based Pharmacokinetic (PBPK) Models: a Transition from Academic Curiosity to Regulatory Acceptance. *Curr Pharmacol Reports* **2**:161–169, Current Pharmacology Reports.

Jamei M, Turner D, Yang J, Neuhoff S, Polak S, Rostami-Hodjegan A, and Tucker G (2009) Population-based mechanistic prediction of oral drug absorption. *AAPS J* **11**:225–237.

Johnson TN, Boussery K, Rowland-Yeo K, Tucker GT, and Rostami-Hodjegan A (2010) A semi-mechanistic model to predict the effects of liver cirrhosis on drug clearance. *Clin Pharmacokinet* **49**:189–206.

Jones H, and Rowland-Yeo K (2013) Basic Concepts in Physiologically Based Pharmacokinetic Modeling in Drug Discovery and Development. *CPT Pharmacometrics Syst Pharmacol* **2**:e63.

Jones HM, Dickins M, Youdim K, Gosset JR, Attkins NJ, Hay TL, Gurrell IK, Logan YR, Bungay PJ, Jones BC, and Gardner IB (2012) Application of PBPK modelling in drug discovery and development at Pfizer. *Xenobiotica* **42**:94–106.

Jones HM, Gardner IB, and Watson KJ (2009) Modelling and PBPK simulation in drug discovery. *AAPS J* **11**:155–66.

Jones HM, Mayawala K, and Poulin P (2013) Dose selection based on physiologically based pharmacokinetic (PBPK) approaches. *AAPS J* **15**:377–87.

Jones HM, Parrott N, Jorga K, and Lavé T (2006a) A novel strategy for physiologically based predictions of human pharmacokinetics. *Clin Pharmacokinet* **45**:511–542.

Jones HM, Parrott N, Jorga K, and Lavé T (2006b) A novel strategy for physiologically based predictions of human pharmacokinetics. *Clin Pharmacokinet* **45**:511–542.

Kärkkäinen S, and Neuvonen PJ (1986) Pharmacokinetics of amitriptyline influenced by oral charcoal and urine pH. *Int J Clin Pharmacol Ther Toxicol* **24**:326–32.

Kaur N, Narang A, and Bansal AK (2018) Use of biorelevant dissolution and PBPK modeling to predict oral drug absorption. *Eur J Pharm Biopharm* **129**:222–246, Elsevier.

KDIGO (2013) The Kidney Disease: Improving Global Outcomes (KDIGO) 2012 Clinical Practice Guideline for the Evaluation and Management of Chronic Kidney Disease (CKD). *Kidney Int Suppl* **3**:19–62.

Kennedy T (1997) Managing the drug discovery/development interface. *Drug Discov Today* **2**:436–444, Elsevier Science Ltd.

Khalil F, and Läer S (2011) Physiologically based pharmacokinetic modeling: methodology, applications, and limitations with a focus on its role in pediatric drug development. *J Biomed Biotechnol* **2011**:907461.

Kiddie MA, Kaye CM, Turner P, and Shaw TR (1974) The influence of urinary pH on the elimination of mexiletine. *Br J Clin Pharmacol* **1**:229–32.

Kim I, Oyler JM, Moolchan ET, Cone EJ, and Huesitis MA (2004) Urinary pharmacokinetics of

methamphetamine and its metabolite, amphetamine following controlled oral administration to humans. *Ther Drug Monit* **26**:664–672.

Kirch W, Ohnhaus EE, Dylewicz P, Pabst J, and Storstein L (1986) Bioavailability and elimination of digitoxin in patients with hepatorenal insufficiency. *Am Heart J* **111**:325–329.

Knights KM, Rowland A, and Miners JO (2013) Renal drug metabolism in humans: The potential for drug-endobiotic interactions involving cytochrome P450 (CYP) and UDP-glucuronosyltransferase (UGT). *Br J Clin Pharmacol* **76**:587–602.

Kuepfer L, Niederalt C, Wendl T, Schlender JF, Willmann S, Lippert J, Block M, Eissing T, and Teutonico D (2016) Applied Concepts in PBPK Modeling: How to Build a PBPK/PD Model. *CPT Pharmacometrics Syst Pharmacol* **5**:516–531.

Kunze A, Huwyler J, Poller B, Gutmann H, and Camenisch G (2014) In vitro-in vivo extrapolation method to predict human renal clearance of drugs. *J Pharm Sci* **103**:994–1001.

Lai HC, Chang SN, Lin HC, Hsu YL, Wei HM, Kuo CC, Hwang KP, and Chiang HY (2019) Association between urine pH and common uropathogens in children with urinary tract infections. *J Microbiol Immunol Infect*, doi: 10.1016/j.jmii.2019.08.002, Elsevier Taiwan LLC.

Lane EA, and Levy RH (1980) Prediction of steady-state behavior of metabolite from dosing of parent drug. *J Pharm Sci* **69**:610–2.

Leeson PD, and St-Gallay SA (2011) The influence of the “organizational factor” on compound quality in drug discovery. *Nat Rev Drug Discov* **10**:749–765, Nature Publishing Group.

Levey AS, and Coresh J (2012) Chronic kidney disease. *Lancet* **379**:165–180, Elsevier Ltd.

Levey AS, Stevens LA, Schmid CH, Zhang Y (Lucy), Castro AF, Feldman HI, Kusek JW, Eggers P, Van Lente F, Greene T, and Coresh J (2009) A New Equation to Estimate Glomerular Filtration Rate. *Ann Intern Med* **150**:604.

Levitt DG (2004) Physiologically based pharmacokinetics modeling of arterial - Antecubital vein concentration difference. *BMC Clin Pharmacol* **4**:1–23.

Li L, Everhart T, Jacob P, Jones R, and Mendelson J (2010) Stereoselectivity in the human metabolism of methamphetamine. *Br J Clin Pharmacol* **69**:187–192.

Lindberg AA, Nilsson LHS, Bucht H, and Kallings LO (1966) Concentration of Chloramphenicol in the Urine and Blood in Relation to Renal Function. *Br Med J* **2**:724–728.

Liu L, and Pang KS (2006) An integrated approach to model hepatic drug clearance. *Eur J Pharm Sci* **29**:215–230.

Luzon E, Blake K, Cole S, Nordmark A, Versantvoort C, and Berglund EG (2017) Physiologically based pharmacokinetic modeling in regulatory decision-making at the European Medicines Agency. *Clin Pharmacol Ther* **102**:98–105.

Maalouf NM, Cameron MA, Moe OW, and Sakhaee K (2010) Metabolic basis for low urine pH in type 2 diabetes. *Clin J Am Soc Nephrol* **5**:1277–1281.

Maalouf NM, Sakhaee K, Parks JH, Coe FL, Adams-Huet B, and Pak CYC (2004) Association of urinary pH with body weight in nephrolithiasis. *Kidney Int* **65**:1422–1425.

Macleod DB, Habib AS, Ikeda K, Spyker DA, Cassella J V, Ho KY, and Gan TJ (2012) Inhaled fentanyl aerosol in healthy volunteers: pharmacokinetics and pharmacodynamics. *Anesth Analg* **115**:1071–7.

Macpherson CR, Milne MD, and Evans BM (1955) The excretion of salicylate. *Br J Pharmacol*

Chemother **10**:484–9.

Manallack DT (2007) The pK(a) Distribution of Drugs: Application to Drug Discovery. *Perspect Medicin Chem* **1**:25–38.

Manga N, Duffy JC, Rowe PH, and Cronin MTD (2003) A hierarchical QSAR model for urinary excretion of drugs in humans as a predictive tool for biotransformation. *QSAR Comb Sci* **22**:263–273.

Marchand A, Aranda-Rodriguez R, Tardif R, Nong A, and Haddad S (2015) Human inhalation exposures to toluene, ethylbenzene, and m-xylene and physiologically based pharmacokinetic modeling of exposure biomarkers in exhaled air, blood, and urine. *Toxicol Sci* **144**:414–424.

MATLAB (2016) version 9.0, The MathWorks Inc., Natick, Massachusetts.

Matsuzaki T, Scotcher D, Darwich AS, Galetin A, and Rostami-Hodjegan A (2019) Towards Further Verification of Physiologically-Based Kidney Models: Predictability of the Effects of Urine-Flow and Urine-pH on Renal Clearance. *J Pharmacol Exp Ther* **368**:157–168.

McNay JL, and Miyazaki M (1973) Regional increases in mass and flow during compensatory renal hypertrophy. *Am J Physiol* **224**:219–222.

Mendelson J, Jones RT, and Upton R (1995) Methamphetamine in humans and ethanol interactions. *Clin Pharmacol Ther* **57**:559–568.

Mendelson J, Uemura N, Harris D, Nath RP, Fernandez E, Jacob P, Everhart ET, and Jones RT (2006) Human pharmacology of the methamphetamine stereoisomers. *Clin Pharmacol Ther* **80**:403–420.

Miller NA, Reddy MB, Heikkinen AT, Lukacova V, and Parrott N (2019) Physiologically Based Pharmacokinetic Modelling for First-In-Human Predictions: An Updated Model Building

Strategy Illustrated with Challenging Industry Case Studies. *Clin Pharmacokinet*, doi: 10.1007/s40262-019-00741-9.

Milne MD, Scribner BH, and Crawford MA (1958) Non-ionic diffusion and the excretion of weak acids and bases. *Am J Med* **24**:709–29.

Min JS, and Bae SK (2017) Prediction of drug-drug interaction potential using physiologically based pharmacokinetic modeling. *Arch Pharm Res* **40**:1356–1379.

Moeller KE, Kissack JC, Atayee RS, and Lee KC (2017) Clinical Interpretation of Urine Drug Tests. *Mayo Clin Proc* **92**:774–796, Mayo Foundation for Medical Education and Research.

Moksnes K, Fredheim OM, Klepstad P, Kaasa S, Angelsen A, Nilsen T, and Dale O (2008) Early pharmacokinetics of nasal fentanyl: Is there a significant arterio-venous difference? *Eur J Clin Pharmacol* **64**:497–502.

Möller E, McIntosh JF, and Van Slyke DD (1928) STUDIES OF UREA EXCRETION. II: Relationship Between Urine Volume and the Rate of Urea Excretion by Normal Adults. *J Clin Invest* **6**:427–65.

Montay G, Jacquot C, Bariety J, and Cunci R (1985) Pharmacokinetics of pefloxacin in renal insufficiency. *Eur J Clin Pharmacol* **29**:345–349.

Mori K, Saito R, Nakamaru Y, Shimizu M, and Yamazaki H (2016) Physiologically based pharmacokinetic-pharmacodynamic modeling to predict concentrations and actions of sodium-dependent glucose transporter 2 inhibitor canagliflozin in human intestines and renal tubules. *Biopharm Drug Dispos* **37**:491–506.

Moviat M, Pickkers P, van der Voort PHJ, and van der Hoeven JG (2006) Acetazolamide-mediated decrease in strong ion difference accounts for the correction of metabolic alkalosis in critically ill patients. *Crit Care* **10**.

Muhiddin KA, Johnston A, and Turner P (1984) The influence of urinary pH on flecainide excretion and its serum pharmacokinetics. *Br J Clin Pharmacol* **17**:447–51.

Müller F, Weitz D, Derdau V, Sandvoss M, Mertsch K, König J, and Fromm MF (2017) Contribution of MATE1 to Renal Secretion of the NMDA Receptor Antagonist Memantine. *Mol Pharm* **14**:1–8.

Musther H, Gill KL, Chetty M, Rostami-Hodjegan A, Rowland M, and Jamei M (2015) Are Physiologically Based Pharmacokinetic Models Reporting the Right Cmax? Central Venous Versus Peripheral Sampling Site. *AAPS J* **17**:1268–1279.

Nakanishi N, Fukui M, Tanaka M, Toda H, Imai S, Yamazaki M, Hasegawa G, Oda Y, and Nakamura N (2012) Low urine pH is a predictor of chronic kidney disease. *Kidney Blood Press Res* **35**:77–81.

Naruhashi K, Tamai I, Sai Y, Suzuki N, and Tsuji A (2001) Secretory transport of p-aminohippuric acid across intestinal epithelial cells in Caco-2 cells and isolated intestinal tissue. *Journalof Phamrcy and Phamacology* **53**:73–81.

Nechita AM, Rădulescu D, Peride I, Niculae A, Bratu O, Ferechide D, Ciocâlteu A, Checheriță IA, and Mischianu D (2015) Determining factors of diuresis in chronic kidney disease patients initiating hemodialysis. *J Med Life* **8**:371–377.

Nelson E (1961) Kinetics of drug absorption, distribution, metabolism, and excretion. *J Pharm Sci* **50**:181–192.

Neuhoff S, Lu G, Howard B, Masoud J, Li L, Tucker GT, and Rostami-Hodjegan A (2013) Accounting for transporters in renal clearance: towards a mechanistic kidney model (Mech Kim). *Transp Drug Dev* 155–177, Springer.

Neuvonen PJ, and Kärkkäinen S (1983) Effects of charcoal, sodium bicarbonate, and ammonium

chloride on chlorpropamide kinetics. *Clin Pharmacol Ther* **33**:386–93.

Newton TF, Roache JD, De La Garza R 2nd, Fong T, Wallace CL, Li S-H, Elkashef A, Chiang N, Kahn R, T.F. N, J.D. R, R. DLGII, T. F, C.L. W, S.-H. L, A. E, and N. C (2005) Safety of intravenous methamphetamine administration during treatment with bupropion. *Psychopharmacology (Berl)* **182**:426–435.

Offman E, and Edginton AN (2015) A PBPK workflow for first-in-human dose selection of a subcutaneously administered pegylated peptide. *J Pharmacokinet Pharmacodyn* **42**:135–50.

Olofsen E, Mooren R, van Dorp E, Aarts L, Smith T, den Hartigh J, Dahan A, and Sarton E (2010) Arterial and venous pharmacokinetics of morphine-6-glucuronide and impact of sample site on pharmacodynamic parameter estimates. *Anesth Analg* **111**:626–32.

Ortiz RH, Maître A, Barbeau D, Lafontaine M, and Bouchard M (2014) Use of physiologically-based pharmacokinetic modeling to simulate the profiles of 3-hydroxybenzo(a)pyrene in workers exposed to polycyclic aromatic hydrocarbons. *PLoS One* **9**.

Oyler JM, Cone EJ, Joseph RE, Moolchan ET, and Huestis MA (2002) Duration of detectable methamphetamine and amphetamine excretion in urine after controlled oral administration of methamphetamine to humans. *Clin Chem* **48**:1703–14.

Paine MF, Hart HL, Ludington SS, Haining RL, Rettie AE, and Zeldin DC (2006) The human intestinal cytochrome P450 “pie.” *Drug Metab Dispos* **34**:880–886.

Paine SW, Barton P, Bird J, Denton R, Menochet K, Smith A, Tomkinson NP, and Chohan KK (2010) A rapid computational filter for predicting the rate of human renal clearance. *J Mol Graph Model* **29**:529–537.

Paine SW, Ménochet K, Denton R, McGinnity DF, and Riley RJ (2011) Prediction of Human Renal Clearance from Preclinical Species for a Diverse Set of Drugs That Exhibit Both

Active Secretion and Net Reabsorption. *Drug Metab Dispos* **39**.

Pang KS, and Rowland M (1977) Hepatic clearance of drugs. I. Theoretical considerations of a "well-stirred" model and a "parallel tube" model. Influence of hepatic blood flow, plasma and blood cell binding, and the hepatocellular enzymatic activity on hepatic drug clearance. *J Pharmacokinet Biopharm* **5**:625–653.

Pennell JP, and Bourgoignie JJ (1981) Adaptive changes of juxtamedullary glomerular filtration in the remnant kidney. *Pflügers Arch Eur J Physiol* **389**:131–135.

Perez-Reyes M, White WR, McDonald SA, Hicks RE, Jeffcoat AR, Hill JM, and Cook CE (1991) Clinical effects of daily methamphetamine administration. *Clin Neuropharmacol* **14**:352–8.

Persson J, Hasselström J, Maurset A, Oye I, Svensson JO, Almqvist O, Scheinin H, Gustafsson LL, and Almqvist O (2002) Pharmacokinetics and non-analgesic effects of S- and R-ketamines in healthy volunteers with normal and reduced metabolic capacity. *Eur J Clin Pharmacol* **57**:869–75.

Phillips MB, Yoon M, Young B, and Tan Y-M (2014) Analysis of biomarker utility using a PBPK/PD model for carbaryl. *Front Pharmacol* **5**:1–10.

Pichardo-Almarza C, and Diaz-Zuccarini V (2016) From PK/PD to QSP: Understanding the Dynamic Effect of Cholesterol-Lowering Drugs on Atherosclerosis Progression and Stratified Medicine. *Curr Pharm Des* **22**:6903–6910.

Pitsiu M, Gries J, Benowitz N, Gourlay SG, and Verotta D (2002) Modeling nicotine arterial-venous differences to predict arterial concentrations and input based on venous measurements: application to smokeless tobacco and nicotine gum. *J Pharmacokinet Pharmacodyn* **29**:383–402.

Posada MM, Bacon JA, Schneck KB, Tirona RG, Kim RB, Higgins JW, Pak YA, Hall SD, and Hillgren KM (2015) Prediction of renal transporter mediated drug-drug interactions for pemetrexed using physiologically based pharmacokinetic modeling. *Drug Metab Dispos* **43**:325–334.

Prentis R, Lis Y, and Walker S (1988) Pharmaceutical innovation by the seven UK-owned pharmaceutical companies (1964-1985). *Br J Clin Pharmacol* **25**:387–396.

Randall B (2004) *Disposition of toxic drugs and chemicals in man, seven edition*.

Reiner JM (1953) The study of metabolic turnover rates by means of isotopic tracers. I. Fundamental relations. *Arch Biochem Biophys* **46**:53–79.

Rentsch KM, Kullak-Ublick GA, Reichel C, Meier PJ, and Fattinger K (2001) Arterial and venous pharmacokinetics of intravenous heroin in subjects who are addicted to narcotics. *Clin Pharmacol Ther* **70**:237–246.

Roberts MS, and Rowland M (1986) A dispersion model of hepatic elimination: 1. Formulation of the model and bolus considerations. *J Pharmacokinet Biopharm* **14**:227–260.

Rodgers T, Leahy D, and Rowland M (2005) Physiologically based pharmacokinetic modeling 1: Predicting the tissue distribution of moderate-to-strong bases. *J Pharm Sci* **94**:1259–1276, Elsevier Masson SAS.

Rodgers T, and Rowland M (2007) Mechanistic approaches to volume of distribution predictions: Understanding the processes. *Pharm Res* **24**:918–933.

Rostami-Hodjegan A (2018) Reverse Translation in PBPK and QSP: Going Backwards in Order to Go Forward With Confidence. *Clin Pharmacol Ther* **103**:224–232.

Rowland M (1969) Amphetamine blood and urine levels in man. *J Pharm Sci* **58**:508–9.

Rowland M , and Tozer T (2012) *Clinical Pharmacokinetics and Pharmacodynamics: Concepts*

and Applications, 4 edition, Lippincott Williams & Wilkins.

Rowland M, Peck C, and Tucker G (2011) Physiologically-based pharmacokinetics in drug development and regulatory science. *Annu Rev Pharmacol Toxicol* **51**:45–73.

Rowland Yeo K, Aarabi M, Jamei M, and Rostami-Hodjegan a (2011) Modeling and predicting drug pharmacokinetics in patients with renal impairment. *Expert Rev Clin Pharmacol* **4**:261–274.

Sager JE, Price LSL, and Isoherranen N (2016) Stereoselective Metabolism of Bupropion to OH-bupropion, Threohydrobupropion, Erythrohydrobupropion, and 4'-OH-bupropion in vitro. *Drug Metab Dispos* **44**:1709–19.

Sager JE, Yu J, Ragueneau-Majlessi I, and Isoherranen N (2015) Physiologically Based Pharmacokinetic (PBPK) Modeling and Simulation Approaches: A Systematic Review of Published Models, Applications, and Model Verification. *Drug Metab Dispos* **43**:1823–37.

Sayama H, Takubo H, Komura H, Kogayu M, and Iwaki M (2014) Application of a Physiologically Based Pharmacokinetic Model Informed by a Top-Down Approach for the Prediction of Pharmacokinetics in Chronic Kidney Disease Patients. *Aaps J* **16**:1018–1028.

Schmidt IM, Hübner S, Nadal J, Titze S, Schmid M, Bärthlein B, Schlieper G, Dienemann T, Schultheiss UT, Meiselbach H, Köttgen A, Flöge J, Busch M, Kreutz R, Kielstein JT, and Eckardt KU (2019) Patterns of medication use and the burden of polypharmacy in patients with chronic kidney disease: The German Chronic Kidney Disease study. *Clin Kidney J* **12**:663–672.

Scotcher D, Jones C, Rostami-Hodjegan A, and Galetin A (2016) Novel minimal physiologically-based model for the prediction of passive tubular reabsorption and renal excretion clearance. *Eur J Pharm Sci* **94**:59–71, Elsevier B.V.

Scotcher D, Jones CR, Galetin A, and Rostami-Hodjegan A (2017) Delineating the Role of Various Factors in Renal Disposition of Digoxin through Application of Physiologically Based Kidney Model to Renal Impairment Populations. *J Pharmacol Exp Ther* **360**:484–495.

Secora A, Alexander GC, Ballew SH, Coresh J, and Grams ME (2018) Kidney Function, Polypharmacy, and Potentially Inappropriate Medication Use in a Community-Based Cohort of Older Adults. *Drugs and Aging* **35**:735–750, Springer International Publishing.

Sharpstone P (1969) The renal handling of trimethoprim and sulphamethoxazole in man. *Postgrad Med J* **45**:Suppl:38-42.

Shebley M, Sandhu P, Emami Riedmaier A, Jamei M, Narayanan R, Patel A, Peters SA, Reddy VP, Zheng M, de Zwart L, Beneton M, Bouzom F, Chen J, Chen Y, Cleary Y, Collins C, Dickinson GL, Djebli N, Einolf HJ, Gardner I, Huth F, Kazmi F, Khalil F, Lin J, Odinecs A, Patel C, Rong H, Schuck E, Sharma P, Wu SP, Xu Y, Yamazaki S, Yoshida K, and Rowland M (2018) Physiologically Based Pharmacokinetic Model Qualification and Reporting Procedures for Regulatory Submissions: A Consortium Perspective. *Clin Pharmacol Ther* **104**:88–110.

Sheiner LB, Rosenberg B, and Marathe V V. (1977) Estimation of population characteristics of pharmacokinetic parameters from routine clinical data. *J Pharmacokinet Biopharm* **5**:445–479.

Shirasaka Y, Sager JE, Lutz JD, Davis C, and Isoherranen N (2013) Inhibition of CYP2C19 and CYP3A4 by omeprazole metabolites and their contribution to drug-drug interactionss. *Drug Metab Dispos* **41**:1414–1424.

Sjöqvist F, Berglund F, Borgå O, Hammer W, Andersson S, and Thorstrand C (1969) The pH-

dependent excretion of monomethylated tricyclic antidepressants. In dog and man. *Clin Pharmacol Ther* **10**:826–833.

Smeets PHE, Van Aubel RAMH, Wouterse AC, Van Den Heuvel JJMW, and Russel FGM (2004) Contribution of multidrug resistance protein 2 (MRP2/ABCC2) to the renal excretion of p-aminohippurate (PAH) and identification of MRP4 (ABCC4) as a novel PAH transporter. *J Am Soc Nephrol* **15**:2828–2835.

Sodhi JK, Wang H-J, and Benet LZ (2020) Are there any experimental perfusion data that preferentially support the dispersion and parallel tube models over the well-stirred model of organ elimination? *Drug Metab Dispos* dmd.120.090530.

Solomon AK (1949) EQUATIONS FOR TRACER EXPERIMENTS. *J Clin Invest* **28**:1297–1307.

Solomon AK (1953) The Kinetics of Biological Processes Special Problems Connected with the Use of Tracers, in *Advances in biological and medical physics* pp 65–97.

Tan ML, Yoshida K, Zhao P, Zhang L, Nolin TD, Piquette-Miller M, Galetin A, and Huang SM (2018) Effect of Chronic Kidney Disease on Nonrenal Elimination Pathways: A Systematic Assessment of CYP1A2, CYP2C8, CYP2C9, CYP2C19, and OATP. *Clin Pharmacol Ther* **103**:854–867.

Teorell T (1937a) Kinetics of distribution of substances administered to the body, I: The extravascular modes of administration. *Arch Int Pharmacodyn Ther* **57**:205–225.

Teorell T (1937b) Kinetics of distribution of substances administered to the body, II : The intravascular modes of administration. *Arch Int Pharmacodyn Ther* **57**:226–240.

Thomas R, Kanso A, and Sedor JR (2008) Chronic Kidney Disease and Its Complications. *Prim Care - Clin Off Pract* **35**:329–344.

Tsamandouras N, Rostami-Hodjegan A, and Aarons L (2015) Combining the “bottom up” and “top down” approaches in pharmacokinetic modelling: Fitting PBPK models to observed clinical data. *Br J Clin Pharmacol* **79**:48–55.

Tucker GT (1981) Measurement of the renal clearance of drugs. *Br J Clin Pharmacol* **12**:761–70.

Tucker GT, and Boas RA (1971) Pharmacokinetic aspects of intravenous regional anesthesia. *Anesthesiology* **34**:538–49.

Tuk B, Danhof M, and Mandema JW (1997) The impact of arteriovenous concentration differences on pharmacodynamic parameter estimates. *J Pharmacokinet Biopharm* **25**:39–62.

Uchino H, Tamai I, Yamashita K, Minemoto Y, Sai Y, Yabuuchi H, Miyamoto KI, Takeda E, and Tsuji A (2000) p-aminohippuric acid transport at renal apical membrane mediated by human inorganic phosphate transporter NPT1. *Biochem Biophys Res Commun* **270**:254–259.

US Food and Drug Administration (FDA). (2019) Development of Best Practices in Physiologically Based Pharmacokinetic Modeling to Support Clinical Pharmacology Regulatory Decision-Making.

Varma MVS, Feng B, Obach RS, Troutman MD, Chupka J, Miller HR, and El-Kattan A (2009) Physicochemical determinants of human renal clearance. *J Med Chem* **52**:4844–4852.

Vogl S, Lutz RW, Schönfelder G, and Lutz WK (2015) CYP2C9 genotype vs. metabolic phenotype for individual drug dosing-A correlation analysis using flurbiprofen as probe drug. *PLoS One* **10**.

Volkow ND, Fowler JS, Wang GJ, Shumay E, Telang F, Thanos PK, and Alexoff D (2010)

Distribution and pharmacokinetics of methamphetamine in the human body: Clinical implications. *PLoS One* **5**:1–6.

Wagner C, Zhao P, Pan Y, Hsu V, Grillo J, Huang SM, and Sinha V (2015a) Application of Physiologically Based Pharmacokinetic (PBPK) Modeling to Support Dose Selection : Report of an FDA Public Workshop on PBPK. *Clin Pharmacol Ther* **4**:226–230.

Wagner C, Zhao P, Pan Y, Hsu V, Grillo J, Huang SM, and Sinha V (2015b) Application of Physiologically Based Pharmacokinetic (PBPK) Modeling to Support Dose Selection: Report of an FDA Public Workshop on PBPK. *CPT pharmacometrics Syst Pharmacol* **4**:226–30.

Wagner DJ, Sager JE, Duan H, Isoherranen N, and Wang J (2017) Interaction and transport of methamphetamine and its primary metabolites by organic cation and multidrug and toxin extrusion transporters. *Drug Metab Dispos* **45**:770–778.

Wang Q, Zheng M, and Leil T (2017) Investigating Transporter-Mediated Drug-Drug Interactions Using a Physiologically Based Pharmacokinetic Model of Rosuvastatin. *CPT pharmacometrics Syst Pharmacol* **6**:228–238.

Wedlund PJ, Aslanian WS, McAllister CB, Wilkinson GR, and Branch RA (1984) Mephenytoin hydroxylation deficiency in Caucasians: frequency of a new oxidative drug metabolism polymorphism. *Clin Pharmacol Ther* **36**:773–780.

Welling LW, and Welling DJ (1988) Relationship between structure and function in renal proximal tubule. *J Electron Microsc Tech* **9**:171–85.

Welling PG, Craig WA, Amidon GL, and Kunin CM (1973) Pharmacokinetics of trimethoprim and sulfamethoxazole in normal subjects and in patients with renal failure. *J Infect Dis* **128**:Suppl:556-66 p.

Welling PG, Shaw WR, Uman SJ, Tse FL, and Craig WA (1975) Pharmacokinetics of minocycline in renal failure. *AntimicrobAgents Chemother* **8**:532–537.

Wilkinson GR, and Shand DG (1975) Commentary: a physiological approach to hepatic drug clearance. *Clin Pharmacol Ther* **18**:377–90.

Williams JA, Hyland R, Jones BC, Smith DA, Hurst S, Goosen TC, Peterkin V, Koup JR, and Ball SE (2004) Drug-drug interactions for UDP-glucuronosyltransferase substrates: a pharmacokinetic explanation for typically observed low exposure (AUCi/AUC) ratios. *Drug Metab Dispos* **32**:1201–8.

Yamashita S, Furubayashi T, Kataoka M, Sakane T, Sezaki H, and Tokuda H (2000) Optimized conditions for prediction of intestinal drug permeability using Caco-2 cells. *Eur J Pharm Sci* **10**:195–204.

Yang X, Doerge DR, Teeguarden JG, and Fisher JW (2015) Development of a physiologically based pharmacokinetic model for assessment of human exposure to bisphenol A. *Toxicol Appl Pharmacol* **289**:442–456, Elsevier B.V.

Yazdanian mehran, Glynn SL, Wright JL, and Hawi A (1998) Correlating Partiitioning and Caco-2 Cell Permeability of Structurally Diverse Small Molecular Weigt Compounds. *Pharm Res* **15**:1490–1494.

Yee KL, Li M, Cabalu T, Sahasrabudhe V, Lin J, Zhao P, and Jadhav P (2018) Evaluation of Model-Based Prediction of Pharmacokinetics in the Renal Impairment Population. *J Clin Pharmacol* **58**:364–376.

Yee S (1997) In vitro permeability across Caco-2 cells (colonic) can predict in vivo (small intestinal) absorption in man - Fact or myth.

Yeh BPY, Tomko DJ, Stacy WK, Bear ES, Haden HT, and Falls WF (1975) Factors influencing

sodium and water excretion in uremic man. *Kidney Int* **7**:103–110, Elsevier Masson SAS.

Yeung CK, Shen DD, Thummel KE, and Himmelfarb J (2014) Effects of chronic kidney disease and uremia on hepatic drug metabolism and transport. *Kidney Int* **85**:522–528.

Yi JH, Han SW, Song JS, and Kim HJ (2012) Metabolic alkalosis from unsuspected ingestion: Use of urine pH and anion Gap. *Am J Kidney Dis* **59**:577–581.

You X, Wu W, Xu J, Jiao Z, Ke M, Huang P, and Lin C (2020) Development of a Physiologically Based Pharmacokinetic Model for Prediction of Pramipexole Pharmacokinetics in Parkinson's Disease Patients With Renal Impairment. *J Clin Pharmacol*, doi: 10.1002/jcph.1593.

Zhang F, Xue J, Shao J, and Jia L (2012) Compilation of 222 drugs' plasma protein binding data and guidance for study designs. *Drug Discov Today* **17**:475–485, Elsevier Ltd.

Zhang Z, Imperial MZ, Patilea-Vrana GI, Wedagedera J, Gaohua L, and Unadkat JD (2017) Development of a novel maternal-fetal physiologically based pharmacokinetic model I: Insights into factors that determine fetal drug exposure through simulations and sensitivity analyses. *Drug Metab Dispos* **45**:920–938.

Zhang Z, and Unadkat JD (2017) Verification of a Maternal-Fetal Physiologically Based Pharmacokinetic Model for Passive Placental Permeability Drugs. *Drug Metab Dispos* dmd.116.073957.

Zhao P, Vieira Mde L, Grillo JA, Song P, Wu TC, Zheng JH, Arya V, Berglund EG, Atkinson Jr. AJ, Sugiyama Y, Pang KS, Reynolds KS, Abernethy DR, Zhang L, Lesko LJ, and Huang SM (2012) Evaluation of exposure change of nonrenally eliminated drugs in patients with chronic kidney disease using physiologically based pharmacokinetic modeling and simulation. *J Clin Pharmacol* **52**:91S-108S.

Zhao P, Zhang L, Grillo J a, Liu Q, Bullock JM, Moon YJ, Song P, Brar SS, Madabushi R, Wu TC, Booth BP, Rahman N a, Reynolds KS, Gil Berglund E, Lesko LJ, and Huang S-M (2011) Applications of physiologically based pharmacokinetic (PBPK) modeling and simulation during regulatory review. *Clin Pharmacol Ther* **89**:259–267.

Ziesenitz VC, König SK, Mahlke NS, Skopp G, Haefeli WE, and Mikus G (2015) Pharmacokinetic interaction of intravenous fentanyl with ketoconazole. *J Clin Pharmacol* **55**:708–717.

Zoccali C, Vanholder R, Massy ZA, Ortiz A, Sarafidis P, Dekker FW, Fliser D, Fouque D, Heine GH, Jager KJ, Kanbay M, Mallamaci F, Parati G, Rossignol P, Wiecek A, and London G (2017) The systemic nature of CKD. *Nat Rev Nephrol* **13**:344–358, Nature Publishing Group.

VITAE

Weize Huang was born in Beijing, China. In 2013, he earned his Honors Bachelor of Science (B.Sc.) in Biochemistry with Highest Distinction (Top 1%) from Purdue University, West Lafayette, Indiana. He then joined the University of Washington for Doctor of Pharmacy (Pharm.D.) program in Seattle, Washington, while working for Dr. Isoherranen as a part-time student. He graduated with Pharm.D. degree in 2017, and joined the Doctor of Philosophy (Ph.D.) program in Pharmaceutics under Dr. Isoherranen's supervision in Seattle, Washington. Weize Huang was the recipient of Ho and Hwang Outstanding Leadership in Biotechnology & Biopharmaceuticals Award (2017), Warren G. Magnuson Scholarship (2018), William E. Bradley Scholarship (2019), and Danny Shen Travel Award (2020) from School of Pharmacy, University of Washington.